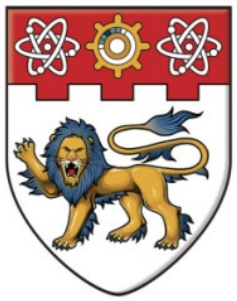

NANYANG TECHNOLOGICAL UNIVERSITY

THE CRYSTAL CHEMISTRY OF ELLESTADITE FOR THE IMMOBILISATION OF INCINERATOR FLY ASH

FANG YANAN

SCHOOL OF MATERIALS SCIENCE AND ENGINEERING

2015

THE CRYSTAL CHEMISTRY OF ELLESTADITE FOR THE IMMOBILISATION OF INCINERATOR FLY ASH

FANG YANAN

School of Materials Science and Engineering

A thesis submitted to the Nanyang Technological University in partial fulfillment of the requirement for the degree of Doctorate of Philosophy

2015

Abstract

Incineration is the method of choice for the volume reduction of municipal waste generated in Singapore. While effective, the total amount of ash produced is substantial, and contains significant quantities of toxic metals, such as Cr, Cd, Pb, As, and V. Typically, incinerator ash is deposited directly in controlled landfills, which is costly and, in some circumstances, leads to the gradual spread of toxic metals via the hydrosphere. Consequently, there is a clear need to investigate new materials for stabilization that address two critical issues - waste loading and chemical durability. This thesis is concerned with the design, synthesis and characterization of ceramic waste form oxides, analogous to durable mineral species, that contain a range of ionic acceptor sites which can capture hazardous cations and anions in their least toxic chemical states.

The structural adaptability of apatite waste forms has attracted significant interest for the stabilization of municipal incinerator waste (MSW) fly ashes. The thermodynamic and chemical stability of apatites under a wide range of conditions, and relative insolubility in natural environments make them effective materials for remediation. Apatites adopt hexagonal (or pseudohexagonal) symmetry, the most common space group being $P6_3/m$, and conform to the general stoichiometry $[A(1)_4][A(2)_6][(BO_4)_6][X_2]$. They are framework structures in which $A(1)_4B_6O_{24}$ walls, composed of $A(1)O_6$ metaprism columns corner-connected to the BO_4 tetrahedra to create tunnels that surround the $A(2)_6X_2$ component. As the relative size of the framework and tunnel contents vary, the metaprism twists through an angle φ. In MSW ash, metalloids such as Si, S, As, and V are often relatively abundant, as are the halides (F, Cl, Br) found widely in consumer products. Therefore, for this study, ellestadite-type apatites with the ideal formula $Ca_{10}[(SiO_4)_3(SO_4)_3](Cl, F)_2$ were chosen for investigation as an immobilization matrices due to their capacity to incorporate cationic and anionic toxic species.

To this end, three ellestadite series $Ca_{10}[(SiO_4)_x(BO_4)_{6-2x}(SO_4)_x][(Cl_{1-y}X_y)_2]$ (B = P, V and X = F) were synthesized and the crystallographic structures studied by powder

X-ray and neutron diffraction. These synthetic materials, unlike mineral specimens that are well equilibrated, show no Si/P/S ordering and conform to $P6_3/m$ symmetry, except for the vanadium endmember $Ca_{10}[(SiO_4)_x(VO_4)_{6-2x}(SO_4)_x]Cl_2$ ($x = 0$) where the rotation of VO_4 tetrahedra lowers the lattice metric to triclinic P-1 to achieve more satisfactory bond-valence sums. As expected, the unit cell volume decreases as smaller cations enter the *B* sites, with a concomitant increase in the CaO_6 metaprism twist angle (φ). For fluor-chlorellestadite solid solutions $Ca_{10}[(SiO_4)_3(SO_4)_3][Cl_{2-x}F_x]$, all compositions conform to $P6_3/m$ symmetry where F^- is located at the 2*a* (0, 0, 1/4) position, while Cl^- is displaced out of the 6*h* Ca(2) triangle plane and occupies 4*e* (0, 0, *z*) split positions with *z* ranging from 0.336(3) to 0.4315(3). Increasing fluorine content, leads to a progressive shift of Cl^- toward the center of the Ca(2) triangle. Calcium and chlorine deficiencies are always observed in ellestadites due to the evaporation of $CaCl_2$ during the synthesis.

Leach tests found increasing dissolution of apatite as Si/S progressively replaces P, with a significant change in solubility, and therefore free energy of formation ΔG_f, especially for $x \geq 1$ in $Ca_{10}[(SiO_4)_x(PO_4)_{6-2x}(SO_4)_x]Cl_2$. Similarly, the incorporation of vanadium (also a proxy for Cr, As) should not exceed a loading of 25 at% V to avoid significant dissolution. The introduction of F in place of Cl improves stability. Moreover, CaF_2 precipitation may serve as a barrier to further ellestadite dissolution. Therefore, ellestadites where Si/S less than 33 at% and V less than 25 at% at *B* sites prove most chemically resistant to TCLP extractions, and this waste loading should not be exceeded for immobilization of silicon, sulphur and toxic metal rich wastes.

These synthetic studies, supported by comprehensive characterization tools, create the systemization required to explore tailoring ellestadites to incorporate MSW ash to high waste loadings and with good durability. Future investigations should include the treatment of real fly ash compositions, with validation of the relationship of crystal structure flexibility and chemical conditioning to enhance durability.

The central hypothesis of this thesis, that the chlorellestadites $Ca_{10}[(SiO_4)_2(PO_4)_2(SO_4)_2]Cl_2$ possesses sufficient crystallochemical flexibility for exploitation as a ceramic waste form for the immobilization of incinerator fly ash

was proven. However, the compositional boundaries to retain the waste are less extensive than originally envisaged.

Acknowledgements

First of all, I would like to express my deepest gratitude to my supervisor Professor Tim White for his guidance, patience and support, providing insightful comments and valuable discussions throughout my postgraduate studies. In addition, I would like to thank Assoc. Prof. Dong Zhili, Prof. Christian Kloc and Prof. Chen Zhong for their suggestions in the Thesis Advisory Committee.

I would like to thank Dr. Clemens Ritter for his help in the neutron diffraction data collection at Institut Laue-Langevin. I extend my gratitude to Prof. Lim Teik-Thye for his support on inductively coupled plasma atomic emission spectroscopy and ion chromatography tests at school of civil and environmental engineering.

I am grateful to my friends Dr. Zhao Ting, Dr. Hou Ran Low, Ms. Eileen Goh, Dr. Li Henan, Dr. Wei Fengxia for their help and friendship throughout my studies. Many thanks to the staff of the Facility for Analysis, Characterization, Testing and Simulation (FACTS) for their cooperative technical assistance.

Finally I thank my family for their continuous support and encouragement all the time.

This work was supported by NTU Research Scholarship provided by Nanyang Technological University.

Publications

1. **Yanan Fang**, C. Ritter, T. White, The Crystal Chemical Characteristics of Ellestadite-type apatite: Implications for Toxic Metal Immobilization. *Dalton Transactions*, 2014, 43, 16031
2. **Yanan Fang**, C. Ritter, T. White, The Crystal Chemistry of $Ca_{10-y}(SiO_4)_3(SO_4)_3Cl_{2-x-2y}F_x$ Ellestadite. *Inorganic Chemistry*, 2011, 50, 12641
3. **Fang Yanan**, Hong Zhanglian, Li Ming, et. al., Effect of buffer solutions on surface adsorbed organics and visible light photocatalytic activity of TiO_2 nano-photocatalyst with single anatase phase. *Rare Metal Materials and Engineering*, 2008 May
4. **Yanan Fang**, T. White, The Crystal Chemistry of Vanadium-bearing Ellestadite Waste forms. *Inorganic Chemistry*, submitted
5. Tom Baikie, **Yanan Fang**, Jeannette M. Kadro, Martin Schreyer, Fengxia Wei, Subodh G. Mhaisalkar, Michael Grätzel and Tim J. White ;Synthesis and Crystal Chemistry of the Hybrid Perovskite $(CH_3NH_3)PbI_3$ for Solid State Sensitized Solar Cell Applications. *J. Mater. Chem. A*, 2013, 1 (18), 5628 – 5641
6. Tom Baikie, N. S. Barrow, **Yanan Fang**, P. J. Keenan, P. R. Slater, et. al., A combined single crystal neutron/X-ray diffraction and solid-state nuclear magnetic resonance study of the hybrid perovskites $CH_3NH_3PbX_3$ (X= I, Br and Cl). *J. Mater. Chem. A*, DOI: 10.1039/c5ta01125f
7. Natalia Yantara, D. Sabba, **Yanan Fang**, Jeannette M. Kadro, Thomas Moehl, Pablo P. Boix, Subodh Mhaisalkar, Michael Grätzel and Carole Grätzel, Loading of mesoporous titania films by $CH_3NH_3PbI_3$ perovskite, single step vs. sequential deposition. *Chem. Commun*., 2015, 51, 4603
8. N. Yantara, **Yanan Fang**, Shi Chen, H. A. Dewi, et. al. Unravelling the Effects of Cl Addition in Single Step $CH_3NH_3PbI_3$ Perovskite Solar Cells. *Chemistry of Materials*, 2015, DOI: 10.1021/cm502710r
9. L. H. Nguyen, V. Aravindan, S. A. Kulkarni, **YN. Fang**, Rajiv R. Prabhakar, Sudip K. Batabyal and Srinivasan Madhavi; Self-Assembled Ultrathin Anatase TiO_2 Nanosheets with Reactive (001) Facets for Highly Enhanced Reversible Li Storage. *ChemElectroChem*, 2014, 14, 539-543
10. Koh, Teck Ming; Fu, Kunwu; **Fang, Yanan**; Chen, Shi; Sum, Tze Chien;

Mathews, Nripan; Mhaisalkar, Subodh; Boix, Pablo P.; Baikie, Tom, Formamidinium-Containing Metal-Halide – An Alternative Material for Near-IR Absorption Perovskite Solar Cells. *J. Mater. Chem. C,* 2013, 13,

11. Kunwu Fu, Swee Sien Lim, **Yanan Fang**, Pablo P. Boix, Nripan Mathews, Tze Chien Sum, et. al., Modulating $CH_3NH_3PbI_3$ perovskite crystallization behavior through precursor concentration. *NANO*, 2014, 9, 1440003

12. X.-M.Ge, **Y.-N. Fang**, S.-H. Chan, Design and Optimization of Composite Electrodes in Solid Oxide Cells. *Fuel Cells*, 2012, 12, 61

13. Xiaoming Ge, Lan Zhang, **Yanan Fang**, Jie Zeng, Siew Hwa Chan, Robust solid oxide cells for alternate power generation and carbon conversion. *RSC Advances*, 2011, 1, 715

14. Ming Li, Z. L. Hong, **Y. Fang**, F. Huang, Synergistic effect of two surface complexes in enhancing visible-light photocatalytic activity of titanium dioxide. *Materials Research Bulletin*, 2008, 43, 2179

15. F. Wei, H. Gasparyan, P. J. Keenan, M. Gutmann, **Y. Fang**, T. Baikie, et. al., Anisotropic oxide ion conduction in melilite intermediate temperature electrolytes. *J. Mater. Chem. A*, 2015, 3, 3091

16. Shijing Sun, **Yanan Fang**, Gregor Kieslich, Tim J. White and Anthony K. Cheetham, Mechanical Properties of Organic-Inorganic Halide Perovskites, $CH_3NH_3PbI_3$ (X=I, Br and Cl) by Nanoindentation, *J. Mater. Chem. A*, submitted.

Table of Contents

List of Tables

statistically significant deficit of Ca appears for (Si/S) rich ellestadites. Chlorine is underestimated due to volatilization under the electron beam. Chlorine contents derived from neutron diffraction (see Table 4.2) are more reliable.

List of Figures

= 0.429) and two Cl^- (z = 0.434 and 0.153) sites in the apatite ($Ca_{10}(PO_4)_6Cl_2$) tunnel. Contour interval is 0.2 e/Å^3 and the first positive contour (solid line) is at 0.2 e/Å^3. Negative difference nuclear density is indicated by the broken contours.

Figure 4.8 Chirographic view of the chlorine ion environment and difference Fourier maps before and after including Cl ions in the tunnel, (a) $Ca_{10}[(SiO_4)_3(SO_4)_3]Cl_2$ and (b) $Ca_{10}(PO_4)_6Cl_2$. The sphere radii represent isotropic thermal displacements. Contour interval is 0.2 e/Å^3 and the first positive contour (solid line) is at 0.2 e/Å^3. Negative difference nuclear density is indicated by the broken contours.

Figure 4.9 Correlation of composition and metaprism twist angle (φ). Errors are within the size of the symbols.

Figure 4.10 Trends in metaprism twist angel for $Ca_{10}[(SiO_4)_x(PO_4)_{6-2x}(SO_4)_x]Cl_2$ as a function of (a) average effective ionic radius for the whole unit cell contents, (b) chlorine content in per formula unit, and (c) average effective *B*-Cation radius.

Figure 4.11 HRTEM images taken from [001] zone axis of (a) $Ca_{10}[(SiO_4)_{1.5}(PO_4)_3(SO_4)_{1.5}]Cl_2$ and (b) $Ca_{10}[(SiO_4)_{0.5}(PO_4)_5(SO_4)_{0.5}]Cl_2$ ellestadite.

Figure 4.12 SAD pattern taken from [001] zone axis of (a) $Ca_{10}[(SiO_4)_3(SO_4)_3]Cl_2$ and (b) $Ca_{10}[(SiO_4)_2(PO_4)_2(SO_4)_2]Cl_2$. No diffuse intensity or split reflections are present.

Figure 5.1 Rietveld fitting pattern for (a) x = 0, (b) x = 0.4 and (c) x = 2. (x in $Ca_{10}[(SiO_4)_3(SO_4)_3][Cl_{2-x}F_x]$) Lines and dots denote observed and calculated profile intensities, respectively. Short vertical bars represent Bragg reflection positions. The difference (observed – calculated) is plotted below.

Figure 5.2 Expanded views of FT-IR spectra for the fluor-chlorellestadite solid solution. (x in $Ca_{10}[(SiO_4)_3(SO_4)_3][Cl_{2-x}F_x]$)

Figure 5.3. Variation in cell parameters (a) a and c, and (b) unit cell volume with

degree of fluorine substitution x in $Ca_{10}[(SiO_4)_3(SO_4)_3][Cl_{2-x}F_x]$. Standard deviation of data is smaller than size of points. The open circles in (b) are taken from the literature.

Figure 5.4 Partial X-ray powder diffraction patterns of ellestadites with x = 0, 0.8, 1.6. (x in $Ca_{10}[(SiO_4)_3(SO_4)_3][Cl_{2-x}F_x]$).

Figure 5.5 Difference Fourier maps of the $Ca_{10}[(SiO_4)_3(SO_4)_3][Cl_{2-x}F_x]$ ellestadite tunnel indicating the positions of F and/or Cl ions that were excluded to emphasize their location. (a) Chlorellestadite (x = 0), (b) Fluor-chlorellestadite (x = 0.8), and (c) Fluorellestadite (x = 2). Contour interval is 0.5 e/Å^3 and the first positive contour (solid line) is at 0.5 e/Å^3. Negative difference nuclear density is indicated by the broken contours.

Figure 5.6 Perspective drawing of Ca(2) triangle arrangement on the screw axis (a) x = 0.4, and (b) x = 1.6. (x in $Ca_{10}[(SiO_4)_3(SO_4)_3][Cl_{2-x}F_x]$) F^- lies in the centre of Ca(2) triangle on the mirror planes, while Cl^- splits into two half-occupied sites above or below the mirror plane. The interatomic distances are in Å. The distances between Cl site and the mirror plane (z = 1/4) are indicated by the dotted lines.

Figure 5.7 Difference Fourier map at y = 0 for $Ca_{10}[(SiO_4)_3(SO_4)_3]Cl_{0.8}F_{1.2}$. Fluorine and chlorine ions were included at z = 1/4 and z = 0.342, respectively. Contour interval is 0.25 e/Å^3 and the first positive contour (solid line) is at 0.25 e/Å^3. Negative difference nuclear density is indicated by the broken contours. The range of difference nuclear density is -0.45 ~ 0.38 e/Å^3.

Figure 5.8 Dependence of (a) z_{Cl} and (b) twist angle on degree of fluorine substitution x in $Ca_{10}[(SiO_4)_3(SO_4)_3][Cl_{2-x}F_x]$.

Figure 5.9 Correlations observed between polyhedral distortion parameters: (a) δ_{Ca1} versus $\phi_{O3\text{-}Ca2\text{-}O3}$, (b) $<\tau_{O\text{-}B\text{-}O}>$ versus $\varphi_{O3\text{-}Ca2\text{-}O3}$, (c) $\Psi_{Ca1\text{-}O1}^{Ca1\ z=0}$ versus α_{Ca1}, and (d) α_{Ca2} versus $\phi_{O3\text{-}Ca2\text{-}O3}$. These figures should be compared with Fig.8 in Mercier et al. Circles: published data; large filled squares: this study. (δ_{Ca1}:counter-rotation

angle of CaO_6 polyhedra; $\phi_{O3\text{-}Ca2\text{-}O3}$: O3-Ca2-O3 bond angle; $<\tau_{O\text{-}B\text{-}O}>$: O-B-O bond-bending angle; $\Psi_{Ca1\text{-}O1}{}^{Ca1\ z=0}$: angle that an $Ca1_{z=0}$-O1 bond makes with respect to *c*; α_{Ca1}: orientation of CaO6 polyhedra with respect to *a*; α_{Ca2}: orientation of Ca2 triangles with respect to *a*.)

Figure 5.10 (a) Wide field [001] HRTEM image of $Ca_{10}[(SiO_4)_3(SO_4)_3][Cl_{0.4}F_{1.6}]$, (experimental, FFT and simulated SAED reflections are provided.) (b) The as-collected images (left) and processed image (right) constrained by *p*6 symmetry are shown.

Figure 6.1 Electron backscatter images (BSI) showing the two-phase textures of $Ca_{10}[(SiO_4)_x(SO_4)_x(VO_4)_{6-2x}]Cl_2$, (a) $x = 1.5$ and (b) $x = 1.0$.

Figure 6.2 Rietveld fit between calculated (black dot) and experimental (black line) diffraction profiles for $Ca_{10}[(SiO_4)_x(SO_4)_x(VO_4)_{6-2x}]Cl_2$, with (a) nominal $x = 1.5$ and (b) $x = 1.0$. At these compositions immiscibility is reflected by co-existing ellestadite phase pairs.

Figure 6.3 FT-IR absorption spectra of $Ca_{10}[(SiO_4)_x(SO_4)_x(VO_4)_{6-2x}]Cl_2$ for $x = 0$, 2, and 3.

Figure 6.4 Variation in cell parameters (*a* and *c*), unit cell volume and metaprism twist angle with degree of Si/S substitution *x* in $Ca_{10}[(SiO_4)_x(SO_4)_x(VO_4)_{6-2x}]Cl_2$. Standard deviation of data is smaller than point size.

Figure 6.5 Difference Fourier maps showing residual electron density along [001] using hexagonal model without *X* anion in the tunnel (a) $Ca_{10}(VO_4)_6Cl_2$, (b) $Ca_{10}[(SiO_4)_3(SO_4)_3]F_2$ [29], and (c) $Ca_{10}(PO_4)_6Cl_2$ [30]. Contour interval is 0.20 e/Å^3 and the first positive contour (solid line) is at 0.20 e/Å^3. (The red, green and blue dots in (a) represent the V, Cl and Ca atoms.) For $Ca_{10}(VO_4)_6Cl_2$ the large residual is indicative of the material not conforming to $P6_3/m$, in contrast to $Ca_{10}[(SiO_4)_3(SO_4)_3]F_2$ and $Ca_{10}(PO_4)_6Cl_2$.

List of Abbreviations:

ANSTO	Australian Nuclear Science and Technology Organization
ATR	Attenuated Total Reflectance
BEI	Backscatter Electron Images
BSE	Backscattered Electron
BVS	Bond Valence Sum
CN	Coordination Number
EDS	Energy Dispersive X-ray Spectroscopy
EPMA	Electron Probe Microanalysis
FTIR	Fourier Transform Infrared Spectroscopy
HRTEM	High Resolution Transmission Electron Microscopy
ILL	Institut Laue-Langevin
OPAL	Open Pool Australian Lightwater
PXRD	Powder X-ray Diffraction
R_{wp}	Weighted R-Bragg
SAED	Selected Area Electron Diffraction
SEM	Scanning Electron Microscopy
SEI	Secondary Electron Images
TEM	Transmission Electron Microscopy
WT %	Wight Percent
XRD	X-ray Diffraction
Z	Atomic Number

Chapter 1

Introduction

Municipal solid waste (MSW) generated in households and by light industrial activity consists primarily of packaging materials, food wastes and discarded appliances. These materials are voluminous, and while often sent directly to landfill, an alternate strategy in larger urban centers is incineration to reduce bulk and destroy hazardous chemicals entrained in the refuse. The products of incineration include bottom ash, composed primarily of metal and slag, and fly ash that is captured through scrubbing flue dust. The physical and chemical properties of fly ash render these residues potentially harmful and consolidation prior to disposal or reuse is necessary. This thesis is concerned with demonstrating the crystal chemical feasibility of incorporating the components of MSW fly ash in ellestadite-type oxides in a process that mimics the closure of lithogenic metal cycles.

1.1 Problem Statement

Incineration is a thermal treatment process which exploits the calorific value of organic substances contained in waste materials while minimizing the discharge of volatile by-products. Ideally, waste combustion offers several benefits including substantial volume reduction to ash, the concentration of toxic chemicals by precipitation of the flue gas, and the co-generation of electricity through heat capture. Ashes are primarily inorganic residues, that while variable in physical appearance and composition, typically take the form of aggregates (bottom ash) or powders (fly ash).

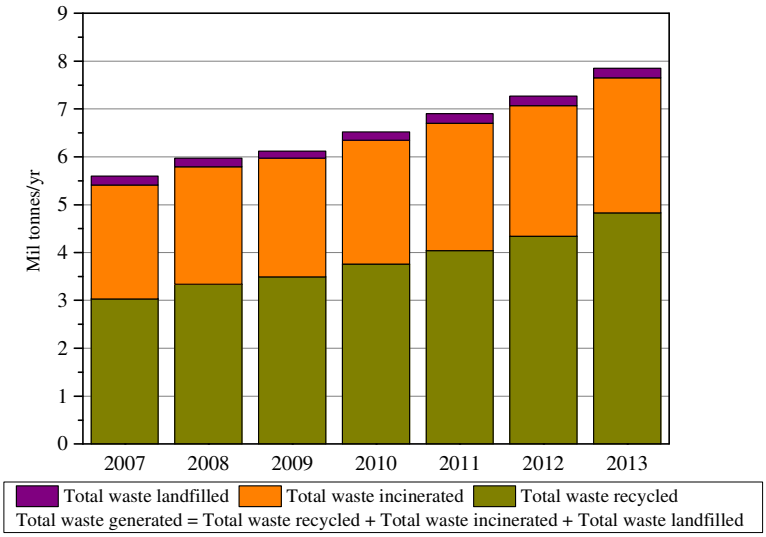

Figure 1.1 Municipal solid waste (MCW) production and treatment in Singapore (Ministry of the Environment and Water Resources, Singapore).

Landfill is the most expedient and inexpensive disposal method for municipal solid waste (MSW) incinerator ash and is used in many countries. However, land disposal space, especially for the most hazardous wastes is limited, and surface and groundwater hydrology may not favor widespread and long-term storage of wastes. Consequently, there is a clear need to investigate new technologies and materials for stabilization that address two critical issues – waste loading and chemical durability.

In Singapore, incineration is deployed for managing municipal solid wastes (MSW)

that cannot be recycled [1, 2] and while the total amount increases year-on-year, the fraction going directly to landfill is constant (Figure 1). After incineration, bottom ash accounts for 250-300 kg/1000 kg of waste and hazardous fly ash 25-30 kg/1000 kg, with additional products of the flue gas cleaning processes collected by dry and /or wet scrubbing [3]. The fly ash is especially problematic as it contains mobile and harmful organic and inorganic compounds [4-7]. A primary concern is potential ground water contamination by heavy metals in leachates released from buried incinerator fly ash. Whether MSW ash is destined for landfills or recycling, technologies that transform the material into environmentally acceptable forms are required.

Immobilization refers to the practice of employing additives and/or binders to limit the hazardous nature of a waste by conversion to solids of lower solubility to attenuate intrinsic toxicity, often with concurrent modification of metal oxidation states. In a holistic sense, the solution to ash mobilization lies in closing metal cycles by converting waste into 'synthetic ores' for reuse, or returning this 'natural waste form' to exhausted mines. This approach is known as Synthetic Mineral Immobilization Technology (SMITE), that directly addresses metal overload in the biosphere by using pyrometallurgical processes to convert waste into synthetic igneous rock [8]. SMITE stabilization is premised upon replicating minerals characterized by their capacity to incorporate high levels of toxic metals and having demonstrable longevity in well-described geological settings. A surprisingly small subset of mineral families is capable of incorporating all the common metal wastes in their crystal lattices. Developing SMITE stabilization technologies requires a good knowledge of mineralogy. Based on the chemical composition and phases present in a waste, a ceramic assemblage is designed using crystallochemical principles that can accommodate all the waste components. In other words, a stabilization system is proposed that can be later tested against expected solid state chemical and geological precepts.

The present research is concerned with the design, synthesis and characterization of ceramic waste form oxides, analogous to durable mineral species, that contain a range of ionic acceptor sites which can capture hazardous cations and anions in their least toxic chemical states.

Many materials have been proposed for heavy metal immobilization, and minerals (e.g. apatite, zeolite, or clay) [9, 10] are considered promising alternatives to currently available remediation methods for certain intractable wastes. For example, apatite-based technologies use compounds of ideal formula $A_{10}(BO_4)_6X_2$ to stabilize toxic metal wastes by chemically binding them in stable phosphate analogues ($A_{10}(PO_4)_6X_2$) [11]. Many phosphate apatites have low solubility, although durability varies as a function of composition and disposal conditions (i.e. temperature, pH). In MSW ash, metalloids such as Si, S, As, and V are often relatively abundant, as are the halides (F, Cl, Br) found widely in consumer products. Therefore, for this study, ellestadite-type apatite with the ideal formula $Ca_{10}[(SiO_4)_3(SO_4)_3][(OH, Cl, F)_2]$, was chosen for investigation as an immobilization matric due to its capacity to incorporate cationic and anionic toxic species.

This thesis tests the hypothesis that synthetic chlorellestadite, prototypically $Ca_{10}[(SiO_4)_2(PO_4)_2(SO_4)_2]Cl_2$, *possesses the crystallochemical capacity to incorporate and retain the principal classes of toxic elements found in municipal solid waste (MSW) fly ash in its crystal structure.*

In nature, ellestadite is a rare member of the apatite mineral family [12]. Apatites are chemically diverse, and ellestadite can incorporate in its structure numerous toxic metals that report to fly ash, including lead, cadmium, arsenic and vanadium [13]. Natural ellestadites found in Crestmore, California and the Chichibu Mine, Japan [14] have been the subjects of limited structural analysis. The important characteristic of this mineral is that phosphate (PO_4^{3-}), the metalloid constituent of hydroxyl, fluoro and chloro apatite ($Ca_{10}(PO_4)_6[(OH,F,Cl)_2]$, is completely replaced by equimolar portions of sulfate (SO_4^{2-}) and the silicate (SiO_4^{4-}) groups without compensating substitutions elsewhere in the structure. For this study, a fundamental understanding of the crystal chemistry, structural properties, and durability of waste bearing ellestadite ceramics is sought. These outcomes allow a preliminary assessment of the viability of this waste form, including approaches to large scale processing, and economic evaluation on the basis of waste loading and potential for reuse or recycling of the stabilized products.

1.2 Objectives and Scope

Four chemical series were synthesized to establish the continuity of ellestadite solid solutions incorporating key toxic species. From these materials, crystallographic data were collected and the relationship between chemical stability and stoichiometry determined. This baseline material was also screened by standard leach testing, to understand the relative importance of congruent and incongruent dissolution.

The objectives of this research were to:

(I) synthesize ellestadite solid solution series by the solid state method;

(II) establish a comprehensive understanding of the crystallochemical capabilities of ellestadite to incorporate ionic species representative of inorganic hazardous; and

(III) design and fabricate products optimized as immobilization matrices for toxic metal concentrates.

The scope of the work includes:

(I) Ellestadite fabrication

Four ellestadite solid solution series were designed, to simulate specific crystallochemical aspects of actual MSW fly ash. These waste forms were prepared using conventional solid-state reaction of metal oxides, carbonates, hydroxides, sulphates and metal halides. The compositional joins investigated were:

(1) $Ca_{10}[(SiO_4)_3(SO_4)_3]Cl_2 – Ca_{10}(PO_4)_6Cl_2$ (to establish baseline data)

(2) $Ca_{10}[(SiO_4)_3(SO_4)_3]Cl_2 – Ca_{10}[(SiO_4)_3(SO_4)_3]F_2$ (to examine the stabilization waste halides)

(3) $Ca_{10}(SiO_4)_3(SO_4)_3Cl_2 – Ca_{10}(VO_4)_6Cl_2$ (where vanadium is a proxy for several toxic metal including V^{5+}, Cr^{5+}, and As^{5+})

(4) $Ca_{10}(VO_4)_6Cl_2 – Cd_{10}(VO_4)_6Cl_2$ (where cadmium is a proxy for Sr^{2+}, Ba^{2+}, and Pb^{2+})

Reactions were conducted as a function of temperature and time to prepare equilibrated ceramics. In particular, the possibility of miscibility gaps was examined.

(II) Comprehensive characterization:

(1) *Powder diffraction*: Powder X-ray (XRD) and neutron powder diffraction (NPD) when used in combination allow many aspects of crystallochemistry to be studied, including atomic-scale disorder, subcell and supercell relationships, and bond-length trends and polyhedral distortions, with especial emphasis on large cation AO_6 metaprismatic twisting.

(2) *Spectroscopy*: Fourier transform infrared spectroscopy (FTIR) quantitatively distinguishes different tetrahedral groups (SiO_4, PO_4, SO_4, and VO_4), and analyzes structural modifications from changes in the number and position of IR absorption bands.

(3) *Electron microscopy*: The morphology and atomic structure of ellestadites were examined by scanning electron microscopy (SEM) and transmission electron microscopy (TEM). High resolution transmission electron microscopy (HRTEM) and selected area electron diffraction (SAED) were used to search for structural defects, confirm crystal structures, and validate symmetry. Backscattered electron imaging, energy dispersive X-ray spectroscopy, and electron microprobe analysis were employed for chemical analysis.

(4) *Solubility and durability*: The durability and leach resistance of the ellestadites were studied with the toxicity characteristic leaching procedure (TCLP). The correlation between corrosion and composition was established, and the environmental implications considered.

1.3 Dissertation Overview

The thesis addresses the design and optimization of ellestadites as potential MSW fly ash stabilization phases. These investigations are essential to establish if such materials have the stability necessary for deployment as recycled secondary products and also consider if fabrication will be economical at large scale. The dissertation first focuses on the systematic crystallochemical study of key ellestadite solid solution series, then describes the performance of ellestadites as eco-materials for

immobilization.

Chapter 1 provides a rationale for the research and outlines the goals and scope.

Chapter 2 reviews the literature concerning immobilization treatments for fly ash generally, and specifically the synthesis and performance of apatite as a waste form product. The crystallochemical flexibility of the apatite family is detailed, which provides a rationale for tailoring ellestadite crystal chemistry for toxic metal fixation.

Chapter 3 discusses the principles underlying the synthesis and characterization techniques employed, and why particular methods are appropriate for analyzing crystallochemical properties and waste form performance.

Chapter 4 elaborates for the first time the solid solution of $Ca_{10}[(SiO_4)_x(PO_4)_{6-2x}(SO_4)_x]Cl_2$ ellestadites using powder neutron diffraction, including Fourier difference mapping to examine the tunnel chlorine contents. All these ellestadites, synthesized by short duration (9 hours) heat treatment, have $P6_3/m$ symmetry and show no evidence of Si/P/S ordering at the tetrahedral sites. In detail, there are calcium and chlorine deficiencies in the Si/S rich compositions ($3 \leq x \leq 2$) due to the evaporation of $CaCl_2$ during the synthesis. For $x \leq 1.5$ where the Ca and Cl sites are fully occupied, a second low occupancy Cl site appears in the tunnel to reduce steric repulsion with the O(3) triangles.

Chapter 5 is concerned with the synthesis and characterization of fluor-chlorellestadite solid solutions $Ca_{10}[(SiO_4)_3(SO_4)_3][Cl_{2-x}F_x]$. The positions of halides in the ellestadite tunnel were studied by neutron diffraction and Fourier difference mapping. Increasing fluorine content, leads to a progressive shift of chlorine toward the center of the Ca(2) triangle leading to a shorter and stronger Ca(2)-Cl bond that may enhance the chemical stability of ellestadite.

Chapter 6 demonstrates the tailoring of ellestadites to incorporate vanadium. $Ca_{10}[(SiO_4)_x(VO_4)_{6-2x}(SO_4)_x]Cl_2$ ($0 < x < 3$) ellestadites were synthesized and characterized by powder XRD, neutron diffraction, EPMA and FTIR. A miscibility

gap is observed for $0.77 < x < 2.44$, where V-rich and Si/S-rich ellestadites coexisted. All the compositions adopt hexagonal $P6_3/m$ symmetry, except for the vanadate endmember ($Ca_{10}(VO_4)Cl_2$) where rotation of the larger VO_4 tetrahedra lowers the symmetry to triclinic P-1. The $Ca(1)O_6$ metaprism twist angle (φ) dilates with the substitution of smaller atoms at BO_4 sites.

Chapter 7 describes the toxicity characteristic leaching procedure (TCLP) for evaluating the solubility of ellestadites series described in *Chapters 4, 5 and 6*. It was found that increasing Si/S content reduces the durability of $Ca_{10}[(SiO_4)_x(PO_4)_{6-2x}(SO_4)_x]Cl_2$, especially for $x \geq 1$. The introduction of F^- in place of Cl^- increases the stability of $Ca_{10}[(SiO_4)_3(SO_4)_3][Cl_{2-x}F_x]$, while the incorporation of vanadium beyond 25 at% leads to substantially higher dissolution rates. From these performance characteristics the compositional boundary conditions were mapped as a basis for tailoring ellestadite waste form chemistry.

Chapter 8 draws together the crystallochemical studies and durability testing of ellestadites to design a ceramic for containment of a real MSW fly ash to a waste loading of 8.59 wt%. The possibly of conditioning ash through mixing with semiconductor industry CaF_2 sludge and fertilizer factory phosphoric acid discharge to increase overall waste loading was considered. Outstanding experiments and modelling required to translate these results into an eco-material technology are summarized.

1.4 Findings and Outcomes

This research led to several novel outcomes by:

1 Establishing a comprehensive understanding of the crystallochemical capabilities of ellestadite for accommodating simulated waste using neutron and X-ray diffraction techniques; and

2 Correlating solubility and leaching performance of ellestadite with composition and physical form, and identifying the optimal composition range of waste forms.

References:

[1] B. L. Sawhney, C. R. Frink. *Water, Air, and Soil Pollution*. **1991**, 57-58, 289-296.

[2] L. C. Tan, V. Choa, and J. H. Tay. *Environ. Monitor. & Assess*. **1997**, 44, 275-284.

[3] A. Jakob, S. Stucki, and P. Kuhn. *Environ. Sci. Technol*. **1995**, 29, 2429.

[4] Z. Abbas, Z. P. Moghaddan, B. M. Steenari. *Waste Manage*. **2003**, 33, 291-305.

[5] H. K. Hansen, A. J. Pedersen, L. M. Ottosen, A. Villumsen. *Chemosphere* **2001**, 45, 123-128.

[6] B. Steenari, L. G. Karlsson, O. Lindqvist. *Biomass Bioenergy* **1999**, 16, 119-136.

[7] K. Wang, K. Chiang, K. Lin, C. Sun. *Hydrometallurgy* **2001**, 62, 73-81.

[8] T. J. White, I. A. Toor. *J. Mater*. **1996**, 48, 54-58.

[9] A. M. Ghrair, J. Ingwersen, T. Streck. *J. Plant Nutrition & Soil Sci*. **2010**, 173, 852-860.

[10] A. Usman, Y. Kuzyakov, K. Stahr. *J. Soils & Sediments*, **2005**, 5, 245-252.

[11] J. L. Conca, J. Wright. *Applied Geochem.* **2006**, 21, 1288-1300.

[12] D. McConnell. *Amer. Mineral*. **1938**, 23, 1-9.

[13] H. Poellmann, Mineral Reservoirs for Immobilisation Purposes of Hazardous Materials, in Advances in Environmental Materials, Volume II, Environmentally Preferred Materials, eds. T. J. White and J. A. Stegemann, Symposium Proceedings ICMAT 2001, Materials Research Society (Singapore), **2001**.

[14] K. Harada. *Amer. Mineral*. **1971**, 56, 1507-1518.

Chapter 2

Literature Review

Many remediation technologies are available for waste treatment that vary in effectiveness and cost. Synthetic Mineral Immobilization Technology is an approach that stabilizes metals in accord with mineralogical principles. For the development of a synthetic mineral immobilization system, two factors must be considered: first, the mineral assemblage should be flexible and accept a wide range of waste compositions, and second, the immobilized elements must be retained near quantitatively as the surrounding physical and chemical conditions change. Ellestadite is a silicon- and sulphur-rich member of the apatite family that may be suitable for the consolidation of municipal waste incinerator fly ash as a ceramic waste form. It is proposed that crystallochemical tailoring, which balances the proportions of additives and waste constituents, will allow durable ellestadites to be synthesized for space-efficient disposal or deployment as a recycled product.

2.1 Overview of Immobilization Treatments for MSW Fly Ash

The threat of groundwater contamination from landfill leachates and the general unsightliness of landfill areas have shifted attention toward incineration as an alternative means of municipal solid waste (MSW) disposal. As a well-developed technology, incineration reduces landfill volume consumption substantially (~ 90%). However, there is much public concern about possible human health hazards associated with emissions from MSW incinerators, the fallout of contaminants in surrounding areas, and the safe disposal of residual ash. Fly ash is a combustion residue comprising fine particles entrained with the flue gases that is removed from exhaust gases primarily by electrostatic precipitators and secondarily by scrubber systems. Fly ash particles are generally spherical in shape, range in size from 0.5 μm to 300 μm and contain the more volatile toxic species such as As, Cd, Cr, Cu, Hg, Ni, Pb, Sb and Zn [1, 2].

The amount of fly ash produced by an MSW incinerator is in the order of 1-3% of the waste input mass on a wet basis, but due to their volatilization and subsequent condensation, fly ash bears high concentrations of heavy metals, salts and organic pollutants. The German experience in managing MSW ashes is instructive [3, 4]. Here, bottom ash is not classified as a hazardous waste according to the European Waste Catalogue, and is frequently deployed as a construction material. For example, iron scrap and other metals are usually recovered from bottom ash and reused in industry, with the remains commonly recycled as a secondary building material for civil engineering applications [5]. In contrast, fly ashes are deployed in low concentration as cement additives and as non-structural construction materials, or are solidified by moistening to activate pozzolanic solidification in the disposal site [6].

The infrequent utilization of MSW fly ash is inevitable due to the potential for leaching and release of heavy metals (Cd, Zn, Pb, Hg, Cu, Cr and Ni) and toxic organic compounds to the environment. In addition, as fly ash is produced by high-temperature processes, it is thermodynamically unstable under ambient conditions and prone to mineralogical alteration when exposed to the wider environment, especially precipitation and ground water [7]. Changes in the phase assemblage,

physio-chemical characteristics, and leaching behavior are inevitable until the ash equilibrates with the surroundings. Environmental instability makes it difficult for fly ash to replace primary raw materials (e.g. sand), unless it is chemically stabilized beforehand. Nonetheless, successful stabilization technologies will simultaneously have positive impacts on waste minimization and extend landfill lifetimes.

Various methodologies including thermal treatment, physical/chemical separation [8, 9], and stabilization/solidification (S/S) [10, 11] are available for fly ash treatment prior to reuse or final disposal. In addition, vitrification has been tested and practiced on a small scale. However, this method is more costly, energy intensive, requires expensive apparatus, and may suffer from heavy metal volatilization during melting [12, 13]. Nonetheless, it is appropriate for certain classes of radioactive waste residues where cost has less impact due to the extreme hazard posed by these materials.

As an alternative to thermal treatment, physical/chemical separation methods employed for extracting heavy metals (Cd, Pb and Zn) from fly ash have been attempted, but with limited success. Consequently, stabilization and solidification (S/S) methods have emerged as viable alternatives for MSW fly ash treatment by blending with Portland cement into stable complexes [14]. In this context, toxic components are incorporated in the cement matrix through either physical or chemical immobilization mechanisms, depending on the particular contaminant and the type of binder used [15]. This technique has long been known as an economical option for waste management; however, solidification with Portland cement presents some disadvantages. Specifically, protection against humidity is required to prevent breakdown and leaching of heavy metals [16]. In addition, salts present in fly ash can interfere with basic hydration reactions of cement, leading to less durable phases and/or physical deterioration of the waste form over time [17].

An overview of several common stabilization technologies, with the advantages and disadvantages for fly ash treatment, is presented in Table 2.1.

Table 2.1 Overview of different technologies for fly ash treatment.

Technologies	Advantages	Disadvantages	References
washing with water	simple process, mainly for soluble chloride and alkali ions	not effective for trace metals removal	[8], [18]
use hydraulic binders including cement, lime and pozzolanic materials	improve the leaching behavior of solidified/stabilized incineration residues	weak stabilization efficiencies for soluble salts; problematic for zinc and lead treatment	[9], [19], [20]
chemical stabilization processes using sulfides, soluble phosphates, and carbonates	good leaching properties at relatively low costs;	increased amounts for landfills; the physical encapsulation from the binder cannot last for long term	[21], [22], [23]
aging and weathering	significant reduction in trace elements and leaching; formation of more stable mineral species;	have the potential of mobilizing sulfate	[24], [25]
vitrification, sintering	a more homogeneous, denser product with improved leaching properties;	require substantial amounts of energy; result in the mobilization of volatile elements such as Hg, Pb	[12], [13]

2.1.1 Cement-based techniques

MSW fly ash can be used as a partial replacement for cement in concrete. The high pH of cement ensures most metals are in the form of insoluble hydroxide or carbonate salts within the hardened structure. This approach is tolerant of variations in the chemical and physical characteristics of ash. The fixation properties of cement can be improved by introducing clay, but there is considerable debate concerning the precise nature of these fixation mechanisms and their contribution to the long-term durability of concrete, as some cations, oxyanions and anions either cannot be chemically incorporated at high levels or degrade key structural properties. Moreover, low-strength cement-waste mixtures can be attacked by acid leaching that accelerates contaminant loses. For instance, metals such as Cd, Cu and Zn [26, 27] from cement can be mobilized by carbonation through the following reactions:

$$Cd(OH)_2 + CO_2 \rightarrow CdCO_3 + H_2O \quad (2\text{-}1)$$

$$2\ CuO + CO_2 \rightarrow Cu_2(OH)_2CO_3 \quad (2\text{-}2)$$

Similar phenomena take place in self-hardened ashes or after immobilization in concrete. From the perspective of product development, the variability of fly ash compositions may prevent its use as a supplementary material wherever consistent performance in structural stability and strength is required.

2.1.2 Glass and Glass-Ceramics

MSW fly ash can be melted at high temperature (above 1300°C), and for certain silica-rich compositions glass-ceramics can be obtained by controlled devitrification through a two stage heat treatment that promotes nucleation and crystallization [28, 29]. In the nucleation stage, stable nuclei form within the parent glass, and from these, crystallization of new phases is seeded. This process can either encapsulate the heavy metals in a silicate matrix, or permit separation by evaporation or differential precipitation. Usually, glass forming agents are introduced to ensure the product has the required physical and chemical characteristics.

Devitrification during fabrication or after disposal/deployment, can adversely affect the durability of glass. Immobilizing glasses are largely amorphous, but may contain crystals susceptible to corrosion, although these phases are usually free of toxic elements [30]. The resistance of glass to leaching arises from the formation of a protective amorphous layer, in a complex process that can be difficult to model over geological time scales.

2.1.3 Ceramic Incorporation Technologies

Compared to other treatments, Synthetic Mineral Immobilization Technology (SMITE) can give a high level of confidence in the long-term stability of materials, especially by analogy to geological settings, and attain higher waste loadings compared to cementitious or vitreous waste forms [31, 32]. Appropriate combinations of metal hydroxy salts, ettringite, zeolite, sodalite, apatite and spinel mineral phases derived from wastes can ensure all toxic components are contained in these mineral reservoirs [33, 34, 89]. These durable minerals act as an internal primary barrier at the atomic-scale, allowing the treated waste to be sent directly for landfill disposal. SMITE products can also be used as secondary raw materials, especially aggregate, and so preserve natural resources. Moreover, modeling and prediction of long-term behavior is feasible due to the resemblance to naturally occurring, durable minerals with definite thermodynamic and kinetic properties. Consequently, synthetic minerals are expected to be more robust than glasses over a wide pH range.

Current approaches normally require the design of waste forms based on a subset of minerals known to display excellent leach resistance. Additives are introduced in proportions appropriate for the synthesis of the desired minerals [35]. The potential advantage of this technology is that high-waste-loaded and high-density waste forms can be fabricated while maintaining excellent chemical durability. These properties can translate into considerable savings during transport and disposal. To achieve these objectives, it is necessary to synthesize specific mineral phases that are capable of incorporating all the hazardous components of the waste, and so produce a durable and environmentally acceptable product.

Apatites are candidate single-phase ceramic forms for municipal incinerator ash, due to their considerable crystal chemical flexibility, with the more insoluble fluoro- or chloro-apatites employed to permanently fix the toxic species. In addition to being sparingly soluble over a range of pH, apatites show the desirable qualities of incorporating many inorganic waste species at high concentration in their least toxic valence states, and are also compatible with cost effective fabrication [36, 37].

2.2 Why Apatites?

A highly adaptable ceramic framework structure for inclusion in SMITE waste forms is the apatite type [38, 39]. The toxic metals stabilized in apatite are retained in a product of high durability and leach resistance that significantly exceeds many other chemically stabilized forms. This is because crystal chemical adaptation of the apatite framework leads to crystals that are stable over a wide environmental range, and can even resist high radiation fluxes [40]. Apatites can maintain their integrity for hundreds of millions of years and virtually guarantee the retention of metals quantitatively. It is for this reason that apatites are often used for geological dating [41].

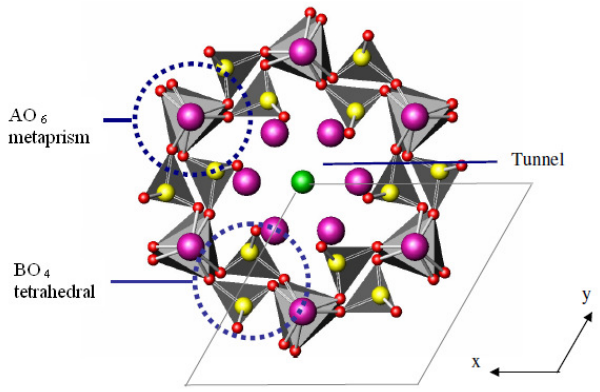

Figure 2.1 The crystal structure of hexagonal $P6_3/m$ apatite projected along the *c*-axis. The unit cell is outlined. The A^{I}-centered oxygen polyhedra are represented as 6-fold coordinated metaprisms. $A^{I}O_6$ metaprism share faces along [001] and are corner-connected to BO_4 tetrahedra to form one-dimensional tunnels that are filled by A^{II} and *X* ions.

For high symmetry $P6_3/m$ apatites, the general formula can be expressed as $[A^{I}_4][A^{II}_6][(BO_4)_6][X]_2$. The framework topology (Figure 2.1) is tolerant to many cation substitutions (see section 2.3) as a result of three crystallochemical adaptations.

(I) There are two crystallographically distinct *A*-sites. The anion coordination of the *A*(1) site is $A(1)O_6$ and metaprismatic, lying between octahedral and trigonal prismatic coordination. The $A(1)O_6$ metaprisms are corner-connected to BO_4 tetrahedra whose topology creates one-dimensional "tunnels". These tunnels contain *A*(2) cations and *X* anions such that the co-ordination polyhedra are $A(2)O_6X$ or $A(2)O_6X_2$. In cases where the *A*(2) cation has stereochemically active electron lone pairs, the *X* anions can be absent (e.g. $[Pb_8K_2](PO_4)_6$ [42]). Additionally, lead- and bismuth-rich silicate apatites can show polymorphic modifications that create Si_2O_7 units (as in $[Ca_8Pb_{12}](Si_2O_7)_6Cl_4$ nasonite [43], and $Pb_{40}(Si_4O_{13})_3(Si_2O_7)_6O_7$ [87]).

(II) Structural flexibility also arises because BO_4 tetrahedra are essentially rigid polyhedra that tilt to accommodate surrounding ions of different size without disrupting polyhedral connectivity – this sometimes leads to the creation of polymorphs. Also, oxygen nonstoichiometry is possible through conversion of some BO_4 tetrahedra to BO_3 (as in $Pb_{10}(AsO_3)_6Cl_2$ [44]) and BO_5 units (as in $Ba_{10}(ReO_5)_6O_2$ [45]).

(III) Apatite may display *X*-site nonstoichiometry that facilitates charge balance for chemically complex substitutions. For example,

$Ca^{2+} + Cl^{-} \rightarrow Na^{+} + \square_{Cl}$ (2-3)

in $[Ca_{4-x}Na_x][Ca_6](PO_4)_6[Cl_{2-x}]$.

These three adaptations make apatites inherently flexible, as the tunnel diameter can dilate or contract to accommodate ions of different size and concentration.

Apatite structural modifications facilitate waste stabilization and can be described quantitatively through the measurement of AO_6 metaprism twisting. This parameter proves to be a very sensitive measure of stoichiometry, and across solid solution series should vary predictably and systematically. Therefore, when there is a departure from ideal stoichiometry or thermodynamic equilibrium, the metaprism twisting will behave anomalously. In $P6_3/m$ apatites, the metaprism twist angle (ϕ) is defined as the (001) projected angle of the O (layer 1)-A^{I}-O (layer 2) bonds, and can be used to describe the deviation of apatites from the prototypes [46]. The degree of twist is controlled by the relative sizes of the wall A^{I} and *B* atoms compared to the tunnel atoms A^{II} and *X*, which in turn is related to chemistry. When anions of smaller ionic radii occupy the tunnel, the bond interactions among *X*, A^{II} and O will be accommodated by adjustment of the metaprism to a smaller or larger twist angle. Consequently, the channel diameter contracts as the ionic radii of the tunnel anion is reduced. This can be illustrated in the simple chemical series $Cd_{10}(PO_4)_6(OH)_2$ (ϕ = 25.8°), $Cd_{10}(PO_4)_6Cl_2$ (ϕ = 19.5°) and $Cd_{10}(PO_4)_6Br_2$ (ϕ = 16.0°) [47], where the twist angle becomes progressively more acute as the tunnel expands to accommodate the larger *X* anion. While $5° < \phi < 24°$ is commonly encountered, larger twist angles require the tetrahedron to rotate about [100] to achieve acceptable bond valence sums, and in so doing, the lattice symmetry is reduced to monoclinic or triclinic. Therefore, for all symmetries, ϕ can be used to investigate crystal chemical trends - hexagonal and trigonal types possess a single twist angle per metaprism, while in monoclinic apatites the $A^{I}O_6$ are distorted with three (space group $P2_1/m$) or six (space group $P2_1$) unique twist angles (Figure 2.2).

In addition, the synthesis of single-phase apatites is relatively straightforward. For example, hydroxyapatite $Ca_{10}(PO_4)_6(OH)_2$ can be prepared by calcium and

phosphate precipitation reactions or high temperature solid state processes, or derived from animal bones by heat treatment or oxidation with hydrogen peroxide to remove the organic fraction. Heat treatment has the advantage of producing a highly crystalline apatite. Well crystallized synthetic apatites should exhibit similar physical and chemical properties to natural apatite, and in the context of waste immobilization, may even show superior performance with appropriate selection of additives (e.g. fluorine-rich compositions are generally less soluble than hydroxyl-rich chemistries).

Synthetic chlorapatite has been widely investigated. It is dimorphic [48], appearing as the monoclinic ($P2_1/b$) and almost stoichiometric form ($Ca_{10}(PO_4)_6Cl_2$), plus a hexagonal ($P6_3/m$) variety that is slightly substoichiometric in chlorine ($Ca_{10-x}(PO_4)_6Cl_{2-2x}$, $x < 23\%$, [49]). For the monoclinic phase, complete filling of the tunnel by Cl requires tilting of the PO_4 tetrahedra that doubles the b-axis with $120° \leq \gamma \leq 120.2°$ [48].

Analysis of the metaprism twist angle (ϕ) in the $P6_3/m$ and $P2_1/b$ phases can be rationalized with respect to chlorine content. When the tunnel is fully occupied by chlorine the tunnel must dilate and $\phi_{min} = 12.4°$. However, by removing some chlorine, the tunnels contracts slightly so that ϕ becomes larger. During this relaxation the centres of inversion are removed, all tetrahedra become crystallographically equivalent, and a single metaprism with $\phi_{hex} \approx 19°$ results. Because the Cl-vacancies are disordered there is no inter-tunnel correlation in the hexagonal form. Differentiation of the hexagonal and monoclinic phases is challenging, and preparation of a specific dimorph requires careful control of chlorine-loss and may also be related to the rate of crystallization.

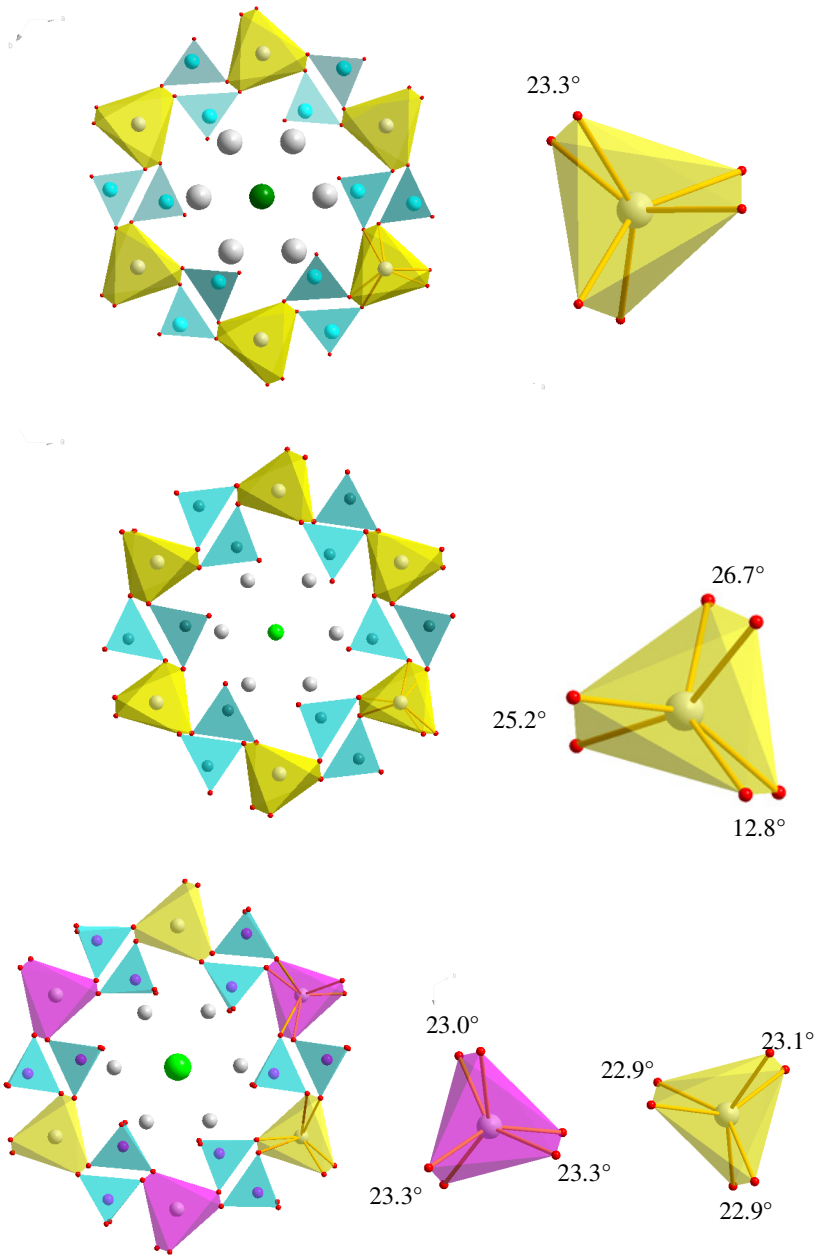

Figure 2.2 Polyhedral drawings for compounds representative of three common apatite space groups with various $Ca^{I}O_6$ metaprism twist angles, (a) $Ca_{10}(PO_4)_6(OH)_2$, hexagonal $P6_3/m$, (b) $Ca_{10}(VO_4)_6F_2$, monoclinic $P2_1/m$ and (c) $Ca_{10}(PO_4)_6Cl_2$, monoclinic $P2_1$.

2.3 Ellestadite Crystallography and Chemistry

Many MSW fly ashes prove difficult to treat due to the high concentration of halides, alkali metals and sulfur. For these compositions, ellestadite-like apatites show particular promise as waste form ceramics, however our crystallochemical knowledge is presently insufficient to tailor formulations and predict durability reliably.

Ellestadites are silicon- and sulphur-rich apatites that for the most part have been studied as minerals, rather than synthetic analogues, with crystallochemical analysis quite limited. Ellestadite and other sulfate-silicate apatites containing halogens and minor amounts of CO_3 and PO_4 were first described by McConnell (1937), who distinguished it from wilkeite[1] chiefly on the basis of chemical composition [50]. Whereas wilkeite contains 20.85% P_2O_5, McConnell found a specimen with only 3.06% P_2O_5 and called it ellestadite. No lowering of space group symmetry was evident for ellestadite, and the mineral was visually indistinguishable from wilkeite. The crystal chemistry of ellestadite, wilkeite, and intermediate compositions was further explored by McConnell (1938) [51] who first recognized isomorphous charge-compensated substitutions of PO_4^{3-} by SiO_4^{4-} and SO_4^{2-} that previously were only known in silicate apatite containing rare-earth elements, e.g. britholite [52]. After this first identification, ellestadite was not studied again for almost 30 years until Harada et al. [53] reported the existence of hydroxyellestadite, $[Ca_{9.66}Na_{0.11}Sr_{0.03}Fe_{0.03}K_{0.02}][(SiO_4)_{2.86}(SO_4)_{2.68}(CO_3OH)_{0.37}(PO_4)_{0.09}][(OH)_{1.88}Cl_{0.26}F_{0.15}]$, from the Chichibu Mine, Saitama Prefecture, Japan where the $(PO_4)^{3-}$ of hydroxyapatite was almost completely displaced by $(SO_4)^{2-}$ and $(SiO_4)^{4-}$ groups via coupled substitution. The new mineral was found to be crystallographically and chemically similar to ellestadite, except for the fact that OH > (F + Cl), and the space group was assigned as $P6_3/m$ on the basis of X-ray precession photographs.

In addition to natural occurrences, Maenami et al. [54] reported hydroxyellestadite in fly ash obtained from pressurized fluidized bed combustion. Klement [55, 56] synthesized fluorellestadite $Ca_{10}[(SiO_4)_3(SO_4)_3]F_2$ and hydroxyellestadite

[1] Wilkeite is now a discredited mineral name and should be referred to as phosphorous-rich ellestadite. The analytical chemist Ruesen B. Ellestad was recognized for his contributions to mineralogy by having this species named after him.

$Ca_{10}[(SiO_4)_3(SO_4)_3](OH)_2$, along with a number of other exotic apatite isotypes containing PO_4, SiO_4, and SO_4 in various proportions, some of which deviated from the ideal apatite stoichiometry. A fluorellestadite-bearing assemblage, containing characteristic blue veins, was identified in burned materials from spoil heaps in the Rosice-Oslavany coalfield, that were pyrometamorphic assemblages of a dolomite-anhydrite-gypsum protolith where $T_m > 800$ °C [57].

Chlorellestadite $Ca_{10}[(SiO_4)_3(SO_4)_3]Cl_2$ topology consists of CaO_6 metaprisms sharing faces along [001], with these metaprism columns corner-connected by SiO_4 and SO_4 tetrahedra to form tunnels that contain CaO_7Cl polyhedra. In common with the majority of apatite compounds, chorellestadite crystallized as hexagonal $P6_3/m$ and presents a polyhedral topology similar to chlorapatite, with replacement of two P^{5+} by one Si^{4+} and one S^{6+} [51]. To our knowledge, crystallization of the stoichiometric chlorellestadite in the monoclinic system has not been reported, unlike chlorapatite, but the monoclinic metric is observed in natural ellestadite, although not with $P2_1/b$ symmetry. For example, in a single crystal X-ray diffraction study of the Chichibu Mine specimen, Sudarsanan [58] assigned $P2_1/m$ with three sets of 2*e* B-site tetrahedra, rather one 6*h* tetrahedra B-site as found in $P6_3/m$. The 2*e* positions were ordered such that SO_4, SiO_4 or $(Si_{0.5}S_{0.5})O_4$ tetrahedra were present, based on the analysis of relative B-O bond lengths. However, this ordering was incomplete and the presence of trace elements prevented deriving an unambiguous solution. In another mineral study, Organova et al. [59] found similar ordering but reported $P2_1$ symmetry and two independent CaO_6 metaprisms.

In general, the detailed analysis of ellestadite symmetry can be complicated due to the wide variety of aliovalent and altervalent ionic substitutions possible that include, but are not limited to:

$$Ca^{2+} \leftrightarrow Cd^{2+} \quad (2\text{-}4)$$

$$Si^{4+} + S^{6+} \leftrightarrow 2\ P^{5+} \quad (2\text{-}5)$$

$$Si^{4+} + S^{6+} \leftrightarrow 2\ V^{5+} \quad (2\text{-}6)$$

$$Ca^{2+} + Si^{4+} \leftrightarrow Na^{+} + P^{5+} \quad (2\text{-}7)$$

$$F^{-} \leftrightarrow Cl^{-} \quad (2\text{-}8)$$

In addition, charge balance can be achieved through coupled cation–anion replacements and non-stoichiometry such as:

$Ca^{2+} + F^- \leftrightarrow Na^+ + \square$ (2-9)

$Si^{4+} + F^- \leftrightarrow P^{5+} + O^{2-}$ (2-10)

While the overall compositional variation accompanying these substitutions is straightforward, the crystallographic changes that permit these replacements are complex. For example, in the simple apatite system $[Ca_xPb_{10-x}](VO_4)_6F_2$ with $0 < x < 10$, order-disorder phenomena at the atomic scale were observed and catalogued [60]. In the context of this study, the preparation of ellestadite with complex ion substitutions is relevant not only for the preparation of new materials, but also for acquiring deeper insights into the crystallographic parameters that control the physical and chemical properties, and ultimately waste form durability.

2.4 Dissolution and Solubility of Apatite Group Minerals

2.4.1 Solubility of Apatite Ceramics

The apatite phosphate group displays a large solubility range and has been extensively studied, with many reports describing the capture of hazardous metals such as lead and arsenic (Table 2.2). Nevertheless, solubility relations are complex, readily modified by pH and temperature, and by the presence of trace foreign metal ions in hydroxyapatite $Ca_{10}(PO_4)_6(OH)_2$ that can enhance durability either by decreasing solubility or increasing its kinetic inertness. For example, the solubilities of endmember $A_{10}(BO_4)_6X_2$ apatites are strongly dependent on the nature of the X group, but this relationship is quite different for Ca versus Pb analogues. For $Ca_{10}(PO_4)_6X_2$ the magnitude of log K varies in the order F < OH < Cl [61, 62], whereas for $Pb_{10}(PO_4)_6X_2$ the order is Cl < OH < F [65-67]. In arsenic apatites, the relationships are more complex because the AsO_4^{3-} and AsO_3^{3-} groups can be accommodated in the apatite. For both $Pb_{10}(AsO_4)_6X_2$ and $Ca_{10}(AsO_4)_6X_2$, the above order is Cl < OH, that reflects a subtle interaction between lattice and hydration energies.

Table 2.2 Solubility products (K_{sp}) of Ca and Pb apatite phosphates and arsenates.

Mineral	Chemical composition	log K_{sp}	References
Chlorapatite	$Ca_{10}(PO_4)_6Cl_2$	-53.08	[61]
Fluorapatite	$Ca_{10}(PO_4)_6F_2$	-59.99	[61]
Hydroxyapatite	$Ca_{10}(PO_4)_6(OH)_2$	-56	[62]
Johnbaumite	$Ca_{10}(AsO_4)_6(OH)_2$	-38.04	[63]
Turneaureite	$Ca_{10}(AsO_4)_6Cl_2$	-51.7	[64]
Pyromorphite	$Pb_{10}(PO_4)_6Cl_2$	-83.61	[65]
Fluorpyromorphite	$Pb_{10}(PO_4)_6F_2$	-71.56	[66]
Hydroxypyromorphite	$Pb_{10}(PO_4)_6(OH)_2$	-76.71	[67]
Mimetite	$Pb_{10}(AsO_4)_6Cl_2$	-83.38	[65]
Hydroxymimetite	$Pb_{10}(AsO_4)_6(OH)_2$	-73	[68]

A theoretical interpretation of the solubility dependence of an ionic crystal on anionic replacement is possible through thermodynamic considerations. For an ionic compound, the change in the Gibbs energy accompanying dissolution, ΔG_{soln}, is related to K_{sp}, at a given temperature, T, and can be calculated by the expression

$$\Delta G_{soln} = -RT \ln K_{sp} \qquad (2\text{-}11)$$

using the experimental value of K_{sp}. Alternatively, it can be evaluated by regarding dissolution of an ionic compound as consisting of two stages: (i) breaking down of the crystal architecture, and (ii) the hydration of the constituent ions set free, resulting in the expression

$$\Delta G_{soln} = \sum \Delta G_{hy} - \Delta G_{lattice} \qquad (2\text{-}12)$$

where $\sum \Delta G_{hy}$ is the sum of the Gibbs energy changes of hydration of the constituent ions of the solute, while $\Delta G_{lattice}$ is the Gibbs energy change during formation of the lattice. The terms on the right-hand side of equation (2-12) can be calculated for an ionic crystal and shown to be dependent on the replacement of a given anion by another with a divergent ionic radius, as is the case with PO_4^{3-} and AsO_4^{3-} ions.

2.4.2 Dissolution Models of Apatite

Several models have been proposed to describe apatite dissolution processes and predict changes associated with solution characteristics (pH, composition saturation, and hydrodynamics), bulk solid properties (chemical composition, solubility, particle sizes), and the surface structure (defects, adsorbed ions, and phase transformation)

of apatite crystals.

(1) Diffusion and Kinetically Controlled Models

In diffusion-controlled models [69-72], the dissolution rate is mainly determined by transport of either chemical reagents or the products of chemical reaction, whereas the kinetically-controlled model emphasizes surface chemical transformation as the limiting factor. An important consequence of these mechanisms is that for surface controlled process the solution immediately next to the crystal surface is under-saturated with respect to apatite, whereas in the diffusion controlled process this solution is saturated [73]. In some cases, the dissolution of apatite was found to be diffusion controlled [71, 74], while in others it was kinetically controlled [72], and intermediate processes (both kinetically and diffusion controlled) are also observed [75]. Therefore, the results obtained are only valid within the experimental conditions studied, and the extreme sensitivity to the surroundings, can be limit the general utility of these models.

(2) Congruent/Incongruent Dissolution

Congruent/incongruent dissolution [76-79] is based on direct measurements either of ionic concentrations in a solution or the surface composition of apatite during dissolution. Ions in a solid may be released simultaneously, with dissolution rates proportional to their molar concentrations, or alternatively, extracted preferentially with distinct dissolution rates for each ion or crystal chemical class of ions. The latter case always results in a surface layer with a chemical composition different to the bulk.

For acidic dissolution of calcium fluorapatite, F ions were released faster than calcium and phosphate [78, 80]. During initial stages, the F/Ca solution ratio was lower than the solid but rose to reach a plateau higher than in the solid as dissolution progressed, with this effect more pronounced in low-F fluor-hydroxyapatite. This suggests a F-enriched FHAp, rather than pure fluorapatite, precipitates during dissolution [78]. A similar phenomenon of faster dissolution of calcium when compared with that of phosphate was also found [76, 78], with a surface layer of

acidic calcium phosphate (HPO_4^{2-} ion) either suggested or found. Moreover, the presence of simple salts (NaCl, CH_3COONa) influences the equilibrium concentrations of phosphate and calcium ions released from apatite [81].

Dissolution of hydroxyapatite in an aqueous medium is always non-stoichiometric initially, but when the solid is successively equilibrated at any given pH, the solution Ca:P ratio approaches a limiting value of 1.67. Once this value is reached, the solid maintains this solution ratio by dissolving stoichiometrically [82]. Thus, the apatite preparation technique and bulk composition will determine whether congruent or incongruent dissolution is favoured.

(3) Ion Exchange Model

The ion exchange dissolution model supposes adsorption of protons (H^+) and acidic anions ($R\text{-}HCO_3$) from the solution onto the apatite surface with concurrent removal of calcium (Ca^{2+}) and phosphate (PO_4^{3-}) ions [83-85]. For example, uptake of citric acid [83] from a dilute aqueous solution by a synthetic hydroxyapatite was found to be time independent and followed Langmuir isotherms. However, this was not the case when more concentrated solutions were used, where the chemical reaction was followed by time dependent precipitation of calcium citrate when its solubility product was exceeded. [85]

To conclude this description of the dissolution models, each has restricted applicability, but will be correct for specific experimental conditions. The models are appropriate for different aspects of the same process of apatite dissolution; in this sense they are complimentary, with the main distinction made between the transport controlled and surface-reaction controlled mechanisms.

2.5 Development of Ellestadite as a Waste Form

This literature review demonstrates the potential of ellestadite ceramics as matrices for the immobilization of halide-rich fly ash residues. In an earlier study, Neubauer and Pöllmann synthesized $A_{10}[(SiO_4)_3(SO_4)_3]Cl_2$ (A = Ca, Sr, Pb) and solid solution

of $Ca_{10}[(SiO_4)_3(SO_4)_3]Cl_2$-$Ca_{10}(PO_4)_6Cl_2$ and $Ca_{10}[(SiO_4)_3(SO_4)_3]Cl_2$-$Ca_{10}(CrO_4)_6Cl_2$ demonstrated the feasibility of using these materials as a mineral-reservoir for heavy metal immobilization in 1992 [86, 88]. However, several fundamental questions remain to be addressed:

(I) For most toxic metals, it is unknown if complete or partial ellestadite solid solutions can form, and the possibility of miscibility gaps cannot be discounted.

(II) The crystal structure of apatite is complex due to the large number of atom acceptor sites, and the inherent flexibility of the tunnel. As a result, pseudomorphic modifications are common. Therefore, ellestadite polymorphism requires further investigation, including the role of composition and crystallization conditions.

(III) While the durability of apatite has been widely studied, comparable data for ellestadites is lacking. Assessing the resistance of ellestadite to corrosion is a basic requirement for evaluating their suitability for MSW ash stabilization.

These questions are addressed in the following chapters that combine materials synthesis, characterization and durability studies to correlate solubility and composition. In this manner, the viability of ellestadite-based waste forms was investigated.

References:

[1] K. A. Rusch, T. Guo, R. K. Seals. *J. Hazard. Mater.* **2001**, B39,167-16.

[2] M. Li, J. Xiang, S. Hu, L. S. Sun, S. Su, P. S. Li, X. X. Sun. *Fuel* **2004**, 83, 1397-1405.

[3] M. Weil, U. Jeske, L. Schebek. *Waste Manag. Res*. **2006**, 24, 197-206.

[4] T. Sabbas, A. Polettini, R. Pomi, T. Astrup, O. Hjelmar, P. Mostbauer, G. Cappai, G. Magel, S. Salhofer, C. Speiser, S. Heuss-Assbichler, R. Klein, P. Lechner. *Waste Manag.,* **2003**, 23, 61-88.

[5] J. Davis, R. Geyer, J. Ley, J. He, R. Clift. *Resources Conservation & Recycling*, **2007**, 51, 118-140.

[6] D. Dermatas, X. Meng. *Engineering Geology*, **2003**, 70, 377-394.

[7] B. Jha, and D. N. Singh. *Acta Geotechnica Slovenica*, **2012**, 2, 63-71.

[8] T. Mangialardi. *J. Hazard. Mater*. **2003**, 98, 225-240.

[9] K. J. Hong, S. Tokunaga, T. Kajiuchi. *J. Hazard. Mater*. **2000**, 75, 57-73.

[10] N. Alba, E. Vázquez, S. Gasso, J. M. Baldasano. *Waste Manag*., **2001**, 21, 313-323.

[11] T. Mangialardi, A. E. Paolini, A. Polettini, P. Sirini. *J. Hazard. Mater*., **1999**, 70, 53-70.

[12] Y. J. Park, J. Heo. *J. Hazard. Mater*., **2002**, 91, 83-93.

[13] K. E. Haugsten, B. Gustavson. *Waste Manag*., **2000**, 20, 167-176.

[14] J. R. Pan, C. Huang, J. Kuo, S. L. *Waste Manag*. **2008**, 28, 1113-1118.

[15] T. S. Singh, K. K. Pant. *J. Hazard. Mater.,* 2006, 131, 29-36.

[16] Q. Yu, S. Nagataki, J. Lin, T. Saeki, M. Hisada. *Cement and Concrete Research*., **2005**, 35, 1056-1063.

[17] W. K. W. Lee, J. S. J. van Deventer. *Cement and Concrete Research.,* **2002**, 32, 577-584.

[18] Y. Jiang, B. Xi, X. Li, L. Zhang, Z. Wei. *J. Hazard. Mater*., **2009**, 161, 871-877.

[19] J. E. Aubert, B. Husson, N. Sarramone. *J. Hazard. Mater.,* **2006**, 136, 624-631.

[20] J. E. Aubert, B. Husson, N. Sarramone. *J. Hazard. Mater.,* **2007**, 146, 12-19.

[21] A. Nzihou, P. Sharrock. *Waste Manag*., **2002**, 22, 235-239.

[22] B. S. Crannell, T. T. Eighmy, J. E. Krzanowski, J. D. Eusen Jr., E. L. Shaw, C. A. Francis. *Waste Manag*., **2000**, 20, 135-148.

[23] K. J. Hong, S. Tokunaga, Y. Ishigami, T. Kajiuchi. *Chemosphere*, **2000**, 41, 345-352.

[24] S. S. S. Lau, J. W. C. Wong. *Water, Air and Soil Pollution*, **2001**, 128, 243-254.

[25] K. Ojha, N. C. Pradhan, A. N. Samanta. *Bulletin of Materials Science*, **2004**, 27, 555-564.

[26] H. Ecke, N. Menad, A. Lagerkvist. *J. Environ. Eng*., **2003**, 129, 435-440.

[27] B. Pandey, S. D. Kinrade, L. J. J. Catalan. *J. Environ. Manag*., **2012**, 101, 59-67.

[28] L. Barbieri, I. Lancellotti, T. Manfredini, I. Queralt, J. Rincon, M. Romero. *Fuel*, **1999**, 78, 271-276.

[29] T. W. Cheng, Y. S. Chen. *Chemosphere*, **2003**, 51, 817-824.

[30] C. R. Ward, D. French. *Fuel*, **2006**, 85, 2268-2277.

[31] T. J. White, I. A. Toor. *J. Mater*. **1996**; 48, 54-58.

[32] N. P. Laverov, S. V. Yudintsev, T. S. Livshits, S. V. Stefanvsky, A. N. Lukiykh, R. C. Ewing. *Geochemistry International*, **2010**, 48, 1-14.

[33] P. Kumarathasana1, G. J. McCarthya, D. J. Hassetta, D. F. Pflughoeft-Hassetta. *MRS Proceedings*, **1989**, 178, 83.

[34] C. F. Lin, H. C. His. *Environ. Sci. Technol.,* **1995**, 29, 1109–1117.

[35] A. Molina, C. Poole. *Minerals Engineering*, **2004**, 17, 167-173.

[36] X. Chen, J. V. Wright, J. L. Conca, L. M. Peurrung. *Water, Air and Soil Pollution*, **1997**, 98, 57-58.

[37] Q. Y. Ma, S. J. Traina, T. J. Logan, J. A. Ryan. *Environ. Sci. Technol.,* **1993**, 27, 1803-1810.

[38] T. J. White, C. Ferraris, J. Kim and S. Madhavi. *Rev. Mineral Geochem.* **2005**; 57, 307-401.

[39] J. Y. Kim, Z. Dong and T. J. White. *J. Amer. Ceram. Soc*. **2005**; 88, 1253-1260.

[40] R. C. Ewing, A. Meldrum and L. M. Wang. *Rev. Mineral Geochem.* **2000**, 39, 319-361

[41] T. A. Dumitru. *Quaternary Geochronology: Methods and Applications, edited by J.S. Noller, J.M., Sowers, and W.R. Lettis, American Geophysical Union Reference Shelf*, **2000**, 4, 131-156.

[42] M. Mathew, W. E. Brown, M. Austin, T. Negas, J. *Solid State Chem*., **1980**, 35, 69-76.

[43] T. Baikie, C. Ferraris, W. T. Klooster, S. Madhavi, S. S. Pramana, A. Pring, G. Schmidt, T. J. White. *Acta. Cryst*., **2008**, B64, 34-41

[44] T. Baikie, S. S. Pramana, C. Ferraris, Y. Huang, E. Kendrick, K. S. Knight, Z. Ahman, T. J. White, *Acta. Cryst*., **2010**, B66, 1-16.

[45] J. N. Rimbert, F. Dumas, C. Kellershohn, G. Baud, J. P. Besse. *Chemical Physics Letters*, **1988**, 145, 562-566.

[46] S. C. Lim, T. Baikie, S. S. Pramana, R. Smith, T. J. White. *J. Solid State Chem*., **2011**, 184, 1978-1986.

[47] T. J. White, Z. L. Dong. *Acta. Cryst*., **2003**, B59, 1-16.

[48] P. E. Mackie, J. C. Elliott, R. A. Young, *Acta. Cryst*., **1972**, B28, 1840-1848.

[49] S. B. Hendricks, M. E. Jefferson, V. M. Mosley, *Z. Kristallogr. Kristallogeom. Kristallphys. Kristallchem*, **1932**, 81, 352-369.

[50] D. McConnell. *Am. Mineral*. **1937**; 22, 977-986.

[51] D. McConnell. *Amer. Mineral*. **1938**, 23,1-9.

[52] D. C. Noe, J. M. Hughes, A. N. Mariano, J. W. Drexler, A. Kato. *Zeitschrift fur Kristallographie*, **1993**, 206, 233-246.

[53] K. Harada, K. Nagashima, K. Nakao, A. Kato. *Am. Mineral*. **1971**, 56, 1507-1518.

[54] H. Maenami, N. Isu, E. H. Ishida, T. Mitsuda. *Cement and Concrete Research*, **2004**, 34, 781-788.

[55] R. Klement. *Naturwissenschaftern*, **1939**, 27, 57-58.

[56] R. Klement, P. Dihn. *Naturwissenschaftern*, **1941**, 29, 301

[57] P. Hršelová, J. Cempírek, S. Houzar, and J. Sejkora. *Can Mineral*, **2013**, 51, 171-188.

[58] K. Sudasan. *Acta. Cryst*., **1980**, B36,1636-1639.

[59] N. I. Organova, R. K. Rastasvetaeva, O. V. Kuz'mina, G. A. Arapova, M. A. Litsarev, V. I. Fin'ko. *Kristallogr*. **1994**, 39, 278-282.

[60] Z. L. Dong and T. J. White. *Acta Cryst*. **2004**; B60,138-145.

[61] V.M. Valyashko, L.N. Kogarko and I.L. Kodakovsky, Geochem. Int., 5 (1968) 21.

[62] M.C.F. Magalhães, P.A.A.P. Marques and R.N. Correia, *Biomineralization, , E. Königsberger and L.-C. Königsberger, eds. Medical Aspects of Solubility,* **2006**, Wiley, Chichester. 71.

[63] J.V. Bothe, Jr. and P.W. Brown. *J. Hazard. Mater.*, **1999**, B69, 197-207.

[64] T.S.B. Narasaraju, P. Lahiri, P.R. Yadav and U.S. Rai. *Polyhedron*, **1985**, 4, 5358.

[65] A.I. Inegbenebor, J.H. Thomas and P.A. Williams. *Miner. Mag*., **1989**, 53, 363-371.

[66] J.O. Nriagu, *Geochim. Cosmochim. Acta*, **1974**, 38, 887-898.

[67] M. Manecki, P.A. Maurice and S.J. Traina, *Am. Mineral*., **2000**, 85, 932-942.

[68] S.V.C. Rao, *J. Indian Chem. Soc*., **1976**, 53, 587-595.

[69] G.H. Nancollas. *J. Dent. Res*. **1974**, 53, 297-302.

[70] M. Okazaki, Y. Moriwaki, T. Aoba, Y. Doi and J. Takahashi, *J. Dent. Res.* **1981**, 60, 1907-1911.

[71] K.O.A. Chin and G.H. Nancollas. *Langmuir*, **1991**, 7, 2175-2179.

[72] E.P. Paschalis, K. Wikiel and G.H. Nancollas. *J. Biomed. Mater. Res*. 1994, 28, 1411-1418

[73] L.C. Chow. *J. Dent. Res.* **1988**, 67, 1058-1059.

[74] J.M. Thomann, J.C. Voegel, Ph. Gramain. *Calcif Tissue Znt.* **1990**, 46, 121-129.

[75] D.G.A. Nelson, J.D.B. Featherstone, J.F. Duncan and T.W. Cutress. *Caries Res*.

1983, 17, 200-211.

[76] A.N. Smith, A.M. Posner and J.P. Quirk. *J. Colloid Interface Sci*. 1974, 48, 442-449.

[77] S. Amrah-Bouali, C. Rey, A. Lebugle and D. Bernache. *Biomaterials,* **1994**, 15, 269-272.

[78] E.I.F. Pearce, N. Guha-Chowdhury, Y. Iwami and T.W. Cutress. *Caries Res*. **1995**, 29, 130-136.

[79] P.W. Brown and R.I. Martin. *J. Phys. Chem. B*,1999, 103, 1671-1675.

[80] E.C. Moreno, M. Kresak and R.T. Zahradnik. *Caries Res*. **1977**, 11, Suppl. 1, 142-171.

[81] S. Shimabayashi and M. Matsumoto. *Nippon Kagaku Kaishi*, 1993, 10, 1118-1122.

[82] H. Mika, L.C. Bell and B.J. Kruger. *Arch. Oral Biol.* **1976**, 21, 697-701.

[83] D.N. Misra. *J. Dent. Res*. **1996**, 75, 1418-1425.

[84] A. Lopez-Macipe, J. Games-Morales and R. Rodriguez-Clemente. *J. Colloid Interface Sci.* **1998**, 200, 114-120.

[85] D.N. Misra. *J. Biomed. Mater. Res*. **1999**, 48, 848-855.

[86] J. Neubauer, H. Pöllmann, *N. Jb. Miner. Mh*., **1992**, 7, 295-310.

[87] P. Stemmermann, Herbert Pöllmann, *Materials Science Forum*, **1993**, 133-136, 703-708.

[88] J. Neubauer, H. Pöllmann, *N. Jb. Miner. Mh*., **1995**, 3, 237-258.

[89] H. Pöllmann, Reservoir Minerals for Immobilization, *Acta Cryst.*, 2007, A63, 217.

[90] Felix Y. Amoako, H. Pöllmann, Wolfgang Gossel, Immobilisation of Hazardous Substances from Mine Tailings using Mineral Reservoir Technology: Case of Mineral Processing Tailings from Ghana, “Mine Water – Managing the Challenges”, IMWA 2011, 259-263.

Chapter 3

Experimental Methodology

A combination of diffraction, microscopic and spectroscopic methods were deployed to investigate the crystallography of ellestadite chemical analogues and examine the durability of these materials. This chapter describes the operating principles of the techniques and instrumentation deployed. X-ray powder diffraction and neutron powder diffraction provided crystal chemical information augmented by scanning electron microscopy, transmission electron microscopy and Fourier transform infrared spectroscopy to observe the microstructure and search for structural and chemical defects. Quantitative chemical compositions were collected by electron microprobe analysis that were correlated with crystallographic structure refinements. To quantify ellestadite durability, the Toxicity Characteristic Leach Test Procedure was employed. Specific characterization and operating methodologies were developed for each of the three ellestadite series examined.

3.1 Ellestadite Chemical Series Selection

Incinerator fly ash, produced from the combustion of industrial and low level nuclear wastes, contains significant quantities of toxic and radioactive elements, such as Sr, Pb, As, Zn, Cl and Br. A typical municipal incinerator fly ash composition is compiled in Table 3.1 [1]. In this research, three ellestadite chemical analogues were studies extensively to provide baseline crystal chemical data concerning the structure and durability of ellestadites and evaluate their potential as waste forms:

(i) apatite-ellestadite $Ca_{10}[(SiO_4)_x(PO_4)_{6-2x}(SO_4)_x]Cl_2$,

(ii) fluor-chlorellestadite $Ca_{10}[(SiO_4)_3(SO_4)_3][Cl_{2-x}F_x]$, and

(iii) vanado-ellestadite $Ca_{10}[(SiO_4)_x(VO_4)_{6-2x}(SO_4)_x]Cl_2$.

In addition, preliminary studies of cadmium-bearing vanadinite were undertaken.

Table 3.1 Chemical composition of municipal waste incinerator fly ash [1].

Major component	(%)	Trace	(ppm)
Al_2O_3	17	Cd	203
CaO	25	Cr	513
Fe_2O_3	2	Cu	1022
MgO	3	Pb	3731
SiO_2	28	Zn	12417
Cl	0.9		
K_2O	1.0		
Na_2O	1.6		
SO_4	2.3		
Loss of ignition	14.4		

The broad aims were to establish the structural and chemical continuity of these series, investigate the relationship between chemistry and waste form durability, and seek a clearer understanding of the dissolution mechanisms through leach testing.

3.1.1 Chloroellestadite $Ca_{10}[(SiO_4)_x(PO_4)_{6-2x}(SO_4)_x]Cl_2$

Because silicon (Si), phosphorus (P) and sulfur (S) appear consecutively in the Periodic Table of the Elements, X-ray diffraction cannot readily differentiate these

elements with similar numbers of electrons and X-ray form factors. Therefore, it was appropriate to use neutron diffraction to probe crystallographic site preferences, because the differences in neutron scattering lengths of Si, P and S (2.167, 3.312 and 1.026 respectively) are an order of magnitude larger than X-ray scattering (Table 3.2) [2]. Ordering of Si/P/S across the tetrahedra can also be assessed from the bond lengths, which will vary systematically with the ionic radii of Si (0.26 Å), P (0.17 Å) and S (0.12 Å). Evidently, when P is replaced by Si, the average *B*-O bond will increase as Si has a larger ionic radius, while incorporation of sulphur shortens the *B*-O tetrahedral bond length. As discussed in Chapter 2 the literature is ambiguous concerning Si/P/S site preferences, with anomalous trends in *B*-O bond lengths across the $Ca_{10}(PO_4)_6Cl_2$ to $Ca_{10}[(SiO_4)_3(SO_4)_3]Cl_2$ join possibly arising from departures in stoichiometry and/or the presence of phase transformations (i.e. changes in symmetry).

Table 3.2 Comparison of atomic number, ionic radii and neutron scattering lengths of Si, P and S.

	Z	**ΔZ (%)**	**ionic radius (Å)**	**σ_{scatt} (fm)**	**$\Delta\sigma_{scatt}$ (%)**
Si	14	0	0.26	2.167	111
P	15	7.14	0.17	3.312	223
S	16	14.2	0.12	1.026	0

3.1.2 Fluoro-Chlorellestadite $Ca_{10}[(SiO_4)_3(SO_4)_3][Cl_{2-x}F_x]$

The *X* anions fluorine, chlorine, and hydroxyl, readily swap in apatites, sometimes though ion exchange [3, 4]. When mixtures are present, the *X* species interact to produce effects not directly predictable from a crystallographic knowledge of the endmember compounds alone. For example, in Chapter 5, it is shown that F-Cl ion positional interactions cause a portion of the substituting F ions to shift along the c-axis from their special location at $z = 1/4$. Likewise, Cl ions at $z = 1/2$ nominal were displaced along [001] by > 0.2 Å to $z = 0.44$. Furthermore, the ordering of Cl in pure chlorapatite that leads to a monoclinic structure can be removed by introducing small amounts (~10%) of other ions (e.g. OH^- [5]). Thus, it is important to know whether nonlinear effects of the fluorine-chlorine substitution observed in apatite are found in ellestadite and, if so, which structural mechanisms are active and what are

the implications on waste form durability. In this regard, it is well known that fluorine tends to increase crystal size by enhancing crystal growth rates, resulting in decreased lattice strain and increased stability of the apatite structure [6, 7]. This change is driven by the highly electronegative fluorine that modifies the bond interactions among calcium and oxygen to strengthen apatite and enhance its durability.

3.1.3 Vanadate-Ellestadite $Ca_{10}[(SiO_4)_x(VO_4)_{6-2x}(SO_4)_x]Cl_2$

The incorporation of vanadium as a *B*-site substitution ion modifies the internal energy of apatite, resulting in changes in its physical properties and solubility. As the V^{5+} (0.355Å) is larger than Si^{4+} and S^{6+}, there will be an expansion of the unit cell. Distinct discontinuities for both the *a* and *c* parameters have been found in the system of P-V chlorapatites, $Ca_{10}[(V_xP_{1-x}O_4)_6]Cl_2$ [8], with the *c* parameter displaying discontinuity for $x \geq 3$, possibly indicating a change in compositions or existing of X-ray amorphous material. To date, no report has dealt with the inclusion of vanadium in ellestadite, although this would be a target element for immobilization, and serves as proxy for toxic transition metals including chromium and arsenic.

3.2 Solid State Synthesis

Solid state synthesis is commonly used for bulk processing of apatite powders, and is particularly appropriate for the study of equilibrated phases. Syntheses are conducted at relatively high temperatures (>500°C) through combining stoichiometric mixtures of oxides, carbonates, hydroxides, and halide salts. These precursors can be treated at different phase-forming temperatures which are deduced from the phase diagrams (Figure 3.1). Depending on the elements involved and the oxidation states required, the sintering atmosphere may be oxidizing, reducing or inert, but here most syntheses were carried out in air.

Preparation involves a series of mixing, grinding, pelletizing and sintering steps which may be repeated to ensure formation of single-phase products. In addition,

precautions may be necessary to prevent the evaporation of volatile species, particularly the halides, which causes non-stoichiometry or oxidation:

$2X^- \rightarrow O^{2-}$ (X = halide) (3-1)

As already noted, three apatite compositional series were synthesized using the solid state method: apatite-ellestadite $Ca_{10}[(SiO_4)_x(PO_4)_{6-2x}(SO_4)_x]Cl_2$ (where x = 0, 0.5, 1, 1.5, 2, 2.5, and 3); fluor-chlorellestadite $Ca_{10}[(SiO_4)_3(SO_4)_3][Cl_{2-x}F_x]$ (where x = 0, 0.4, 0.8, 1.2, 1.6, and 2); and vanado-ellestadite $Ca_{10}[(SiO_4)_x(VO_4)_{6-2x}(SO_4)_x]Cl_2$ (where x = 0, 0.5, 1, 1.5, 2, 2.5, and 3). All materials were obtained with good crystallinity and high purity suitable for crystallographic characterization.

The nominal solid state synthesis reactions were:

(1) $4x\ CaO + x\ CaSO_4 + x\ SiO_2 + (3\text{-}x)\ Ca_3(PO_4)_2 + CaCl_2{\cdot}2H_2O \rightarrow$

$Ca_{10}[(SiO_4)_x(PO_4)_{6-2x}(SO_4)_x]Cl_2 + 2\ H_2O\uparrow$ (3-2)

(2) $6\ CaO + 3\ CaSO_4 + 3\ SiO_2 + (x/2)\ CaF_2 + (1\text{-}x/2)\ CaCl_2{\cdot}2H_2O \rightarrow$

$Ca_{10}[(SiO_4)_3(SO_4)_3][Cl_{2-x}F_x] + (2\text{-}x)\ H_2O\uparrow$ (3-3)

(3) $4x\ CaO + x\ CaSO_4 + x\ SiO_2 + (3\text{-}x)\ Ca_3(VO_4)_2 + CaCl_2{\cdot}2H_2O \rightarrow$

$Ca_{10}[(SiO_4)_x(PO_4)_{6-2x}(SO_4)_x]Cl_2 + 2\ H_2O\uparrow$ (3-4)

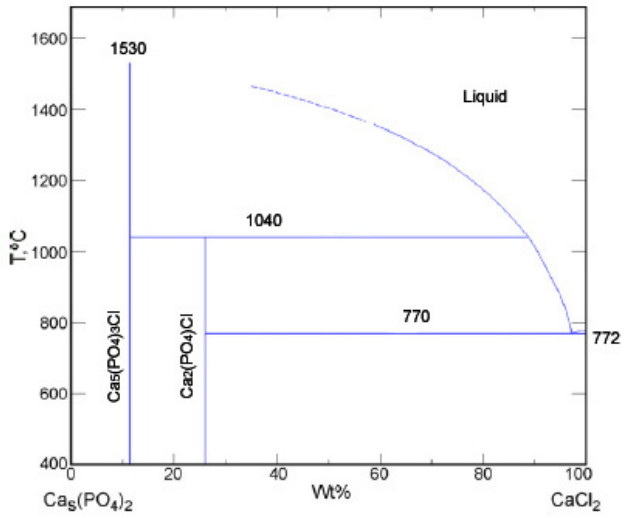

Figure 3.1 Phase diagram for the $CaCl_2 - Ca_3(PO_4)_2$ system. [9]

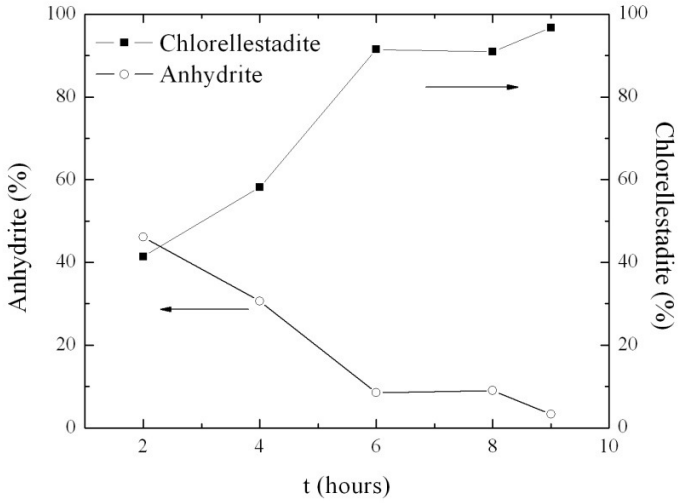

Figure 3.2 Near 100% ellestadite $Ca_{10}(SiO_4)_3(SO_4)_3Cl_2$ yield was achieved by firing at 950°C for 9 hours.

Fresh CaO was obtained by firing $CaCO_3$ (Merck – 99%) at 1000°C for 10 hours to achieve decomposition: $CaCO_3 \rightarrow CaO + CO_2\uparrow$. The CaO was used immediately after cooling to avoid conversion to $CaCO_3$ or $Ca(OH)_2$. Anhydrous $CaSO_4$ was obtained by heating $CaSO_4 \cdot 2H_2O$ (Aldrich – 99%) at 600°C for 2 hours.

The starting materials were mixed in acetone and ground manually in an agate mortar for 30 minutes. After oven drying (100°C / 8 hours), the mixtures were sintered in alumina crucibles. A second alumina crucible was used as a loose fitting lid to minimize $CaCl_2$ evaporation. As no phase diagrams for ellestadite were available, yield as a function of temperature and time was studied, with optimal conditions for ellestadite formation that minimizes anhydrate ($CaSO_4$) as a secondary product, found to be 950°C and 9 hours (Figure 3.2). It was observed that the reaction was incomplete at 800°C, and ellestadites decomposed if fired at higher temperatures (1000°C) or for longer times (12 h). The final products were cooled slowly in the furnace to reduce thermal stress. Later chapters provide specific synthesis conditions for each chemical join.

3.3 Characterization

3.3.1 Powder X-ray Diffraction (XRD)

Powder X-ray diffraction analysis (XRD) was the primary characterization tool to investigate crystallographic structure, grain size and preferred orientation in polycrystalline ellestadite pellets and powdered solids. When X-ray radiation is directed on a sample, the X-rays are scattered by electrons in the material. If the atoms are arranged in a regular structure, i.e. if the material is crystalline, this scattering results in maxima and minima in the diffracted intensity, with reflections appearing according to Bragg's Law (Equation 3-4),

$$n\lambda = 2d\sin\theta \qquad (3\text{-}4)$$

where λ is the wavelength of the X-rays, θ is the angle between the incident rays and the surface of the crystal, d is the spacing between atomic layers of atoms, and constructive interference occurs when n is an integer [10]. (Figure 3.3) Thus, for each lattice spacing d, Bragg's law predicts a maximum at a characteristic diffraction angle θ. During an XRD measurement the angles of incidence and detection are scanned. When the intensity of detected X-rays is plotted as a function of angle an X-ray diffraction pattern is obtained, which is characteristic of the crystal structure.

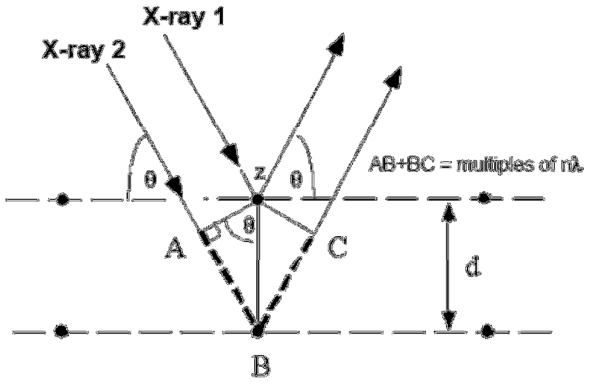

Figure 3.3 Bragg's Law, assuming that atomic lagers behave as reflecting planes [10].

In X-ray powder diffraction the position and intensity of the diffraction peaks are characteristic of the crystallographic structure and the chemical composition. The position of the diffraction peaks, and the d-spacings that they represent, provide

information about the location of lattice planes in the crystal structure, with each peak at a d-spacing consistent with a family of lattice planes. Every reflection has a characteristic intensity that distinguishes it from other peaks in the pattern and indicates the relative strength of diffraction from those lattice planes. For a specific space symmetry (usually $P6_3/m$ for apatite), variations in measured intensity arise from changes in the scattering efficiency of the atoms and their arrangement in the lattice. Diffraction interference will be enhanced, attenuated or extinguished from particular lattice planes if there is a change of symmetry. [11]

The overall integrated intensity (peak area) of each powder diffraction peak is given by the following expression:

$$I(hkl) = |F(hkl)|^2 \times M_{hkl} \times LP(\theta) \times TF(\theta) \qquad (3\text{-}5)$$

where F(hkl) = structure factor; M_{hkl} = multiplicity; LP(θ) = Lorentz and polarization factors; and TF(θ) = temperature factor (more correctly referred to as the atomic displacement parameter). Additional influences on diffraction intensity include absorption and preferred orientation.

3.3.1.1 The Structure Factor

The structure factor quantitatively describes X-ray interference arising from the electronic structure and positioning of atoms in the lattice. All of the information regarding relative atom location is contained in the structure factor F(hkl), that is given by the summation over all atoms (from 1 to j) in the unit cell:

$$F(hkl) = \Sigma_j f_j \exp [2\pi i(hx_j+ky_j+lz_j)] \qquad (3\text{-}6)$$

where f_j = atomic form factors for the j^{th} atom; h, k and l = Miller indices of the hkl reflection; and x_j, y_j and z_j = the fractional coordinates of the j^{th} atom.

X-ray scattering arises from the electron cloud surrounding the atom, and each electron follows the Thompson equation (Equation 3-7).

$$I = I_o/r^2(e^2/m_ec^2)[1+\cos^2(2\theta)/2] \qquad (3\text{-}7)$$

where I_o is the intensity of the incident X-ray beam; e the charge on the electron; m_e the mass of the electron; c the speed of light; r the distance from the scattering electron to the detector; and θ is the angle between the incident rays and the surface

of the crystal. Therefore, the larger the atomic number the greater will be the X-ray interaction, with the scattering degrading at larger angles. This phenomenon is captured in the atomic form factor, described by the quantity *f*, and is normalized in units of the amount of scattering occurring from a single electron in the Thompson equation. *f* is expressed as a function of sin θ and λ as shown in Figure 3.4 [12].

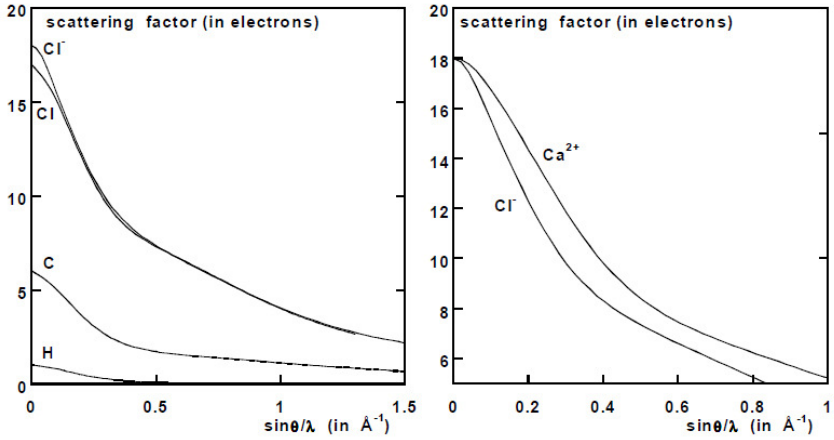

Figure 3.4 Atomic form factors *f* for hydrogen, carbon, chlorine and calcium, plotted against sinθ/λ [12].

3.3.1.2 Multiplicity Factor

The number of identically spaced planes cutting a unit cell in a particular *hkl* family is called the plane multiplicity factor. For low symmetry systems, the multiplicity factor will always be low. For high symmetry systems, a single family of planes may be duplicated many times leading to a higher intensity peaks in powder diffraction. Multiplicity factors for the various crystal classes and planes are given in Table 3.3 [13]

Table 3.3 Plane Multiplicity Factors, M_{hkl}.

System	*hkl*	*hhl*	*hh0*	*0kk*	*hhh*	*hk0*	*h0l*	*0kl*	*h00*	*0k0*	*00l*
Cubic	48*	24	12	(12)	8	24*	(24*)	(24*)	6	(6)	(6)
Tetragonal	16*	8	4	(8)	(8)	8*	8	(8)	4	(4)	2
Hexagonal	24*	12*	6	(12)	(12)	12*	(12*)	12*	6	(6)	2
Orthorhombic	8	(8)	(8)	(8)	(8)	4	(4)	(4)	2	(2)	(2)
Monoclinic	4	(4)	(4)	(4)	(4)	(4)	(2)	(4)	2	(2)	(2)
Triclinic	2	(2)	(2)	(2)	(2)	(2)	(2)	(2)	(2)	(2)	(2)

* When all permutations of indices do not yield equivalent planes, M must be halved.

3.3.1.3 Lorentz-polarization Factor

Lorentz-polarization is a combination of the Lorentz factor and the polarization factor, that influence the intensity of the diffracted beam according to the expression:

$$\text{Lorenz-polarization factor} = (1+\cos^2 2\theta)/(\sin^2\theta \cos\theta) \qquad (3\text{-}8)$$

The polarization factor originates from the fact that although the incident beam from a laboratory X-ray source is unpolarized, it may be resolved into two plane-polarized components, and the total scattered intensity is the sum of the intensities of these two components, which depends on the scattering angle. The Lorentz factor takes into account certain geometrical factors related to the orientation of the reflecting planes in the crystal. The Lorentz-polarization factor varies strongly with Bragg angle, θ, and the overall effect is that the intensity of reflections at intermediate Bragg angles (~50-100° 2θ for Cu K_α radiation) is less compared to those at higher or lower diffraction angles (Fig 3.4).

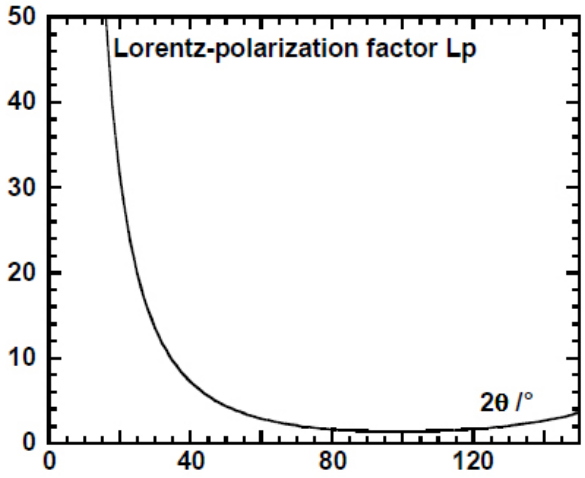

Figure 3.5 The relationship between Lorenz-polarization factor and Bragg angle θ [13].

3.3.1.4 Temperature Factor

The temperature factor takes into consideration the effect of thermal atomic vibration on reflections in the X-ray diffraction pattern. At all temperatures, even absolute zero, the atoms in a crystal are vibrating about their mean positions. A pronounced effect of this vibration is that the reflection intensity decreases as the temperature increases. Thermal vibration of the atoms causes the reflections to become broader as their position is less constrained. The thermal factor is described

as [13]:

$$TF(\theta) = \exp\left[B(\sin\theta/\lambda)^2\right] \quad (3\text{-}9)$$

where the coefficient B is the Debye-Waller temperature factor, that is proportional to the mean squared displacement (U^2) of atomic vibration, and is directly related to the thermal energy (kT) available with other terms related to atomic mass and the strength of interatomic bonds. Qualitatively, as T increases, B will increase, and the intensity reduces in amplitude (Figure 3.5).

The simplest assumption to make about atomic displacements is to consider them as isotropic; in this case, only a single term is needed, named B_{iso}. However, atoms in crystals seldom have isotropic environments, and a better approximation is to describe the atomic motion in terms of an ellipsoid, with larger amplitudes of vibration in some directions than in others. Six parameters described by anisotropic displacement parameters (ADPs) are then introduced for each atom. The ADPs define the symmetric atomic mean-square displacement tensor

$$U = \begin{pmatrix} U_{11} & U_{12} & U_{13} \\ U_{12} & U_{22} & U_{23} \\ U_{12} & U_{23} & U_{33} \end{pmatrix} \quad (3\text{-}10)$$

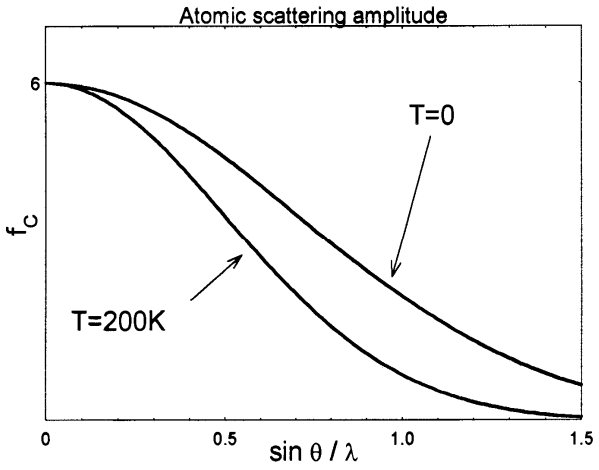

Figure 3.6 The effect of temperature on scattering factor [13].

3.3.2 Laboratory X-ray Powder Diffraction

Powder X-ray diffraction patterns were collected using either a Shimadzu X-ray Diffractometer-6000 fitted with scintillation detector for serial data collection or a

Bruker D8 Advance X-Ray Diffractometer with a Vantec500 2D detector for accelerated parallel data acquisition. Both instruments operate using a reflection configuration with the Shimadzu X6000 employing the Bragg-Brentano θ-2θ geometry and Bruker D8 using the θ-θ geometry. The difference between these two configurations involves the sample and the detector rotating around a fixed axis in the former, and the rotation of the X-ray source and detector around a fixed sample in the latter.

Patterns were gathered using a Cu Kα radiation source operating at 40 kV and 40 mA. Acquisitions used a step size of 0.01° (2θ) over an angular range of 10 to 140° (2θ) at a scanning rate of 0.01 per second. All specimens were spiked with a silicon standard (10 wt%, NIST660a, a = 5.40825 Å) to determine the unit cell constants absolutely. To collect a diffraction pattern, the samples were finely ground using an agate mortar and pestle to minimize particle size, X-ray absorption, and the effect of preferred orientation that cumulatively broaden peak widths and bias peak intensities. A flat and uniform top surface was made by compacting with a glass microscope slide, to ensure the sample uniformly intercepts the entire incident X-ray beam at all 2θ angles. A plane surface minimizes instrumental errors associated with the peak shape and position, and reduces porosity that modifies X-ray absorption non-systematically.

Crystal structures were refined by Rietveld analysis using TOPAS, initially in monoclinic ($P2_1/b$), but subsequently in $P6_3/m$. Crystallographic parameters were ultimately refined simultaneously, but initially, these variables were released in the sequence: scale factor, zero shift, Chebyshev background polynomial, crystallite size (i.e. coherently scattering domain size), and finally lattice parameters. Isotropic temperature factors for the *A* site and *B* site cations in $A_{10}(BO_4)_6Cl_2$ were refined; however those for oxygen and chlorine were fixed at 1 $Å^2$. Cation positions were refined first, followed by the oxygen positions. To ensure reasonable bond lengths in the SiO_4, PO_4, SO_4 and VO_4 tetrahedra, fractional coordinates were constrained close to the average *B*-O bond lengths.

3.3.3 Fixed Wavelength Powder Neutron Diffraction (PND)

Neutron diffraction is a form of elastic scattering where the neutrons exiting the material have nearly the same energy as the incident neutrons. The geometry is similar to X-ray diffraction, but the different radiation gives complementary information [14], as X-rays and neutrons interact with matter in a fundamentally different manner. X-rays are scattered by electrons while neutrons are scattered by the nuclei. Consequently, an X-ray diffraction experiment is dependent on the electron density of the atoms, and heavy atoms with many electrons, scatter X-rays more strongly than lighter elements with fewer electrons; for neutrons, their interaction is with the nuclei only and will change as a function of isotope abundance. The X-ray scattering factor is approximately proportional to the number of electrons in an atom and expressed by a relationship between scattering factor and atomic number, and are sensitive to oxidation state. Neutron scattering length varies from isotope to isotope; for example, the isotopes hydrogen (H) and deuterium (D) contribute differently. The neutron scattering lengths of H and D are σ_{scatt} = -3.7406(11) fm and σ_{scatt} = 6.671(4) fm [2] respectively, and have opposite sign, which allows them to be distinguished.

Neutrons offer three advantages over X-rays for diffraction experiments. Samples containing two neighboring elements with similar electron density would be indistinguishable using X-ray diffraction, since the difference in scattering factor would be minimal (Table 3.2). This is less problematic for neutron diffraction because the scattering lengths of neighboring elements can vary substantially (Table 3.2) [2]. The second advantage of neutron diffraction is the ability to detect lighter elements in the presence of heavier elements. The neutron scattering lengths of the heavy and light elements, whilst different, are usually in the same order of magnitude. Thus, it is possible to determine the oxygen anion position in apatite with a much higher degree precision than possible with X-rays. With a better understanding of these oxygen positions, a more accurate structural model of the crystal, as well as the bonding environment, can be obtained. Finally, there is no angular dependence of neutron scattering, resulting in strong diffraction to high diffraction angles that allows reliable analysis of anisotropic atomic displacements and site occupancies.

Neutron diffraction data was acquired at the Institute Laue-Langevin (ILL) Grenoble (France) using the high resolution D1B diffractometer [Figure 3.7(a) and (b)] with a wavelength of 1.89Å, a 2-theta range of 0°-150° and scan step of 0.05° at room temperature. The diffractometer is equipped with a focusing Ge monochromator at a take-off angle of 123° and 2 standard ^{3}He counter detectors. A cylindrical vanadium sample container (0.9 cm diameter) was used during the measurement. Vanadium has a coherent scattering length that is a small negative value (σ_{scatt} = -0.38 fm), and is very suitable as a container material.

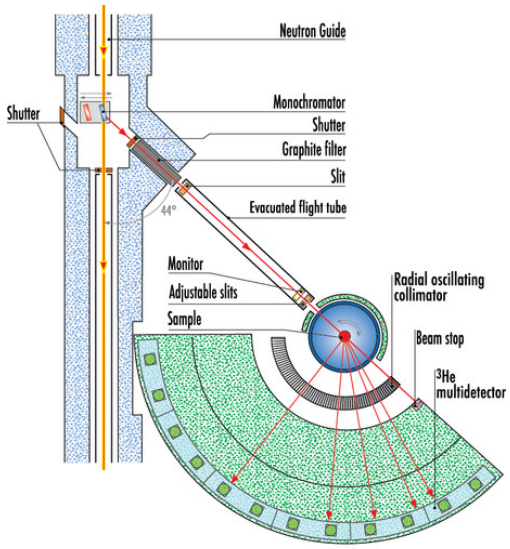

Figure 3.7(a) Layout of the high resolution D1B diffractometer of ILL, showing the setup of the Position Sensitive Detector (PSD) with 1280 cells covering a total of 128º, and the Radial Oscillating Collimator (ROC).

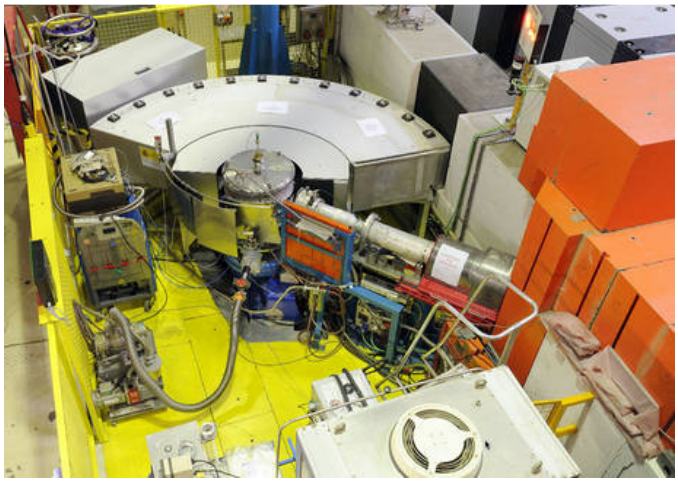

Figure 3.7(b) A general view of D1B (Photo by Ecliptique / Laurent Thion, July 2012)

All neutron diffraction data was analyzed using TOPAS V3.0 with the refinement parameters being zero shift, cell parameters, fractional occupancies and thermal factors. The peak profile was fitted with a pseudo Voigt function where the parameters U, V, W (0.12, -0.21, 0.17) were fixed to values supplied by ILL.

3.3.4 Transmission electron microscopy (TEM)

The transmission electron microscope (TEM) has become the premier tool for the microstructural characterization of materials. A modern TEM can image variations in diffraction across the specimen (diffraction contrast imaging), the phase contrast of the specimen (high-resolution imaging), obtain diffraction patterns from selected areas of the specimen, and perform electron energy loss spectroscopy (EELS) and energy dispersive X-ray spectroscopy (EDS) measurements with a focused electron beam. Many apatite compositions are electron beam sensitive with microdomains and nano-scale modulation introduced as artifacts [15].

TEM uses a high voltage electron beam emitted by a cathode and focused by magnetic lenses, that when partially transmitted through a thin (semitransparent for electrons) specimen carries crystallographic and chemical information. The spatial variation in this information (the "image") is then magnified by a series of magnetic lenses until it is recorded with a fluorescent screen or light sensitive sensor such as a CCD (charge-coupled device) camera or energy dispersed using a magnetic prism. The image detected by the CCD can be displayed in real time [16].

In this work, specimens were prepared by ultrasonically separating a small quantity of powder in acetone then placing a drop of suspension on a holey carbon-coated copper grid that was allowed to air dry. High-resolution transmission electron microscopy (HRTEM) was carried out with a JEOL-2010 TEM (JEOL, Tokyo, Japan C_s=0.5mm and C_c=1.1mm) (Figure 3.6) operated at 200 kV with a LaB_6 source. Samples were analyzed after orientating to specific crystallographic directions with a double tilting holder and the selected area electron diffraction (SAD) patterns recorded.

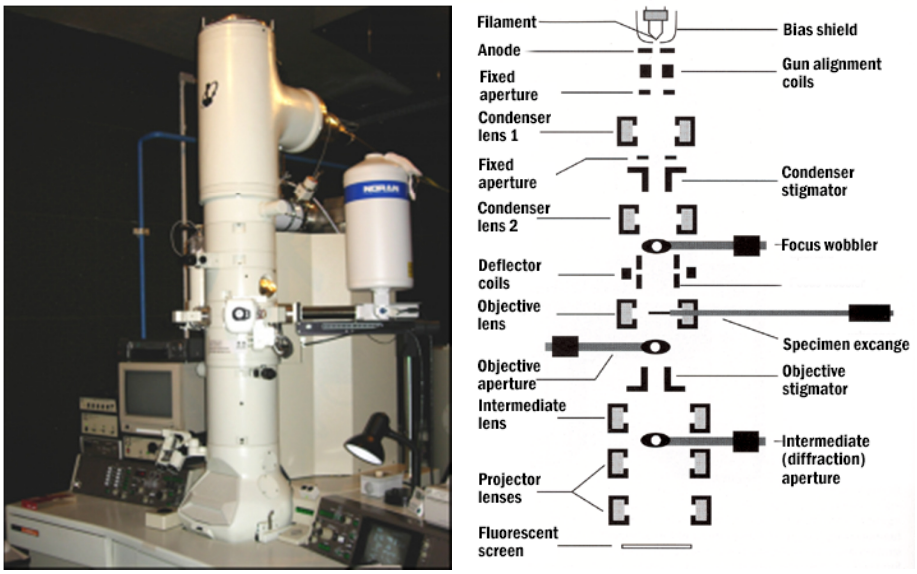

Figure 3.8 JEOL -2010 TEM and layout of optical.

3.3.5 Fourier transform infrared (FTIR) spectroscopy

Infrared (IR) spectroscopy is a chemical analytical technique sensitive to the vibrational characteristics of functional groups. Vibrations arise from changes in bond lengths and angles and in many simple, non-cyclic molecules these vibrational modes can be thought of separately and are referred to as bond stretching and bending modes [17]. In diatomic molecules the vibration of the point masses occurs only along the line connecting two atoms, and the frequency ν of the vibrating diatomic molecule is related to the force constant and the reduced mass $\mu = (m_1 \cdot m_2)/(m_1 + m_2)$, representing the atomic masses, by the equation [17]

$$\nu = 1/2\pi\sqrt{k/\mu}) \qquad (3\text{-}11)$$

In polyatomic groups (e.g. CO_3, SiO_4, PO_4 groups), analysis is more complicated because all the atoms perform their own harmonic oscillations. A system of *N* atoms has 3*N* degrees of freedom corresponding to the three independent coordinates, with respect to a Cartesian system, of each of the *N* atoms [18]. Three of these are just translations of the entire atomic group along the *x*, *y*, and *z* axes, and another three are taken up by rotation of the molecule about the three principal axes of inertia that intersect at the center of mass. The number of vibrational degrees of freedom *Z* is identical to the number of fundamental or normal vibrations

$Z = 3N\text{-}6$ (3-12)

for a non-linear molecule.

Figure 3.9 represents the normal modes of vibration of a tetrahedral SiO_4 group [18]. ν_1 and ν_3 correspond to symmetric and asymmetric stretching, and ν_2 and ν_4 to the corresponding bending vibrations. As nine vibrational modes are expected (Equation 3-12), ν_2 is doubly degenerate, while ν_3 and ν_4 are triply degenerate.

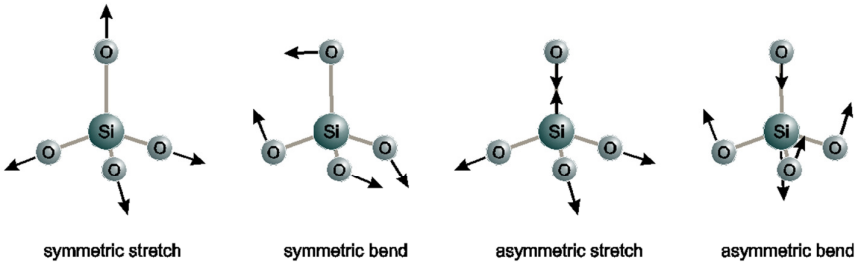

Figure 3.9 The vibrational modes of a non-linear tetrahedral SiO_4 group. (a) ν_1 symmetric stretch, (b) ν_3 symmetric bend, (c) ν_2 asymmetric stretch, and (d) ν_4 asymmetric bend [18].

By using the harmonic oscillator model for the energetics of IR-active vibrations, the substitution of one element by another will shift the wavenumber of a vibration according to the masses and the bonding behavior of the respective atoms, and also modify the shape of the respective absorption band [19]. The relationship in Equation 3-11 between the vibrational frequency ν, the bond strength (expressed by the force constant k) and the atomic mass (expressed by the reduced mass μ), allows a coarse classification of the IR absorption spectrum. The wavenumber increases with increasing bond strengths and decreasing atomic masses. The frequencies of atomic groups relevant for apatite minerals are compiled in Table 3.1 [20].

Table 3.4 IR spectra of species containing $(BO_4)^{x-}$ groups with T_d site symmetry [20].

Modes	ν_1	ν_3	ν_4
SO_4^{2-}	983	1105	611
PO_4^{3-}	938	1017	567
CrO_4^{2-}	847	884	368
AsO_4^{3-}	837	878	463
VO_3^{3-}	827	780	341
SiO_4^{4-}	780	890	556

Fourier Transform Infrared (FTIR) spectrometery records infrared spectra by first collecting an interferogram that contains all of the infrared frequencies simultaneously. For this work, FTIR spectroscopy was used to identify chemically distinct tetrahedral groups in ellestadites, and search for changes from BO_4 tetrahedral co-ordination to BO_5 or BO_3 as these structural modifications are sometimes observed in apatites.

Infrared spectra were recorded over the range 4000 – 400 cm^{-1} with a Fourier Transform Infrared Spectrometer (Perkin-Elmer Spectrum 2000) using the KBr pellet technique. Samples for FT-IR absorption measurements were prepared by grinding ca. 1 mg of the ellestadite samples and dispersing into 200 mg of KBr. This homogenized mixture was pressed into a 10-mm-diameter transparent pellet. Measurements were carried out with a spectral resolution of 4 cm^{-1}, and measurements averaged over 64 scans.

Attenuated total reflection (ATR) FTIR was used to analyze the pellets, and measure the totally internally reflected infrared beam. In ATR FTIR infrared beam is directed onto an optically dense crystal with high refractive index at a certain angle. This internal reflectance creates an evanescent wave that extends beyond the surface of the crystal into the sample held in contact with the crystal. In regions of the infrared spectrum where the sample absorbs energy, the evanescent wave will be attenuated or altered. The attenuated energy from each evanescent wave is passed back to the IR beam, which then exits the opposite end of the crystal to the detector in the IR spectrometer. The system then generates an infrared spectrum. [21]

3.4 Leach Testing

Leaching of hazardous constituents from immobilized waste is a function of both the intrinsic properties of the waste form and the hydrologic and geochemical properties of the disposal site [22]. Laboratory leaching experiments can be designed to simulate the behavior of waste forms under static or dynamic conditions. For a single-phase solid material, the interpretation leaching can be relatively simple, with the key factors controlling leachability being pH, leachant composition, solubility of

the chemical compound, and the surface area.

A European Union wide validation study provides a basis for comparing compliance of leaching test data with characterization of the solid [23]. Specifically, although short term tests are frequently used for quality control purposes, these should be correlated with microstructural and surface characterization to identify dissolution or corrosion products, with leachant concentrations interpreted through the perspective of materials alteration. Where obvious inconsistencies in microstructure and leach data arise, reasons for the deviation (e.g. analytical error, or waste feed saturation) should be investigated.

As noted earlier, leaching methods are broadly differentiated according to whether the leaching fluid is introduced as a single addition (static extraction tests) or renewed continuously (dynamic tests) (Table 3.5) [24-29]. Methods can also be classified as batch leaching in which the sample is placed in a given volume of leachant solution, as column or flow-through systems, and as bulk or flow-around systems for monolithic samples. Results are generally reported as the concentration in the leachant solution (mg/L) or as the leached concentration from the solid (mg/kg). In many methods, the liquid to solid ratio (L/S) is used to quantify the volume of leachant with respect to the amount of solid sample, usually as mL/g or L/kg.

Table 3.5 Summary of leaching test types and standard methods.

Type of Test	Description	Properties measured	Methods
Agitate test	waste and leachant co-mingled and agitated	chemical	TCLP [24]
Non-agitated test	co-mingled and not agitate	physical, rate-limiting	Strategic Leach test, Static Leach test [25]
Sequential chemical extraction	a series of agitated extraction test	chemical	ASTM sequential batch extraction [26]
Serial batch test	granular samples mixed with successive batch of fresh leachant	kinetic information	Multiple Extraction Procedure [27]
Flow-around test	waste in leaching vessel and flow of fresh leachant around	kinetic information	ISO leach test ANS 16-1 [28, 29]

The static extraction test used in this study was the Toxicity Characterization Leaching Procedure (TCLP) in which extractions are conducted on individual pellets

using acetic acid at pH 2.88, prepared by diluting 5.7mL of glacial acid with deionized water to a volume of 1L. The total leach periods were 18 hours and 72 hours. TCLP, as a batch leaching test, provides the maximum exposure of waste materials to leachant, and is frequently used for quality control purposes. In practice, the limitation of the approach is that the short duration of the test precludes an estimation of long-term durability. Moreover, TCLP results do not show the mechanism of dissolution, including the contribution of precipitates or passivation layers to the overall leach rate. Thus, there remains uncertainly in the estimation of immobilization durability, its mechanism, and the manner in which apatite-related phases may enhance or degrade performance.

3.5 Overview of Methodologies

In this work, solid-state reactions were employed to prepare a range of polycrystalline ellestadites to establish solid solution limits and allow crystallographic refinements. Compounds synthesized included nominal $A_{10}(BO_4)_6X_2$ compositions with substituents at *B* sites, and charge balance maintained by combining Si^{4+}, S^{6+} and P^{5+} (Chapter 4), and Si^{4+}, S^{6+} and V^{5+} (Chapter 6). Substitution of $X = Cl^-$ with F^- was used to study the effect of tunnel species on structure and durability (Chapter 5). Reconnaissance investigations of cadmium incorporation were also conducted (Chapter 8). Correlations between crystal structure and chemical composition were established by Rietveld refinement of X-ray powder diffraction patterns, with deeper analysis of the atomic arrangements derived from neutron powder diffraction. These data were supplemented and confirmed by microanalytical (EPMA, SEM and TEM) and spectroscopic (FTIR) investigations. Finally, TCLP was used as a standard leach test to establish the relationship between materials processing, crystal chemistry and durability (Chapter 7).

References:

[1] G. Song, K Kim, Y. C. Seo, S. C. Kim. Waste Manag. 2004, 24, 99-106.

[2] V. F. Sears. *Neutron News*, **1992**, 3, 29-37.

[3] D. McConnell. *Its Crystal Chemistry, Mineralogy, Utilization and Geologic and Biologic Occurrences. Springer, New York*, **1973**.

[4] J. C. Elliott. *Structure and Chemistry of the apatites and other Calcium Orthophosphates. Elsevier, Amsterdam*, **1994**.

[5] J. M. Hughes, M. Cameron, K. D. Crowley. *Amer. Mineral*. **1990**, 75, 295–304.

[6] H. T. Dean, *Public Health Rep. Wash*. **1938**, 53, 1443–1452.

[7] D. Lexa. *Metall. Mater. Trans*. **1999**, 30A, 147–153.

[8] J. K. Kim, Z. Dong, Z.; T. J. White. *J. Am. Ceram. Soc.* **2005**, 88, 1253-1260

[9] R. Nacken. *Zentralbl. Mineral. Geol. Palaeontol.,* **1912**, 545–559

[10] W.L. Bragg, *Proceedings of the Cambridge Philosophical Society*, **1913**, 17, 43–57.

[11] B. E. Warren. *X-ray diffraction, Addison–Wesley, Mineola NY*, **1969/1990**.

[12] A. R. West. *Solid State Chemistry and its Applications, John Wiley & Sons, UK*, **2014**.

[13] C. Suryanarayana, M. G. Norton. *X-ray Diffraxtion: A Practical Approach, Plenum Press, New York*, **1998**.

[14] M. Richard, Ibberson, W. I. F. David, *Chapter 5 of Structure determination form powder diffraction data IUCr monographs on crystallography, Oxford scientific publications,* **2002**

[15] C. Ferraris, T. J. White, J. Plévert, R. Wegner. *Physics and Chemistry of Minerals*, **2005**, 32, 485-492.

[16] D. Williams, C. B. and Carter. *Transmission Electron Microscopy. 1 – Basics. Plenum Press, New York*, **1996**.

[17] J. H. van der Maas. *Basic Infrared Spectroscopy. Heyden*, **1972**.

[18] G. Socrates. *Infrared Characteristic Group Frequencies. 2nd Ed. Chichester: Wiley*, **1994**.

[20] W. P. Griffith. *Nature*, **1969**, 224, 264-266.

[21] FT-IR Spectroscopy Technical Note, Perkin Elmer Life and Analytical Sciences. www.perkinelmer.com.

[22] D. S. Kosson, H.A. van der Sloot, F. Sanchez, A.C. Garrabrants. *Environmental Engineering Science*. **2002**, 19, 159-204.

[23] H.A. van der Sloot and J.J. Dijkstra. *ECN report: ECN-C 04-060*, **2005**.

[24] S. S. Sorini, L. P. Jackson. *Nuclear Chem. Waste Management*, **1988**, 8, 217-223.

[25] D. M. Strachan, *Nuclear Chem. Waste Management,* **1983**, 4, 177-188.

[26] American Society for Testing and Materials, D5284-09.

[27] B. Ludwig, P. Khanna, J. Prenzel, F. Beese. *Waste Manag*., **2005**, 25, 1055-1066.

[28] C. S. Poon, Z. Q. Chen. *Chemosphere*, **1999**, 38, 663-680.

[29] A. Barkatt, P. B. Macedo, W. Sousanpour, M. A. Boroomand, C. F. Fisher, J. J. Shirron, P. Szoke, V. L. Rogers. *Nuclear Chem. Waste Management*, **1983**, 4, 153-169.

Chapter 4*

Crystal Chemistry of Apatite-Ellestadite Solid Solution

The ellestadite apatites $Ca_{10}[(SiO_4)_x(PO_4)_{6-2x}(SO_4)_x]Cl_2$ were studied by powder X-ray and neutron diffraction to establish baseline crystallographic data of the waste form. These synthetic materials, unlike mineral specimens that are well equilibrated, show no Si/P/S ordering and conform to $P6_3/m$ symmetry. The unit cell volume increases in tandem with higher (Si/S) contents at the B site because PO_4 is slightly smaller than the average size of SiO_4 and SO_4. The CaO_6 metaprism twist angle (φ) increases linearly as PO_4 displaces SiO_4/SO_4. Loss of $CaCl_2$ is found in the Si/S rich compositions ($3 \leq x \leq 2$), but for $x \leq 1.5$, the Ca and Cl sites are fully occupied with a second low occupancy Cl site appearing in the tunnel.

*This section published substantially as Fang *et al.* (2014) Dalton Trans., **43**,16031.

4.1 Introduction

Chlorapatite ($Ca_{10}(PO_4)_6Cl_2$) has been investigated for the immobilization of chloride contaminated actinide waste [1], and chlorellestadites ($Ca_{10}[(SiO_4)_3(SO_4)_3]Cl_2$), synthesized from industrial wastes, show promise as ceramic waste forms for stabilizing incinerator fly ash containing chlorides, sulphates and heavy metals [2]. This chapter describes the synthesis of the chlorapatite–chlorellestadite solid solution series to serve as a model structure for the incorporation of toxic metals, and investigate crystallochemical properties as a function of the P–(Si/S) ratio. Here, the synthesis of these ellestadites is described and the crystal chemistry of the materials evaluated. X-ray and neutron diffraction used in combination with electron probe microanalysis and infrared spectroscopy examined the incorporation of SiO_4^{4-} and SO_4^{2-} into the apatite framework and determine the chlorine position along the tunnel. Metaprism twist angle analysis was employed to monitor the relative size of the framework and tunnel, which is directly related to compositional changes.

4.2 Experimental Methods

4.2.1 Synthesis

Ellestadites of composition $Ca_{10}[(SiO_4)_x(PO_4)_{6-2x}(SO_4)_x]Cl_2$ were prepared in the solid-state where the nominal overall reaction was:

$$(6\text{-}x)\ CaO + CaCl_2 + (3\text{-}x/2)\ SiO_2 + (3\text{-}x/2)\ CaSO_4 + x/2\ Ca_3(PO_4)_2 \rightarrow Ca_{10}[(SiO_4)_{3\text{-}x/2}(PO_4)_x(SO_4)_{3\text{-}x/2}]Cl_2 \qquad (4\text{-}1)$$

Fresh CaO (prepared by firing analytical reagent grade $CaCO_3$ at 900 °C), $CaSO_4$, SiO_2, $Ca_3(PO_4)_2$ and $CaCl_2$ powders were mixed in stoichiometric amounts. After grinding in acetone and drying, the mixtures were fired (950 °C/air/9 hours) in alumina crucibles covered by an alumina slide to slow chlorine volatilization.

4.2.2 Chemical Analysis

Ellestadite chemical compositions were determined by electron probe microanalysis (EPMA) using a JEOL JXA-8200 operated at 20 kV, with a beam current of 20 nA, beam diameter of 2.5 μm and peak counting times of 40 seconds for all elements (both peak and background). The standards used were quartz (Si), a natural apatite (P and Ca), pyrrhotite (S) and NaCl (Cl). Chlorine is always underestimated due to electron beam induced anisotropic diffusion of chlorine along the ellestadite c-axis and subsequent volatilization [3].

4.2.3 Fourier-transform Infrared (FTIR) Spectroscopy

Infrared absorption spectra were recorded over the range 4000–400 cm^{-1} with a Fourier transform infrared spectrometer (Perkin-Elmer spectrum 2000). Ellestadite powders were prepared for FTIR measurements by manually grinding ca. 1 mg of powder in an agate mortar with a pestle and dispersing it through 200 mg of KBr. The homogenized mixture was pressed into 10 mm diameter transparent pellets. Spectra were averaged over 32 scans with 2 cm^{-1} resolution, and background subtracted using a pure KBr pellet without the sample. Gaussian peaks were fitted to the FTIR with prominent shoulders modeled by the Fityk program [4].

4.2.4 Powder X-ray and Neutron Diffraction

Powder X-ray diffraction (PXRD) data were collected with a Shimadzu Lab XRD-6000 diffractometer (Bragg–Brentano geometry) equipped with a Cu Kα X-ray tube operated at 40 kV and 40 mA using a step size of 0.01° over the range 8–140° 2-theta. All specimens were spiked with a silicon standard (10 wt%, NIST660a, a = 5.40825 Å) to determine the unit cell constants absolutely using a full-pattern fitting method. Crystal structures were refined by Rietveld analysis using TOPAS 3 [5].

The neutron powder diffraction (NPD) data were acquired at the Institute Laue-Langevin (ILL) Grenoble (France) using the high resolution D1A diffractometer with a wavelength of 1.389 Å, a 2-theta range of 0–150° and scan step size of 0.05°

at room temperature. The diffractometer was equipped with a focusing Ge monochromator at a take-off angle of 123° and 25 standard ^{3}He counter detectors. A cylindrical vanadium sample container (0.9 cm diameter) was used during the measurement.

The structure refinements were carried out with TOPAS employing a pseudo-Voigt peak shape profile (U = 0.12, V = −0.21, W = 0.17 as supplied by ILL) and a starting model using the atomic positions of $Ca_{10}(SiO_4)_3(SO_4)_3Cl_2$ in hexagonal $P6_3/m$ [6]. Although monoclinic forms have been documented, such occurrences were not observed in this study, as 2*b* superstructure reflections were absent, and improvements in R values with lower symmetries ($P2_1/m$; $P2_1$) were insignificant. For each data set, a five-coefficient Chebyshev function and 1/x background, a zero error, unit cell parameters, and crystal size were refined sequentially with temperature displacement parameters and occupation factors of each atomic site kept constant. Scattering lengths of 0.4700, 0.4149, 0.513, 0.2847, 0.5803, and 0.9577 × 10^{-12} cm were used for Ca, Si, P, S, O, and Cl respectively [7]. To ensure reasonable bond lengths in the SiO_4, PO_4, and SO_4 tetrahedra, fractional coordinates were constrained close to the average of the Si–O, P–O, and S–O bond lengths at 1.542 Å using a penalty function. After several refinement cycles, the calcium positions (Ca(1) and Ca(2)) were released, followed by the silicon/sulphur/phosphorus and oxygen positions. The oxygen sites were fully tenanted, while the occupancies of calcium and chlorine were allowed to vary. For nonstoichiometric ellestadites, the occupancy factors of Ca and Cl were constrained to maintain charge balance according to [8]

$$Ca^{2+} + 2Cl^- \rightarrow \square_{Ca} + 2\square_{Cl} \qquad (4\text{-}2)$$

As the refinements do not suggest nonstoichiometry in the samples for $x \leqslant 1$, the standard occupancy factors (SOF) of Ca and the 4*e* Cl(1) + Cl(2) sum were fixed at SOF = 1 and SOF = 0.5 respectively. The mole ratio of Si : S at the tetrahedral site was 1:1 to maintain overall electrostatic neutrality in the crystal structure, and the sum of the occupancy of the Si/S/P was fixed to 6. Isotropic temperature displacement parameters for all atoms were refined in Ca(1)/Ca(2)/Cl and Si/P/S/O(1)/O(2)/O(3) groups to the same value. The refinement cycles were terminated when convergence was reached. Difference Fourier maps were

generated using Jana2006 [9] specifically to examine the location of chlorine neutron scattering centers in the tunnels.

4.2.5 Transmission Electron Microscopy (TEM)

Specimens were prepared by ultrasonically dispersing a small quantity of powder in acetone then placing a drop of suspension on a holey carbon-coated copper grid that was allowed to dry. High-resolution transmission electron microscopy (HRTEM) was carried out with a JEOL-2010 TEM (JEOL, Tokyo, Japan Cs = 0.5 mm and Cc = 1.1 mm) operated at 200 kV with a LaB_6 source. Samples were analyzed after orientation with a double tilting holder and the selected area electron diffraction (SAD) patterns were recorded.

4.3 Crystal Chemistry of $Ca_{10}[(SiO_4)_x(PO_4)_{6-2x}(SO_4)_x]Cl_2$

4.3.1 Homogeneity of Apatite

The phase purity of each sample was ascertained by quantitative powder XRD, with $CaSO_4$ appearing as a secondary phase for $0 < x \leqslant 3$ in $Ca_{10}[(SiO_4)_x(PO_4)_{6-2x}(SO_4)_x]Cl_2$ (Figure 4.1); mass balance requires other secondary phases, such as quartz, that were detected, but at levels too low for treatment by Rietveld refinement.

4.3.2 Metalloid Speciation

FTIR spectroscopy was used to study the interaction of phosphate with the substituting silicate and sulfate groups, where the systematic changes in atomic mass shift the wavenumber vibration and also modify the shape of the absorption bands. As the atomic masses of Si and S bracket that of P, the wavenumber of IR absorption will shift proportionally to confirm that a solid solution has formed.

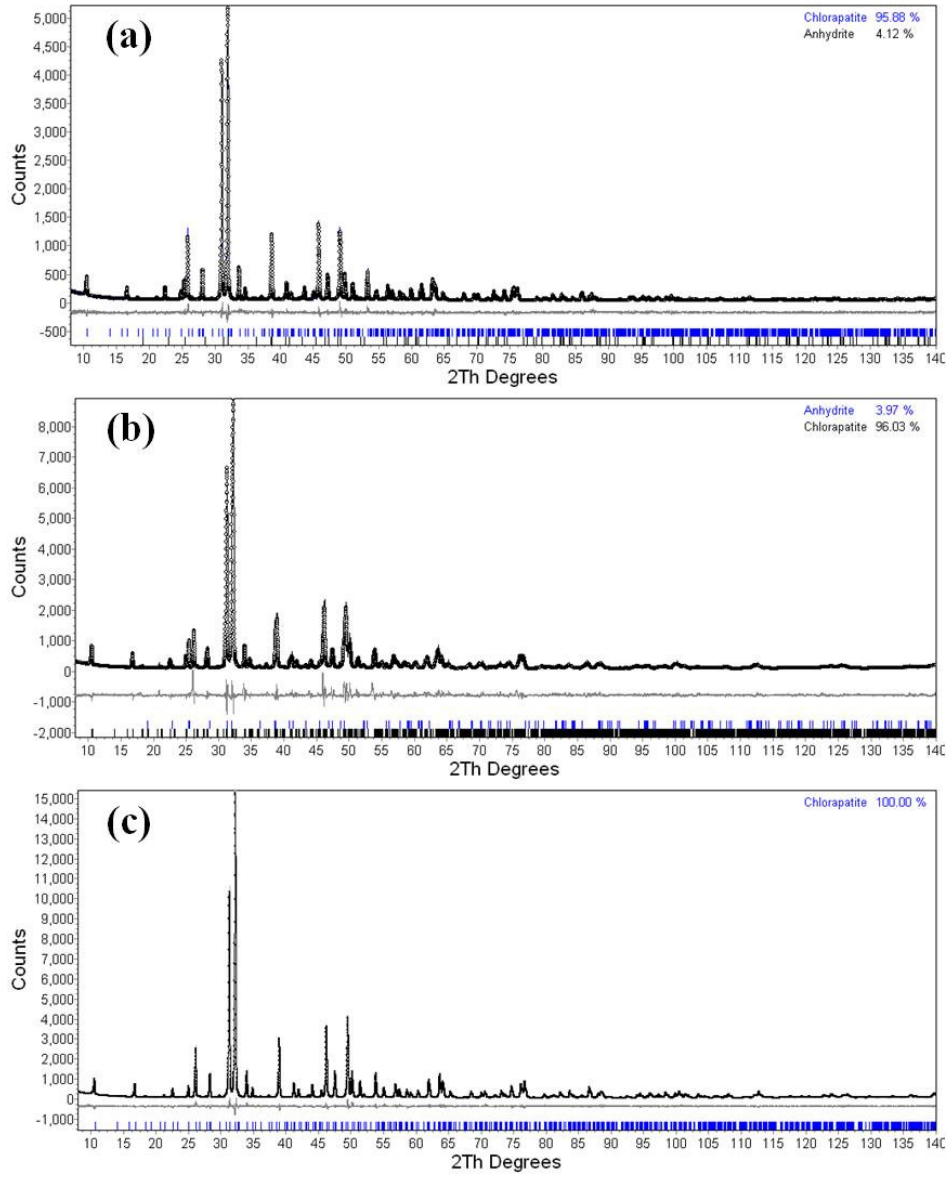

Figure 4.1 Experimental X-ray diffraction data (line) and Rietveld fit (solid dots) of the synthetic chlorellestadite ($Ca_{10}[(SiO_4)_x(PO_4)_{6-2x}(SO_4)_x]Cl_2$): (a) x =3, (b) x = 1.0, (c) x = 0, heated in air at 950 °C. Proportions of $CaSO_4$ secondary phase in each composition are listed in Table 4.2.

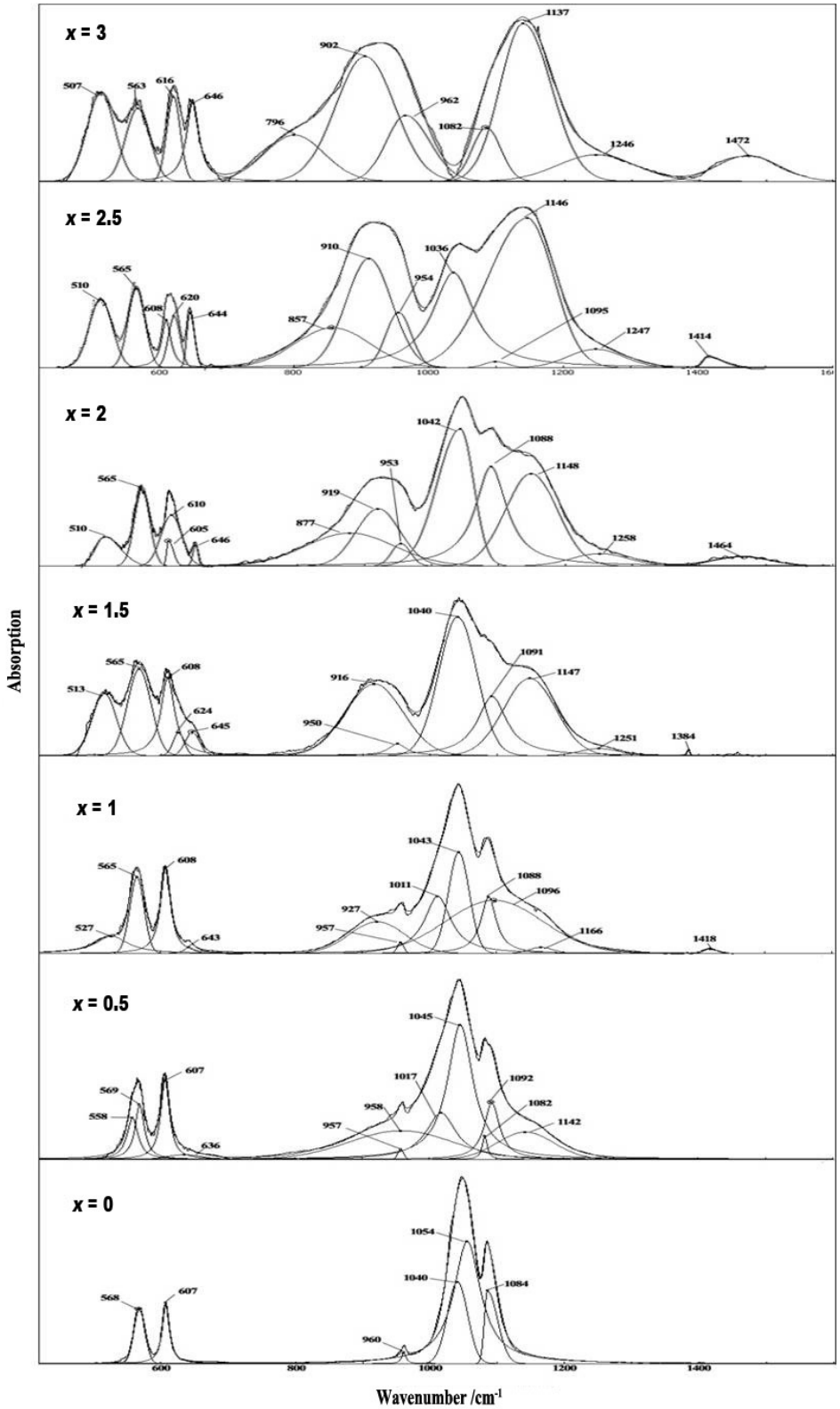

Figure 4.2 Peak-fitted FT-IR spectra of apatite–ellestadite solid solutions. Sample labels indicate x in $Ca_{10}[(SiO_4)_x(PO_4)_{6-2x}(SO_4)_x]Cl_2$.

Table 4.1 FT-infrared frequencies (cm^{-1}) and assignments for apatite–ellestadite solid solutions.

Absorption bands of $Ca_{10}[(SiO_4)_x(PO_4)_{6-2x}(SO_4)_x]Cl_2$ (cm^{-1})								
vibration		*x*=3 Ellestadite	*x*=2.5	*x*=2.0	*x*=1.5	*x*=1.0	*x*=0.5	*x*=0 Apatite
SiO_4^{4-}	ν_4	508	512	511	515	533	523	
		563	565	566	560	558	559	
	ν_3	931 broad	926 broad	926 broad	920 broad	927 broad	927 broad	
SO_4^{2-}	ν_4	616	623	610	629	635	634	
		646	644	646	646			
	ν_3	1137 broad	1139 broad	1148 broad	1147 broad	1146 broad	1142 broad	
PO_4^{3-}	ν_4				566	566	569	567
			610	606	608	607	607	607
	ν_3		1046 broad	1047 broad	1046 broad	1044 broad	1047 broad	1046 broad
				1089	1091	1085	1082	1085
	ν_1					957	958	961

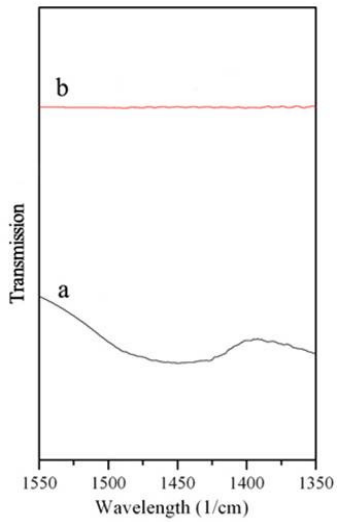

Figure 4.3 FTIR spectra of $Ca_{10}[(SiO_4)_{2.5}(PO_4)(SO_4)_{2.5}]Cl_2$ (a) before and (b) after treatment in dilute acid.

Peak-fitted FT-IR spectra of apatite–ellestadite samples are shown in Figure 4.2, and allowed the identification of individual tetrahedral groups and the estimation of their relative proportions. Comparing the spectra of pure chlorapatite and fully substituted ellestadite (Figure 4.2, $x = 0$ and $x = 3$), the most notable effects of Si/S substitution are shifts in the BO_4 group bands between 1100–800 cm^{-1} and 700–500 cm^{-1}. For chlorapatite ($x = 0$) the PO_4^{3-} groups v_3 mode appears at 1046 and 1085 cm^{-1}, v_4 mode at 607 and 567 cm^{-1}; and v_1 mode at 961 cm^{-1}, consistent with the published values of Wilson [11], who reported infrared bands for hydroxyapatite at ~1090 and ~1050 cm^{-1} assigned to P–O anti-symmetric stretching vibration modes (v_3), vibrations at ~602 and ~570 cm^{-1} for O–P–O bending modes (v_4), and ~962 cm^{-1} for P–O symmetric modes (v_1). Spectra for pure ellestadite ($x = 3$) show prominent bands at approximately ~1137 and ~931 cm^{-1} attributable to v_3 stretching modes of the SO_4^{2-} and SiO_4^{4-} groups respectively. The doublet bands at 646 and 616 cm^{-1} are assigned to the v_4 bending mode of SO_4^{2-}, whereas doublet bands at 563 and 508 cm^{-1} are the v_4 bending modes of the SiO_4^{4-} group [2]. These changes are consistent with the "harmonic oscillator model" for the energy of IR-active vibrations, thus the wavenumber increases with increasing bond strengths and decreasing atomic masses.

At intermediate compositions, the shape and intensity change progressively, and the phosphate mode v_3 at ~1046 cm^{-1} in $Ca_{10}[(SiO_4)_{2.5}(PO_4)(SO_4)_{2.5}]Cl_2$ becomes more intense with increasing phosphate content, while the bands of SO_4^{2-} and SiO_4^{4-} groups diminish. The partial, or very weak appearance, of absorption corresponding to the PO_4^{3-} v_1 (961 cm^{-1}) vibration in some samples (x = 2.5, 2, and 1.5, x in $Ca_{10}[(SiO_4)_x(PO_4)_{6-2x}(SO_4)_x]Cl_2$) is caused by the proximity of the PO_4^{3-} v_1 (961 cm^{-1}) and the SiO_4^{4-} v_3 (941 cm^{-1}) modes so that v_1 cannot be separated from the stronger v_3 absorption. Although the Rietveld refinements of XRD show anhydrite as the secondary phase in some compositions, the characteristic band of $CaSO_4$ at ~680 cm^{-1} is not detected in the FTIR spectra [11]. This may be due to the low abundance of anhydrite. Table 4.1 collates the frequencies of IR absorption bands of the apatite–ellestadite solid solution.

According to Matthews [12], the carbonate ion will be expelled from the apatite structure at about 800 °C with the band-doublet at 1424 and 1456 cm^{-1} related to carbonate-apatite disappearing. As the synthesis temperature here is 950 °C, the existence of structural carbonate in ellestadite was precluded. The weak carbonate band observed at ~1415 and ~1450 cm^{-1} in samples x = 2.5, 2, 1.5 and 1 may be due to absorption of atmospheric CO_2 post synthesis. Treatment in dilute HCl acid [13] removes adsorbed carbonate and confirms that it is not bound crystallographically (Figure 4.3). A broad hydroxyl band from 2500 to 3500 cm^{-1} arises from atmospheric water adsorbed to the KBr specimen pellet, and removed by oven drying the KBr powder at 300 °C. It is concluded, that to the limit of detection, all the apatites are fully chlorinated.

4.3.3 Crystal Structure

The details of the crystal structure refinements including atomic positional parameters and atomic displacement parameters are given in Table 4.2, with selected atomic distances and bond angles collected in Table 4.3. Preliminary analysis of the X-ray diffraction patterns assumed the samples to be single-phase apatite. Inspection of the X-ray (Figure 4.1) and neutron diffraction patterns (Figure 4.4) did not obviously indicate peak splitting or significant line broadening that might have led to a supposition of phase separation or lower symmetry.

Table 4.2 Lattice parameters and crystallographic data for $Ca_{10}[(SiO_4)_x(PO_4)_{6-2x}(SO_4)_x]Cl_2$ from Rietveld refinements of powder neutron diffraction data.*

Ellestadite (wt%)		95.6(6)	97.6(2)	98.6(2)	95.7(6)	98.1(3)	100
$CaSO_4$ (wt%)		4.3(6)	2.3(2)	1.4(2)	4.2(6)	1.9(3)	--
nominal *x*		3	2.5	2	1	0.5	0
refined *x*		3	2.4	2.03	0.66	0.27	0
a (Å)		9.6691(3)	9.6622(3)	9.6537(5)	9.6257(4)	9.6299(2)	9.6182(1)
c (Å)		6.8531(3)	6.8438(2)	6.8354(4)	6.7892(3)	6.7833(2)	6.7920(1)
V (Å^3)		554.88(4)	553.32(4)	551.67(7)	544.77(5)	544.77(3)	544.15(2)
R_p		0.040	0.036	0.037	0.046	0.040	0.044
R_{wp}		0.052	0.047	0.048	0.059	0.052	0.056
R_{exp}		0.067	0.078	0.075	0.077	0.077	0.082
GOF**		0.77	0.59	0.64	0.77	0.67	0.69
R_b		0.032	0.028	0.022	0.021	0.022	0.029
Ca(1)	z	-0.0022(1)	-0.0027(9)	-0.003(1)	0.002(1)	0.0012(8)	-0.0009(6)
4*f*	Occ	0.9837(81)	0.9958(69)	0.9952(74)	1	1	1
	B	2.04(5)	1.91(4)	1.61(5)	1.02(4)	0.89(3)	0.87(3)
Ca(2)	x	0.2600(7)	0.2596(6)	0.2602(7)	0.2584(6)	0.2586(4)	0.2582(4)
6*h*	y	-0.0004(8)	-0.0008(7)	-0.0004(8)	0.0024(7)	0.0031(5)	0.0006(5)
	Occ	0.9830(53)	0.9754(44)	0.9753(48)	1	1	1
	B	2.04(5)	1.91(4)	1.61(5)	1.02(4)	0.89(3)	0.87(3)
P	x	0.4030(4)	0.4044(3)	0.4053(3)	0.4071(3)	0.4077(2)	0.4064(2)
6*h*	y	0.3728(4)	0.3739(3)	0.3746(3)	0.3750(3)	0.3752(2)	0.0.3740(2)
	Occ (Si)	0.5	0.40(1)	0.34(1)	0.11(1)	0.04(1)	
	Occ (S)	0.5	0.40(1)	0.34(1)	0.11(1)	0.04(1)	
	Occ (P)		0.20(2)	0.32(3)	0.78(3)	0.92(2)	1.00
	B	2.04(5)	2.14(3)	1.87(3)	1.12(3)	0.95(2)	1.05(2)
O(1)	x	0.3361(3)	0.3379(3)	0.3390(3)	0.3415(3)	0.3422(2)	0.3408(2)
6*h*	y	0.4880(3)	0.4894(3)	0.4898(3)	0.4918(3)	0.4917(2)	0.4906(2)
	B	2.20(3)	2.14(3)	1.87(3)	1.12(3)	0.95(2)	1.05(2)
O(2)	x	0.5886(3)	0.5895(3)	0.5903(4)	0.5919(3)	0.5925(2)	0.5913(2)
6*h*	y	0.4672(5)	0.4675(4)	0.4687(5)	0.4669(5)	0.4672(4)	0.4670(3)
	B	2.20(3)	2.14(3)	1.87(3)	1.12(3)	0.95(2)	1.05(2)
O(3)	x	0.3538(3)	0.3535(3)	0.3534(3)	0.3514(3)	0.3525(2)	0.3518(2)
12*i*	y	0.2665(3)	0.2667(2)	0.2668(3)	0.2664(3)	0.2665(2)	0.2653(2)
	z	0.0657(3)	0.0667(3)	0.0677(3)	0.0671(4)	0.0672(2)	0.0674(2)
	B	2.20(3)	2.14(3)	1.87(3)	1.12(3)	0.95(2)	1.05(2)
Cl(1)	z	0.425(1)	0.4290(9)	0.4308(1)	0.4388(1)	0.4418(8)	0.4343(8)
4*e*	Occ	0.416 (23)	0.418(192)	0.42(2)	0.4039(8)	0.4107(67)	0.3741(56)
	B	2.04(5)	1.91(4)	1.61(5)	1.02(4)	0.89(3)	0.87(3)
Cl(2)	z				0.154(5)	0.140(4)	0.153(3)
4*e*	Occ				0.0961(8)	0.0893(6)	0.1259(5)
	B				1.02(4)	0.89(3)	0.87(3)

* $R_p = (\Sigma_i|y_i - y_{ci}|)/\Sigma_i y_i$, $R_{wp} = [(\Sigma_i w|y_i - y_{ci}|^2)/\Sigma_i w|y_i|^2]^{1/2}$, $R_{exp} = [(\sum(M-P)/\sum w_m Y^2_{o,m}]^{1/2}$, $GOF = R_{wp}/R_{exp} = \Sigma_i w\,(y_i - y_{ci})^2/(n - p)$

Table 4.3 Bond lengths (Å) and angles (°) for $Ca_{10}[(SiO_4)_x(PO_4)_{6-2x}(SO_4)_x]Cl_2$, and Bond-Valence Sums (BVS) of Ca(1) and Ca(2) sites.

x	3	2.5	2	1	0.5	0
Ca(1)-O(1) × 3	2.453(5)	2.450(2)	2.449(5)	2.411(5)	2.416(4)	2.428(4)
Ca(1)-O(2) × 3	2.471(6)	2.463(5)	2.464(6)	2.453(6)	2.449(5)	2.444(4)
Ca(1)-O(3) × 3	2.793(4)	2.795(3)	2.794(4)	2.808(4)	2.800(3)	2.797(2)
twist angle (φ)	20.4(2)	19.8(1)	19.2(1)	18.4(1)	18.1(8)	18.7(7)
Ca(2)-O(2)	2.288(7)	2.287(4)	2.270(7)	2.294(7)	2.291(3)	2.293(4)
Ca(2)-O(3) × 2	2.331(4)	2.335(4)	2.341(3)	2.327(3)	2.332(3)	2.326(3)
Ca(2)-O(3) × 2	2.597(7)	2.595(6)	2.581(3)	2.554(3)	2.549(5)	2.557(4)
Ca(2)-Cl(1)	2.787(7)	2.795(7)	2.798(6)	2.788(7)	2.797(3)	2.778(5)
Ca(2)-Cl(2)				2.56(1)	2.585(8)	2.566(5)
O(3)-O(3)	5.346(5)	5.340(4)	5.335(5)	5.294(5)	5.310(3)	5.289(3)
O(3)-Cl(1)	3.087(2)	3.083(2)	3.080(3)	3.056(3)	3.066(2)	3.054(2)
O(3)-Cl(2)				3.114(3)	3.105(5)	3.108(4)
Ca(2)-Ca(2)	4.355(1)	4.351(1)	4.347(1)	4.288(1)	4.287(8)	4.295(7)
B-O(1)	1.542(6)	1.540(5)	1.536(5)	1.540(5)	1.536(4)	1.538(4)
B-O(2)	1.553(4)	1.549(4)	1.546(4)	1.541(4)	1.541(2)	1.540(2)
B-O(3) × 2	1.547(3)	1.542(3)	1.538(2)	1.537(3)	1.536(2)	1.535(2)
O(1)-B-O(2)	110.7(2)	110.8(2)	110.6(9)	110.9(3)	110.9(2)	110.6(2)
O(1)-B-O(3)	112.3(2)	112.2(2)	112.1(2)	111.5(2)	111.6(1)	111.7(1)
O(2)-B-O(3)	105.7(2)	106.2(2)	106.7(2)	107.5(2)	107.3(1)	107.4(9)
O(3)-B-O(3)	109.6(2)	108.8(2)	108.2(2)	107.7(2)	107.7(2)	107.8(2)
$Ca(1)_{BVS}$	1.98	1.99	1.94	2.00	2.04	2.00
$Ca(2)_{BVS}$	1.98	1.99	2.01	2.00	2.00	2.05

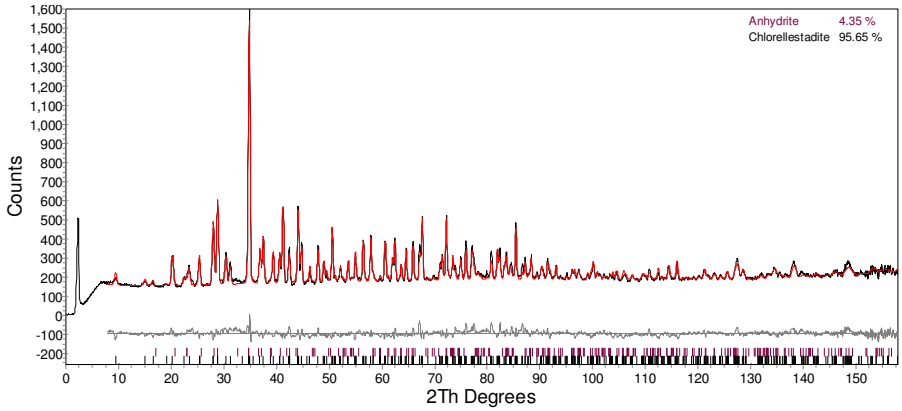

Figure 4.4(a) Neutron data and Rietveld refinement of $Ca_{10}[(SiO_4)_3(SO_4)_3]Cl_2$.

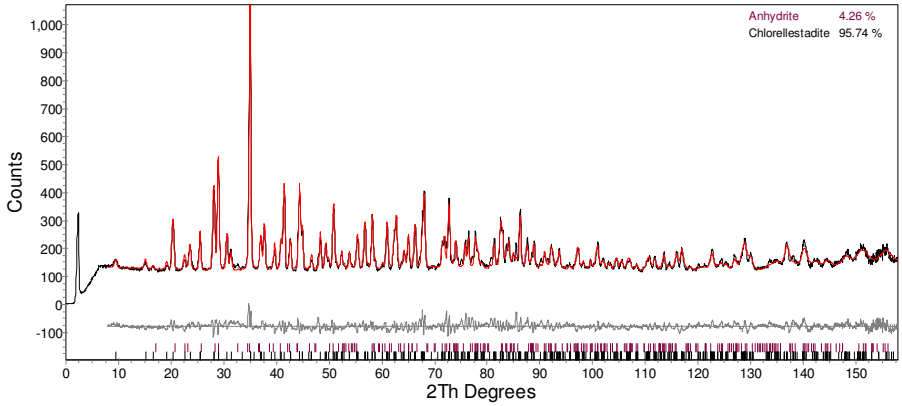

Figure 4.4(b) Neutron data and Rietveld refinement of $Ca_{10}[(SiO_4)(PO_4)_4(SO_4)]Cl_2$.

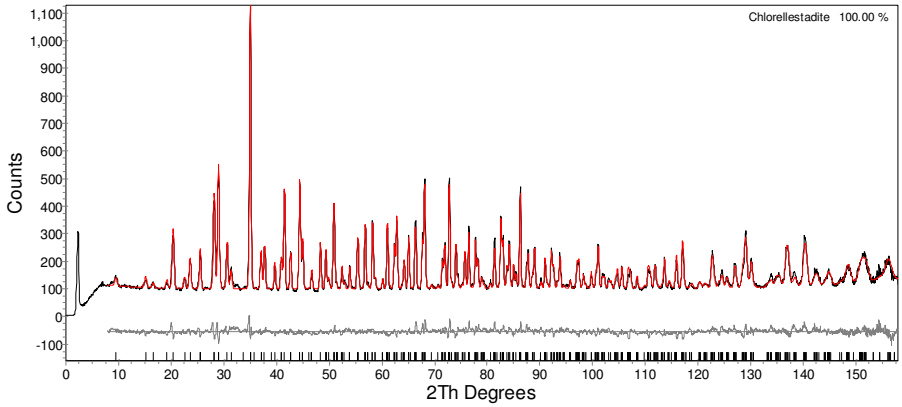

Figure 4.4(c) Neutron data and Rietveld refinement of $Ca_{10}(PO_4)_6Cl_2$.

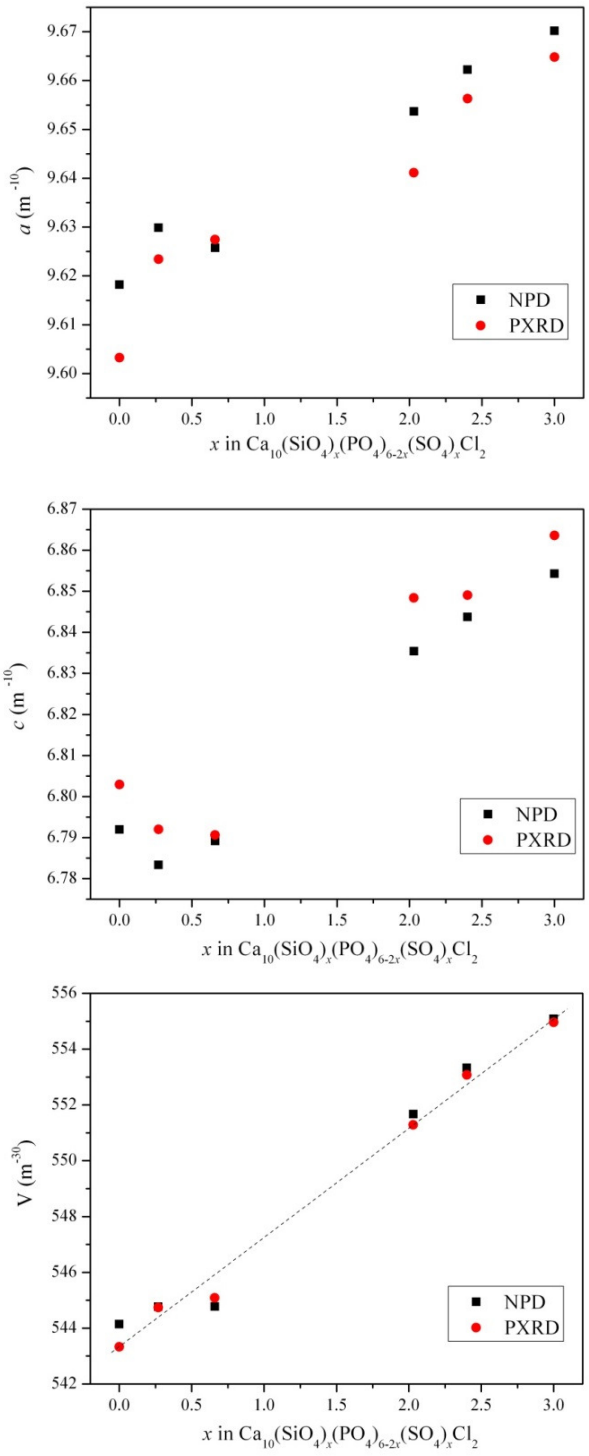

Figure 4.5 Unit cell parameters *a, c* and volume V derived from Rietveld refinements of neutron (black square) and XRD (red dot) data as a function of the phosphorus content. Errors are within the size of the symbols.

Figure 4.5 shows that the relationship between the refined chemical compositions and unit cell parameters is almost linear from chlorellestadite to chlorapatite. Vegard's law is therefore obeyed by this solid solution series. Both unit cell parameters *a* and *c* increased with the incorporation of silicon and sulphur. The effective size of PO_4 is slightly smaller than the average size of SiO_4 and SO_4, as seen from the variation of *B*–O bond lengths in Table 4.3. Thus, increasing the silicon and sulphur contents dilates the unit cell. This result is consistent with the study of Rouse and Dunn [14], who described a solid solution series between ellestadite and calcium phosphate apatite. Those naturally occurring ellestadites containing F^- and OH^- instead of Cl^- show a linear variation of lattice parameters when exchanging SiO_4^{4-} and SO_4^{2-} by $2PO_4^{3-}$.

Table 4.4 Bond lengths in monoclinic structure ($P2_1/m$). Note that in all tetrahedra some B-O bond lengths refine to non-physical values. A reasonable spread of B-O distances would be 1.49 – 1.61 Å.

x	bond lengths (Å)					
3	*B*(1)-O(1)	1.43(3)	*B* (2)-O(2)	1.52(2)	*B* (3)-O(3)	1.49(2)
	B (1)-O(4)	1.69(3)	*B* (2)-O(5)	1.81(4)	*B* (3)-O(6)	1.69(3)
	B (1)-O(7) × 2	1.63(2)	*B* (2)-O(8) × 2	1.63(2)	*B* (3)-O(9) × 2	1.57(2)
	B (1)-O	1.59	*B* (2)-O	1.64	*B* (3)-O	1.58
2.5	*B* (1)-O(1)	1.22(3)	*B* (2)-O(2)	1.30(2)	*B* (3)-O(3)	1.17(4)
	B (1)-O(4)	1.73(2)	*B* (2)-O(5)	1.83(2)	*B* (3)-O(6)	1.88(4)
	B (1)-O(7)	1.71(1)	*B* (2)-O(8) × 2	1.62(2)	*B* (3)-O(9) × 2	1.83(3)
	B (1)-O	1.59	*B* (2)-O	1.59	*B* (3)-O	1.67

To study the ordering of BO_4 tetrahedra in ellestadite, the $P2_1/m$ space group was used for the neutron data refinements. However, the similarity of neutron scattering lengths for Si, P, and S prevented successful occupancy refinement at the tetrahedral site. According to Sudarsanan [15], some degree of Si/S ordering in monoclinic hydroxyellestadite is evidenced by the three different sizes of the BO_4 tetrahedra. The average *B*–O bond distances are 1.57 Å and 1.52 Å respectively for Si and S tetrahedral sites, and 1.54 Å for the site with Si/S with 1:1 occupancy. In $P2_1/m$ the tetrahedrally coordinated atoms (Si/S) are divided among three 2-fold Wyckoff positions; however, refinement did not reveal such ordering, but rather the spread of *B*–O bond lengths in the crystallographically distinct BO_4 became non-physical

(Table 4.4). Therefore, refinements were carried out in $P6_3/m$ and all tetrahedrally coordinated atoms are undifferentiated in a single 6-fold (6*h*) position (Table 4.3).

4.3.4 Chlorine Deficiency and Position in The Tunnel

A Ca-deficiency was found in x = 3, 2.5, and 2 compositions (Table 4.5) with the loss of chlorine from the tunnel (Table 4.2), but Ca and Cl deficits were not observed for x = 1, 0.5, and 0. Hounslow and Chao [16] studied the dependence of monoclinic character on the chlorine content in mineral chlorapatite, and suggested that 10 to 15% of chlorine ions can be lost before the hexagonal form becomes evident by polarized light microscopy and X-ray diffraction. In our study, the atomic occupancies (Table 4.2) indicate that only about 80% of the stoichiometric amount of Cl is present in x = 3, 2.5, and 2 compositions, which eliminates the possibility of monoclinic ($P2_1/b$) chlorellestadite formation, since the loss of chlorine atoms removes the stereochemical driver for inter-tunnel chlorine ordering.

Table 4.5 Atomic proportions of selected ellestadites obtained by EPMA. A statistically significant deficit of Ca appears for (Si/S) rich ellestadites. Chlorine is underestimated due to volatilization under the electron beam. Chlorine contents derived from neutron diffraction (see Table 4.2) are more reliable.

	Ca	Si	P	S	Cl	O
x = 3	9.88	2.96	0.02	3.06	1.65	24.27
error	0.06	0.07	0.01	0.05	0.09	0.10
x = 2.5	9.84	2.41	1.09	2.56	1.58	24.25
error	0.07	0.10	0.07	0.17	0.04	0.16
x = 1.0	9.97	0.68	4.51	0.82	1.28	24.12
error	0.09	0.04	0.14	0.06	0.04	0.08
x = 0	9.95		5.94		1.26	24.33
error	0.04		0.03		0.08	0.14

Difference Fourier maps (Figure 4.6) of neutron scattering along the apatite tunnel show that across the ellestadite–apatite series the chlorines occupy different positions. For x = 3, 2.5 and 2 compositions, there is only one Cl position $z \approx 0.43$, and in x = 1, 0.5, and 0, a splitting of neutron scattering centres is evident. In synthetic $Mn_{10}(PO_4)_6Cl_2$ Engel et al. [17] explained a similar elongated electron density in the c direction and a slightly low chlorine occupancy by a 10%

substitution of chlorine by OH ions. Our samples did not show OH bands in the infrared spectra. To investigate the positions of chlorines along the c-axis, refinements and difference Fourier maps were prepared (i) without Cl^-, (ii) with one Cl^-, and (iii) two Cl^- for the compositions x = 1, 0.5, and 0. In pure apatite (x = 0) when there is only one chlorine (z = 0.429) in the tunnel, the difference Fourier map (Figure 4.7) shows some remaining neutron scattering, implying the possibility of multiple chlorine positions. By introducing a second Cl^- (z = 0.153), the difference Fourier map exhibits low neutron density residuals in the range of −0.85 e $Å^{-3}$ to 0.85 e $Å^{-3}$, and lower R-factors. Hence, difference maps show that, although most of the Cl ions are at the $z \approx 0.44$ sites, some might be present at $z \approx 0.15$ sites in the same tunnels. The environment of the chlorine ions is shown in Figure 4.8. In the chlorellestadite (x = 3) structure, Cl ions are approximately in the center of an O(3) triangle (O(3)–O(3) : 5.346(5) Å) in which the Cl–O(3) distances are 3.087(2) Å. With increasing phosphate content, the unit cell became smaller, and the O(3) triangle shrinks (O(3)–O(3) is 5.289(3) Å for chlorapatite, x = 0). To keep the average separation of O(3) and Cl reasonable, some of the Cl ions are displaced from the center of the O(3) triangle towards the Ca(2) triangle. The bond valences of Ca(1) and Ca(2) were calculated (Table 4.3), and no deficit of valence charge was found confirming the Rietveld refinements.

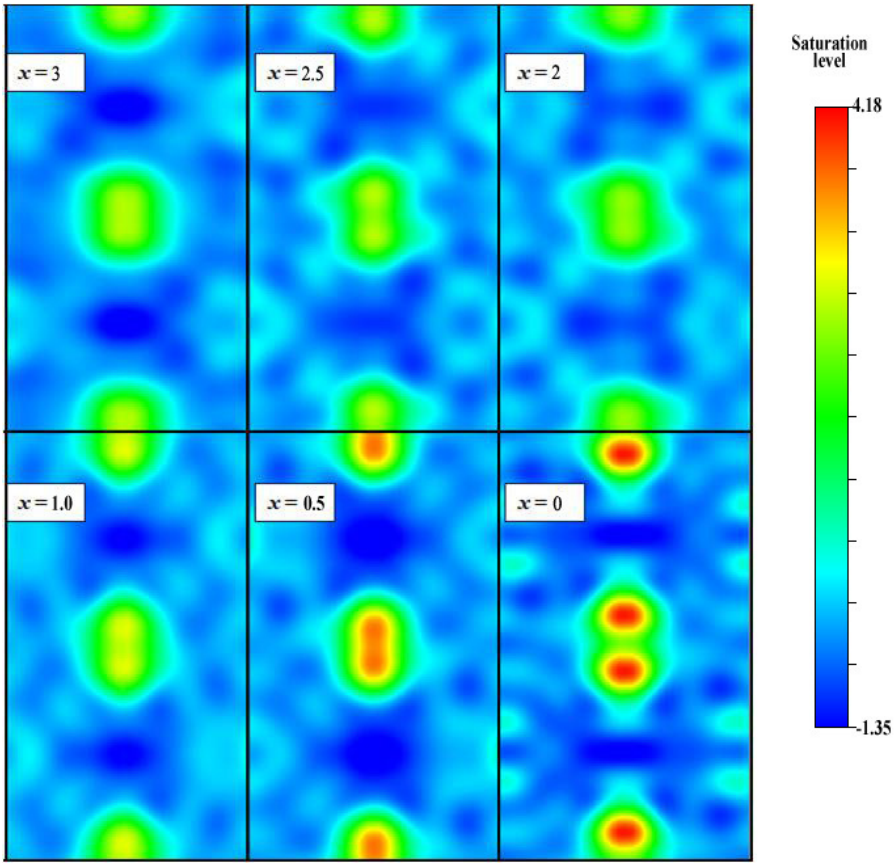

Figure 4.6 Difference Fourier maps of $Ca_{10}[(SiO_4)_x(PO_4)_{6-2x}(SO_4)_x]Cl_2$ ellestadites tunnel indicating the positions of Cl ions that were excluded to emphasize their location.

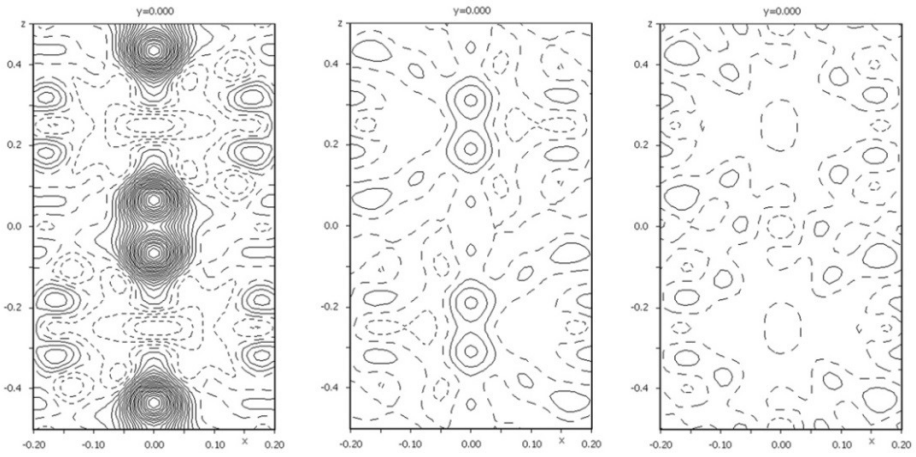

Figure 4.7 Difference Fourier maps of neutron scattering with no Cl^-, one Cl^- (z = 0.429) and two Cl^- (z = 0.434 and 0.153) sites in the apatite ($Ca_{10}(PO_4)_6Cl_2$) tunnel. Contour interval is 0.2 e/Å^3 and the first positive contour (solid line) is at 0.2 e/Å^3. Negative difference nuclear density is indicated by the broken contours.

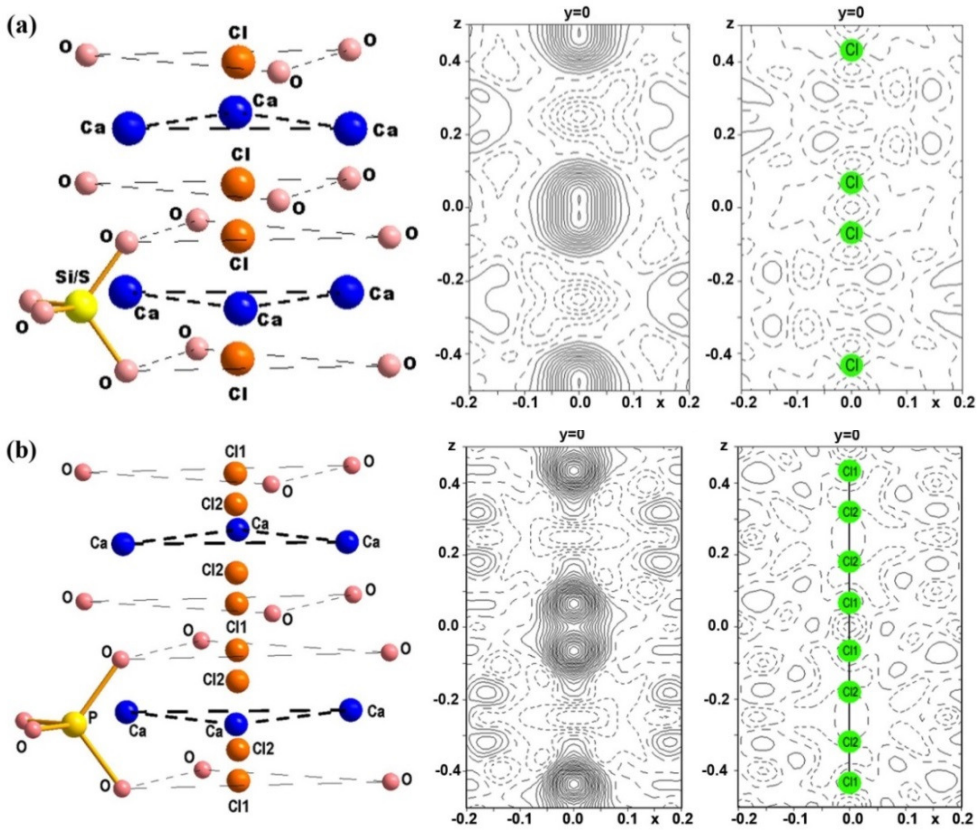

Figure 4.8 Chirographic view of the chlorine ion environment and difference Fourier maps before and after including Cl ions in the tunnel, (a) $Ca_{10}[(SiO_4)_3(SO_4)_3]Cl_2$ and (b) $Ca_{10}(PO_4)_6Cl_2$. The sphere radii represent isotropic thermal displacements. Contour interval is 0.2 e/Å^3 and the first positive contour (solid line) is at 0.2 e/Å^3. Negative difference nuclear density is indicated by the broken contours.

4.3.5 Twist Angle Systematics

The CaO_6 metaprism twist angle (φ) can be used as a diagnostic tool to validate apatite structures, and was calculated for all the compositions using the fractional coordinates of *A*(1), O(1) and O(2) (Figure 4.9). For *P6₃/m* apatite structures 5° < φ < 25° typically, and when the *A*(1) and *A*(2) are chemically identical, there is a linear relationship between φ and the average crystal radii regardless of whether substitution is made on the *B* or *X* sites. Broadly, the ellestadites fall into two groups – those that are stoichiometric with respect to chlorine (2Cl per formula unit) and those sub-stoichiometric with less than two chlorines. Twist angle systematics predict that as chlorine is removed, the tunnel will constrict and φ becomes larger. Figure 4.10a compares the $Ca(1)O_6$ twist angle with the average effective atomic

radius per unit cell that is consistent with the analysis [18] – when the tunnel chlorine sites are filled 18.1° ⩽ φ ⩽ 18.7°, but when the tunnel contains vacancies 19.2° ⩽ φ ⩽ 20.4°. If these two groups are studied in detail then the sub-stoichiometric group shows that a reduction of φ accompanies the in-filling of the tunnel with chlorine (Figure 4.10b). For the stoichiometric group Si and S have a larger average ionic than P, leading to a wider tunnel and smaller φ. The observed value of φ (18.1°) for x = 0.5 is slightly below trend (Figure 4.10c), and likely reflects the difficulty in structurally refining chemically complex ellestadites, and the possibility of arriving at false minima using Rietveld refinements.

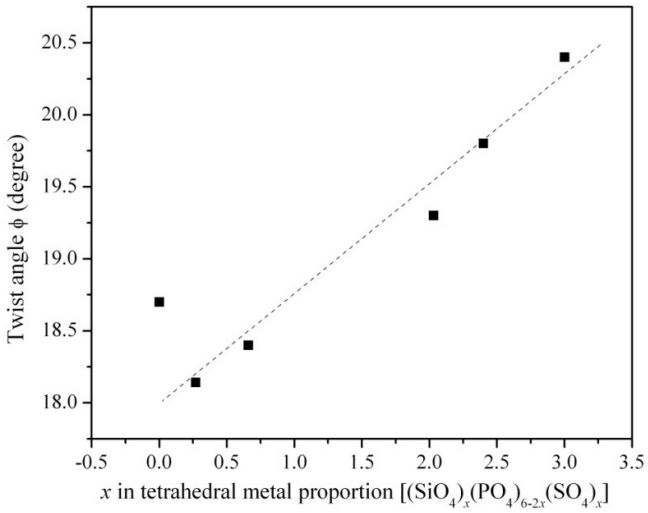

Figure 4.9 Correlation of composition and metaprism twist angle (φ). Errors are within the size of the symbols.

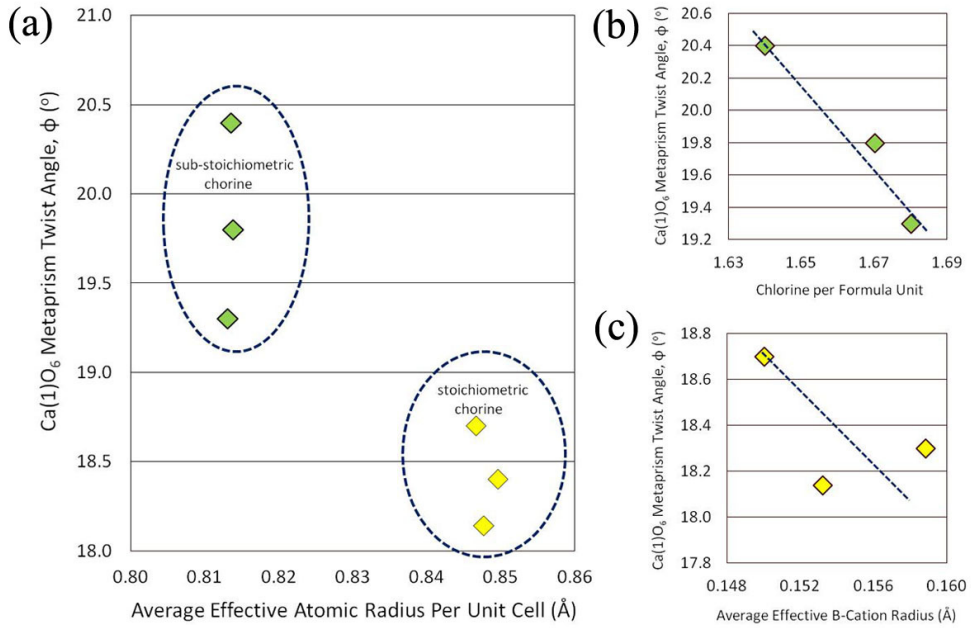

Figure 4.10 Trends in metaprism twist angel for $Ca_{10}[(SiO_4)_x(PO_4)_{6-2x}(SO_4)_x]Cl_2$ as a function of (a) average effective ionic radius for the whole unit cell contents, (b) chlorine content in per formula unit, and (c) average effective *B*-Cation radius.

4.3.6 Nanostructure

High-resolution TEM images of $Ca_{10}[(SiO_4)_{1.5}(PO_4)_3(SO_4)_{1.5}]Cl_2$ and $Ca_{10}[(SiO_4)_{0.5}(PO_4)_5(SO_4)_{0.5}]Cl_2$ show well developed crystals without obvious imperfections, in the sense that no extended defects are observed (Figure 4.11). The intensity distribution of experimental SAD reflections (Figure 4.12) was consistent with $P6_3/m$ symmetry. In a study of a Brazilian gem-grade apatite, $[(Ca_{3.948}Na_{0.052})Ca_{5.99}][(P_{5.686}Si_{0.182}S_{0.132})O_{24}][(F_{1.517}Cl_{0.120}OH_{0.363})]$, Ferraris et al. [19] found some Si/S-rich crystals of ellestadite embedded in a host fluorapatite (F-Ap) and a guest chlorapatite (Cl-Ap). Such domains were not detected in any of our samples, with the thin ellestadite crystals appearing to be homogeneous. Similarly, the reduction of symmetry to $P2_1/m$ that was proposed earlier for $Ca_{10}(PO_4)_6Cl_2$ was not distinguishable by high-resolution imaging and diffraction.

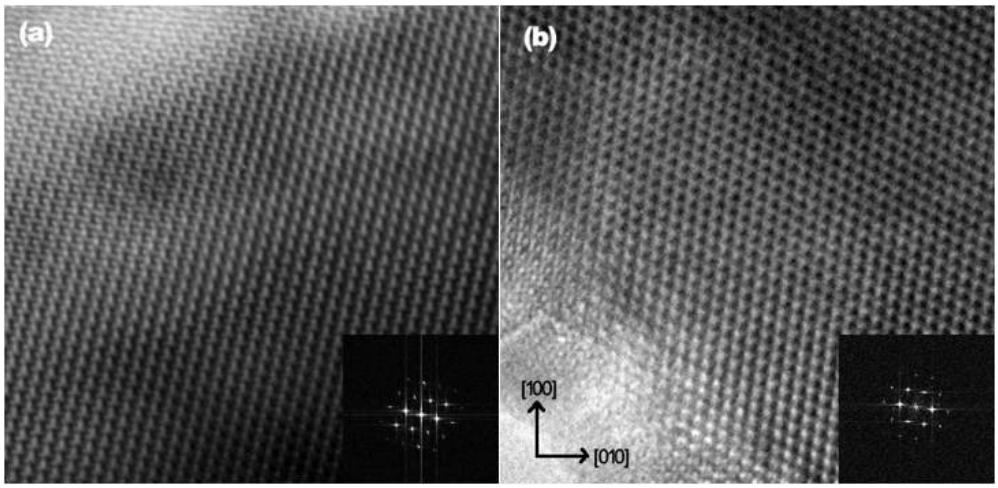

Figure 4.11 HRTEM images taken from [001] zone axis of (a) $Ca_{10}[(SiO_4)_{1.5}(PO_4)_3(SO_4)_{1.5}]Cl_2$ and (b) $Ca_{10}[(SiO_4)_{0.5}(PO_4)_5(SO_4)_{0.5}]Cl_2$ ellestadite.

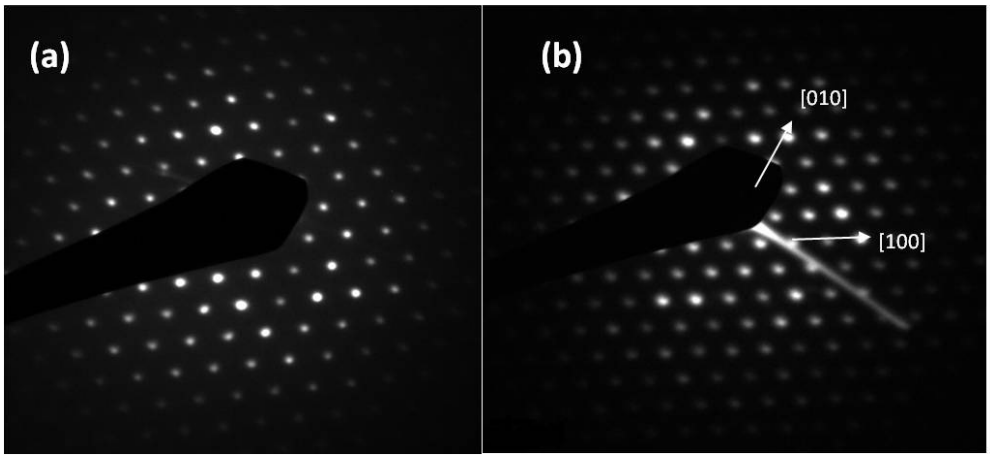

Figure 4.12 SAD pattern taken from [001] zone axis of (a) $Ca_{10}[(SiO_4)_3(SO_4)_3]Cl_2$ and (b) $Ca_{10}[(SiO_4)_2(PO_4)_2(SO_4)_2]Cl_2$. No diffuse intensity or split reflections are present.

4.4 Conclusions

X-ray and neutron diffraction data analysis found all ellestadites $Ca_{10}[(SiO_4)_x(PO_4)_{6-2x}(SO_4)_x]Cl_2$ synthesized by short duration (9 hours) heat treatment are $P6_3/m$ and show no evidence of Si/P/S ordering at the tetrahedral sites. In detail, there are calcium and chlorine deficiencies in the Si/S rich compositions ($3 \leq x \leq 2$) due to the evaporation of $CaCl_2$ during the synthesis. For $x \leq 1.5$ where the Ca and Cl sites are fully occupied, a second low occupancy Cl site appears to reduce steric repulsion with the O(3) triangles.

References:

[1] B. L. Metcalfe, I. W. Donald, S. K. Fong, L. A. Gerrard, D. M. Strachan and R. D. Scheele, *J. Nucl. Mater*., **2009**, 385, 485-488.

[2] J. Neubauer and H. Pöllmann, *Neues. Jahrb. Mineral., Abh*., **1995**, 168, 237-258.

[3] J. C. Stormer, M. L. Pierson and R. C. Tacker, *Am. Mineral*., **1993**, 78, 641-648.

[4] M. Wojdyr, *J. Appl. Crystallogr*., **2010**, 43, 1126-1128.

[5] Bruker, TOPAS Version3, Bruker AXS Inc., Madison, WI, USA, 25005.

[6] S. J. Saint-Jean, E. Jøns, N. Lundgaard and S. Hansen, *Cem. Concr. Res*., **2005**, 35, 431–437.

[7] V. F. Sears, *International Tables for Crystallography*, Kluwer Academic Publishers, Dordrecht, **1993**, vol. C, p. 383.

[8] Y. N. Fang, C. Ritter and T. White, *Inorg. Chem*., **2011**, 50, 12641–12650.

[9] V. Petricek, M. Dusek and L. Palatinus, Jana2006, The Crystallographic Computing System, Institute of Physics, Praha, Czech Republic, 2006.

[10] H. Morgan, R. M. Wilson, J. C. Elliott, S. E. P. Dowker and P. Anderson, *Biomaterials*, **2000**, 21, 617–627.

[11] K. Tonsuaadu, M. Peld, M. Quarton, et al., *Phosphorus, Sulfur Silicon Relat. Elem*., **2002**, 177, 1873–1876.

[12] A. Matthews and Y. Nathan, *Am. Mineral*., **1977**, 62, 565–573.

[13] S. Madhavi, C. Ferraris and T. J. White, *J. Solid State Chem*., **2005**, 178, 2838–2845.

[14] R. C. Rouse and R. J. Dunn, *Am. Mineral.*, **1982**, 67, 90–96.

[15] K. Sudarsanan, *Acta Cryst.,* **1980**, B36, 1636–1639.

[16] A. W. Hounslow and G. Y. Chao, *Can. Mineral*., **1970**, 10, 252–259.

[17] G. Engel, J. Pretzsch, V. Gramlich and W. H. Baur, *Acta Cryst*., **1975**, B31, 1854–1860.

[18] T. J. White, C. Ferraris, J. Kim and S. Madhavi, *Rev. Mineral. Geochem*., **2005**, 57, 307.

[19] C. Ferraris, T. J. White, J. Plévert and R. Wegner, *Phys. Chem. Miner.,* **2005**, 32, 485–492.

Chapter 5*

Solid Solution Series of Fluor-Chloroellestadite

The lattice parameters of the fluor-chlorellestadites vary linearly with composition and show the expected shrinkage of unit cell volume as fluorine (IR = 1.33 Å) displaces chlorine (IR = 1.81 Å). FTIR spectra indicate little or no hydroxyl (OH) in the solid solutions. All compositions conform to $P6_3/m$ symmetry where F is located at the 2a (0, 0, ¼) position, while Cl is displaced out of the 6h Ca(2) triangular plane and occupies 4e (0, 0, z) split positions with z ranging from 0.336(3) to 0.4315(3). Si/S randomly occupy the 6h tetrahedral site. Ellestadites rich in Cl ($x \leq 1.2$) show an overall deficiency in halogens (< 2 atom per formula unit), particularly Cl as a result of $CaCl_2$ volatilization, with charge balance achieved by the creation of Ca vacancies ($Ca^{2+} + 2Cl^- \rightarrow \square_{Ca} + 2\square_{Cl}$) leading to the formula $Ca_{10-y}[(SiO_4)_3(SO_4)_3][Cl_{2-x-2y}F_x]$. For F-rich compositions the vacancies are found at Ca(2), while for Cl-rich ellestadites, vacancies are at Ca(1). It is likely the loss of $CaCl_2$, which leads to tunnel anion vacancies, promotes intertunnel positional disorder, preventing the formation of a $P2_1/b$ monoclinic dimorph, analogous to that reported for $Ca_{10}(PO_4)_6Cl_2$.

*This section published substantially as Fang *et al.* (2011) Inorg. Chem. 50, 12641.

This chapter describes the synthesis and characterization of fluor-chlorellestadites, $Ca_{10}[(SiO_4)_3(SO_4)_3][Cl_{2-x}F_x]$, as simplified surrogates for apatite derived from the stabilization of halide-rich solid waste ashes, with the aim of establishing the continuity of the solid solution series. In terms of waste form durability it is relevant that fluorine promotes greater chemical stability (e.g. reducing dental caries [1]) and thermal resistance (e.g. higher melting points [2]), with the interaction between fluorine and chlorine attenuating these properties.

5.1 Introduction

Commonly, the fluor- and chlor-ellestadites are regarded as isostructural, although the halides reside at different locations along the *c*-axis anion tunnels. In the synthetic fluor-ellestadite ($P6_3/m$) endmember, F^- at 0, 0, 1/4 and 0, 0, 3/4 lies in the centre of a Ca(2) triangle on the mirror planes at z = 1/4 and z = 3/4. [3] In the corresponding chlorellestadite endmember, Cl^- cannot fit into the Ca(2) triangle (ionic radii for $^{VI}F^-$ = 1.33 Å and $^{VI}Cl^-$ = 1.81 Å [4]), and statistically occupies (0, 0, z) sites, ~1.1 Å above or below the mirror plane [5]. In the case of natural hydroxyellestadite, Sudarsanan [6] refined separate sites for OH^- (0, 0, 0.2033), F^- (0, 0, 1/4), and Cl^- (0, 0, 0.3644) in $P2_1/m$ with site occupancies of 0.806(9), 0.15(6), and 0.092(5) respectively. Onac et al. [7] suggested minor substitutions of F^- and Cl^- at the same site as OH^- in a hydroxyellestadite ($P6_3/m$) from Cioclovina Cave, Romania, although at the unit cell scale this is unlikely to satisfy bond valence sum criteria. In general, the interaction between F^- and Cl^-, and the influence on $Ca_{10}[(SiO_4)_3(SO_4)_3]X_2$ (where X = F, Cl) ellestadite require clarification. Two reports concerning the structural adjustments and anion tunnel accommodation in binary solid solutions of (Cl, OH) or (F, OH) in calcium phosphate apatite $Ca_{10}(PO_4)_6X_2$, and ternary solutions of (F, Cl, OH) [8, 9] have appeared, but less is known about the (F, Cl) system. Mackie and Young [10] studied two fluor-chlorapatite compositions with F/(F+Cl) ratios of 0.17 and 0.41, and included a second fluorine site in addition to that on the mirror plane. Hughes et al. [11] suggested that OH^- may be an essential component in stabilizing natural fluor-chlorapatite solid solutions. The presence of a miscibility gap in natural gem-grade apatite from Brazil has been described by Ferraris et al. [12], where atomic scale

studies by high-resolution and analytical TEM revealed the phase separation of fluorine-enriched and chlorine-enriched phosphate apatite domains from ellestadite in the nanoscale.

5.2 Experimental Methods

5.2.1 Synthesis

$Ca_{10}[(SiO_4)_3(SO_4)_3][Cl_{2-x}F_x]$ (x = 0, 0.4, 0.8, 1.2, 1.6, and 2) were synthesized by solid-state reaction. The starting materials were prepared by preheating $CaCO_3$ (Merck, p.a.) at 1000°C for 12 h; SiO_2 (Sigma-Aldrich, 99.99%) and $CaSO_4 \cdot 2H_2O$ (Merck, p.a.) at 600°C for 4 h; and $CaCl_2 \cdot 2H_2O$ (Riedel-de Haën, puriss.) at 400°C for 4 h. Stoichiometric mixtures of CaO, $CaSO_4$, SiO_2, $CaCl_2$ and CaF_2 were manually ground with acetone and calcined at 900°C for 5 h in an alumina crucible, then reground and sintered at 950°C for a further 9 h.

5.2.2 Crystallographic Characterization

Powder X-ray diffraction (PXRD) and neutron diffraction (PND) were combined for structural characterization. PXRD measurements were performed for phase identification and mass balance using a Bruker D8 high-resolution X-ray powder diffractometer (Cu-Kα radiation) operated at 40 kV and 40 mA. Scans were collected from 8° to 140° with a step size of 0.01° and a dwell time per step of 1 s. All specimens were spiked with standard silicon (10 wt%, NIST660a, a = 5.40825 Å) to determine the unit cell constants absolutely. Powder neutron diffraction patterns were acquired at the Institute Laue-Langevin (ILL) Grenoble (France) using the high resolution D1A diffractometer with a wavelength of 1.3894Å, a 2-theta range of 0° to 150° and scan step of 0.05° at room temperature. The diffractometer is equipped with a focusing Ge monochromator set at a take-off angle of 123°, and 25 standard ^{3}He counter detectors. Approximately 2 g of ellestadite was loaded into a 9 mm diameter cylindrical sample container that was rotated during acquisition.

The structure refinements were carried out by the Rietveld method using TOPAS [13]

with a pseudo-Voigt peak shape profile and a starting model using the atomic positions of $Ca_{10}[(SiO_4)_3(SO_4)_3]Cl_2$ in hexagonal $P6_3/m$ [14]. No superstructure reflections were observed which precludes the possibility of lower symmetries ($P2_1/m$; $P2_1$). For each data set, a five-coefficient Chebychev function and $1/x$ background, a peak shift, a zero error, unit cell parameters and crystal size were refined sequentially with temperature displacement parameters and occupation factors of each atomic site kept constant. After several refinement cycles, the calcium positions (Ca(1) and Ca(2)) were released, followed by the silicon/sulfur and oxygen positions. The mole ratio of Si:S at the tetrahedral site was fixed at 1:1. The oxygen sites were fully tenanted, while the occupancies of calcium, chlorine and fluorine were allowed to vary. For nonstoichiometric ellestadites, the occupancy factors of Ca and Cl were constrained to maintain charge balance (see Discussion and Table 5.3). Isotropic temperature displacement parameters for all atoms were refined in Ca(1)/Ca(2)/Cl/F and Si/S/O(1)/O(2)/O(3) groups to the same value. The refinement cycles were terminated when convergence was reached. Scattering lengths of 0.4700, 0.4149, 0.2847, 0.5803, 0.5654, and 0.9577×10^{-12} cm were used for Ca, Si, S, O, F and Cl, respectively [15]. Difference-Fourier maps were generated using Jana2006 [16], specifically to examine the location of anion scattering centres in the tunnels. The $Ca(1)O_6$ metaprism twist angle (φ) was calculated for crystallochemical diagnosis to verify trends in bond angles as a function of composition. To objectively assess the reliability of the Rietveld refinements singular value decomposition as implemented in SVDdiagnostic [16], was used to confirm the statistical robustness of the analysis.

5.3 Crystal Structure of $Ca_{10}[(SiO_4)_3(SO_4)_3][Cl_{2-x}F_x]$

5.3.1 Quantitative Phase Analysis

Powder XRD shows that ellestadite is always dominant (> 95 wt %) (Figure 5.1). Additionally, the reactants quartz SiO_2 (< 0.5 wt%) or anhydrite $CaSO_4$ (< 3.5 wt%) persist for low fluorine substituted samples.

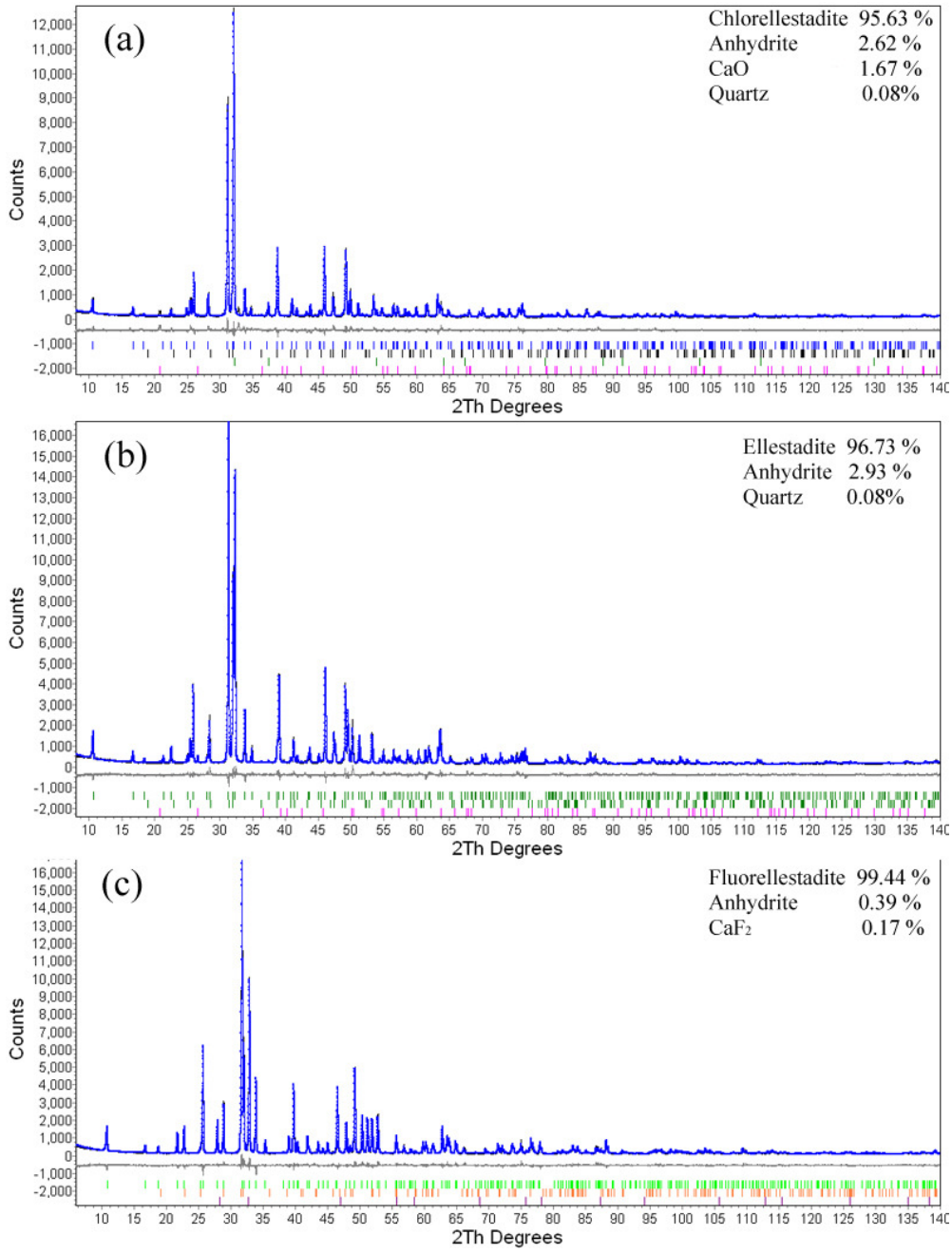

Figure 5.1 Rietveld fitting pattern for (a) $x = 0$, (b) $x = 0.4$ and (c) $x = 2$. (x in $Ca_{10}[(SiO_4)_3(SO_4)_3][Cl_{2-x}F_x]$) Lines and dots denote observed and calculated profile intensities, respectively. Short vertical bars represent Bragg reflection positions. The difference (observed – calculated) is plotted below.

5.3.2. Metalloid Speciation

The incorporation of fluorine did not obviously affect the FTIR spectra of chlorellestadite (Figure 5.2). The sulphate ν_3 and ν_4 vibration modes were identified by three features (at 1138, 644, 615 cm^{-1}) as were the silicate ν_3 and ν_4 modes (at 938, 561, 508 cm^{-1}) [17]. CO_3^{2-} incorporation, if present, was below the limit of detection. For x = 0.4 and 0.8 (x in $Ca_{10}[(SiO_4)_3(SO_4)_3)][Cl_{2-x}F_x]$), the OH^- librational mode appears very weakly at 660 cm^{-1}.

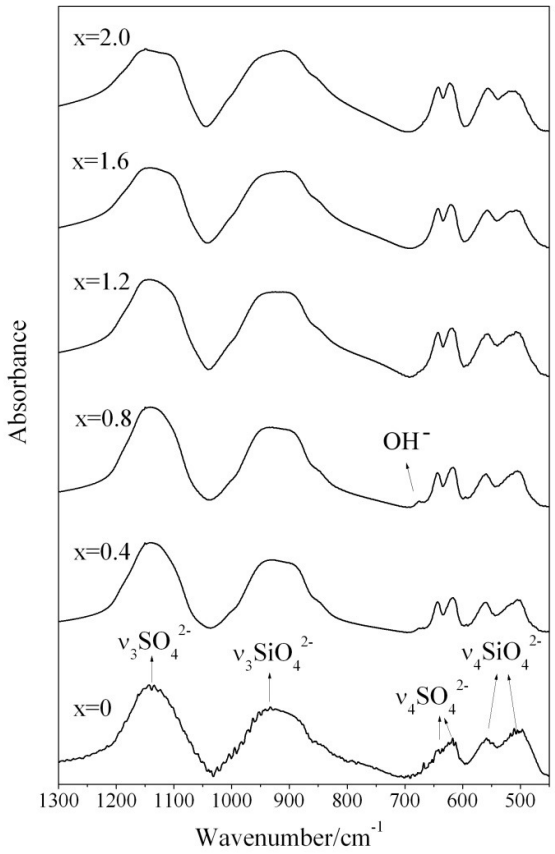

Figure 5.2 Expanded views of FT-IR spectra for the fluor-chlorellestadite solid solution. (*x* in $Ca_{10}[(SiO_4)_3(SO_4)_3][Cl_{2-x}F_x]$)

5.3.3 Trends in Lattice Parameters

The details of the crystal structure refinements including atomic positional parameters and temperature displacement parameters are given in Table 5.1, with selected atomic distances and bond angles collected in Table 5.2.

As the content of fluorine increases, *a* contracts while *c* dilates, but overall the unit cell volume is reduced (Table 5.1, Figure 5.3), because fluorine is smaller than chlorine. In addition, the splitting of the intense doublet reflections (121)/(211) and (112)/(030) in the chlorellestadite endmember pattern into a resolved triplet (121)/(211), (112), and (030) provides further confirmation of the mixed anion structure [14] (Figure 5.4). The loss of $CaCl_2$ from the structure also contributes to unit cell shrinkage. According to Young & Elliott [18], the small increase in *c* may be related to the different atomic positions of halogen ions. As fluorine is centred in the Ca(2) triangle (z = 1/4), it will not affect the *c* axes. However, chlorine is displaced > 1 Å along *c*, weakly bonding to the neighboring calcium Ca(2) triangles that leads to slight contraction of the *c* axis.

Differences in the anion content of the tunnel negligibly disturbs the $(Si/S)O_4$ tetrahedra, which are essentially rigid bodies, and the $Ca(1)O_9$ polyhedra (Table 5.2). There are only minor changes in the (Si/S)-O bond lengths and no evidence for a Si/S ordering which would lower the symmetry to monoclinic. The refined mean bond length Si/S-O = 1.545 Å, close to the average value of 1.55 Å calculated from Si-O = 1.61 Å in silicates [19] and S-O = 1.49 Å in sulphates [20], is also consistent with a statistical distribution of SiO_4 and SO_4 tetrahedra.

Table 5.1 Lattice parameters and crystallographic data for $Ca_{10}[(SiO_4)_3(SO_4)_3][Cl_{2-x}F_x]$.

x	0	0.4	0.8	1.2	1.6	2.0
Space Group	$P6_3/m$	$P6_3/m$	$P6_3/m$	$P6_3/m$	$P6_3/m$	$P6_3/m$
a (Å)	9.6702(3)	9.6239 (3)	9.5772(2)	9.5312(2)	9.5064(2)	9.4486(1)
c (Å)	6.8543(3)	6.87749 (3)	6.8950(1)	6.9181(2)	6.9263(1)	6.9426(1)
Volume (Å^3)	555.09(4)	551.64(2)	547.70(3)	544.27(3)	542.09(2)	536.77(2)
φ(deg)	19.9_2	20.4_4	21.8_9	22.0_1	22.6_3	24.1_5
R_{wp}	5.62%	4.30%	5.43%	6.72%	6.74%	8.55%
R_p	4.28%	3.37%	4.21%	5.24%	5.05%	6.48%
GOF	0.84	0.58	0.61	0.73	0.74	0.89
Ca(1), 4*f* (1/3, 2/3, *z*)						
z	-0.0013(1)	0.0009(4)	0.0010(5)	0.0037(9)	0.0028(4)	0.0026(1)
B (Å^2)	1.88(6)	1.85(7)	1.81(6)	1.52(7)	1.52(7)	1.46(7)
Ca(2), 6*h* (*x, y,* 1/4)						
x	0.2603(5)	0.2562(4)	0.2497(3)	0.2435(1)	0.2420(3)	0.2390(4)
y	0.0012(6)	-0.0017(3)	-0.0068(4)	-0.0101(4)	-0.0094(3)	-0.0088(2)
B (Å^2)	1.88(6)	1.85(7)	1.81(6)	1.52(7)	1.52(7)	1.46(7)
Si/S, 6*h* (*x, y,* 1/4)						
x	0.4062(1)	0.4045(2)	0.4008(2)	0.3996(1)	0.3996(1)	0.3980(1)
y	0.3767(1)	0.3755(4)	0.3721(1)	0.3705(2)	0.3706(1)	0.3704(3)
B (Å^2)	1.84(3)	2.00(4)	1.79(3)	1.60(4)	1.52(4)	1.51(3)
O(1), 6*h* (*x, y,* 1/4)						
x	0.3368(5)	0.3359(4)	0.3331(1)	0.3296(4)	0.3302(4)	0.3245(3)
y	0.4900(4)	0.4902(8)	0.4885(1)	0.4859(4)	0.4870(3)	0.4843(3)
B (Å^2)	1.84(3)	2.00(4)	1.79(3)	1.60(4)	1.52(4)	1.51(3)
O(2), 6*h* (*x, y,* 1/4)						
x	0.5907(1)	0.5898(1)	0.5872(1)	0.5867(1)	0.58724(8)	0.5868(3)
y	0.4676(4)	0.4667(3)	0.4651(2)	0.4662(4)	0.4660(3)	0.4676(3)
B (Å^2)	1.84(3)	2.00(4)	1.79(3)	1.60(4)	1.52(4)	1.51(3)
O(3), 12*i* (*x, y, z*)						
x	0.3549(4)	0.3512(1)	0.3483(1)	0.3443(4)	0.3426(3)	0.3410(3)
y	0.2675(3)	0.2647(2)	0.2628(1)	0.2599(3)	0.2587(2)	0.2573(2)
z	0.0684(3)	0.0701(1)	0.0688(1)	0.0700(2)	0.0712(2)	0.0717(2)
B (Å^2)	1.84(3)	2.00(4)	1.79(3)	1.60(4)	1.52(4)	1.51(3)
Cl, 4*e* (0, 0, *z*)						
z	0.4315(3)	0.4169(1)	0.3818(6)	0.342(6)	0.336(3)	
B (Å^2)	1.88(6)	1.85(7)	1.81(6)	1.52(7)	1.52(7)	
F, 2*a* (0, 0, 1/4)						
Occ.		0.199(1)	0.398(2)	0.607(9)	0.804(5)	1.00
B (Å^2)		1.85(7)	1.81(6)	1.52(7)	1.52(7)	1.46(7)

$R_p = (\Sigma_i | y_i - y_{ci} |)/\Sigma_i yi$, $R_{wp} = [(\Sigma_i w | y_i - y_{ci} |^2)/\Sigma_i w | y_i^2]^{1/2}$, GOF = $\Sigma_i w (y_i - y_{ci})^2/(n - p)$.

Table 5.2 Bond lengths and angles for $Ca_{10}[(SiO_4)_3(SO_4)_3][Cl_{2-x}F_x]$.

Composition *x*	0	0.4	0.8	1.2	1.6	2.0
Bond length (Å)						
Ca(1)-O(1) × 3	2.438(3)	2.420(4)	2.419(2)	2.411(5)	2.408(2)	2.405(1)
Ca(1)-O(2) × 3	2.466(3)	2.474(2)	2.475(3)	2.496(5)	2.484(3)	2.491(2)
Ca(1)-O(3) × 3	2.791(3)	2.808(4)	2.815(2)	2.835(5)	2.841(2)	2.834(4)
< Ca(1)-O>	2.565	2.567	2.569	2.580	2.578	2.577
Ca(2)-O(1)	2.893(4)	2.855(1)	2.786(2)	2.726(4)	2.736(3)	2.687(3)
Ca(2)-O(2)	2.283(4)	2.313(1)	2.369(1)	2.400(3)	2.408(3)	2.409(4)
Ca(2)-O(3) × 2	2.582(3)	2.569(2)	2.585(4)	2.574(2)	2.550(1)	2.522(1)
Ca(2)-O(3) × 2	2.358(3)	2.363(1)	2.348(6)	2.353(2)	2.364(2)	2.375(1)
< Ca(2)-O>	2.509	2.505	2.503	2.497	2.495	2.482
Ca(2)-Cl	2.803(4)	2.727(1)	2.589(1)	2.454(1)	2.421(6)	
Ca(2)-F		2.474(1)	2.425(1)	2.370(1)	2.346(6)	2.301(4)
Ca(2)-Ca(2)	4.351(1)	4.286(3)	4.200(6)	4.106(2)	4.063(5)	3.985(5)
Si/S-O(1)	1.544(5)	1.5442(5)	1.544(1)	1.545(5)	1.546(4)	1.5450(1)
Si/S-O(2)	1.545(1)	1.545(1)	1.545(1)	1.545(1)	1.5451(7)	1.5452(1)
Si/S-O(3)	1.545(2)	1.545(1)	1.544(1)	1.5438(2)	1.544(1)	1.5453(6)
Average	1.545	1.545	1.544	1.544	1.545	1.545
Angle (degree)						
O(1)-Si/S-O(2)	112.6(2)	112.2(1)	111.4(2)	111.2(2)	111.1(1)	112.027(2)
O(1)-Si/S-O(3)	112.3(2)	112.4(1)	112.2(1)	111.4(2)	111.4(1)	111.04(1)
O(2)-Si/S-O(3)	105.9(2)	106.4(1)	106.4(2)	107.6(2)	108.0(1)	108.016(1)
O(3)-Si/S-O(3)	107.4(1)	106.5(1)	108.06(6)	107.5(1)	106.67(9)	106.469(2)

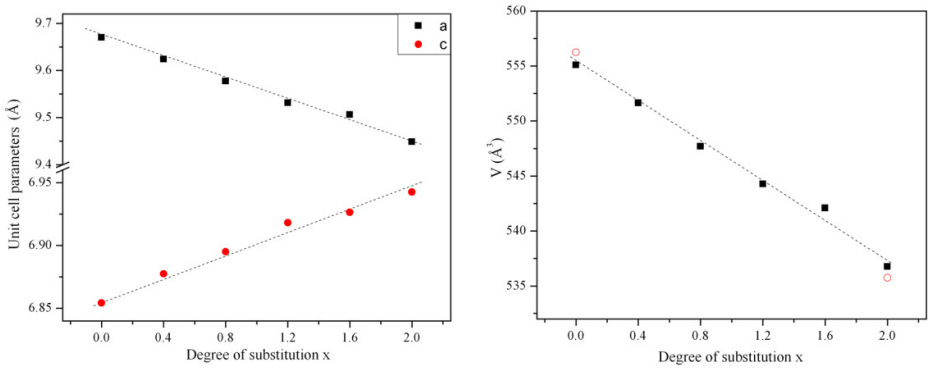

Figure 5.3. Variation in cell parameters (a) a and c, and (b) unit cell volume with degree of fluorine substitution x in $Ca_{10}[(SiO_4)_3(SO_4)_3][Cl_{2-x}F_x]$. Standard deviation of data is smaller than size of points. The open circles in (b) are taken from the literature [2, 3].

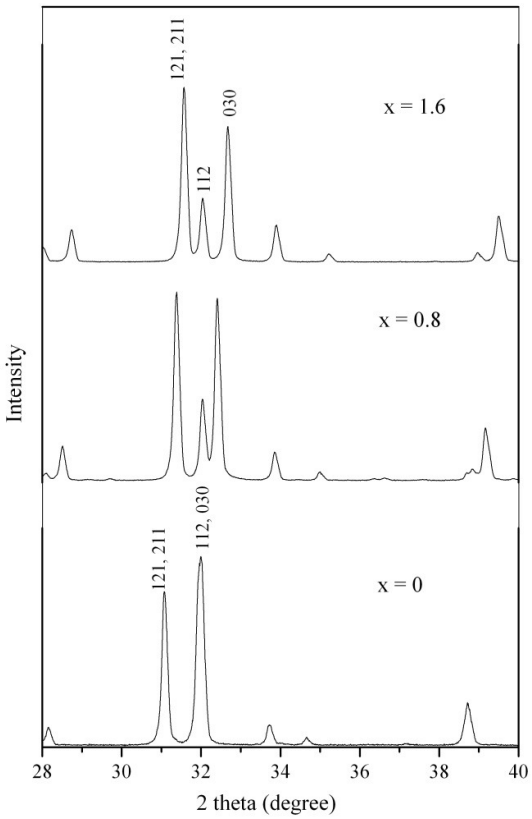

Figure 5.4 Partial X-ray powder diffraction patterns of ellestadites with x = 0, 0.8, 1.6. (x in $Ca_{10}[(SiO_4)_3(SO_4)_3][Cl_{2-x}F_x]$).

5.3.4 Substitution for *X* (Cl, F) Anions and Loss of $CaCl_2$

The Rietveld refinement and difference Fourier maps show that across the fluor-chlorellestadite series, the halides occupy the 2*a* (F^-) or 4*e* (Cl^-) Wyckoff positions. The location of chlorine ions in the chlorellestadite endmember ($x = 0$) show nuclear scattering at 4*e* (0, 0, 0.431), while in fluorellestadite ($x = 2$), scattering at 2*a* (0, 0, 1/4) was assigned to F^- (Table 5.1). Similar bilocation was used for intermediate F/Cl compositions (Figure 5.5). The Cl^- position shifts from $z = 0.431$ in the endmember towards the mirror plane with increasing fluorine content ($z = 0.412$, 0.382, 0.342, and 0.336 for $x = 0.4$, 0.8, 1.2, and 1.6, respectively) (Figure 5.6a). It is likely that the weak OH^- signature observed by FTIR arises from a non-ellestadite phase, since a residual feature in the Fourier map cannot be assigned to hydroxyl. Examination of the difference Fourier maps (Figure 5.7) revealed low electron densities in the range of -0.85 e/Å^3 to 0.85 e/Å^3, which discounts the possibility of multiple Cl^- positions [8] or splitting of the Ca(2) site [5] as suggested by earlier studies.

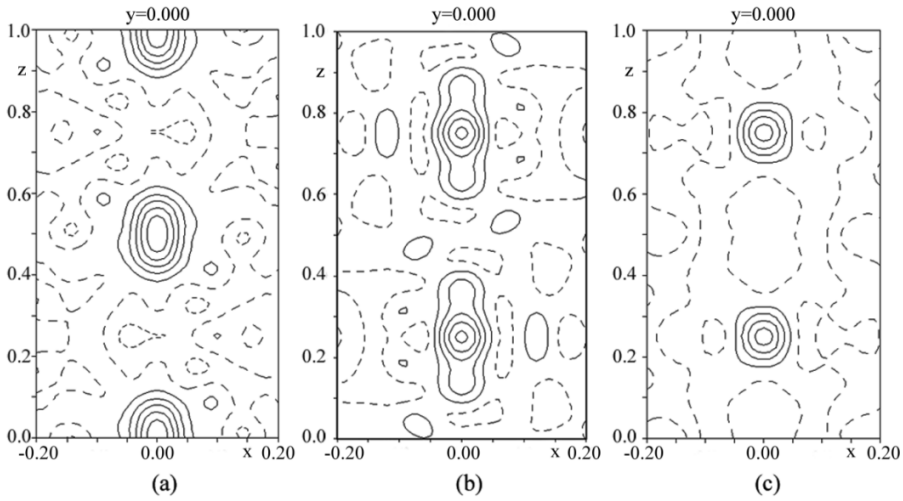

Figure 5.5 Difference Fourier maps of the $Ca_{10}[(SiO_4)_3(SO_4)_3][Cl_{2-x}F_x]$ ellestadite tunnel indicating the positions of F and/or Cl ions that were excluded to emphasize their location. (a) Chlorellestadite ($x = 0$), (b) Fluor-chlorellestadite ($x = 0.8$), and (c) Fluorellestadite ($x = 2$). Contour interval is 0.5 e/Å^3 and the first positive contour (solid line) is at 0.5 e/Å^3. Negative difference nuclear density is indicated by the broken contours.

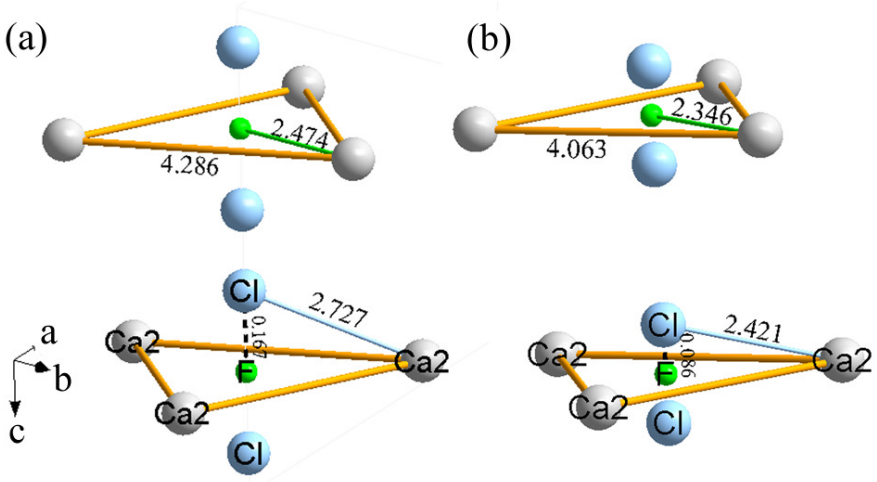

Figure 5.6 Perspective drawing of Ca(2) triangle arrangement on the screw axis (a) x = 0.4, and (b) x = 1.6. (x in $Ca_{10}[(SiO_4)_3(SO_4)_3][Cl_{2-x}F_x]$) F^- lies in the centre of Ca(2) triangle on the mirror planes, while Cl^- splits into two half-occupied sites above or below the mirror plane. The interatomic distances are in Å. The distances between Cl site and the mirror plane (z = 1/4) are indicated by the dotted lines.

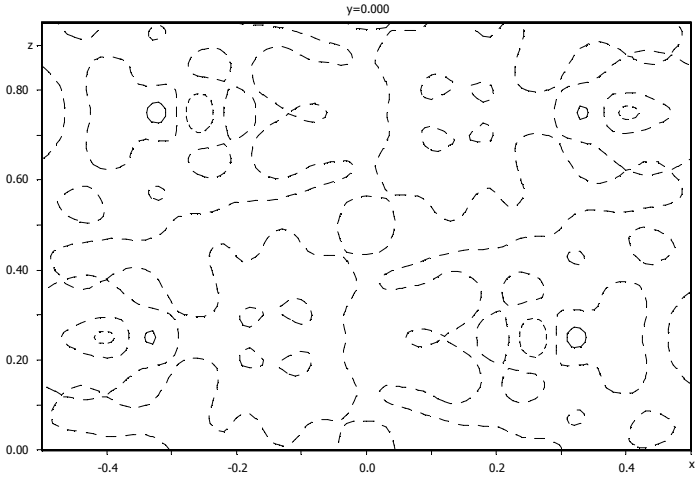

Figure 5.7 Difference Fourier map at y = 0 for $Ca_{10}[(SiO_4)_3(SO_4)_3][Cl_{0.8}F_{1.2}]$. Fluorine and chlorine ions were included at z = 1/4 and z = 0.342, respectively. Contour interval is 0.25 e/Å^3 and the first positive contour (solid line) is at 0.25 e/Å^3. Negative difference nuclear density is indicated by the broken contours. The range of difference nuclear density is -0.45 ~ 0.38 e/Å^3.

The Cl content was less than nominal for samples with $x \leq 1.2$. Halogen loss might occur during the solid state processing, as chlorine is susceptible to volatilization, with possible charge compensation mechanisms being:

$$Cl^- \rightarrow OH^- \qquad (5\text{-}1)$$

$$2\,Cl^- \rightarrow O^{2-} + \square_{Cl} \qquad (5\text{-}2)$$

$$Ca^{2+} + 2Cl^- \rightarrow \square_{Ca} + 2\square_{Cl} \qquad (5\text{-}3)$$

Mechanism (5-1) is not supported by FTIR or structure refinement. In the case of mechanism (5-2), attempts to insert extra oxygen at additional (0, 0, *z*) positions on the hexagonal axis were unsuccessful, as the temperature displacement parameter of oxygen atom became negative. Prener [21] studied nonstoichiometry in calcium chlorapatite, and stated that synthetic chlorapatite (often $P2_1/b$) became hexagonal $P6_3/m$ when grown from the melt due to Cl deficiency created by loss of $CaCl_2$. In our study, the formation of Ca and Cl structural vacancies (mechanism (5-3)) is possible as $CaCl_2$ partially evaporates during sintering at 950°C ($m_p(CaCl_2)$ = 782°C). This would be consistent with the smaller unit cell parameter *a* (9.6702(3) Å) and volume (555.09(4) Å^3) of the chlorellestadite endmember, compared with stoichiometric chlorellestadite (*a* = 9.6773(3) Å, V = 556.25(4) Å^3) reported previously [5].

To examine this question, the occupancies of calcium and chlorine were refined with the constraint $Ca^{2+} + 2Cl^- \rightarrow \square_{Ca} + 2\square_{Cl}$ applied in three ways:

(1) the occupancies of Ca(1) and Ca(2) were jointly refined together with Cl,

(2) the Ca(1) site was constrained with Cl site, with the Ca(2) site fully occupied, and

(3) the Ca(2) site was released with Ca(1) fixed to full occupancy.

In this manner, any preference to create Ca-site vacancies within the framework or tunnel could be distinguished (Table 5.3). While the differences in refinement residuals are small, it does appear that for Cl-rich compositions, Ca(1) vacancies may be present, while for F-rich ellestadites the reverse is true. However, further analysis would be required. It is noted that modeling with the Ca(1) and Ca(2) sites fully occupied lead to substantially inferior residuals, and in addition, cannot charge

balance halogen substoichiometry. On the basis of these assessments, the formulas for these compounds are most generally written as $Ca_{10-y}(SiO_4)_3(SO_4)_3Cl_{2-x-2y}F_x$, rather than the nominal $Ca_{10}[(SiO_4)_3(SO_4)_3][Cl_{2-x}F_x]$.

Table 5.3 Comparison of neutron data refinement results based on cation vacancies at Ca(1)/Ca(2), Ca(1) and Ca(2), respectively.

x	vacancy site	Occupancy Factor			content per unit cell				B (Å^2)	R_b
		Ca(1)	Ca(2)	Cl	Ca	Cl	F	anio		
0	Ca(1)&Ca(2)	0.954(8)	1.000(5)	0.41(2)	9.82	1.64	0	0.36	1.88(6)	2.86
	Ca(1)	0.954(2)	1*	0.408(5)	9.82	1.63	0	0.37	1.88(6)	2.86
	Ca(2)	1*	0.972(2)	0.416(5)	9.83	1.66	0	0.34	1.92(6)	2.91
0.4	Ca(1)&Ca(2)	0.979(9)	0.967(7)	0.26(2)	9.72	1.04	0.40	0.56	1.85(7)	2.10
	Ca(1)	0.938(3)	1*	0.275(7)	9.75	1.10	0.40	0.50	1.86(7)	2.07
	Ca(2)	1*	0.952(7)	0.255(4)	9.71	1.02	0.40	0.58	1.85(7)	2.17
0.8	Ca(1)&Ca(2)	0.985(8)	0.988(5)	0.23(2)	9.87	0.94	0.80	0.26	1.81(6)	2.67
	Ca(1)	0.967(3)	1*	0.234(6)	9.87	0.94	0.80	0.26	1.82(6)	2.62
	Ca(2)	1*	0.978(2)	0.235(5)	9.87	0.94	0.80	0.26	1.82(6)	2.72
1.2	Ca(1)&Ca(2)	1.01(1)	0.977(7)	0.158(3)	9.92	0.63	1.21	0.16	1.52(7)	2.54
	Ca(1)	0.983(3)	1*	0.163(7)	9.93	0.65	1.21	0.14	1.55(7)	2.56
	Ca(2)	1*	0.987(2)	0.156(7)	9.92	0.63	1.21	0.16	1.53(7)	2.53
1.6	Ca(1)&Ca(2)	1.02(1)	0.989(7)	0.10(3)	10.01	0.40	1.60	0	1.52(7)	2.61
	Ca(1)	1.001(3)	1*	0.102(7)	10.00	0.40	1.60	0	1.53(7)	2.63
	Ca(2)	1*	0.999(2)	0.098(7)	9.99	0.39	1.60	0.01	1.53(7)	2.62
2.0					10	0	2.0	0	1.46(7)	2.81

* Not refined

$R_b = \Sigma_i \, |I_{ko} - I_{kc}| / \Sigma_i \, I_{ko}$

Singular value decomposition (SVD) as adapted by Mercier et al. [22, 23] for the evaluation apatite structures, found the numerical stability of the Rietveld refinements was satisfactory: in particular, the tunnel site occupancy was reliable. Typical outputs (Appendix) from *SVDdiagnostic* of the pre-conditioned normal matrices for the models in which the Ca(1) and Ca(2) sites were refined simultaneously (see also Table 3), give condition numbers of around 10^2-10^3 indicative of good conditioning of the least-squares matrices, that confirms the occupancy factors refinements are reasonable and not over interpreted. Similar results were obtained if Ca(1) or Ca(2) were refined alone.

5.3.5 Tunnel Adaptation and Twist Angle

The major structural response to fluorine substitution occurs in the $Ca(2)O_6(F/Cl)(O)$ polyhedron (a seventh weak bond to O(1) exists in fluorellestadite) (Table 5.2). As noted the Ca(2) atoms located on the mirror planes at z = 1/4 and 3/4 form triangles that are centred around the [001] $\bar{3}$ axis containing the F/Cl (Figure 5.6). The Cl^- ion located in 4*e* shifts from z = 0.4315(3) in the chlorellestadite endmember towards the Ca(2) triangles as z decreases to 0.336(3) (Figure 5.8a). The interatomic distances between Ca(2) and Cl decreased from 2.803(4) Å in the chlorellestadite (x = 0) to 2.421(6) Å when x = 1.6. The Ca(2)-F bond length also follows this trend, decreasing from 2.474(5) Å in x = 0.4 to 2.3018(1) Å in fluorellestadite (x = 2.0) (Table 5.2). As the F^- ion lies in the centre of the Ca(2) triangle, the decrease of the Ca(2)-F distances with reduction of chlorine content leads to a contraction in the unit cell *a*-parameter (Table 5.1, Figure 5.3).

The twist angle (φ) is related to the relative sizes of the *A*, *B* and *X* ions [24] and also sensitively detects disequilibrium and non-stoichiometry. In passing from fluorellestadite (x = 2) to chlorellestadite (x = 0), the twist angle (φ) decreases from 24.1° to 19.9°, with increasing chlorine content leading to a tunnel dilation and to increased Ca(2)-F/Cl distances. The near linear change in twist angle (φ) is expected, and small departures from linearity may be indicative of the Cl deficient nature of some compositions (Figure 5.8b).

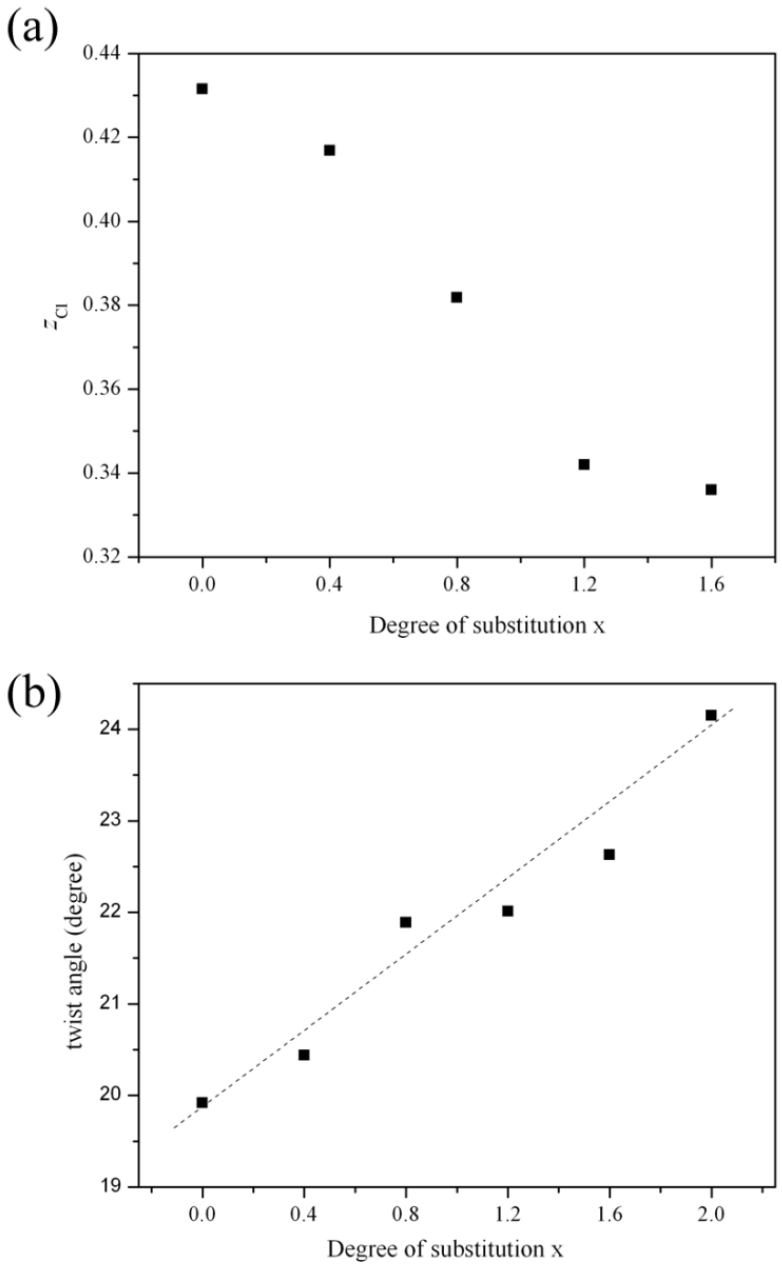

Figure 5.8 Dependence of (a) z_{Cl} and (b) twist angle on degree of fluorine substitution x in $Ca_{10}[(SiO_4)_3(SO_4)_3][Cl_{2-x}F_x]$.

5.3.6 Polyhedral Distortions

As further validation of the refined structures, the crystal-chemical parameters proposed by Mercier et al. [25] (Table 5.4) were extracted for the refined ellestadite structures; the geometrical derivation of these parameters can be found in this earlier work. The principle correlations among those crystal-chemical parameters, including data from this study and published work are shown in Figure 5.9. As the fluorine content increases, the $(Si/S)O_4$ tetrahedra ($\tau_{O3\text{-}Ca2\text{-}O3}$ decreases) and CaO_6 polyhedra (δ_{Ca1} decreases) are distorted to accommodate the increase of the O3-Ca2-O3 bond angle ($\phi_{O3\text{-}Ca2\text{-}O3}$). These correlations conform to the trends observed by Mercier et al. [25], and of particular interest, fill a gap noted in their work for apatites with $131^o < \phi_{O3\text{-}Ca2\text{-}O3} < 135^o$. Furthermore, the crystal chemical parameters are clustered for F-rich compositions consistent with loss of Cl, and confirm there is little change in halide content for these materials.

None of the ellestadites show measurable deviation from the hexagonal metric. This behavior is distinct from the $Ca_{10}[(V_xP_{1-x}O_4)_6]F_2$ apatites [26] and vanadium doped ellestadite (see Chapter 6), which at the largest vanadium contents become triclinic. For these materials, the approach of α_{AII} to 120^o was seen to precede a reduction in symmetry. However, in these studies it was found that $Ca_{10}[(SiO_4)_3(SO_4)_3]Cl_2$ with $\alpha_{AII} = 120.23^o$ could be convincingly modeled in $P6_3/m$. It has already been noted that mineral ellestadites may be monoclinic, and long annealing of synthetic $Ca_{10}[(SiO_4)_3(SO_4)_3]Cl_2$ may allow SiO_4/SO_4 ordering with stabilization as $P2_1/m$ or $P2_1$ structures.

Table 5.4 Crystal-chemical parameters extracted from the crystallographic descriptions (*a*, *c*, atom coordinates) according to the methods of Mercier et al. [25].

Composition	Ref.	$\langle\tau_{O\text{-}B\text{-}O}\rangle$	ρ_{Ca2}	α_{Ca2}	$\phi_{O3\text{-}Ca2\text{-}O3}$	$\Psi_{Ca1\text{-}O1}^{Ca1\ z=0}$	δ_{Ca1}	α_{Ca1}	φ_{Ca1}
$Ca_{10}(SiO_4)_3(SO_4)_3Cl_2$		112.41	4.349	120.23	135.46	45.20	20.03	-19.06	19.94
$Ca_{10}(SiO_4)_3(SO_4)_3Cl_{1.6}F_{0.4}$		112.33	4.285	119.67	137.33	44.86	19.77	-19.05	20.46
$Ca_{10}(SiO_4)_3(SO_4)_3Cl_{1.2}F_{0.8}$		111.91	4.199	118.67	138.92	44.69	19.03	-19.10	21.93
$Ca_{10}(SiO_4)_3(SO_4)_3Cl_{0.8}F_{1.2}$		111.31	4.106	117.98	140.36	44.60	18.56	-19.60	22.87
$Ca_{10}(SiO_4)_3(SO_4)_3Cl_{0.4}F_{1.6}$		111.31	4.064	118.11	140.46	44.36	18.68	-19.56	22.63
$Ca_{10}(SiO_4)_3(SO_4)_3F_2$		111.33	3.985	118.21	140.21	44.12	17.94	-20.40	24.12
$Ca_{9.4}(SO_4)_3(SiO_4)_3Cl_{0.8}$	[5]	113.63	4.258	120.88	138.03	45.18	17.77	-18.71	24.45
$Ca_{10}(SO_4)_3(SiO_4)_3Cl_2$	[5]	109.07	4.330	119.14	141.86	44.26	20.17	-18.44	19.64
$Ca_{10}(SO_4)_3(SiO_4)_3F_2$	[3]	110.67	3.990	118.37	141.03	43.97	17.79	-20.57	24.41
$Ca_{10}(SO_4)_3(SiO_4)_3(OH)_2$	[8]	111.76	4.096	118.66	138.75	44.50	18.38	-19.98	23.23
$Ca_5(PO_4)_3F$	[27]	110.91	3.898	122.23	133.88	44.02	18.10	-20.89	23.80
$Ca_5(PO_4)_3F_{0.09}Cl_{0.88}$	[11]	111.69	4.273	119.78	136.18	45.57	20.39	-18.47	19.21
$Ca_5(PO_4)_3F_{0.17}Cl_{0.83}$	[28]	111.90	4.300	119.48	136.25	45.61	20.69	-18.38	18.62
$Ca_5(PO_4)_3F_{0.41}Cl_{0.59}$	[28]	111.65	4.224	120.36	135.78	45.20	19.88	-18.98	20.24
$Ca_5(PO_4)_3F_{0.94}Cl_{0.1}$	[11]	111.07	4.002	121.43	135.47	44.34	18.35	-20.03	23.30
$Ca_5(PO_4)_3F$	[28]	111.13	3.986	121.63	135.37	44.23	18.25	-20.23	23.50
$Ca_{10}(V_{0.6}P_{0.4}O_4)_6F_2$	[26]	111.69	4.039	119.22	137.03	43.39	18.53	-21.09	22.93
$CaLa_4(SiO_4)_3O$	[29]	111.56	3.991	116.94	139.74	43.09	19.46	-20.96	21.07
$Na_{6.39}Ca_{3.61}(SO_4)_6Cl_{1.61}$	[30]	110.95	4.177	122.04	134.74	46.43	17.42	-18.65	25.15
$Na_{6.35}Ca_{3.65}(SO_4)_6F_{1.65}$	[30]	110.58	4.025	122.07	137.51	45.95	15.63	-19.58	28.72

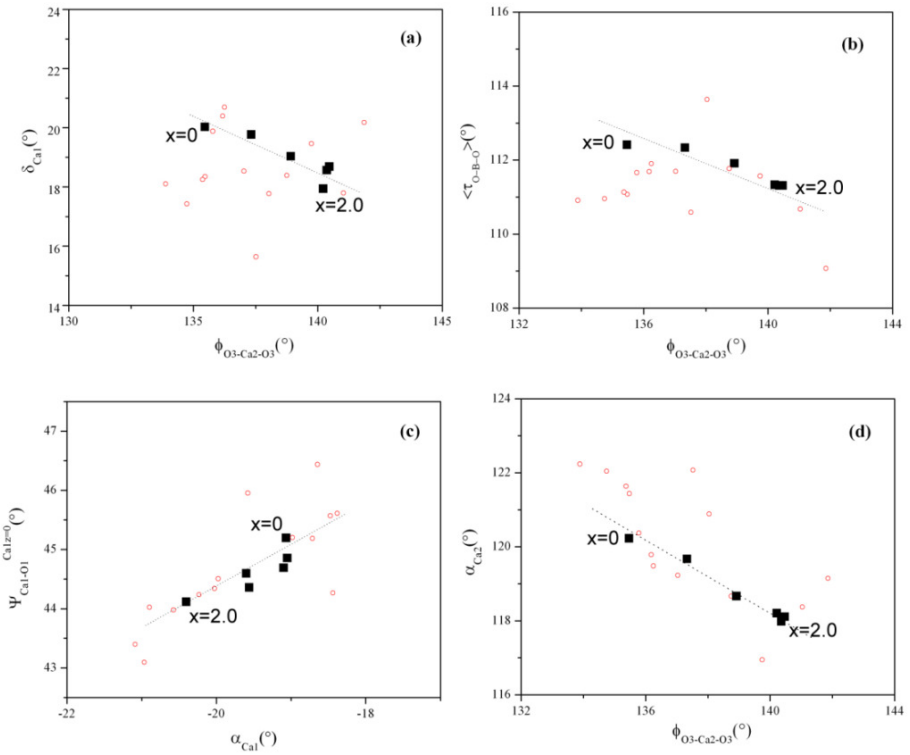

Figure 5.9 Correlations observed between polyhedral distortion parameters: (a) δ_{Ca1} versus $\phi_{O3\text{-}Ca2\text{-}O3}$, (b) $<\tau_{O\text{-}B\text{-}O}>$ versus $\varphi_{O3\text{-}Ca2\text{-}O3}$, (c) $\Psi_{Ca1\text{-}O1}^{Ca1\ z=0}$ versus α_{Ca1}, and (d) α_{Ca2} versus $\phi_{O3\text{-}Ca2\text{-}O3}$. These figures should be compared with Fig.8 in Mercier et al.[33] Circles: published data; large filled squares: this study. (δ_{Ca1}:counter-rotation angle of CaO_6 polyhedra; $\phi_{O3\text{-}Ca2\text{-}O3}$: O3-Ca2-O3 bond angle; $<\tau_{O\text{-}B\text{-}O}>$: O-B-O bond-bending angle; $\Psi_{Ca1\text{-}O1}^{Ca1\ z=0}$: angle that an $Ca1_{z=0}$-O1 bond makes with respect to *c*; α_{Ca1}: orientation of CaO_6 polyhedra with respect to *a*; α_{Ca2}: orientation of Ca2 triangles with respect to *a*.)

5.3.7 Local structure

A high-resolution TEM image of $Ca_{10}[(SiO_4)_3(SO_4)_3]Cl_{0.4}F_{1.6}$ shows a well-developed crystal without obvious imperfection, in the sense that no extended defects are observed (Figure 5.10a). A comparison of the intensity distribution of experimental and simulated SAED reflections was consistent with $P6_3/m$ symmetry. The SAED pattern did not show split reflections, precluding the possibility of coexisting mixed-phase ellestadite [12], or localized order with respect to anionic sequences within the anion tunnels that would lower the symmetry to monoclinic. Fourier reconstruction of the images yield potential maps (Figure 5.10b) most

plausibly constrained to the plane group *p*6 which is the [001] symmetry projection for $P6_3/m$. In the HR image, the darker feature represents the positions of $Ca(1)O_{6+3}$ polyhedral columns which share (001) pinacoid faces to form chains parallel to *c*, while the bright contrast corresponds to the anion columns at the tunnel centres.

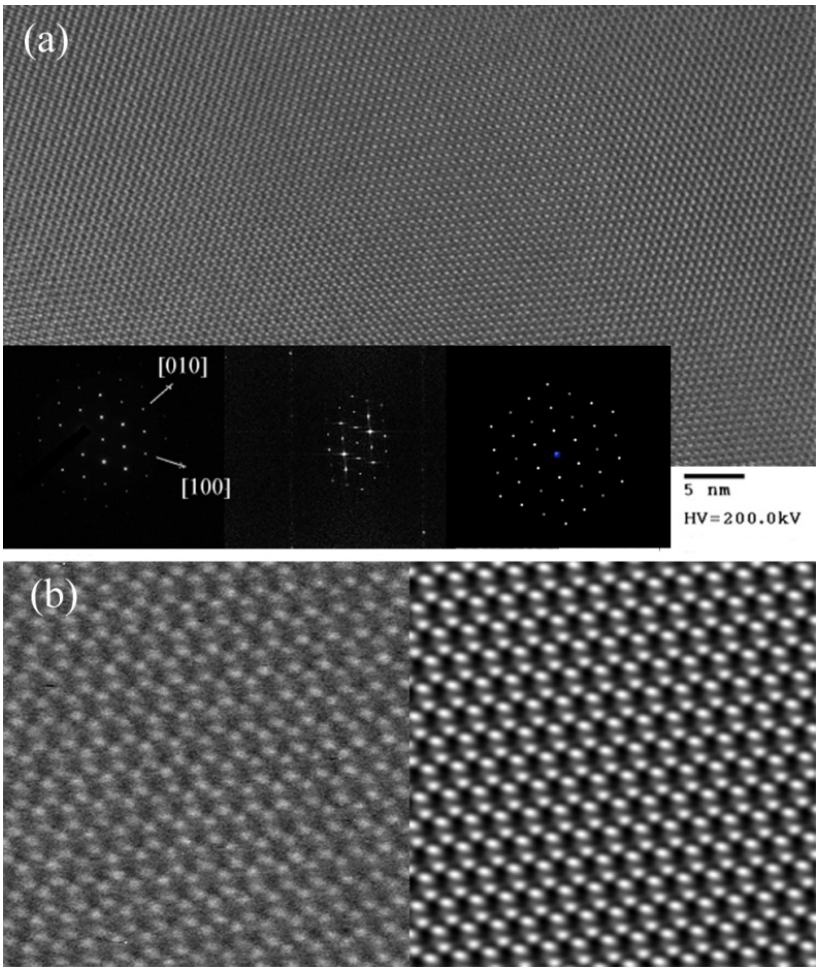

Figure 5.10 (a) Wide field [001] HRTEM image of $Ca_{10}[(SiO_4)_3(SO_4)_3]Cl_{0.4}F_{1.6}$, (experimental, FFT and simulated SAED reflections are provided.) (b) The as-collected image (left) and processed image (right) constrained by *p*6 symmetry are shown.

5.4 Conclusions

The synthesis of fluorine-substituted chlorellestadites has been achieved by the solid state method, and the crystal structures refined via powder X-ray and neutron diffraction using $P6_3/m$ symmetry. Ordering of the Si and S atoms within the tetrahedra, or halides between the tunnels can be excluded, as this would lead to $P2_1/m$ or $P2_1/b$ structures respectively, with a possible doubling of the unit cell in the *a* or *b* directions. In natural ellestadites, described in $P2_1/m$ and $P2_1$, equilibration over very long geological periods may favor lower symmetry. For the synthetic ellestadites studied here, increasing fluorine content, leads to a progressive shift of Cl^- towards the centre of the Ca(2) triangle; the formation of a shorter, stronger bond between Ca(2) and Cl may enhance the chemical stability of ellestadite. Minor loss of $CaCl_2$ during sintering induces Ca-vacancies within ellestadite was confirmed by powder neutron diffraction, and verified by the spread of $Ca(1)O_6$ metaprism twist angles as a function of composition, although the overall trend is linear. For charge balance, halide vacancies in the anion tunnel were compensated by calcium vacancies, and may be required to provide structural accommodation for larger Cl ions, or reduce structural strain due to the mismatch of the framework and tunnel dimensions. The reliability of these intricate Rietveld refinements was confirmed by Singular Value Decomposition and correlations of various crystal-chemical parameters.

References:

[1] H. T. Dean. *Publ. Hlth Rep. Wash.* **1938**, 53, 1443-1452.

[2] D. Lexa. *Metall. Mater. Trans.* **1999**, 30A, 147-153.

[3] I. Pajares, Á. G. de la Torre, S. Martínez-Ramírez, F. Puertas. *Powder Diffr*. **2002**, 17, 281-286.

[4] R. D. Shannon. *Acta Cryst.,* **1976**, 32A, 751-767.

[5] S. J. Saint-Jean, S. H. Sweden. *Solid State Sci.* **2005**, 7, 97-102.

[6] K. Sudarsanan, K. *Acta Cryst*., **1980**, 36, 1636-1639.

[7] B. P. Onac, H. Effenberger, K. Ettinger, S. C. Panzaru. *Am. Mineral.* **2006**, 91, 1927-1931.

[8] J. M. Hughes, J. Rakovan. *Rev. Mineral. Geochem.* **2002**, 48(1), 1-12.

[9] F. M. McCubbin, H. E. Mason, H. Park, B. L. Phillips, J. B. Parise, H. Nekvasil, D. H. Lindsley. *Am. Mineral*. **2008**, 93, 210-216.

[10] P. E. Mackie, R. A. Young. *J. Solid State Chem*. **1974**, 11, 319-329.

[11] J. M. Hughes, M. Cameron, K. D. Crowley. *Am. Mineral*. **1990**, 75, 295-304.

[12] C. Ferraris, T. J. White, J. Plévert, R. Wegner. *Phys. Chem. Mineral.* **2005**, 32, 485-492.

[13] Bruker, TOPAS Version 3, Bruker AXS Inc., Madison, WI, USA, **2005**.

[14] S. J. Saint-Jean, E. Jøns, N. Lundgaard, S. Hansen. *Cem. Concr. Res.* **2005**, 35, 431-437.

[15] V. F. Sears, *International Tables for Crystallography, vol. C* Kluwer Academic Publishers, Dordrecht, **1993**, 383.

[16] V. Petricek, M. Dusek, L. Palatinus. Jana2006. The crystallographic computing system. Institute of Physics, Praha, Czech Republic, **2006**.

[17] W. P. Griffith. *Nature* **1969**, 224, 264-266.

[18] R. A. Young, J. C. Elliott. *Archs. oral. Biol*. **1966**, 11, 699-707.

[19] J. V. Smith, S. W. Baily. *Acta Cryst*., **1963**, 16, 801-811.

[20] B. J. Wuench. *Sulfur, 16-A Crystal chemistry*, in: K. H. Wedepohl (Ed.), Handbook of Geochemistry, Vol. Ⅱ/2, Springer-Verlag, Berlin, **1970**, 16A 1-19.

[21] J. S. Prener. *J. Solid State Chem*. **1971**, 3, 49-55.

[22] P. H. J. Mercier, Y. Le Page, P. S. Whitfield, L. D. Mitchell. *J. Appl. Crystallogr*. **2006**, 39, 458-465.

[23] P. H. J. Mercier, Y. Le Page, P. S. Whitfield, L. D. Mitchell. *J. Appl. Crystallogr*. **2006**, 39, 369-375.

[24] T. J. White, C. Ferraris, J. Kim, S. Madhavi. *Rev. Mineral. Geochem.* **2005**, 57, 307-401.

[25] P. H. J. Mercier, Y. Le Page, P. S. Whitfield, L. D. Mitchell, I. J. Davidson, T. J. White. *Acta Cryst. B* **2005**, B 61, 635-655.

[26] P. H. J. Mercier, Z. Dong, T. Baikie, Y. le Page, T. J. White, P. S. Whitfield, L. D. Mitchel. *Acta Cryst. B* **2007**, B63, 37-48.

[27] P. Comodi, Y. Liu, P. F. Zanazzi, M. Montagnoli. *Phys. Chem. Mineral.* **2001**, 28, 219-224.

[28] P. E. Mackie, R. A. Young. *J. Appl. Crystallogr*. **1973**, *6*, 26-31

[29] L. W. Schroeder, M. Mathew. *J. Solid State Chem*. **1978**, 26, 383-387.

[30] A. Piotrowski, V. Kahlenberg, R. X. Fischer. *J. Solid State Chem*. **2002**, 163, 398-405.

Chapter 6

The Incorporation of Vanadium in Ellestadite

Vanadate ellestadites $Ca_{10}[(SiO_4)_x(VO_4)_{6-2x}(SO_4)_x]Cl_2$, serving as prototype crystalline matrices for the fixation of pentavalent toxic metals (V, Cr, As), were synthesized and characterized by powder X-ray and neutron diffraction (PXRD and PND), electron probe microanalysis (EPMA) and Fourier transform infrared spectroscopy (FTIR). The ellestadites $0.19 < x < 3$, adopt the $P6_3/m$ structure, while the vanadate endmember $Ca_{10}(VO_4)_6Cl_2$ is triclinic, space group P-1. A miscibility gap exists for $0.77 < x < 2.44$.

6.1 Introduction

This chapter examines the preparation and characterization of the ellestadite series $Ca_{10}[(SiO_4)_x(VO_4)_{6-2x}(SO_4)_x]Cl_2$ with $0 \leq x \leq 3$, to establish the continuity of the vanadate ellestadite solid solution series. A compilation of vanadate containing apatites (Table 6.1) reflects the very limited exploration of vanadium in this structure-type [1-18]. Vanadinite ($Pb_{10}(VO_4)_6Cl_2$) and synthetic vanadate apatites can accommodate extensive substitution of VO_4^{3-} by PO_4^{3-} [1-5], and the analogous calcium series $Ca_{10}[(PO_4)_{6-x}(VO_4)_x](OH)_2$ with $P6_3/m$ symmetry has been reported by Boechat et al. [7]. The comparable fluorine solid solution between $Ca_{10}(PO_4)_6F_2$ and $Ca_{10}(VO_4)_6F_2$ is also known [19], but with distortion to P-1 for the vanadium endmember [8]. Distinct discontinuities for both the a and c parameters have been found in the P-V chlorapatites, $A_{10}[(PO_4)_{6-x}(VO_4)_x]Cl_2$ (A = Ca, Cd, or Pb), with the unit cell edges displaying erratic behavior for $x \geq 3$, possibly reflecting the presence of X-ray amorphous material and changes in apatite composition [9]. In the current context, the inclusion of vanadium in ellestadite, also serves as proxy for the toxic metals chromium (Cr) and arsenic (As).

Table 6.1 Vanadate apatites.

Composition	Space Group	Reference
$Ca_{10}(VO_4)_6(OH)_2$	$P6_3/m$	Kutoglu (1974) [2]
		Ogo et al. (2008) [10]
$Ca_{10}(VO_4)_6F_2$	$P\text{-}1$	Baikie et al. (2007) [8]
$Ca_{10}(VO_4)_6(F_{0.9}O_{0.05}\square_{0.05})_2$	$P2_1/m$	Dong & White (2004) [11]
$Ca_{10}(VO_4)_6Cl_2$	$P6_3/m$	Beck et al. (2006) [6]
$Cd_{10}(VO_4)_6Br_2$	$P6_3/m$	Sudarsanan et al. (1977) [3]
$Cd_{10}(VO_4)_6I_2$	$P6_3/m$	Sudarsanan et al. (1977) [3]
$Ba_{10}(VO_4)_6Cl_2$	$P6_3/m$	Beck et al. (2006) [6]
$Pb_{10}(VO_4)_6(OH)_2$	$P6_3/m$	Engel (1970) [4]
$Pb_{10}(VO_4)_6F_2$	$P6_3/m$	Merker & Wondratschek (1959) [12]
		Grisafe & Hummel (1970) [13]
$Pb_{10}(VO_4)_6Cl_2$	$P6_3/m$	Trotter et al. (1958) [1]
		Dai & Hughes (1989) [14]
		Okudera (2013) [15]
$Sr_{10}(VO_4)_6(OH)_2$	$P6_3/m$	Mayer et al. (1975) [5]
$Sr_{10}(VO_4)_6Cl_2$	$P6_3/m$	Beck et al. (2006) [6]
		Ogo et al. (2008) [10]
$Ca_{10}(PO_4)_{6-x}(VO_4)_x(OH)_2$	$P6_3/m$	Boechat et al. (2000) [7]
		Onda et al. (2008) [16]
$Ca_{10}(PO_4)_{6-x}(VO_4)_xF_2$	$P6_3/m$	Kreidler & Hummel (1970) [5]
$(Ca_{10-x}Pb_x)(VO_4)_6F_2$	$P6_3/m$	Dong & White (2004) [8, 17]
$Ca_{10}(PO_4)_{6-x}(VO_4)_xCl_2$	$P6_3/m$	Kim et al. (2005) [9]
$Pb_{10}(PO_4)_{6-x}(VO_4)_xF_2$	$P6_3/m$	He et al. (2011) [18]

6.2 Experimental Methods

6.2.1 Synthesis

The $Ca_{10}[(SiO_4)_x(VO_4)_{6-2x}(SO_4)_x]Cl_2$ ellestadite series with $0 \leq x \leq 3$ was synthesized in the solid-state. The nominal synthesis reaction was:

$$2x\ CaO + x\ CaSO_4 + x\ SiO_2 + (3-x)\ Ca_3(VO_4)_2 + CaCl_2 \cdot 2H_2O \rightarrow$$

$$Ca_{10}[(SiO_4)_x(VO_4)_{6-2x}(SO_4)_x]Cl_2 + 2\ H_2O\uparrow \qquad (6\text{-}1)$$

The starting materials were prepared by preheating $CaCO_3$ (Merck, p.a.) at 1000°C for 12 h; SiO_2 (Sigma-Aldrich, 99.99%) and $CaSO_4 \cdot 2H_2O$ (Merck, p.a.) at 600°C for 4 h; and $CaCl_2 \cdot 2H_2O$ (Riedel-de Haën, puriss.) at 400°C for 4 h. Assuming the substitution is $2V^{5+}$ by Si^{4+} and S^{6+}, stoichiometric mixtures of CaO, $CaSO_4$, SiO_2, $CaCl_2$, V_2O_5 and $CaCl_2$ were manually ground with acetone and calcined at 950 °C for 5 h in an alumina crucible, then reground and sintered at 950 °C for a further 9 h.

6.2.2 Chemical Analysis

The chemical composition of the ellestadites were determined by electron probe microanalysis (EPMA) using a JEOL JXA-8200 at 20 kV, with a beam current of 20 nA, beam diameter of 2.5 μm and peak counting times of 40 s for all elements (both peak and background). The standards used were quartz (Si), a natural apatite (Ca), pyrrhotite (S), vanadium (V) and NaCl (Cl). A ZAF correction procedure was applied to all EPMA analyses. Chlorine is always underestimated due to the apparent anisotropic diffusion of chlorine along the c-axis channel of ellestadite and volatilization under the electron beam [20].

6.2.3 Crystallographic Characterization

Powder X-ray diffraction (PXRD) and neutron diffraction (PND) were combined for structural characterization. PXRD measurements were performed for phase identification and mass balance using a Bruker D8 high-resolution X-ray powder diffractometer (Cu-Kα radiation) operated at 40 kV and 40 mA. Scans were collected from 8° to 140° with a step size of 0.01° and a dwell time per step of 1 s. Powder neutron diffraction patterns were acquired on the High Resolution Powder

Diffractometer at the Open Pool Australian Lightwater (OPAL) reactor operated by the Australian Nuclear Science and Technology Organization (ANSTO). Approximately 2 g of the ellestadite was loaded into a 5 mm diameter vanadium can that was rotated during collection. The diffraction data were accumulated at ambient temperature using a neutron wavelength of 2.439 Å from 2.75° to 163.95° with a step size of 0.05°.

The structure refinements were carried out by the Rietveld method using TOPAS [21] from 10 to 140° 2θ. A pseudo-Voigt peak shape was used with the refined parameters including five polynomial background coefficients, peak half widths U, V, W and an asymmetry parameter. The scattering lengths 0.4700, 0.4149, 0.2847, 0.5803, 0.5654, and 0.9577 × 10^{-12} cm were used for Ca, Si, S, O, F and Cl, respectively [22]. As vanadium is transparent to neutrons (b = -0.03824 × 10^{-12} cm), its position was determined *via* X-ray powder diffraction. Most compositions were refined in hexagonal $P6_3/m$ [23], although for the V-rich materials a triclinic distortion [8] was evident and the subgroup P-1 was used. For each data set, a peak shift, a zero error, unit cell parameters and crystal size were refined sequentially with temperature displacement parameters and occupation factors of each atomic site kept constant. After several refinement cycles, the calcium positions were released, followed by the oxygen positions. The mole ratio of Si:S at the tetrahedral site was constrained to be equal and the standard site occupancy factor of V + (Si/S) kept as 1. The oxygen sites were fully tenanted, while the occupancies of calcium and chlorine were allowed to vary. Isotropic temperature displacement parameters for all atoms were refined in Ca(1)/Ca(2)/Cl/F and Si/S/V/O(1)/O(2)/O(3) groups to the same value. The refinement cycles were terminated when convergence was reached. Difference-Fourier maps were generated using Jana2006 [24], specifically to examine the location of anion scattering centres in the tunnels. The $Ca(1)O_6$ metaprism twist angle (φ) was calculated according to the method of White and Dong [25] to check that bond angles change systematically with composition.

6.2.4 Fourier Transform Infrared (FTIR) Spectroscopy

Infrared spectra were recorded over the range 400 to 4000 cm^{-1} with a Fourier Transform Infrared Spectrometer (Perkin-Elmer Spectrum 2000) using the KBr pellet technique, where ellestadite (~1 mg) was ground with oven dried KBr (200 mg). This homogenized mixture was pressed into 10-mm-diameter transparent pellets. Measurements were carried out with a spectral resolution of 4 cm^{-1} and accumulated for 32 scans.

6.3 Crystal Chemistry of $Ca_{10}(SiO_4)_x(VO_4)_{6-2x}(SO_4)_xCl_2$

6.3.1 Phase Chemistry

The EPMA data (Table 6.2) suggested that the compositions of $Ca_{10}[(SiO_4)_x(VO_4)_{6-2x}(SO_4)_x]Cl_2$, ($x$ = 0, 0.5, 2.5 and 3) materials were compositionally homogeneous, indicating equilibrium was reached during synthesis. However, a miscibility gap was observed for $1 \leq x \leq 2$, where a two-phase ellestadite assemblage was identified by the electron backscatter images (BSI) (Figure 6.1) and confirmed by powder X-ray diffraction (Figure 6.2). The atomic ratio of vanadium+silicon+sulfur to calcium for all the samples was constant, but a little lower than the ideal value of 1.67 (= 10 *A* cations / *6* B cations). This suggests either Ca is deficient or underestimated, as *B*-site non-stoichiometry (Si+S+V) has not been reported in any apatite structure-types. Fleet [26] observed non-stoichiometry for their synthetic lead apatite prepared by the solid-state reaction (Pb/(P+V) = 1.56), and He [18] found Pb/(P+V) ratios from 1.51 to 1.61 for their synthetic lead phosphate and vanadate apatite solid solution. It appears that synthetic apatites prepared by high temperature solid-state reaction are usually non-stoichiometric. Presnser [27] and Saint-Jean [23] studied chlorapatite and chlorellestadite respectively with both of experiencing a loss of $CaCl_2$ during the annealing. The slight depletion of Ca and Cl in our analysis can be similarly explained.

Table 6.2 Mean composition of ellestadite solid solution $Ca_{10}[(SiO_4)_x(VO_4)_{6-2x}(SO_4)_x]Cl_2$.

Expected *x*	Ellestadite (atomic ratio)*						Ca/(Si+S+V)
	Ca	**Si**	**S**	**V**	**Cl**	**O**	(mol%)**
0	9.81(5)	-	-	6.00	1.69(5)	23.96(4)	1.64
0.5	9.75(6)	0.45(3)	0.42(3)	5.12(9)	1.65(5)	23.95(4)	1.63
1.0	9.72(6)	2.46(3)	2.43(4)	1.11 (7)	1.53(2)	23.94(7)	1.62
	9.73(5)	0.20(3)	0.18(4)	5.62(8)	1.30(4)	24.02(7)	1.62
1.5	9.76(5)	2.64(3)	2.60(3)	0.76(5)	1.46(6)	24.02(5)	1.63
	9.78(7)	0.46(2)	0.43(2)	5.11(9)	1.26(4)	24.13(6)	1.63
2.0	9.72(6)	2.47(3)	2.43(4)	1.10 (7)	1.53(2)	23.94(7)	1.62
	9.73(5)	0.78(3)	0.77(4)	4.45(8)	1.30(4)	24.02(7)	1.62
2.5	9.73(7)	2.45(3)	2.55(5)	1.00(9)	1.33(3)	24.12(9)	1.62
3.0	9.88(6)	2.96(6)	3.04(5)	-	1.65(9)	24.27(9)	1.65

* Atomic ratio were calculated from EPMA data based on 6 small cations (Si + S + V = 6) afpu. For each sample, more than 20 EPMA analyses were made. For $1.0 \leq x \leq 2.0$, analyses were made on two-phase assemblage.

** The Ca/(Si+S+V) molar ratio suggests either Ca is underestimated, or (Si+S+V) overestimated, or these ellestadites non-stoichiometric (the ideal Ca/(Si+S+V) ratio of ellestadite is 1.667)

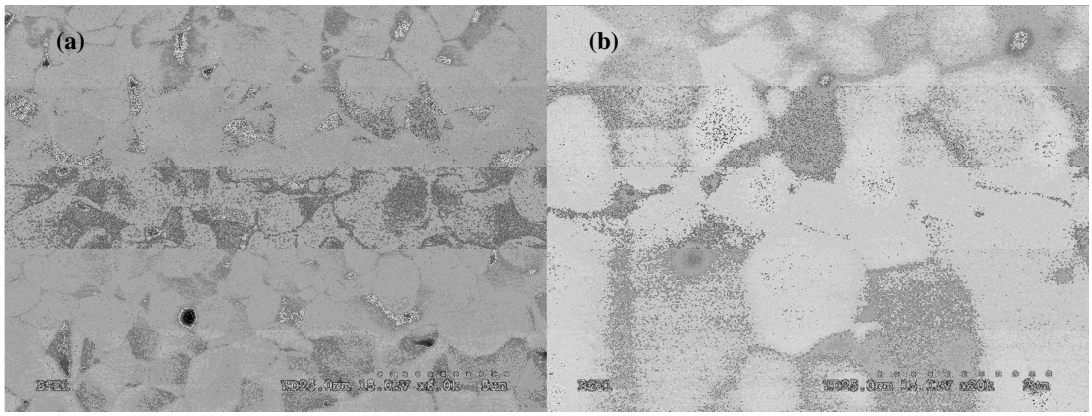

Figure 6.1 Electron backscatter images (BSI) showing the two-phase textures of $Ca_{10}[(SiO_4)_x(VO_4)_{6-2x}(SO_4)_x]Cl_2$, (a) $x = 1.5$ and (b) $x = 1.0$.

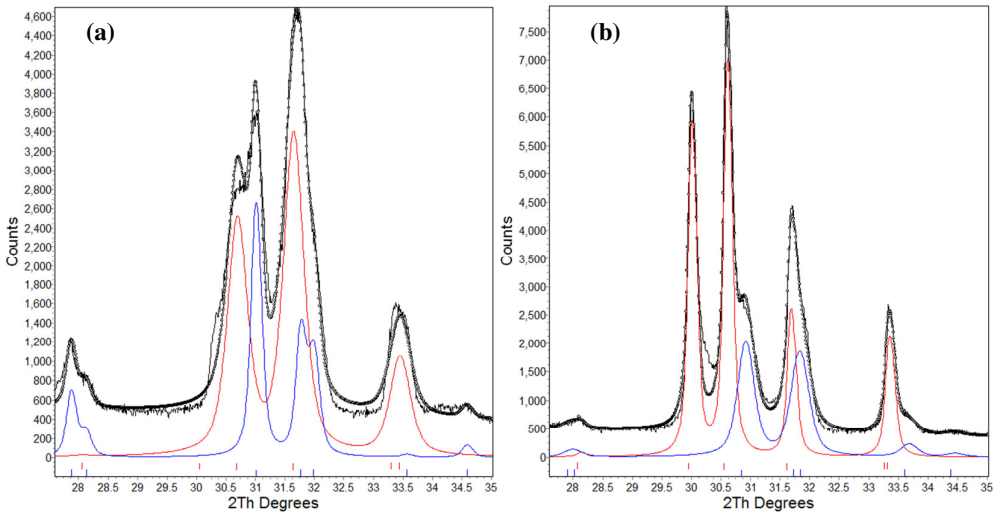

Figure 6.2 Rietveld fit between calculated (black dot) and experimental (black line) diffraction profiles for $Ca_{10}[(SiO_4)_x(VO_4)_{6-2x}(SO_4)_x]Cl_2$, with (a) nominal x = 1.5 and (b) x = 1.0. At these compositions immiscibility is reflected by co-existing ellestadite phase pairs.

6.3.2 Metalloid Speciation

The FT-IR absorption spectra (Figure 6.3) show the characteristic bands of VO_4^{3-}, SiO_4^{4-} and SO_4^{2-} for selected compositions of $Ca_{10}[(SiO_4)_x(VO_4)_{6-2x}(SO_4)_x]Cl_2$, x = 0, 2 and 3. The V-O stretching modes (v_3) of VO_4 appear around 800-900 cm^{-1}, with three bands clearly observed for $Ca_{10}(VO_4)_6Cl_2$ at 870, 848 and 809 cm^{-1}. Although no FT-IR data of the same composition has been reported, Boechat [7] observed three $v_3(VO_4)$ stretching modes in $Ca_{10}(VO_4)_6(OH)_2$ at 891, 851 and 819 cm^{-1}, the slight differences in wavenumber arising from replacing Cl^- by OH^-. The SO_4 bands appear at 616, 646 cm^{-1} and around 1000-1200 cm^{-1}, while those of SiO_4 are found at 508, 563 cm^{-1} and 800-1000 cm^{-1} for $Ca_{10}[(SiO_4)_3(SO_4)_3]Cl_2$ [28, 29]. The vibration mode does not appear clearly for the intermediate composition due to the overlap of $v_3(VO_4)$ and $v_3(SiO_4)$ (Figure 6.3 x = 2) stretching modes. As the composition changes, both the band shape and position vary systematically. No features were ever observed at 1450 cm^{-1}, which precludes the incorporation of CO_3^{2-} in the BO_4 site or channel.

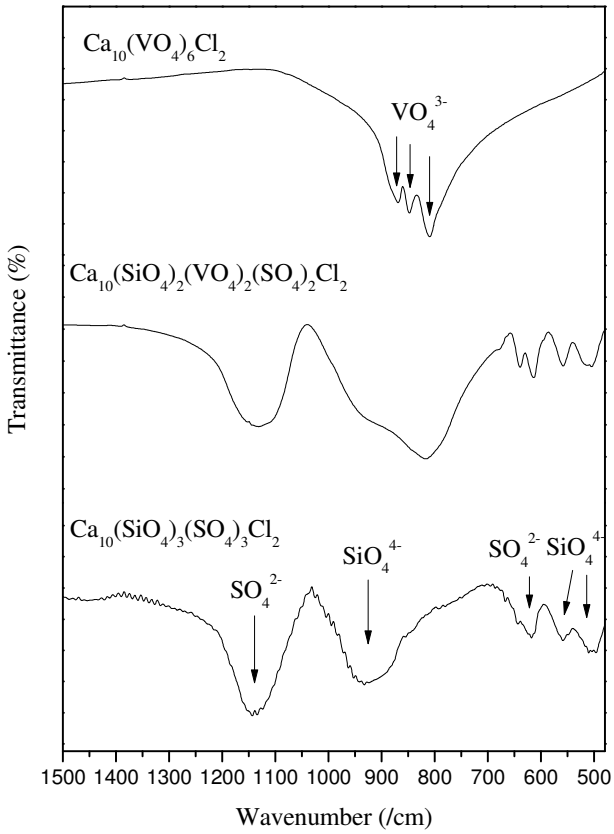

Figure 6.3 FT-IR absorption spectra of $Ca_{10}[(SiO_4)_x(VO_4)_{6-2x}(SO_4)_x]Cl_2$ for $x = 0$, 2, and 3.

6.3.3 Unit Cell Constant Refinement

A miscibility gap was observed for $Ca_{10}[(SiO_4)_x(VO_4)_{6-2x}(SO_4)_x]Cl_2$, $0.75 \leq x \leq 2.25$. Inspection of the Rietveld traces clearly differentiates Bragg reflections due to two phases (Figure 6.2), and is consistent EPMA. The nominal $x = 1$ material consists of $x = 0.19$ (68.6 wt%) and 2.44 (31.4 wt%) structures, $x = 1.5$ was composed of $x = 0.45$ (52.9 wt%) and 2.62 (47.5 wt%) structures, and $x = 2$ contains $x = 0.77$ (10.7 wt%) and 2.45 (84.4 wt%) compounds. The overall average composition for the two phases yields $x = 0.9$, 1.47 and 2.14, respectively, comparable to nominal values 1.0, 1.5 and 2.0. The substitution of larger vanadium ion by the Si/S is accompanied by contraction of the unit cell constant a and unit cell volume V (about 4.6% and 8.1% respectively) (Figure 6.4, Table 6.3). The small expansion of c (less than 1%) may be due to more complete chlorine retention in the tunnel for vanadium-poor ellestadites. The same miscibility gap was also reported for $(Pb_xCa_{10-x})(VO_4)_6F_2$ ($2 < x < 3$), where dissociation into coexisting vanadinites is observed [11]. Kim et al. [9] found a discontinuity in the cell parameters for the $A_{10}[(PO_4)_{6-x}(VO_4)_x]Cl_2$ (A = Ca, Cd, or Pb) series, but chemical analysis or BSI were not employed to check for phase separation. The refined structural parameters for $Ca_{10}[(SiO_4)_x(VO_4)_{6-2x}(SO_4)_x]Cl_2$ with $0.5 < x < 3$ are collated in Table 3. As x increased from 0.19 to 3 average bond lengths of BO_4 decreased as the Si/S content was raised (Table 6.4). The large difference of the BO_4 sizes could be a driver for immiscibility.

Table 6.3 Lattice parameters and crystallographic data for hexagonal $Ca_{10}[(SiO_4)_x(VO_4)_{6-2x}(SO_4)_x]Cl_2$, $0.19 \leq x \leq 3$.

Single phase		Miscibility gap							Single phase
x		0.90 (average)		1.47 (average)		2.14 (average)			
	0.44	0.19	2.44	0.45	2.62	0.77	2.45	2.50	3.0
Space group	$P6_3/m$	$P6_3/m$	$P6_3/m$	$P6_3/m$	$P6_3/m$	$P6_3/m$	$P6_3/m$	$P6_3/m$	$P6_3/m$
Wt	99.4%	68.6%	31.4%	52.8%	47.1%	10.7%	84.3%	100%	95.6%
a (Å)	10.0541(4)	10.1132(3)	9.749(1)	10.0583(7)	9.6967(8)	10.0177(4)	9.7333(6)	9.7245(4)	9.6691(3)
c (Å)	6.8223(3)	6.8004(4)	6.865(1)	6.8256(9)	6.8803(1)	6.7744(4)	6.8750(8)	6.8722(4)	6.8531(3)
V (Å^3)	597.23(6)	602.34(5)	565.10(2)	598.03(1)	560.25(1)	595.00(1)	564.06(1)	562.81(6)	554.88(4))
φ(deg)	15.6_8	13.4_6	18.5_2	15.4_8	20.2_2	16.0_3	20.0_9	19.9_2	20.4_2
R_{wp}	0.076	0.072	0.072	0.078	0.078	0.075	0.075	0.079	0.052
R_p	0.059	0.056	0.056	0.061	0.061	0.058	0.058	0.062	0.040
R_b	0.023	0.026	0.014	0.024	0.016	0.014	0.023	0.028	0.032
Ca(1), 4*f* (1/3, 2/3, *z*)									
z	0.0039(9)	0.001(1)	-0.009(3)	0.0022(2)	0.0023(2)	0.0073(1)	0.0002(1)	0.006(1)	0.0022(1)
B (Å^2)	1.85(7)	1.06(2)	0.50(2)	0.43(3)	0.91(2)	0.87(7)	0.82(7)	0.51(7)	2.04(5)
Ca(2), 6*h* (*x, y,* 1/4)									
x	0.2671(5)	0.2688(9)	0.251(2)	0.2721(1)	0.2499(1)	0.2687(1)	0.2549(1)	0.2595(7)	0.2600(7)
y	0.0223(6)	0.0201(9)	-0.016(2)	0.0257(1)	0.0122(2)	0.0200(3)	0.0054(1)	0.0033(9)	0.0004(8)
B (Å^2)	1.85(7)	1.06(2)	0.50(2)	0.43(3)	0.91(2)	0.87(7)	0.82(7)	0.51(7)	2.04(5)
Si/S, 6*h* (*x, y,* 1/4)									
x	0.4057(2)	0.4060(2)	0.4070(2)	0.4055(2)	0.4072(2)	0.4046(1)	0.4070(1)	0.407(1)	0.4030(4)
y	0.3755(4)	0.3756(3)	0.3744(1)	0.3760(2)	0.3746(4)	0.3733(1)	0.3746(8)	0.374(1)	0.3728(4)
B (Å^2)	0.80(4)	1.39(2)	0.86(2)	1.39(2)	1.38(4)	0.87(7)	1.16(3)	0.82(6)	2.04(5)
Occ. Si	0.073	0.032	0.408	0.075	0.437	0.128	0.408	0.42	0.50
S	0.073	0.032	0.408	0.075	0.437	0.128	0.408	0.42	0.50
V	0.853	0.936	0.184	0.85	0.126	0.744	0.184	0.16	
O(1), 6*h* (*x, y,* 1/4)									
x	0.3491(2)	0.3543(4)	0.3436(7)	0.3499(6)	0.3299(6)	0.3438(4)	0.3338(5)	0.3368(3)	0.3361(3)
y	0.5042(2)	0.5090(4)	0.4956(8)	0.5060(6)	0.4881(6)	0.4960(3)	0.4883(5)	0.4885(3)	0.4880(3)
B (Å^2)	0.80(4)	1.39(2)	0.86(2)	1.39(2)	1.38(4)	0.87(7)	1.16(3)	0.82(6)	2.20(3)
O(2), 6*h* (*x, y,* 1/4)									
x	0.5986(2)	0.6008(4)	0.5935(7)	0.5998(6)	0.5958(6)	0.6005(8)	0.5960(5)	0.5929(3)	0.5886(3)
y	0.4648(4)	0.4662(7)	0.4659(1)	0.4659(1)	0.4761(1)	0.4701(3)	0.4674(8)	0.4696(3)	0.4672(5)
B (Å^2)	0.80(4)	1.39(2)	0.86(2)	1.39(2)	1.38(4)	0.87(7)	1.16(3)	0.82(6)	2.20(3)
O(3), 12*i* (*x, y, z*)									
x	0.3521(3)	0.3530(4)	0.3493(1)	0.3508(8)	0.3507(8)	0.3521(3)	0.3481(6)	0.3487(4)	0.3538(3)
y	0.2611(2)	0.2618(3)	0.2750(1)	0.2587(5)	0.2675(5)	0.2618(2)	0.2650(5)	0.2659(3)	0.2665(3)
z	0.0541(2)	0.0527(4)	0.0572(5)	0.0563(6)	0.0627(6)	0.0053(2)	0.0655(5)	0.0661(3)	0.0657(3)
B (Å^2)	0.80(4)	1.39(2)	0.86(2)	1.39(2)	1.38(4)	0.87(7)	1.16(3)	0.82(6)	2.20(3)
Cl, 12*i* (*x, y, z*)									
x	0.017(7)	0.011(6)	0	0.019(7)	0	0.011(8)	0	0	0
y	-0.020(7)	-0.029(4)	0	-0.030(6)	0	-0.023(9)	0	0	0
z	0.3183(1)	0.3223(1)	0.358(4)	0.287(5)	0.353(2)	0.404(4)	0.327(4)	0.381(2)	0.425(1)
B (Å^2)	1.85(7)	1.06(2)	1.06(2)	0.43(3)	0.91(2)	0.87(7)	0.82(7)	0.51(7)	2.04(5)
Occ	0.144(2)	0.154(3)	0.50	0.137(5)	0.50(4)	0.146(2)	0.50	0.488(9)	0.416(2)

Table 6.4 Bond lengths and angles for $Ca_{10}[(SiO_4)_x(VO_4)_{6-2x}(SO_4)_x]Cl_2$.

Composition x	0.19	0.44	0.45	0.77	2.44	2.45	2.50	2.62	3.0
Bond length (Å)									
Ca(1)-O(1) × 3	2.407(1)	2.402(2)	2.402(1)	2.411(5)	2.416(1)	2.445(5)	2.421(6)	2.440(4)	2.438(3)
Ca(1)-O(2) × 3	2.462(1)	2.473(3)	2.468(1)	2.502(4)	2.474(6)	2.454(2)	2.516(7)	2.500(8)	2.466(3)
< Ca(1)-O>	2.434	2.437	2.435	2.456	2.445	2.450	2.468	2.47	2.452
Ca(2)-O(1)	3.407(7)	3.318(2)	3.389(3)	3.224(2)	2.827(2)	2.836(8)	2.866(9)	2.746(1)	2.893(4)
Ca(2)-O(2)	2.327(1)	2.345(3)	2.294(1)	2.274(6)	2.387(2)	2.340(8)	2.241(8)	2.301(9)	2.283(4)
Ca(2)-O(3) × 2	2.330(5)	2.354(2)	2.374(9)	2.320(1)	2.223(1)	2.315(4)	2.331(4)	2.289(4)	2.582(3)
Ca(2)-O(3) × 2	2.534(7)	2.495(2)	2.451(1)	2.511(8)	2.837(2)	2.640(9)	2.572(8)	2.706(5)	2.358(3)
< Ca(2)-O>	2.577	2.56	2.555	2.527	2.555	2.514	2.485	2.506	2.509
B-O(1)	1.673(5)	1.653(3)	1.660(7)	1.621(5)	1.581(9)	1.586(9)	1.554(3)	1.609(7)	1.544(5)
B-O(2)	1.707(4)	1.681(2)	1.694(5)	1.699(2)	1.575(6)	1.593(3)	1.571(3)	1.587(5)	1.545(1)
B-O(3)	1.671(2)	1.667(1)	1.671(4)	1.644(3)	1.571(5)	1.569(6)	1.562(2)	1.573(4)	1.545(2)
Average	1.680	1.667	1.674	1.652	1.574	1.579	1.562	1.585	1.545

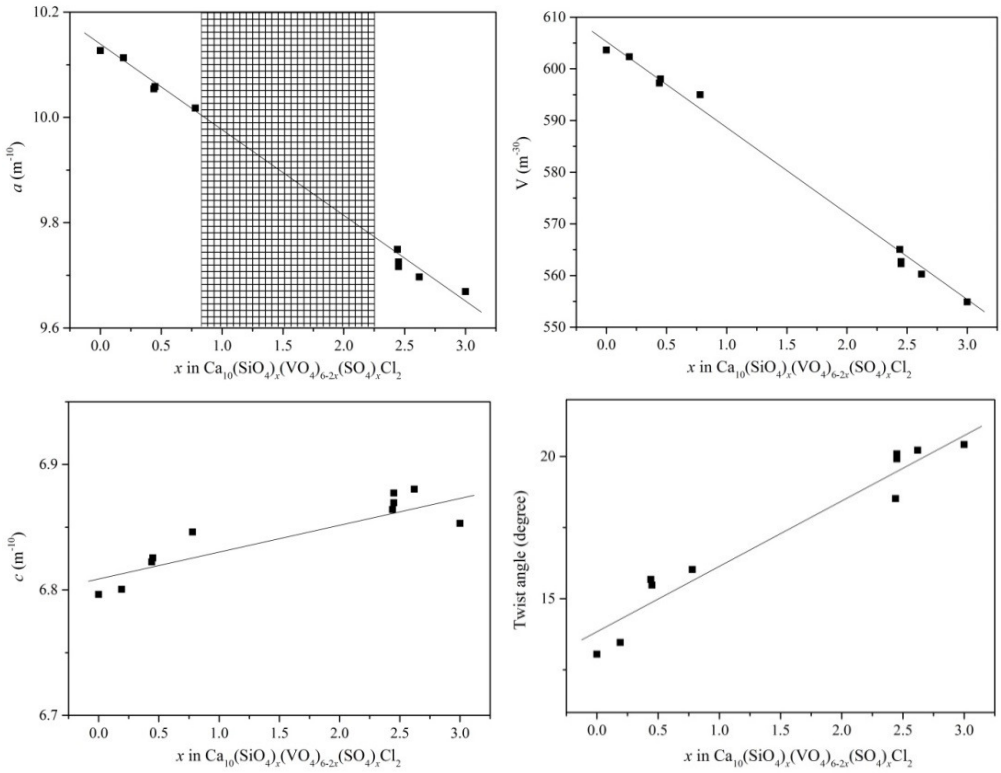

Figure 6.4 Variation in cell parameters (a and c), unit cell volume and metaprism twist angle with degree of Si/S substitution x in $Ca_{10}[(SiO_4)_x(VO_4)_{6-2x}(SO_4)_x]Cl_2$. Standard deviation of data is smaller than point size.

6.3.4 Structure Refinement of Triclinic Chlor-Vanadinite

Kreidler and Hummel [19] first observed the structure distortion of $Ca_{10}(VO_4)_6F_2$ from hexagonal $P6_3/m$ as the ionic radius of the *B*-type metalloid was large relative to the *A* cation, with a similar phenomenon found for $Pb_{10}[(PO_4)_{6-x}(VO_4)_x]Cl_2$ with high vanadium content (> 80%) [14, 18]. Dong et al. [11] initially assigned space group $P2_1/m$ to $Ca_{10}(VO_4)_6F_2$ which was later corrected by Baikie et al. [8] to triclinic *P*-1. It can be shown empirically that the driver for the transformation from $P6_3/m$ to *P*-1 is to produce acceptable bond-valence sums (BVS) at the *A* and *B* sites. For hexagonal ellestadite ($Ca_{10}[(SiO_4)_3(SO_4)_3]Cl_2$), Ca^{2+} fits neatly in the *A*(1) and *A*(2) site with a BVS of +2 v.u. (valence units). As the vanadium content increases and refinement is fixed as $P6_3/m$, the *B*-O bond length of the BO_4 tetrahedron increases with a concomitant lengthening of the average *A*-O distance. Ultimately, the tetrahedral *B* site becomes quite compressed (BVS = 5.41 v.u.) at the V endmember. Thus, structural distortion is necessary to relax O away from the *B* cation. The [001] difference Fourier map for $P6_3/m$ at z = 0.320 (Figure 6.5a) also suggests topological distortion when compared with hexagonal $Ca_{10}[(SiO_4)_3(SO_4)_3]F_2$ (z = ¼) and $Ca_{10}(PO_4)_6Cl_2$ (z = 0) [28, 29] (Figure 6.5b and c). Le Bail fitting of $Ca_{10}(VO_4)_6Cl_2$ with a triclinic (P-1) cell yielded significantly lower R_b (0.24%) than that obtained using the hexagonal cell (R_b = 0.45%). In the triclinic structure, tetrahedra are free to rotate around an axis perpendicular to *c* by removing the mirror plan [8]. Thus, VO_4 tetrahedra tilt to relieve stress at the metalloid sites to yield reasonable bond-valence sums (BVS) and overbonding is considerably reduced (BVS = 5.13 v.u.). The unit cell parameters and atomic positions (Table 6.5) were extracted from the neutron diffraction profile by Rietveld refinement (Figure 6.6).

Difference Fourier analysis was used to study the position of chlorine in the tunnel. Figure 6.7 shows the residual neutron scattering distribution in the tunnel with F_c calculated omitting chlorine. In Si/S rich ellestadite the Cl locates at the $P6_3/m$ 4e (0, 0, z) site, while in $Ca_{10}(VO_4)_6Cl_2$, and vanadium rich phases, there are non-circular contours indicative of a small deviation from the z-axis that is best described by placing Cl in the general position 12i (x, y ,z).

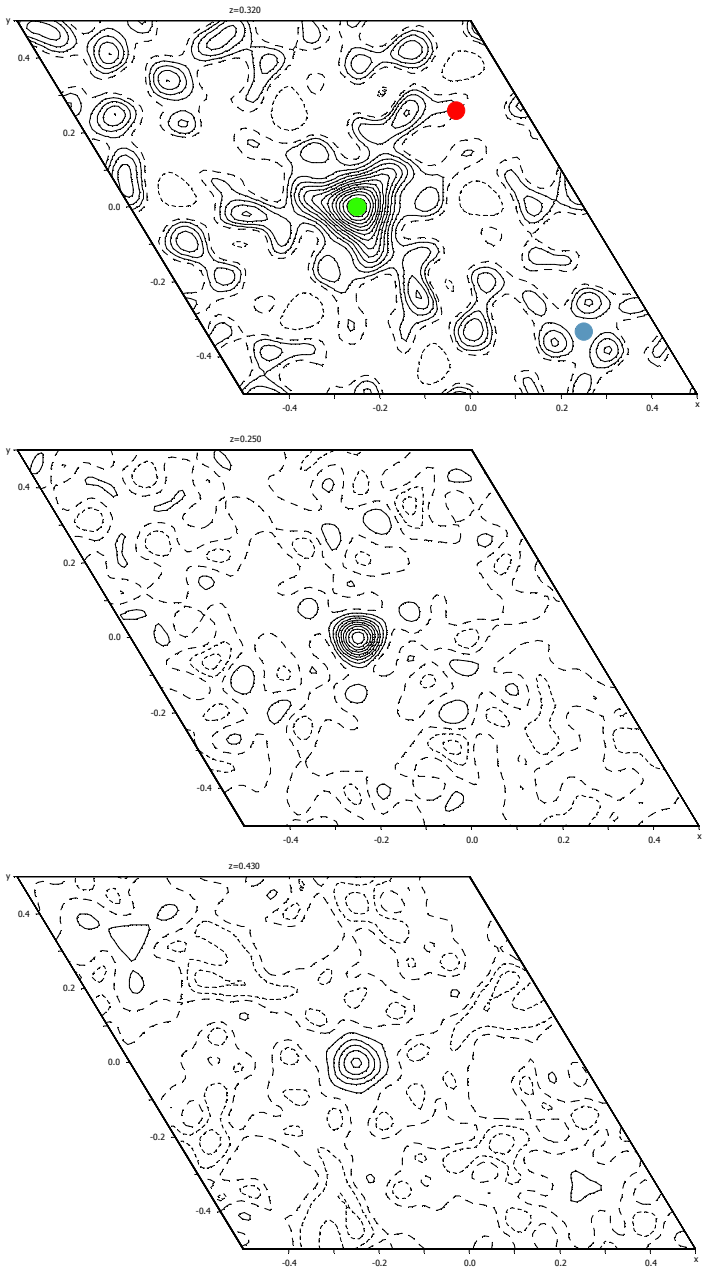

Figure 6.5 Difference Fourier maps showing residual electron density along [001] using hexagonal model without *X* anion in the tunnel (a) $Ca_{10}(VO_4)_6Cl_2$, (b) $Ca_{10}[(SiO_4)_3(SO_4)_3]F_2$ [29], and (c) $Ca_{10}(PO_4)_6Cl_2$ [30]. Contour interval is 0.20 e/Å^3 and the first positive contour (solid line) is at 0.20 e/Å^3. (The red, green and blue dots in (a) represent the V, Cl and Ca atoms.) For $Ca_{10}(VO_4)_6Cl_2$ the large residual is indicative of the material not conforming to $P6_3/m$, in contrast to $Ca_{10}[(SiO_4)_3(SO_4)_3]F_2$ and $Ca_{10}(PO_4)_6Cl_2$.

Table 6.5 Unit-cell and atomic parameters for triclinic $Ca_{10}(VO_4)_6Cl_2$ determined from powder neutron diffraction.

a = 10.1371(3) Å, b = 10.1101(4) Å, c = 6.7969(9) Å, α = 90.12(3), β = 89.85(1), γ = 119.93(6), V = 603.6(4) Å^3; space group P-1; R_{wp} = 0.066, R_p = 0.052, R_b = 0.019

Site	*x*	*y*	*z*	U_{iso}
Ca1	0.3383(5)	0.6611(5)	0.0029(6)	0.094
Ca2	0.3358(5)	0.6695(5)	0.4962(6)	0.005
Ca3	0.2923(1)	0.05143(1)	0.0175(1)	0.029
Ca4	-0.0168(1)	0.2486(1)	0.2611(3)	0.035
Ca5	0.7440(1)	0.7467(2)	0.2562(3)	0.023
V1*	0.4086(4)	0.3746(8)	0.2467(6)	0.006
V2*	0.6253(1)	0.0284(3)	0.2523(3)	0.006
V3*	0.9672(2)	0.5867(3)	0.2475(2)	0.006
O1	0.3525(6)	0.5065(5)	0.2459(2)	0.045
O2	0.4831(1)	0.8441(8)	0.2420(3)	0.057
O3	0.1536(6)	0.6357(1)	0.2261(3)	0.030
O4	0.6034(5)	0.4721(6)	0.2471(1)	0.073
O5	0.5466(6)	0.1407(7)	0.2487(2)	0.064
O6	0.8574(2)	0.3910(7)	0.2549(2)	0.009
O7	0.3509(1)	0.2650(8)	0.0417(1)	0.040
O8	0.7442(1)	0.0943(2)	0.0529(1)	0.086
O9	0.9050(1)	0.6510(1)	0.0584(1)	0.073
O10	0.6755(1)	0.7516(9)	0.5691(1)	0.018
O11	0.2549(1)	0.9111(2)	0.5499(1)	0.051
O12	0.0904(1)	0.3644(1)	0.5440(1)	0.041
Cl	0.0012(3)	-0.024(3)	0.3095(1)	0.012

*Atomic coordinates for V sites were evaluated by Rietveld refinement of XRD powder data; the same value of isotropic thermal displacement parameter U_{iso} was assumed for all three V sites.

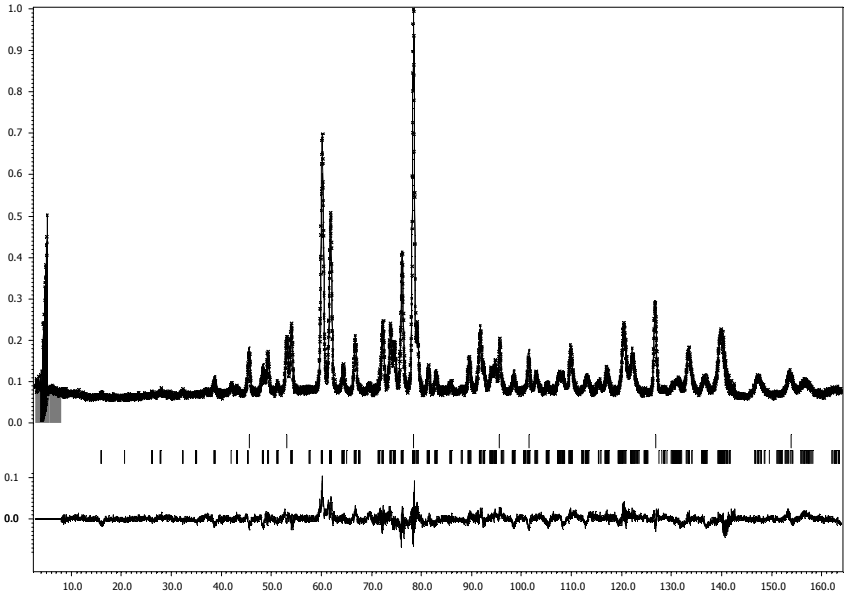

Figure 6.6 Neutron diffraction Rietveld profiles of $Ca_{10}(VO_4)_6Cl_2$.

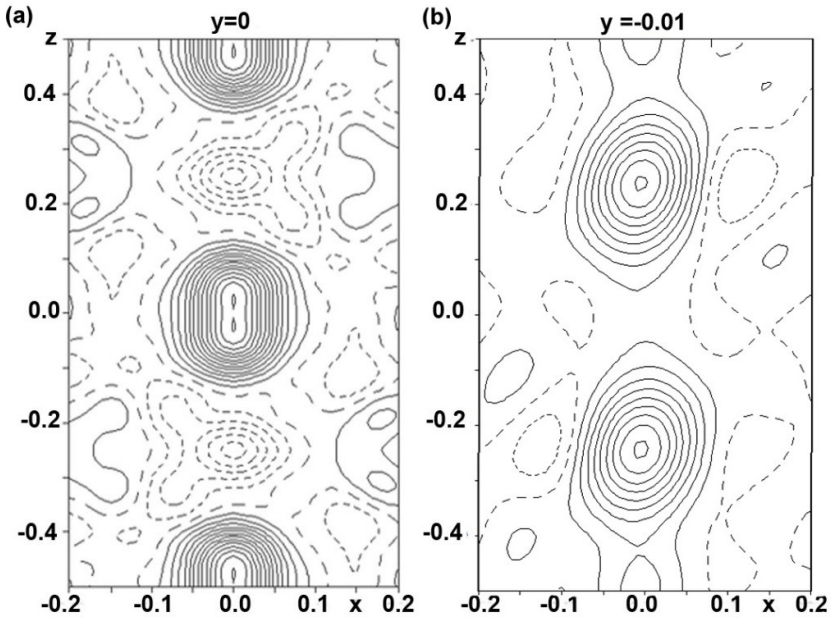

Figure 6.7 Difference Fourier maps showing residual electron density in the tunnel of (a) $Ca_{10}[(SiO_4)_3(SO_4)_3]Cl_2$ (b) $Ca_{10}(VO_4)_6Cl_2$ without chlorine atoms. Contour interval is 0.20 e/Å^3 and the first positive contour (solid line) is at 0.20 e/Å^3.

6.3.5 Twist Angle

It has been noted previously that the $A(1)O_6$ trigonal prisms are twisted by an angle φ to form metaprisms such that the degree of rotation varies inversely with the average ionic/crystal radius of the unit cell contents [25]. This relationship was observed for the present ellestadite structures and other published work [30-34] as shown in Table 6.6 and Figure 6.8. This correlation serves as a diagnostic tool to validate the quality of apatite structure refinements, across solid solution series. Most simply, three sites are available for substitution: cationic *A*, the metalloid *B* and the *X* anionic sites. As a general observation, replacement of VO_4 by PO_4 increases the twist angle for constant *A* and *X* chemistry; e.g. for $Cd_{10}(VO_4)_6Br_2$ φ = 8.8° and for $Cd_{10}(PO_4)_6Br_2$ φ = 16.0° [3]. A similar twist angle relationship is seen for the $Ca_{10}(CrO_4)_6(OH)_2$ - $Ca_{10}(PO_4)_6(OH)_2$ join where φ increases from 17.8° to 23.2° [32].

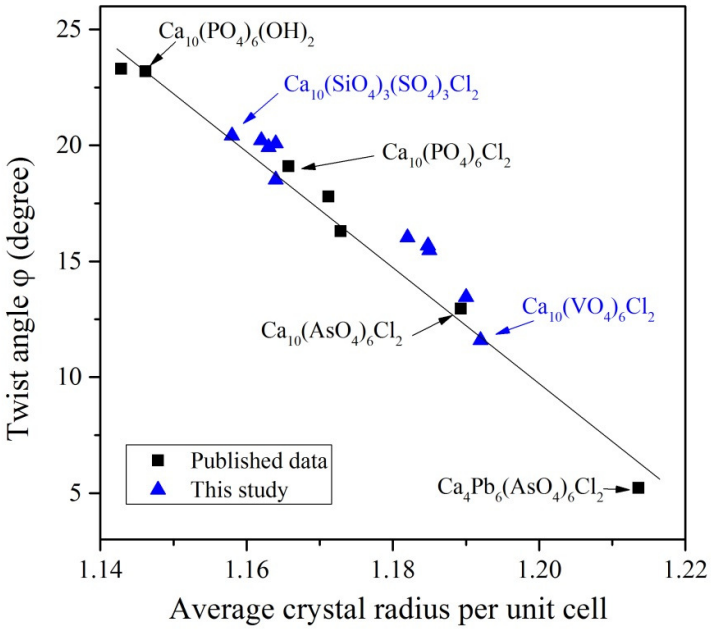

Figure 6.8 Correlation of the $Ca(1)O_6$ metaprism twist angle obtained from Rietveld analysis with the average crystal radius of the whole unit cell.

Table 6.6 Variation in the metaprism twist angle of calcium apatite as a function of average crystal radius.

Composition	Average crystal radius (Å)	Twist angle (φ°)	Refernce
$Ca_{10}(PO_4)_6F_2$	1.143	23.3	[30]
$Ca_{10}(PO_4)_6(OH)_2$	1.146	23.2	[31]
$Ca_{9.82}(SiO_4)_3(SO_4)_3Cl_{1.64}$	1.158	20.4	this study
$Ca_{10}(PO_4)_6Cl_2$	1.166	19.1	[31]
$Ca_{10}(CrO_4)_6(OH)_2$	1.171	17.8	[32]
$Ca_{10}(PO_4)_6Br_2$	1.173	16.3	[31]
$Ca_{10}(AsO_4)_6Cl_2$	1.189	13.0	[33]
$Ca_{10}(VO_4)_6Cl_2$	1.192	11.6*	this study
$Ca_4Pb_6(AsO_4)_6Cl_2$	1.214	5.2	[34]

* The twist angle of $Ca_{10}(VO_4)_6Cl_2$ is the average value of three twist angles in a triclinic *P*-1 structure.

Where there is a reduction in symmetry, as in triclinic $Ca_{10}(VO_4)_6Cl_2$, the $Ca(1)O_6$ metaprism is defined by three independent φ (11.59°, 10.04°, and 13.18°) with an average value of 11.60° (Figure 6.9). For hexagonal $Ca_{10}[(SiO_4)_x(VO_4)_{6-2x}(SO_4)_x]Cl_2$ ellestadites the $A(1)O_6$ metaprism twist angle (φ) increases linearly from 13.4° to 20.4° for $0.19 < x < 3.0$ [Fig. 5] as VO_4 is replaced by $(Si/S)O_4$. Smaller Si/S ions at the BO_4 tetrahedra gives *B*-O bond lengths of 1.54 Å that co-exist with VO_4 tetrahedra (1.68 Å). As the population of VO_4 tetrahedra decreases, the tetrahedra contract and further separate, with the $Ca(1)O_6$ trigonal prisms twisting more to meet the increasing projected distances between O(1) and O(2) [Figure 6.10].

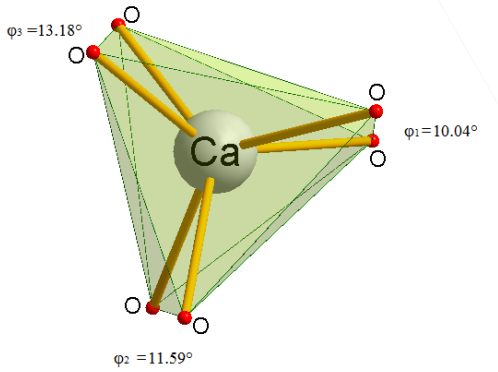

Figure 6.9 Structure drawing of the CaO_6 metaprism with three twist angles as found in *P*-1 triclinic $Ca_{10}(VO_4)_6Cl_2$.

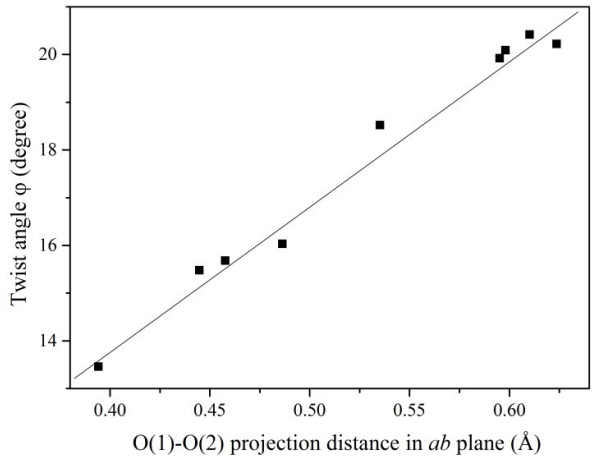

Figure 6.10 The relationship between twist angle and the O(1)-O(2) projection distance in *ab* plane.

6.4 Conclusions

The synthetic vanadate ellestadites $Ca_{10}[(SiO_4)_x(VO_4)_{6-2x}(SO_4)_x]Cl_2$ ($0.19 \leq x \leq 3$) adopt $P6_3/m$ structure, except for the vanadate endmember ($x = 0$) where rotation of the VO_4 tetrahedra lowers the symmetry to *P*-1 to achieve more satisfactory bond-valence sums. A miscibility gap is evident for $0.77 < x < 2.44$, where coexisting ellestadites are observed and there is a loss of $CaCl_2$ during the synthesis. Unit cell contraction with increasing replacement of V (IR (CN IV) = 0.355 Å) by Si (IR (CN IV) = 0.26 Å) and S (IR (CN IV) = 0.12 Å) is observed. The $Ca(1)O_6$ metaprism

twist angle (φ) dilates with the substitution of smaller atoms at the BO_4 sites, and the relationship of φ and the average crystal radius is consistent with published work.

Reference:

[1] J. Trotter; W. H. Barnes, *Can. Mineral*., **1958**, 6, 161-173.

[2] A. von Kutoglu, *N Jahrb Mineral Monatsh,* **1974**, 210-218.

[3] K. Sudarsanan, R. A. Young, A. J. C. Wilson, *Acta. Crystallogr.,* **1977**, B33, 3136-3142.

[4] G. J. Engel, *Naturwissen-schaften,* **1970**, 57, 355.

[5] I. Mayer, E. Fischbein, S. J. Cohen, *Solid State Chem*., **1975**, 14, 307-312.

[6] H. P. Beck, M. Douiheche, R. Haberkorn, H. Kohlmann, *Solid State Sci*., **2006**, 8, 64-70.

[7] C. B. Boechat, J. Eon, A. M. Rossi, C. A. Perez, R. A. Gil, *Phys. Chem. Chem. Phys*., **2000**, 2, 4225-4230.

[8] T. Baikie, P. H. J. Mercier, M. M. Elcombe, J. Y. Kim, Y. L. Page, L. D. Mitchell, T. J. White, P. S. Whitfield, *Acta Cryst.,* **2007**, B63, 251-256.

[9] J. K. Kim, Z. Dong, T. J. White, *J. Am. Ceram. Soc.,* **2005**, 88, 1253-1260.

[10] S. Ogo, A. Onda, K. Yanagisawa, *Applied Catalysis A: General,* **2008**, 348, 129-134.

[11] Z. Dong, T. J. White, *Acta Cryst.,* **2004**, B60, 146-154.

[12] L. Merker, H. Z. Wondratschek, *Anorg. Allg. Chem*., **1959**, 300, 41–50.

[13] D. A. Grisafe, F. A. Hummel, *J. Solid State Chem*., **1970**, 2, 160–166.

[14] Y. Dai, J. M. Hughes, *Can. Mineral.,* **1989**, 27, 189-192.

[15] H. Okudera, *Amer. Mineral.,* **2013**, 98, 1573-1579.

[16] A. Onda, S. Ogo, K. Kajiyoshi, K. Yanagisawa, *Mater. Lett*., **2008**, 62, 1406-1409.

[17] Z. Dong, T. J. White, *Acta Cryst.,* **2004**, B60, 138-145.

[18] Q. He, X. Liu, X. Hu, S. Li, H. Wang, *Phys. Chem. Minerals,* **2011**, 38, 741-752.

[19] E. R. Kreidler, F. A. Hummel, *Am. Mineral*., **1970**, 55, 170-184.

[20] J. C. Stormer, M. L. Pierson, R. C. Tacker, *Amer. Minerl*., **1993**, 78, 641-648.

[21] Bruker, TOPAS Version3, Bruker AXS Inc., Madison, WI, USA, 25005.

[22] V. F. Sears, International Tables for Crystallography, Kluwer Academic Publishers, Dordrecht, 1993, vol. C, p. 383.

[23] S. J. Saint-Jean, S. Hansen, *Solid State Sci*., **2005**, 7, 97-102.

[24] M. Wojdyr, *J. Appl. Crystallogr.*, **2010**, 43, 1126–1128.

[25] T. J. White, Z. Dong, *Acta Cryst.,* **2003**, B59, 1-16.

[26] M. E. Fleet, X. Liu, S. R. Shieh, *Phys. Chem. Mineral* **2010**, 37, 1-9.

[27] J. S. Prener, *J. Solid State Chem*. **1971**, 3, 49-55.

[28] Y. N. Fang, C. Ritter, T. J. White, *Inorg. Chem.,* **2011**, 50, 12641-12650.

[29] Y. N. Fang, C. Ritter, T. J. White, *Dalton Trans*., **2014**, 43, 16031-16043.

[30] K. Sudarsanan, P. E. Mackie, R. A. Young, *Mater. Res. Bull*., **1972**, 7, 1331-1338.

[31] J. Y. Kim, R. R. Fenton, B. A. Hunter, B. J. Kennedy, *Aust. J. Chem*., **2000**, 53, 679-686.

[32] K. A. Wilhelmi, O. Jonsson, *Acta Chem*., **1965**, 19, 177-184.

[33] T. A. Wardojo, S. J. Hwu, *Acta Cryst.,* 1996, C52, 2959-2960.

[34] R. C. Rouse, P. J. Dunn, D. R. Peacor, *Am. Mineral*., **1984**, 89, 920-927.

Chapter 7

Leach Testing and Stability of Ellestadite

The toxicity characteristic leaching procedure (TCLP) is a useful screening method to evaluate the performance of ceramic waste forms. Combined with XRD, SEM-EDS and ATR-FTIR, these investigation show that ellestadites where Si/S is less than 33 at% in $Ca_{10}[(SiO_4)(PO_4)_4(SO_4)]Cl_2$ *and V less than 25 at% in* $Ca_{10}[(SiO_4)_{2.25}(VO_4)_{1.5}(SO_4)_{2.25}]Cl_2$ *at the tetrahedral* BO_4 *site are required to ensure chemical resistant to TCLP extractions. In addition, introducing F to replace Cl in* $Ca_{10}[(SiO_4)_3(SO_4)_3][Cl_{2-x}F_x]$ *improves the durability of ellestadite. From these results, waste loading guidelines were proposed to tailor ellestadite waste forms for the immobilization of MSW fly ash wastes.*

7.1 Leach Testing

Leach testing is a primary screening tool for assessing the performance of ceramic waste forms. A widely used standard test appropriate for MSW fly ash waste forms is the toxicity characteristic leach procedure (TCLP) [1, 2]. However, TCLP results do not convey information concerning the dissolution mechanism, and this work includes microstructural studies to identify alteration products.

7.1.1 The Toxicity Characteristic Leaching Procedure

The toxicity characteristic leaching procedure (TCLP), as described in the US EPA protocol SW 846 [3], was used to evaluate ellestadite leachability. Individual sintered pellets of different composition were placed in glass bottles with a leaching solution of acetic acid (pH 2.88) prepared by diluting 5.7 mL of glacial acetic acid with deionized water to a volume of 1 L. An initial solid-to-extraction solution weight ratio of 1:20 was used, with all tests carried out at ambient temperature (25 ± 5 °C) and pressure, in sealed containers to minimize absorption of atmospheric oxygen and carbon dioxide. The containers were rotated at 30 rpm for leach periods of 18 h and 72 h. The pH of the leaching solution became progressively more basic through the experiment as calcium was released, and no attempt was made to maintain a constant pH. After the leaching process, the leachants were filtered through 0.45 μm pore diameter membrane filters, and the pH was determined immediately after collection. The samples were then protected from light and refrigerated at 4 °C (±2 °C) prior to analysis. Element concentrations in the leachates were determined with a Perkin-Elmer 3000 inductively coupled plasma optical emission spectrometer (ICP-OES). Quantitation was completed using manufacturer software and calibrated against nitric acid standard solutions. Four different calibration standard concentrations were used to cover the recommended linear range. Standards were prepared by serial dilution from 1000 ppm certified atomic absorption stock solutions. A set of three replicates was performed in each case, the precision of these measurements always being better than 4%.

7.1.2 Observation of Alteration and Corrosion

To ascertain if metal dissolution was congruent from the lattice, and also to identify precipitates, solid residue surfaces were investigated. After leaching for 18 h or 72 h, the pellets were removed from the leach vessels, washed with ethanol, and then oven-dried (100°C), followed by surface characterization with powder X-ray diffraction (XRD), attenuated total reflection Fourier transform infrared (ATR-FTIR), secondary electron microscopy (SEI) and energy-dispersive X-ray spectroscopy (EDS).

7.2 Results and Discussion

7.2.1 Leaching Behavior of $Ca_{10}[(SiO_4)_x(PO_4)_{6-2x}(SO_4)_x]Cl_2$

TCLP test data, including weight loss, pH changes and Ca leachability of $Ca_{10}[(SiO_4)_x(PO_4)_{6-2x}(SO_4)_x]Cl_2$ examined durability as a function of (Si+S):P content (Table 7.1 and Figure 7.1). The dissolution of ellestadite is congruent, followed by precipitation of insoluble salts. Based on the XRD analysis (Figure 7.2) of the leached materials, the primary dissolution and precipitation reactions are:

$$Ca_{10}(SiO_4)_x(PO_4)_{6-2x}(SO_4)_xCl_2 + 20H^+ \rightarrow$$
$$10Ca^{2+} + xH_2SO_4 + xH_4SiO_4 + (6-2x)H_3PO_4 + 2HCl \quad (7.1)$$

$$Ca^{2+} + H_4SiO_4 \rightarrow CaSiO_3\ (s) + H_2O \quad (7.2)$$

$$CaSiO_3 + SO_4^{2-} + 2H^+ + 2H_2O \rightarrow CaSO_4{\cdot}2H_2O\ (s) + H_2SiO_3 \quad (7.3)$$

$$Ca^{2+} + SO_4^{2-} + H_2O \rightarrow CaSO_4{\cdot}2H_2O\ (s) \quad (7.4)$$

$$CaSiO_3 + 2CH_3CO_2H \rightarrow Ca^{2+} + 2CH_3CO_2^- + SiO_2\ (s) + H_2O \quad (7.5)$$

Table 7.1 Leachability* (concentration (M) and weight loss) of $Ca_{10}[(SiO_4)_x(PO_4)_{6-2x}(SO_4)_x]Cl_2$

x	pH**	Weight loss (%)	Ca (10^{-2}M)	Leachability in %
3	6.51	10.38	6.21	12.8
2.5	5.45	8.29	5.12	10.5
2	5.13	7.13	4.59	9.5
1.5	4.78	7.11	4.19	8.6
1	4.89	5.17	3.87	8.0
0.5	4.43	6.89	2.75	5.7
0	3.92	--	0.76	1.5

* Leachability = (weigh of Ca in leaching solution)/(weight of Ca in the pellet before leach test).

** The initial pH is 2.88 (glacial acid with deionized water)

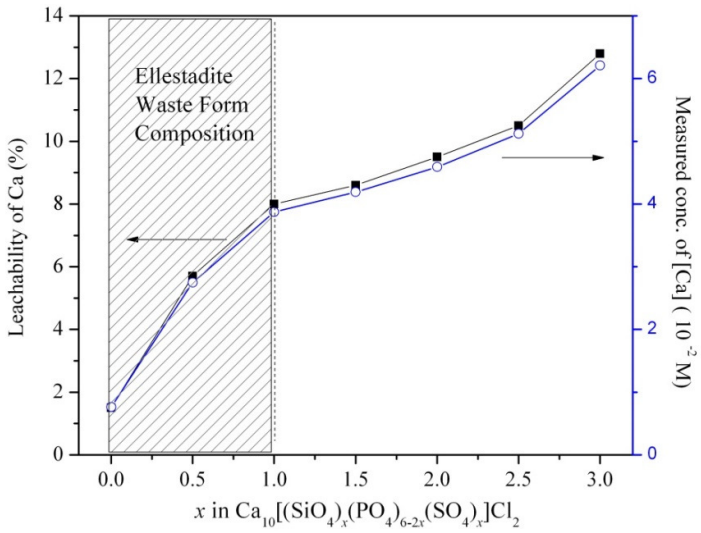

Figure 7.1 Leachability of ellestadite in acetic acid and concentration of Ca in the leaching solution. The preferred compositional range for ellestadite waste forms is shaded.

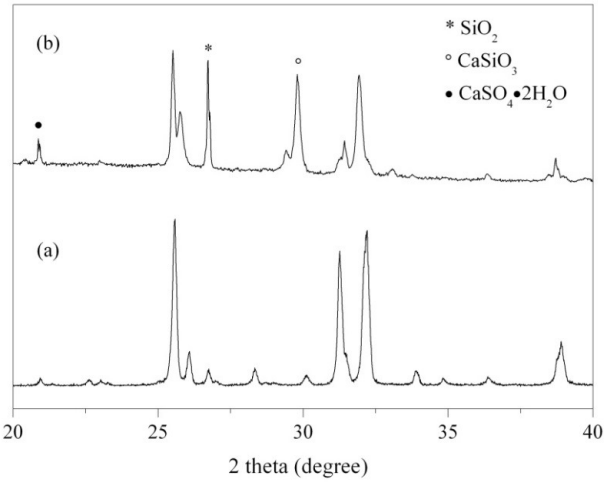

Figure 7.2 Representative X-ray diffraction profiles of $Ca_{10}[(SiO_4)_3(SO_4)_3]Cl_2$ (a) before and (b) after leach testing.

With increasing substitution of Si/S for phosphorus, there is greater weight loss and the final pH is less acidic. The increase in pH may be attributed to basic SiO_4 ions that bind H^+ and release more free OH^- ions into solution. Dissolution becomes progressively evident in passing from the pure chlorapatite ($Ca_{10}(PO_4)_6Cl_2$: [Ca] = 0.76×10^{-2} M) endmember towards the pure ellestadite endmember ($Ca_{10}[(SiO_4)_3(SO_4)_3]Cl_2$: [Ca] = 6.21×10^{-2} M); leachability increases with the increasing of Si/S content. By comparing the secondary electron images (SEI) before and after leaching, it is seen the size and shape of $Ca_{10}(PO_4)_6Cl_2$ crystals (Figure 7.4) remain intact, while $Ca_{10}[(SiO_4)_2(PO_4)_2(SO_4)_2]Cl_2$ crystals (Figure 7.5) become smaller. It is evident that ellestadite waste forms should be tailored to be phosphate-rich such that no more than 1/3 of the tetrahedral *B*-sites contain Si/S (Figure 7.1).

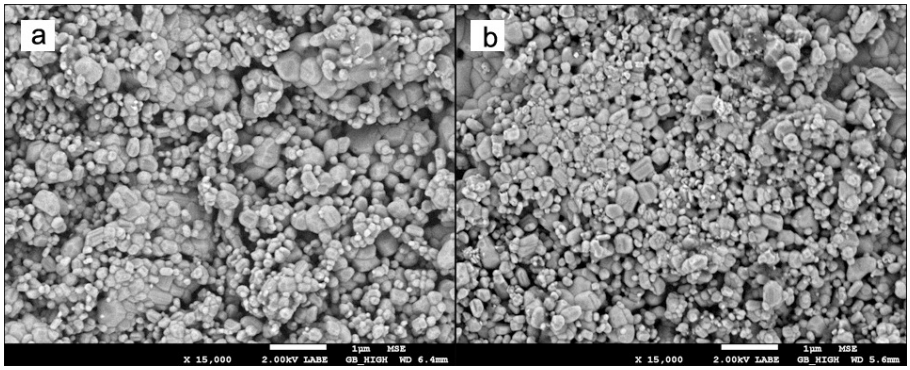

Figure 7.4 SEI images of $Ca_{10}(PO_4)_6Cl_2$ pellets (a) before and (b) after leach testing for 72 hours.

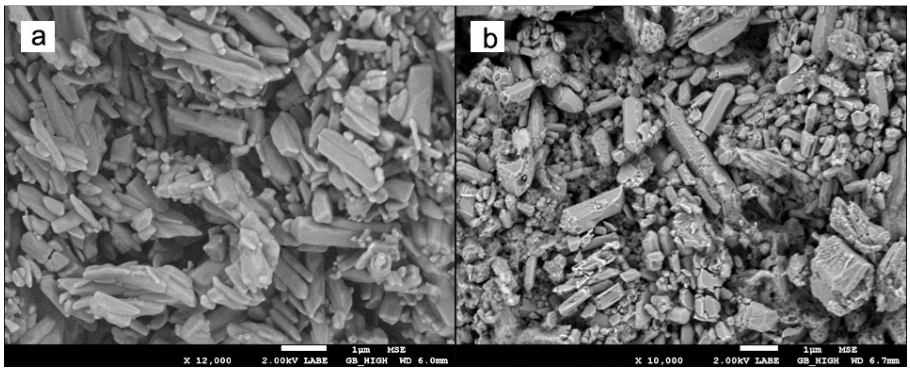

Figure 7.5 SEI images of $Ca_{10}[(SiO_4)_2(PO_4)_2(SO_4)_2]Cl_2$ pellets (a) before and (b) after leach testing for 72 hours.

7.2.2 Leaching Behavior of $Ca_{10}[(SiO_4)_3(SO_4)_3][Cl_{2-x}F_x]$

TCLP testing of $Ca_{10}[(SiO_4)_3(SO_4)_3][Cl_{2-x}F_x]$ as a function of F/Cl content found the concentrations of F^-, Si and SO_4^{2-} nearly invariant with composition, while those of Ca and Cl^- decreased gradually as chlorine was replaced by fluorine, except for the pure chlorellestadite (Figure 7.6). The concentration of F^- in the leachate was constant ($[F^-] \approx 1.0 \times 10^{-4}$ M) with leach period, while Cl^- increased (1.8 to 2.7×10^{-2} M for $Ca_{10}[(SiO_4)_3(SO_4)_3][Cl_{1.6}F_{0.4}]$) with leaching time. These results are consistent with corrosion of ellestadite followed by precipitation of CaF_2 [4] for all ceramic compositions. The mole ratios of Ca/(Si+S) in solution range from 6.31-7.79 and are evidentially much higher than the stoichiometric ratio of 1.67 found in ellestadite, $Ca_{10}[(SiO_4)_3(SO_4)_3][Cl_{2-x}F_x]$. This suggests that either Ca was preferentially released compared to Si and S from the structure, or re-precipitation of silicates and sulphates was significant.

XRD patterns from the surface of the pellets after leaching confirmed the presence of precipitates (Figure 7.7), and specifically the crystallization of CaF_2 during ellestadite dissolution. In addition, $CaSO_4$, SiO_2 and $CaSO_4 \cdot 2H_2O$, were found on the pellets surface after 18 h leaching. CaF_2, $CaSiO_3$, and amorphous content increased after the 72 h test, while $CaSO_4$ decreased and $CaSO_4 \cdot 2H_2O$ disappeared. In addition, cuspidine, $Ca_4(Si_2O_7)F_2$, may form on the surface. Figure 7.8 shows the XRD results of $Ca_{10}[(SiO_4)_3(SO_4)_3][Cl_{0.4}F_{1.6}]$ pellets before and after the 18 h and 72 h tests. The increasing CaF_2 surface covering of pellets accounts for the removal of Ca from solution with the growing substitution of chlorine by fluorine, as CaF_2 is sparingly soluble compared to $CaCl_2$.

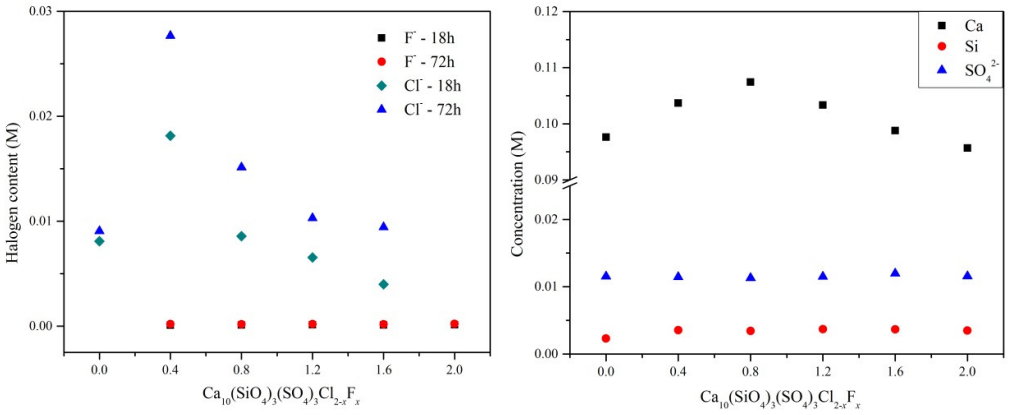

Figure 7.6 Ellestadite leaching as a function of composition (x in $Ca_{10}[(SiO_4)_3(SO_4)_3][Cl_{2-x}F_x]$).

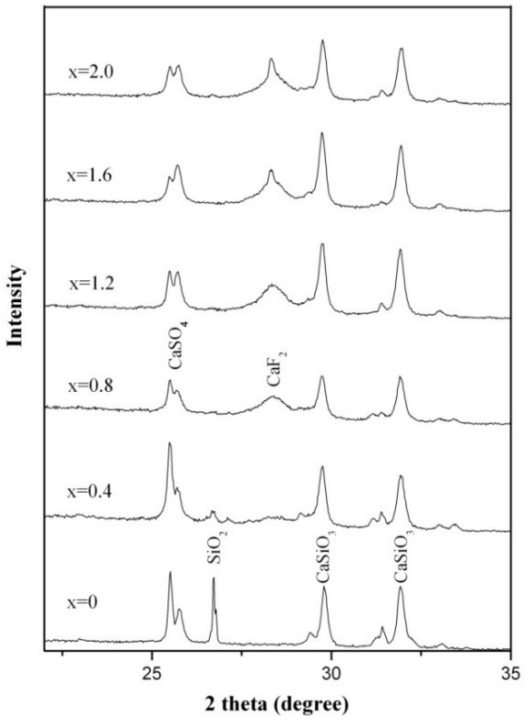

Figure 7.7 XRD patterns of $Ca_{10}[(SiO_4)_3(SO_4)_3][Cl_{2-x}F_x]$ ellestadites after immersion in pH 2.88 acetic acid for 72 hours.

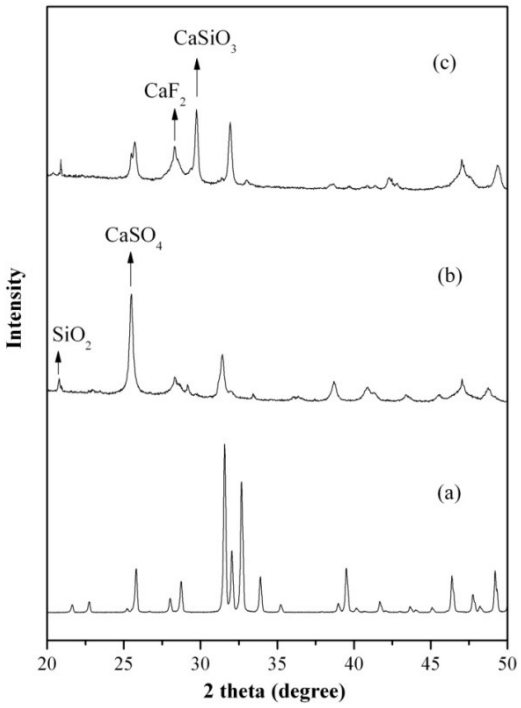

Figure 7.8 XRD patterns of $Ca_{10}[(SiO_4)_3(SO_4)_3][Cl_{0.4}F_{1.6}]$ ellestadite pellets before (a) and after pH 2.88 acetic acid leach tests for 18 h (b), and 72 h (c).

Attenuated total reflectance (ATR) FTIR analyzes of the ellestadite pellet surfaces were collected from the $Ca_{10}[(SiO_4)_3(SO_4)_3][Cl_{0.4}F_{1.6}]$ material before (Figure 7.9a) and after leaching (Figure 7.9b. 18 h and 7.9c. 72 h). The absorption band from the SiO_4 group is located at 1000-800 cm^{-1}, while the bands from 1200-1100 cm^{-1} arise from the SO_4 group. After 18 h leaching, the SiO_4 band disappears and that of SO_4 shifts a little to lower wavenumber between 1200 and 1050 cm^{-1} [5]. Furthermore, after longer treatment (72 h), the band around 1100 cm^{-1} became broader and its intensity decreased. These observations are consistent with the XRD results. After 18 h treatment, the pellet surface was covered by $CaSO_4$, which causes a band shift due to the different chemical environments of SO_4 in ellestadite and $CaSO_4$. After prolonged leaching, the SO_4 absorption band diminishes as $CaSO_4$ surface content decreased. This band broadening from 1250-1000 cm^{-1} after 72 h leaching arises from the convolution of S-O and Si-O stretching modes that was fitted to a Lorentz-Gauss function (Figure 7.9). The features at 1120 and 1150 cm^{-1} are stretching vibration modes ν_3 for the S-O bond, while 1022 cm^{-1} is attributed to ν_3 of the Si-O bonds [6]. The peak at 1084 cm^{-1} is a mixture of S-O and Si-O stretching vibrations [7-9].

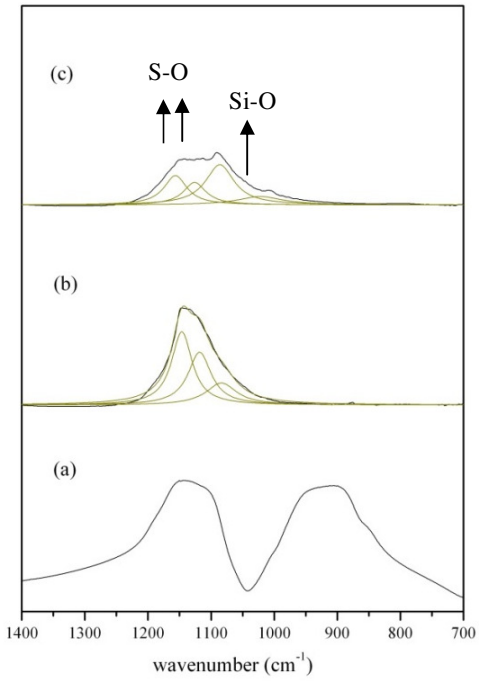

Figure 7.9 FTIR-ATR spectra of $Ca_{10}[(SiO_4)_3(SO_4)_3][Cl_{0.4}F_{1.6}]$ pellets before (a) and after leach testing for 18 h (b), and 72 h (c).

The microstructural and chemical changes after leaching were investigated by SEM-EDS. For the pristine material, facetted ellestadite crystals were observed, but after 18 h leaching $CaSO_4$ rods covered the surface (Figure 7.10), with the XRD pattern recording highly-crystalline $CaSO_4$ (Figure 7.8), and ATR-FTIR only detecting the absorption band of S-O bond (Figure 7.9). A coarse layer formed after 72 h leaching (Figure 7.10c) consists of CaF_2 crystal precipitates that agglomerate to form a surface covering (Figure 7.11); both the microscopy, and full-width of the XRD peaks, suggest the CaF_2 crystals are small (< 50 nm on average).

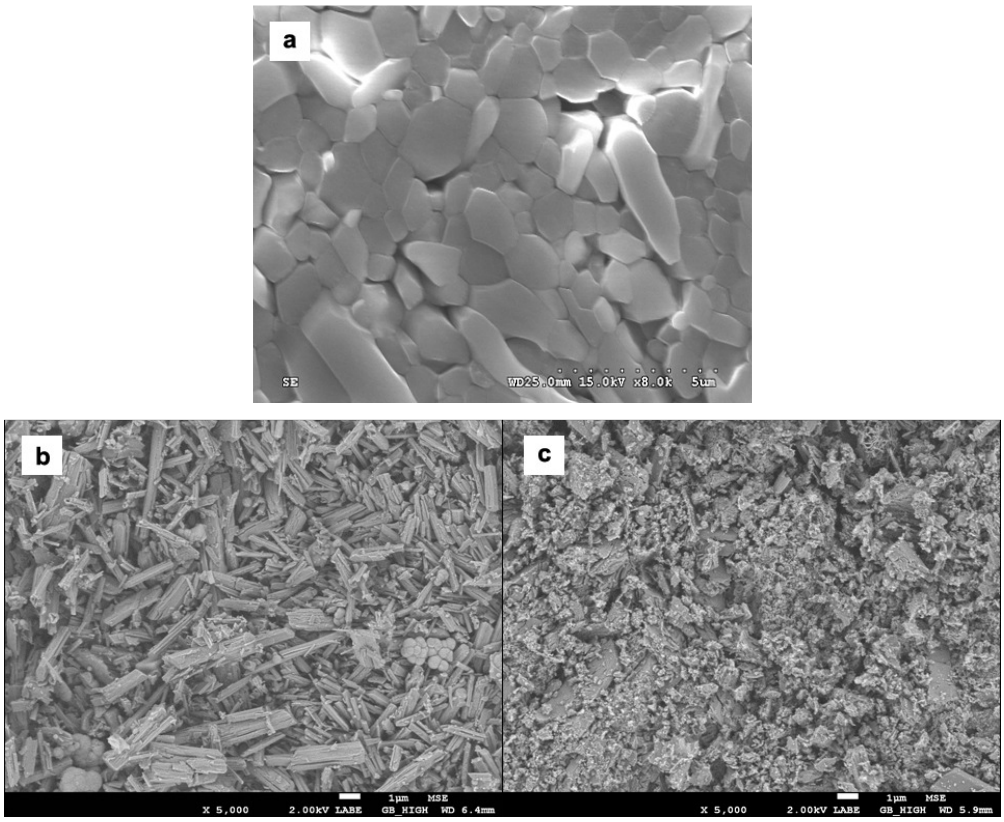

Figure 7.10 SEI micrographs of $Ca_{10}[(SiO_4)_3(SO_4)_3][Cl_{0.4}F_{1.6}]$ pellets surface before (a) and after leach testing for 18 h (b) and 72 h (c).

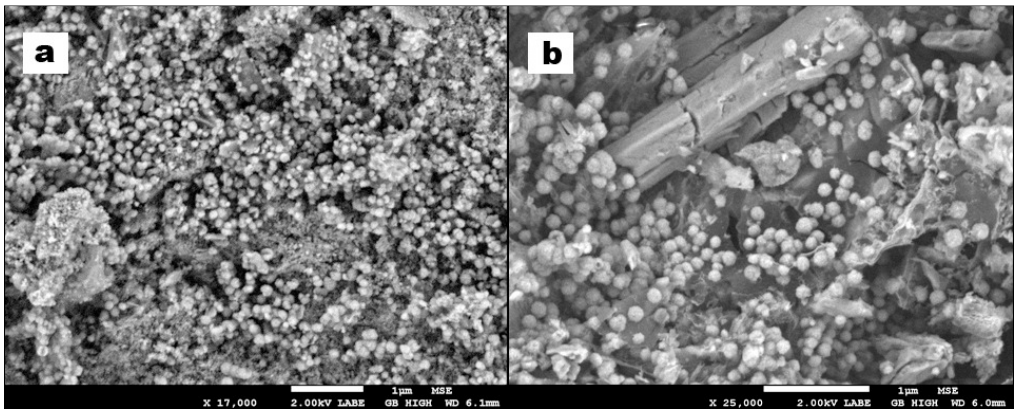

Figure 7.11 SEI micrographs of surface of ellestadite, (a) $Ca_{10}[(SiO_4)_3(SO_4)_3][Cl_{1.2}F_{0.8}]$ and (b) $Ca_{10}[(SiO_4)_3(SO_4)_3]F_2$ pellets after leach testing for 72 h.

To better clarify the leaching behavior and solubility of ellestadite, pellet cross sections were analyzed by SEM-EDS. Figure 7.13 shows the SEI and EDS mapping analysis for the $Ca_{10}[(SiO_4)_3(SO_4)_3][Cl_{0.4}F_{1.6}]$ pellet after 72 h leach testing. EDS demonstrates that a layer of $CaSO_4$ was deposited outermost to a depth of about 85 µm (Figure 7.12). As expected, the distribution of calcium tracks that of fluorine, confirming calcium is removed from solution by fluorine. A zone deficient in calcium and sulfate, but abundant in silicon and oxygen, was observed to a depth of around 100µm confirming the formation of SiO_2 and possibly calcium silicates. These corrosion products are separated from the unaltered ellestadite by a sharp boundary, where Cl is retained (Figure 6.10).

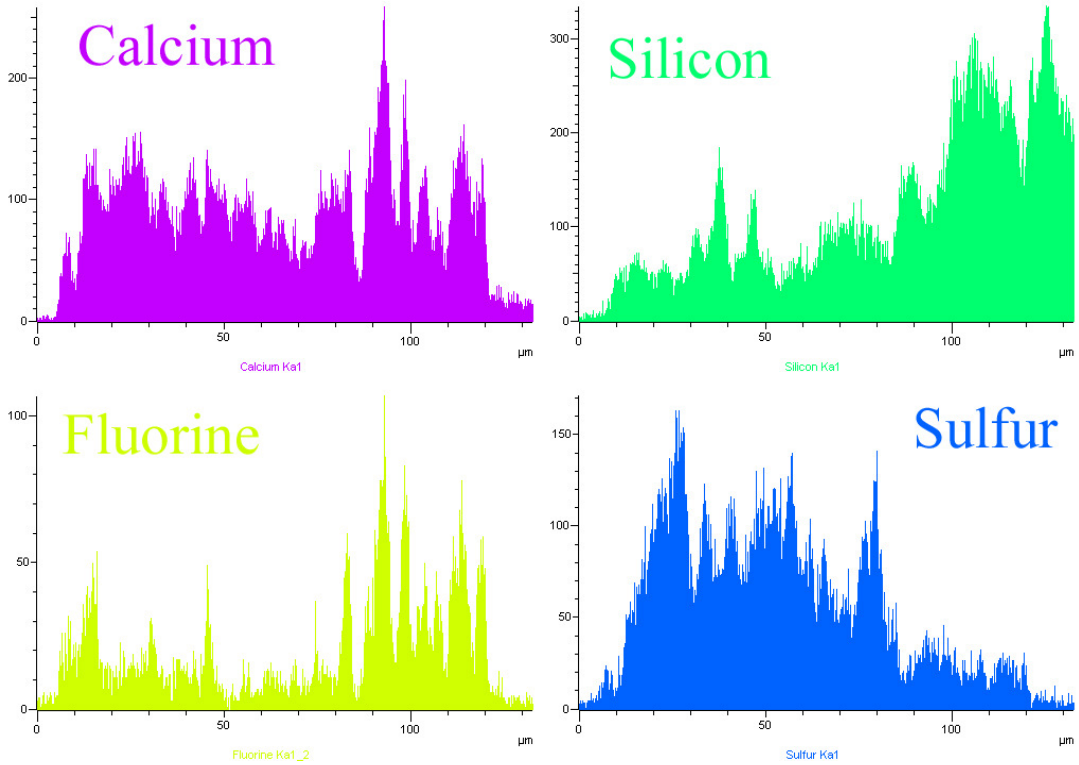

Figure 7.12 EDS element line scans (Ca, Si, F and S) of the leached ellestadite $Ca_{10}[(SiO_4)_3(SO_4)_3][Cl_{0.4}F_{1.6}]$ pellet cross section.

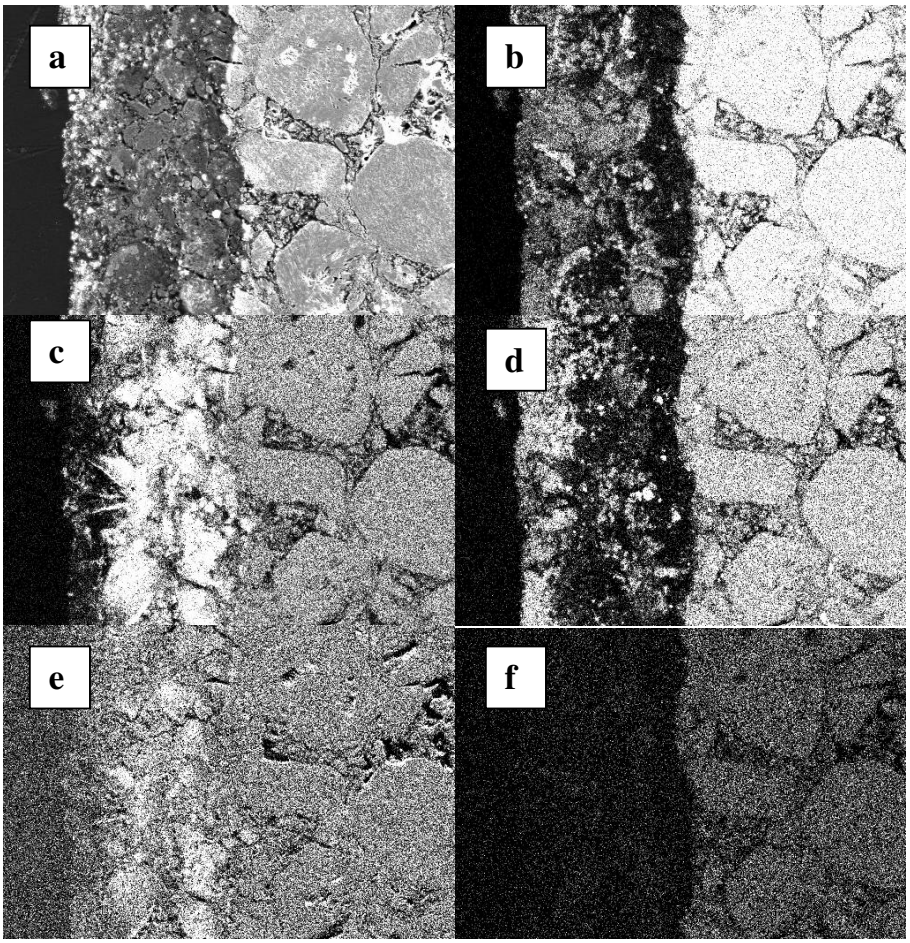

Figure 7.13 SE cross section image (a) of $Ca_{10}[(SiO_4)_3(SO_4)_3][Cl_{0.4}F_{1.6}]$ after TCLP testing for 72 h together with elemental maps for (b) Ca, (c) Si, (d) S, (e) O, and (f) Cl.

Based on the analysis above, the primary dissolution and precipitation processes for $Ca_{10}[(SiO_4)_3(SO_4)_3][(Cl, F)_2]$ are:

(1) At initial pH = 2.88, H^+ diffuses from the solution into the surface layers;

(2) Chemical transformation proceeds by Ca dissolution as;

$$Ca_{10}(SiO_4)_3(SO_4)_3(Cl, F)_2 + H^+ \rightarrow$$
$$10\ Ca^{2+} + 3\ H_2SO_4 + 3\ H_4SiO_4 + 2\ (HF + HCl) \qquad (7.6)$$

(3) H_4SiO_4 is stable at low pH, but as the pH increases SiO_2 precipitates;

$$H_4SiO_4 \rightarrow SiO_2 + 2\ H_2O \qquad (7.7)$$

(4) Ca^{2+}, F^-, Cl^- and SO_4^{2-} solubilize from the surface;

(5) Re-precipitation from solution takes place by the reactions;

$$Ca^{2+} + 2\ F^- \rightarrow CaF_2\ (s) \qquad (7.8)$$

$$Ca^{2+} + H_4SiO_4 \rightarrow CaSiO_3\ (s) + H_2O \qquad (7.9)$$

$$Ca^{2+} + SO_4^{2-} + 2\ H_2O \rightarrow CaSO_4 \cdot 2H_2O\ (s) \quad (7.10)$$

$$CaSiO_3 + SO_4^{2-} + 2H^+ \rightarrow CaSO_4\ (s) + H_2SiO_3 \quad (7.11)$$

7.2.3 Leaching Behavior of $Ca_{10}[(SiO_4)_x(VO_4)_{6-2x}(SO_4)_x]Cl_2$

The surface morphology of a $Ca_{10}[(SiO_4)(VO_4)_4(SO_4)]Cl_2$ pellet is shown in Figure 7.14. Before leaching, euhedral ellestadite crystals were evident, but after 72 hours these were obscured by coarse precipitates, with BSI showing immersion preferentially etched grain boundaries to make them more prominent. Analysis of TCLP leachates found the concentrations of Cl^-, Si and Ca were essentially constant as a function of ellestadite composition, while dissolution of V rises with increasing vanadium content in the waste form (Figure 7.15). There is no significant change of VO_4^{3-} concentrations in the solute after 18 and 72 hours indicating the leaching process equilibrates rapidly. XRD of the leached surfaces found for V rich compositions found silicocarnotite $Ca_5(SiO_4)_2(SO_4)$ and $Ca_3(VO_4)_2$ accounted for more than 50 wt% of the surface precipitates. Ellestadite durability increases in tandem with (Si/S) content of ellestadite increases durability increases although bassanite ($CaSO_4 \cdot 0.5H_2O$) and parawollastonite ($CaSiO_3$) were found. The leaching process for the vanadate ellestadite series is complex, with the final surface composition shown in Figure 7.16.

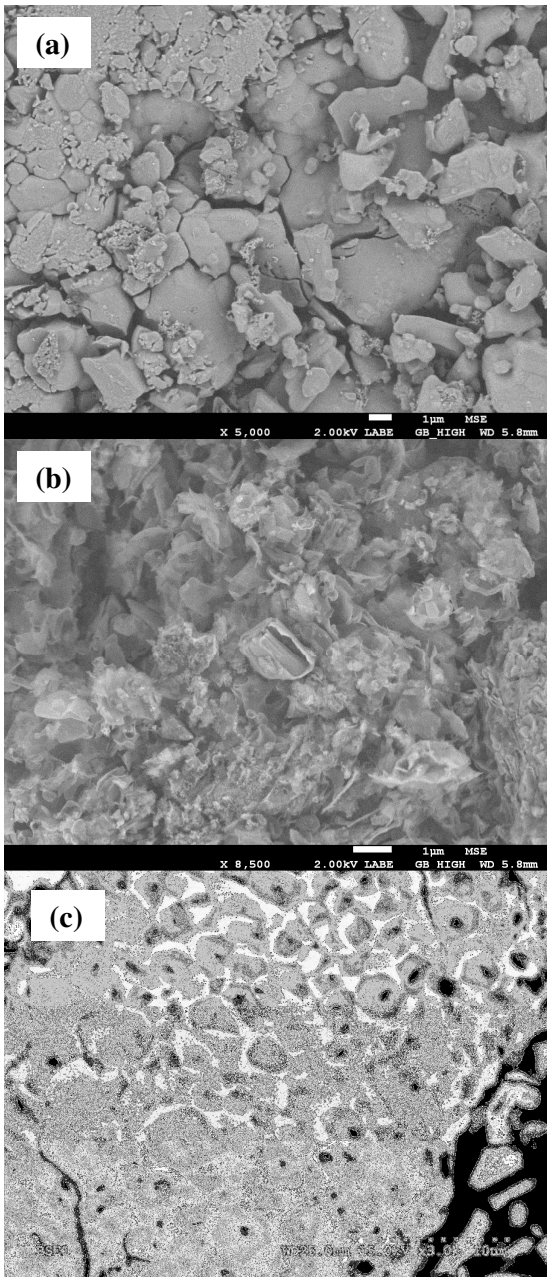

Figure 7.14 SEI (a, b) and BSI (c) micrographs of the surface of $Ca_{10}[(SiO_4)(VO_4)_4(SO_4)]Cl_2$ (a) before and (b, c) after 72 hours leaching.

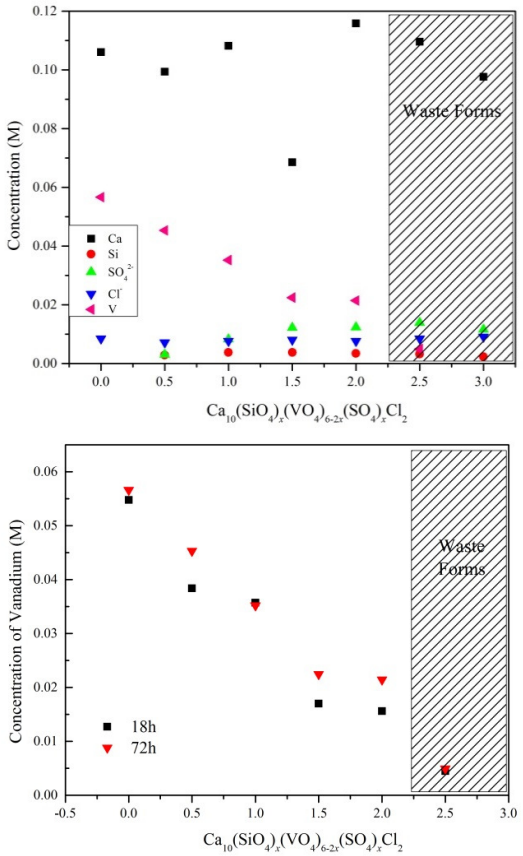

Figure 7.15 Leach liquor species concentration for ellestadite (a) after 72 h TCLP treatment, and (b) comparison for vanadium after 18h and 72h extraction. The preferred compositional range for vanadium-bearing ellestadite waste forms is shaded.

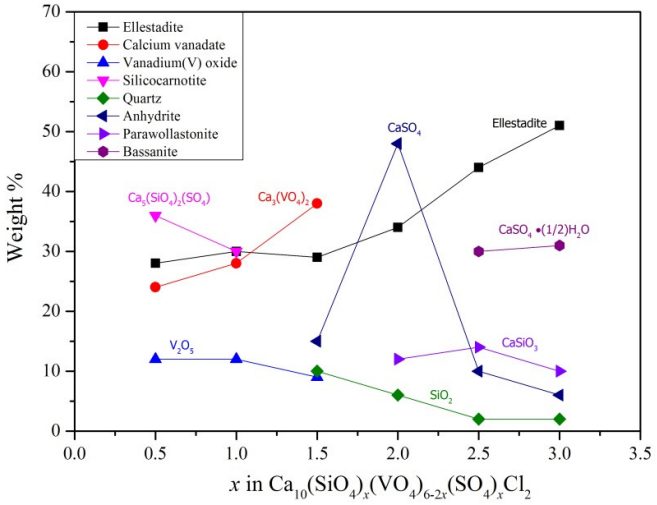

Figure 7.16 Surface compositions of the pellets after 72 hours TCLP test. The wt% was calculated by XRD analysis.

7.3 Dissolution Mechanism and Conclusions

The systematics of ellestadite solubility can be examined in two ways. The first described by Gupta et al. [10], considers the difference in the Gibbs free energy for hydration (ΔG_{hy}) and the lattice ($\Delta G_{lattice}$) to derive the Gibbs free energy of dissolution (ΔG_{soln}) such that $\Delta G_{soln} = \Sigma\Delta G_{hy} - \Delta G_{lattice}$. As the lattice expands, $\Delta G_{lattice}$ also becomes larger and solubility increases. This is particularly important in apatites where there is large different in the size of the anionic tetrahedra; for example, vanadate VO_4^{3-} apatites (IR V^{5+} = 0.35 Å) have an expanded lattice compared to phosphate PO_4^{3-} apatites (IR P^{5+} = 0.15 Å) and consequently are more soluble [10]. For $Ca_{10}[(SiO_4)_x(VO_4)_{6-2x}(SO_4)_x]Cl_2$, as the vanadium content increases the unit cell dilates, $\Delta G_{lattice}$ becomes larger, and ellestadites are more soluble.

However, in the case of $Ca_{10}[(SiO_4)_x(PO_4)_{6-2x}(SO_4)_x]Cl_2$, this mechanism is not dominant as the lattice parameters change modestly with composition (see Table 4.2) because the $Si^{4+} + S^{6+}$ average ionic radii is almost equal to that of P^{5+}. For these compounds, Leshkivich and Monroe [11] suggest that smaller free energies of formation correspond to higher solubility. If ΔG_f is compared for apatite $Ca_{10}(PO_4)_6F_2$ (-6755 kJ mol^{-1}) and ellestadite $Ca_{10}[(SiO_4)_3(SO_4)_3]F_2$ (-5760 kJ mol^{-1}) this explanation is seen to be consistent with the higher solubility of the latter. In addition, the decomposition temperature of $Ca_{10}(PO_4)_6Cl_2$ (1300°C) exceeds that of $Ca_{10}[(SiO_4)_3(SO_4)_3]Cl_2$ (1000°C) as also expected with a higher ΔG_f.

For $Ca_{10}[(SiO_4)_3(SO_4)_3][Cl_{2-x}F_x]$, the lattice contracts when F replaces Cl in the tunnel, $Ca_{10}(SiO_4)_3(SO_4)_3F_2$ is least soluble with a smaller $\Delta G_{lattice}$. This qualitative assessment is consistent with the ΔG_{soln} calculated by Flora et al. [12], who found $Ca_{10}(PO_4)_6Cl_2$ (507 kJ mol^{-1}) is more soluble than $Ca_{10}(PO_4)_6F_2$ (596 kJ mol^{-1}). From a crystallochemical considerations, the F ion resides in a triangular plane of three Ca atoms (z = ¼) in the tunnel to create a very stable molecular unit. The Cl ion, on the other hand, is out of this plane, and when combined with tendency for Cl substoichiometry provides less structural stability.

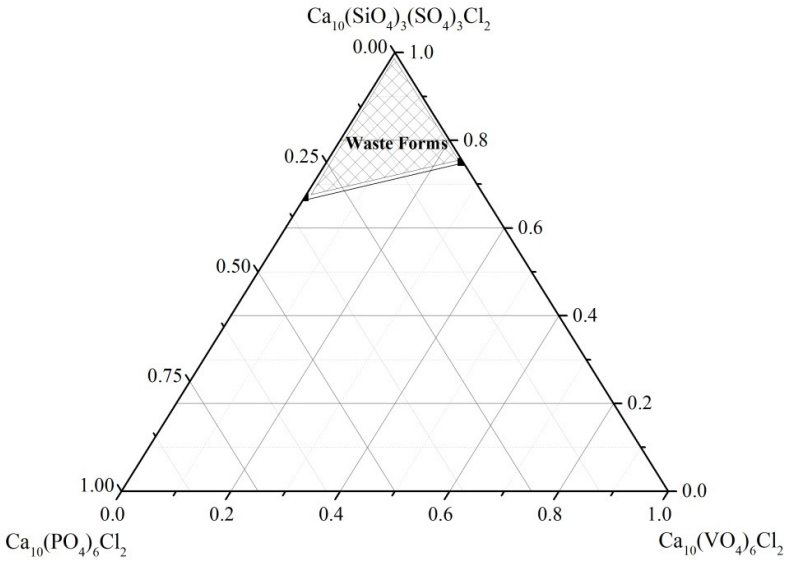

Figure 7.17 Preferred composition range for ellestadite waste forms that can accommodate Si+S rich MSW fly ash.

To summarize, this study found increasing dissolution of chlorapatite as Si/S progressively replaces P, with a significant change in solubility, and therefore ΔG_f, especially for $x \geq 1$ in $Ca_{10}[(SiO_4)_x(PO_4)_{6-2x}(SO_4)_x]Cl_2$ (Figure 7.1). The incorporation of vanadium (also a proxy for Cr, As) will lead to higher releases of vanadium when the loading exceeds 25 at% V in the structure (Figure 7.15). The replacement of Cl by F increases durability; the CaF_2 formed in the leaching process may prevent further dissolution of ellestadite. Therefore, fluor-chlorellestadites where Si/S content is less than 33 at% and V less than 25 at% at *B* sites (Figure 7.17) will prove most chemically resistant to TCLP extractions, and these waste loading guidelines can be used to tailor ellestadite waste forms for the immobilization of silicon, sulphur and vanadium rich wastes. The following chapter describes the procedure for chemically conditioning MSW fly ashes as ellestadite immobilization matrices.

References:

[1] J. R. Conner, *Chemical Fixation and Solidification Hazardous Wastes*, Van Nostrand Reinhold, New York, 1990, 638-651.

[2] T. A. Ioannidis, A. I. Zouboulis, *J. Hazardous Mater.*, **2003**, B97, 173-191.

[3] The EPA publication SW-846: *Test Methods for Evaluating Solid Waste,*

Physical/Chemical Methods. United States Environmental Protection Agency; Office of Solid Waste; Economic, Methods, and Risk Analysis Division. 1996.

[4] Å. Bengtsson, A. Shchukarev, P. Persson, S. Sjöberg, *Langmuir*, **2009**, 25, 2355-2362.

[5] P. Roonasi, A. Holmgren, *J. Colloid Interface Sci.*, **2009**, 333, 27-32.

[6] A.V. Valkenburg, G. F. Rynders, *Am. Mineral*, **1958**, 43, 1195-1202.

[7] P. Ptáček, M. Nosková, J. Brandštertr, F. Šoukal, T. Opravil, *Thermochimi. Acta*., **2010**, 498, 54-60.

[8] P. Siriphannon, Y. Kameshima, A. Yasumori, K. Okada, S. Hayashi, *J. Eur. Ceram. Soc*., **2002**, 22, 511-520.

[9] S. Gunasekaran, G. Anbalagan, *Spectrochimi. Acta*., **2008**, 69A, 1246-1251.

[10] S. K. Gupta, P. V. R. Rao, G. George, T. S. B. Narasaraju, *J. Mater. Sci*., **1987**, 22, 1286-1290.

[11] K. S. Leshkivich, E. A. Monroe, *J. Mater. Sci*., **1993**, 28, 9-14.

[12] N. J. Flora, C. H. Yoder, *Inorg. Chem*. **2004**, 43, 2340-2345.

Chapter 8

Waste Form Design and Future Work

This thesis focused on the design, synthesis and characterization of eco-ceramics for the transformation of municipal incinerator waste fly ash into recyclable secondary products or for volume-efficient disposal. In particular, the crystal chemistry of three key ellestadite solid solution series were studied in depth through a combination of diffraction, microscopic and spectroscopic techniques. These results are consolidated and translated to a procedure for tailoring an ellestadite-based ceramic for the immobilization of a real fly ash composition. The potential for waste blending that generate cost savings during disposal are discussed. Further validation of ellestadite properties and performance is required before large-scale demonstration, and to this end reconnaissance studies have shown the successful synthesis of cadmium and vanadium containing apatite. Future work would include solubility modelling to investigate long term durability and the synthesis of ellestadites bearing a selection of MSW fly ashes over a range of waste loadings as the first stage of proof-of-concept for this technology.

8.1 Crystallochemical Flexibility of Ellestadite

Ellestadite has the ideal formula $Ca_{10}[(SiO_4)_3(SO_4)_3][(F, Cl, OH)_2]$ and belongs to the apatite mineral family. Taking into account compliance with $P6_3/m$ hexagonal symmetry, the complete formula of chlorellestadite is $[Ca(1)_4Ca(2)_6][(Si/S)_6O(1)O(2)O(3)_2]Cl_2$. Because apatites are chemically diverse and topological flexibility is an inherent characteristic of its tunnel structure, the prototype ellestadite can be crystallochemically modified to incorporate numerous toxic metals that report to fly ash, including lead, cadmium and zinc [1]. While the overall compositional variation accompanying the substitutions is simple, the crystallographic changes that permit these replacements are complex, and have a direct and measurable effect on the durability of synthetic mineral waste forms.

The present investigations represent the most comprehensive systematic crystallochemical analysis to date of ellestadites as potential fly ash stabilization phases. The reference solid solution series $Ca_{10}[(SiO_4)_x(PO_4)_{6-2x}(SO_4)_x]Cl_2$ ($0 \leq x \leq 3$) was synthesized and examined by powder X-ray and neutron diffraction to establish baseline crystallographic data. These synthetic materials, unlike mineral specimens that are well equilibrated, show no Si/P/S ordering and conform to $P6_3/m$ symmetry. In detail, there are calcium and chlorine deficiencies in the Si/S rich compositions ($3 \leq x \leq 2$) due to the evaporation of $CaCl_2$ during the synthesis. For $x \leq 1.5$ where the Ca(1) and Ca(2) and Cl sites are fully occupied, a second low occupancy Cl site is present to reduce steric repulsion within the O(3) triangles. Leach testing found durability decreased as Si/S progressively replaced P, with a significant change in solubility, and therefore free energy of formation (ΔG_f), especially for $x \geq 1$ in $Ca_{10}[(SiO_4)_x(PO_4)_{6-2x}(SO_4)_x]Cl_2$. Additionally, Ca and Cl non-stoichiometry also leads to Si/S rich compositions being more soluble, at least under the standard Toxicity Characteristic Leaching Procedure (TCLP) test conditions.

As MSW ash often contains halide mixtures the fluor-chlorellestadite solid solution series $Ca_{10}(SiO_4)_3(SO_4)_3Cl_{2-x}F_x$ was prepared, with all compositions accommodated in $P6_3/m$ symmetry where F^- is located at the 2*a* (0, 0, 1/4) position, while Cl^- is displaced out of the 6*h* Ca(2) triangle plane and occupies 4*e* (0, 0, *z*) split positions with *z* ranging from 0.336(3) to 0.4315(3). Increasing fluorine content, leads to a

progressive shift of Cl^- toward the center of the Ca(2) triangle. Si/S randomly occupy the 6*h* tetrahedral site. Ellestadites rich in Cl ($x \leq 1.2$) show an overall deficiency in halogens (<2 atom per formula unit), particularly Cl as a result of $CaCl_2$ volatilization, with charge balance achieved by the creation of Ca vacancies ($Ca^{2+} + 2Cl^- \rightarrow \square Ca + 2\square Cl$) leading to the formula $Ca_{10-y}[(SiO_4)_3(SO_4)_3][Cl_{2-x-2y}F_x]$. For F-rich compositions vacancies are found at Ca(2), while for Cl-rich ellestadites, the Ca(1) position is stoichiometrically deficient. Moreover, the loss of $CaCl_2$ which leads to tunnel anion vacancies promotes intertunnel positional disorder that prevents the formation of a $P2_1/b$ monoclinic dimorph, analogous to that reported for $Ca_{10}(PO_4)_6Cl_2$. Leach testing shows that the introduction of F^- in place of Cl^- increases stability, with CaF_2 re-precipitation also attenuating further dissolution of ellestadite. It is concluded, the different crystallographic environments for Cl^- and F^- in the tunnel act to reduce halide mobility and significantly modify dissolution behavior.

The synthetic vanadate ellestadites $Ca_{10}[(SiO_4)_x(VO_4)_{6-2x}(SO_4)_x]Cl_2$ ($0.19 \leq x \leq 3$) were used to mimic V, Cr, and As stabilization. All compositions adopt a $P6_3/m$ structure, except for the vanadate endmember ($x = 0$) where the rotation of VO_4 tetrahedra lowers the symmetry to triclinic P-1 to achieve more satisfactory bond-valence sums. Under the synthesis conditions used, a miscibility gap is evident for $0.77 < x < 2.44$, where coexisting V-rich and V-poor ellestadites are observed, with a loss of $CaCl_2$ during the synthesis. Unit cell contraction with increasing replacement of V (IR (CN IV) = 0.355 Å) by Si (IR (CN IV) = 0.26 Å) and S (IR (CN IV) = 0.12 Å) is observed. The Ca(1)O_6 metaprism twist angle (φ) dilates with the substitution of smaller atoms at BO_4 sites. The incorporation of vanadium beyond 25 at. % V at the *B* sites leads to substantially higher dissolution rates. Therefore, ellestadites where Si/S is less than 33 at. % and V less than 25 at. % at the *B* site proves most chemically resistant to TCLP extractions, and this waste loading should not be exceeded for immobilization of wastes containing silicon, sulphur and vanadium.

8.2 Tailoring Ellestadite Waste Forms

The examination of key solid solution series derived from a chlorellestadite $Ca_{10}(SiO_4)_3(SO_4)_3Cl_2$ matrix have established a set of working parameters for designing waste forms suitable for the stabilization of municipal incinerator fly ash (MSW). Specifically, the crystallochemical flexibility of $[A_{10}][(BO_4)_6][X_2]$ towards the introduction of hazardous cations and anions has been confirmed with the chemical durability, as established through toxicity characteristic leach testing, and the compositional boundary conditions for waste fixation mapped. A key outcome is that tailoring will require the introduction phosphorus and fluorine to ensure the ellestadite ceramics are resistant to corrosion. Here, the procedure for designing a ceramic to treat MSW residues is described.

Earlier, the composition of a typical MSW fly ash was presented (see Table 3.1) to illustrate the range of metals and anions to be captured by a putative ellestadite waste form. For chemical tailoring these raw analyses are first sorted into A-type, B-type and X-type species with respect to the general apatite formula and then converted moles of waste element/kg (Table 8.1). It is noted that the ash as presented summed to 95.5 wt% with the balance due to moisture. In addition, the loss-on-ignition was 14.4% that is likely accounted for primarily by organics contamination, with contributions from carbonates and hydroxides.

Based upon the preferred compositional boundaries to achieve acceptable chemical durability (Figure 7.17) the notional composition for a waste form ellestadite can be expressed as $[Ca_{10}][(SiO_4)_{0.5}(PO_4)_5(SO_4)_{0.5}][F_{1.7}Cl_{0.3}]$. Expressing this base line composition as moles element/kg (Table 8.2) allows a direct comparison with the fly ash composition (Table 8.1), and reveals the key difference is enrichment of phosphorous and fluorine in the idealized ellestadite showing these will be required tailoring additives.

Table 8.1 MSW fly ash composition expressed in terns of ellestadite crystallochemical criteria (adapted from Table 3.1).

	Oxide Composition		Moles Element/kg	
A-Type Cations				
CaO	25	wt%	**Ca**	5.5026
MgO	3	wt%	**Mg**	0.9186
Fe_2O_3	2	wt%	**Fe**	0.3092
Na_2O	1.6	wt%	**Na**	0.6373
K_2O	1	wt%	**K**	0.2621
Zn	12417	ppm	**Zn**	1.5327
Pb	3731	ppm	**Pb**	0.4605
Cd	203	ppm	**Cd**	0.0251
				9.6480
B-Type Cations				
SiO_2	28	wt%	**Si**	5.7516
Al_2O_3	17	wt%	**Al**	2.0580
SO_4	2.3	wt%	**S**	0.2955
Cr	513	ppm	**Cr**	0.0122
				8.1174
X-Type Anions and Cations				
Cl	0.9	wt%	**Cl**	0.3134
Cu	1022	ppm	**Cu**	1.99E-05
				0.3134
Loss on Ignition				
	14.4	wt%		
Sum	**95.2**	wt%		

Table 8.2 Composition of $[Ca_{10}][(SiO_4)_{0.5}(PO_4)_5(SO_4)_{0.5}][F_{1.7}Cl_{0.3}]$ ellestadite stabilization matrix.

		Moles Element	Moles Metal/kg
A-Type Cations			
	Ca	10	9.8750
B-Type Cations			
	Si	0.5	0.4937
	P	5	4.9375
	S	0.5	0.4937
			5.9250
X-Type Halides			
	Cl	0.3	0.2962
	F	1.7	1.6787
			1.9750

Finally, the major ionic substitutions between the ellestadite host and the waste elements should be considered (Table 8.3). The principle altervalent and aliovalent charge balance equations being:

$$Ca^{2+} \leftrightarrow Mg^{2+}/Zn^{2+}/Pb^{2+}/Cd^{2+} \quad (8.1)$$

$$Ca^{2+} + Si^{4+} \leftrightarrow Fe^{3+} + Al^{3+} \quad (8.2)$$

$$Ca^{2+} + Si^{4+} \leftrightarrow Na^{+}/K^{+} + P^{5+} \quad (8.3)$$

Naturally, the mechanisms in the actual use will be mixed, and also include the creation of *A*(2) and *X*-site vacancies, with this added intricacy allowing the ellestadite to respond to atomic scale chemical heterogeneity of the waste. Nonetheless, following these simple rules it becomes possible to adjust the composition the MSW to match that required for stabilization, with the approach being to:

(i) satisfy the requirement to have the *B*-site occupied by a molar ratio of Si:P = 0.5:5;

(ii) introduce Ca to the *A*-site such that the ratio of all *A*-type to all *B*-type cations satisfies *A*:*B* = 10:6;

(iii) increase the F content such the mole proportions of F:Cl = 1.7:3; and

(iv) as fluorine will be introduced as CaF_2, subtract this additional *A*-site content from that calculated in step (ii).

Table 8.3 Ellestadite waste form composition for treatment of the MSW fly ash.

		Moles		wt Oxide	wt% Oxide	
Tailoring Additives						
Ca	2+	92.407	**CaO**	5182.180	50.75	
P	5+	57.516	**P_2O_5**	4081.932	39.98	
F	1-	1.776	**CaF_2**	69.326	0.68	
						91.41
Waste						
Ca	2+	5.503	**CaO**	61.583	0.60	
Mg	2+	0.919	**MgO**	37.030	0.36	
Fe	3+	0.309	**Fe_2O_3**	24.687	0.24	
Na	1+	0.637	**Na_2O**	19.749	0.19	
K	1+	0.262	**K_2O**	12.343	0.12	
Zn	2+	1.533	**ZnO**	124.730	1.22	
Pb	2+	0.461	**PbO**	102.791	1.01	
Cd	2+	0.025	**CdO**	3.217	0.03	
Si	4+	5.752	**SiO_2**	345.615	3.38	
Al	3+	2.058	**Al_2O_3**	104.919	1.03	
S	6+	0.296	**SO_4**	28.390	0.28	
Cr	5+	0.012	**Cr_2O_3**	0.925	0.01	
Cl	1-	0.313	**Cl**	11.109	0.11	
Cu	2+	1.99E-05	**Cu_2O**	0.001	1.39102E-05	
						8.59
				10210.529	100	

In this manner, the proportion of additives to waste can be established (Table 8.3). The location of certain waste metals appearing at low concentration remains uncertain. For example, early reports placed copper at the *A*-site in hydroxyapatite [2], but more recent work proved the correct location is in the tunnel where O-Cu-O linear bonding is favored [3]. Moreover, the co-existence of secondary phases, particularly calcium aluminates, calcium silicates, or cuspidine cannot be excluded, but these are likely to be in minor quantities as the phosphate additive would be introduced as phosphoric acid that will rapidly scavenge most metals, thereby promoting ellestadite crystallisation.

The final composition of the product satisfies the boundary compositions necessary to ensure good durability (Figure 7.16), with a waste loading of 8.59 wt %. While this ash content is modest, significantly greater effectiveness can be achieved by

blending ash with other industrial residues. For example, calcium fluoride is a voluminous sludge generated by the semiconductor manufacturers [4] that typically contains less than 10 wt % contamination with calcium, aluminium, iron, phosphorus and sodium, all of which can be accommodated in ellestadite. In addition, a wide variety of industries produce phosphoric acid as a by-product of chemical processes [5] including the fertilizer and phosphoric acid manufacturers, and this may be used as an additive. Thus, by combining wastes much larger effective waste loadings are feasible.

While a detailed techno-economic analysis of the feasibility of ellestadite MSW treatment is beyond the scope of this thesis, a case exists for further investigation given that the durability of the ceramics can be tuned to meet environmental limits, the waste loading can be enhanced by blending byproducts, and processes and technologies for blending phosphoric acid with wastes is well established (e.g. Apatite II [6, 7]).

8.3 Reconnaissance of Cadmium Doped Chlorvanadoapatite

This research focused on the incorporation of toxic elements in the *B*- and *X*-sites of calcium ellestadites $Ca_{10}[(SiO_4)_x(BO)_{6-2x}(SO_4)_x][(Cl_{1-y}X_y)_2]$, but elements including Pb, Cd, Sr and Ba can displace calcium. Therefore, a reconnaissance study was made of cadmium incorporation. Cadmium has an ionic radius similar to calcium and potentially can enter either the *A*(1) and *A*(2) site. The *A*(2) sites are invariably more voluminous than the *A*(1) sites and in ellestadite ions larger than Ca are likely to preferentially occupy *A*(2) sites. Earlier studies found cadmium is not randomly distributed over the *A* positions. Piro [8] who examined cadmium incorporation in $Ca_{10}(PO_4)F_2$ stated that the distribution is dependent on cadmium concentration in the apatite. Nounah et al. [9] using the Rietveld method found cadmium had a slight preference for the Ca(1) site in fluorapatite, and the *A*(2) site in hydroxyapatite, but at low concentration cadmium partitioning over *A*(1)/*A*(2) can be reversed. The mechanism of cadmium substitution being poorly understood, a preliminary examination of the interaction of cadmium with calcium in the apatite structure was undertaken. Because of the extreme toxicity and carcinogenic nature of cadmium

and vanadium, the series $[Ca_{10-x}]Cd_x(VO_4)_6Cl_2$ was selected for synthesis and characterization.

Stoichiometric and highly crystalline cadmium doped chlorvanadoapatite $Ca_{10-x}Cd_x(VO_4)_6Cl_2$ (where x = 6, 8, 10) was prepared by solid state reaction of high purity oxides CaO, CdO, $CaCl_2$, and V_2O_5 at 600 °C for 15 hours in air. The starting materials were combined as follows:

$$(9-x)\ CaO + x\ CdO + CaCl_2 + 3\ V_2O_5 \rightarrow [Ca_{10-x}Cd_x](VO_4)_6Cl_2 \qquad (8\text{-}1)$$

The powder XRD data were refined with TOPAS beginning with the endmember of $Cd_{10}(VO_4)_6Cl_2$ in space group $P6_3/m$ [10]. Vanadoapatite was dominant (> 90 wt %) for x = 8 and 10 (Figure 8.1a and b), but when the Ca:Cd mole ratio = 4:6, $Cd_2V_2O_7$ appears as a secondary phase reaching as high as 18.8 wt % for x = 8 (Figure 8.1c). The refined lattice parameter c and unit cell volumes contract with increasing Cd content as Cd^{2+} (CN VIII, 0.95 Å) has a smaller ionic radius compared to Ca^{2+} (CN VIII, 1.0 Å) (Table 8.1), while there is a slight dilation of cell parameter a. The lattice parameters of $Cd_{10}(VO_4)Cl_2$ are in good agreement with previous studies [10, 11]. The preliminary refinement shows that Cd is preferentially tenanted at the $A(2)$ site, while Ca is dominant at $A(1)$ site. As secondary phase formation is significant, chemical analyses were essential to check mass balance. In common with other apatite investigations, neutron diffraction should be used to locate oxygen and chlorine in the structure for a better understanding of the structural modification accompanying Cd substitution, but this has not yet been conducted. The synthesis conditions used in this reconnaissance experiment produced undesirable secondary phases which might lead to less than optimal durability. An alternate synthesis approach would be to join $Ca_{10}[(SiO_4)_3(SO_4)_3]Cl_2$ with $Cd_{10}(VO_4)_6Cl_2$ to create a wide compositional suite of cadmium and vanadium bearing chlorellestadites.

Table 8.4 Refined lattice parameter data (hexagonal cell with the space group $P6_3/m$) from laboratory power X-ray diffraction.

Compositions	a	c	V	R_p	R_{wp}	R_b	GOF
$Cd_{10}(VO_4)_6Cl_2$	10.1160(1)	6.5586(1)	581.24(1)	0.059	0.075	0.031	1.455
$[Ca_2Cd_8](VO_4)_6Cl_2$	10.0802(1)	6.6198(1)	582.53(1)	0.062	0.079	0.026	1.499
$[Ca_4Cd_6](VO_4)_6Cl_2$	10.0698(1)	6.6788(1)	586.51(2)	0.057	0.074	0.022	1.383

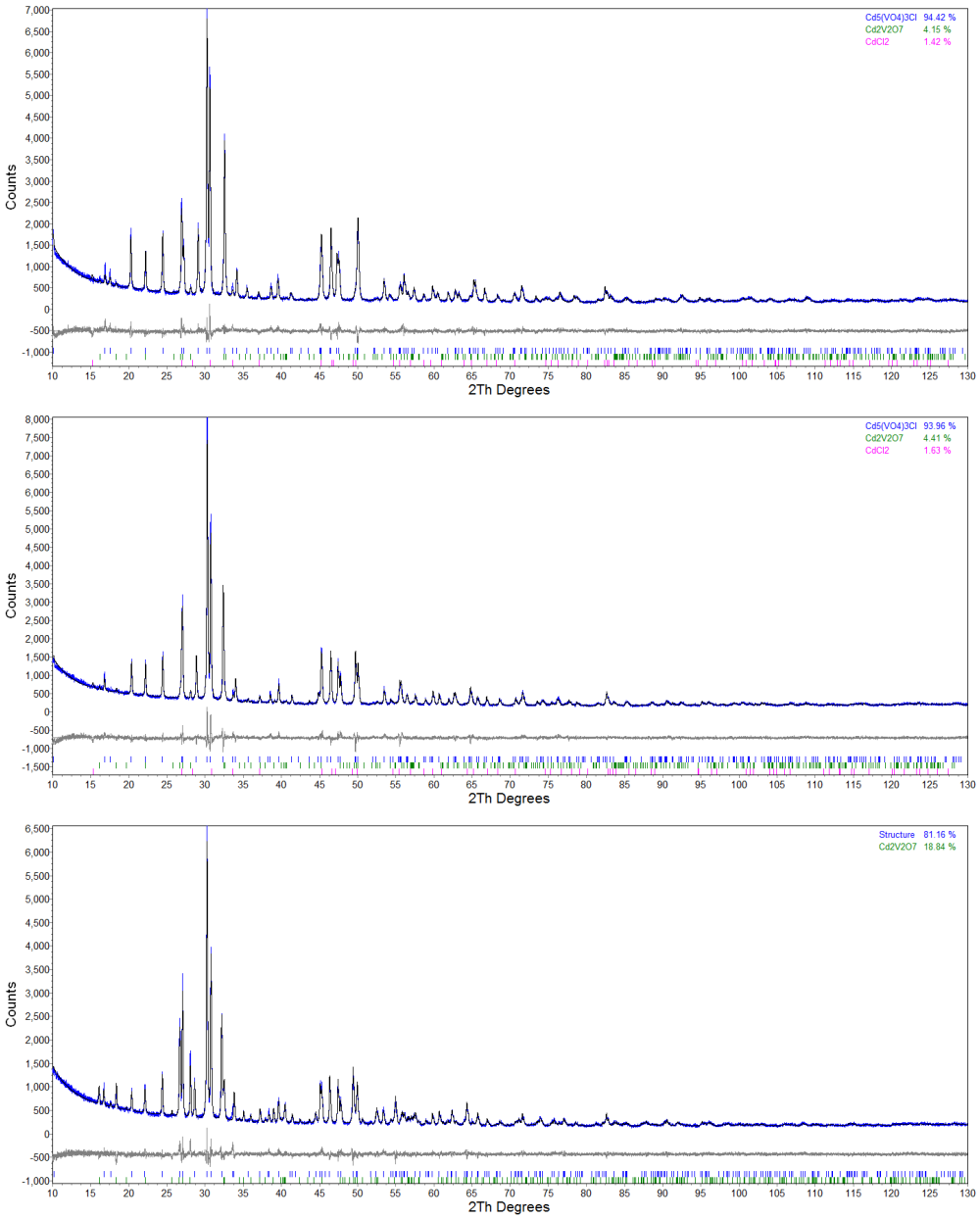

Figure 8.1 Rietveld fitting pattern for (a) x = 10, (b) x = 8 and (c) x = 6. (x in $[Ca_{10-x}Cd_x](VO_4)_6Cl_2$).

8.4 Outstanding Questions

The tailoring of ellestadite, compositionally and structurally, requires a deep understanding of crystal chemistry, and this thesis was primarily concerned with developing a fundamental understanding of simulated waste forms. The research is not yet closed as there remain unexplored linkages of structure with performance, and future work should be broadened substantially to provide a more complete underpinning for crystallographic engineering. Some important outstanding questions include:

(i) The loss of $CaCl_2$ leads to non-stoichiometry that reduces ellestadite durability. Process modifications should be directed towards the optimization of synthesis conditions (temperature and time) and the inclusion of sintering additives (e.g. boric acid at 1-2 wt %) to enhance sinterability and yield denser, more homogeneous waste forms;

(ii) The short duration of the TCLP test precludes an estimation of long-term durability of ellestadite, and the results do not convey information concerning the mechanism of dissolution. Consequently, there remains some uncertainty as to the longevity of waste form ellestadite, and the mechanism of immobilization. Moreover, to gain a wide appreciation of durability a range of experiments including the American Nuclear Society (ANS) 16.1 Leach Test Procedure [12] should be used to complement the TCLP method;

(iii) To confidentially predict durability, leach testing must be complemented by the simulation of dissolution and precipitation using programs such as PHREEQC [13] that consider both thermodynamic and chemical kinetic factors. This may be non-trivial as the PHREEQC database will require development of supplementary parameters for ellestadites of various compositions;

(iv) Demonstration of the immobilization of more complex waste streams where a full suite of toxic simulants are used to validate that precursor tailoring will yield phase pure ellestadite products.

The central hypothesis of this thesis, that the ellestadite

$Ca_{10}[(SiO_4)_2(PO_4)_2(SO_4)_2]Cl_2$ possesses sufficient crystallochemical flexibility for exploitation as a ceramic waste form for the immobilization of incinerator fly ash was proven. However, the compositional boundaries to retain the waste are less extensive, and Si/S should not exceed 33 at% at the *B* site, $Ca_{10}[(SiO_4)_x(PO_4)_{6-2x}(SO_4)_x]Cl_2$, $x \leq 1$. Moreover, the performance of chlorellestadite can be enhanced by introducing fluorine in place of chlorine.

References:

[1] J. Neubauer, H. Pöllmann, *N. Jb. Miner. Mh.*, **1992**, 7, 295-310.

[2] B. Badraoui, M. Othmani, H. Bachouâ, *Ann. Chim. Sci. Mat.*, **2008**, 33, 329-337.

[3] T. Baikie, G. M. H. Ng, S. Madhavi, S. S. Pramana, K. Blake, M. Elcombe, T. J. White, *Dalton Trans.*, **2009**, 34, 6722-6726.

[4] W. Liu, K. Li, *J. Air & Waste Manage. Assoc*. **2011**, 61, 85-91.

[5] P. Nawghare, N. N. Rao, R. Bejankiwar, L. Szyprkowicz, S. N. Kaul, *J. Environ. Sci. Health*, **2001**, A36, 2011-2026.

[6] J. L. Conca, J. Wright, *Applied Geochemistry*, **2006**, 21, 1288-1300.

[7] J. Oliva, J. De Pablo, J. Cortina, J. Cama, C. Ayora, *J. Hazard Mater.*, **2010**, 184, 364-374.

[8] O.E. Piro, M.C. Apella, E. Baran, B.E. Rivero, *Rev. Chim. Miner*. **1982**, 19, 11-18.

[9] A. Nounah, J. L. Lacout, J. M. Savariault, J.M. *J. Alloys & Compounds*, **1992**, 188, 141-146.

[10] H. P. Beck, M. Douiheche, R. Haberkorn, H. Kohlmann, *Solid State Sci.*, **2006**, 8, 64-70.

[11] А.В. Князев, Е.Н. Буланов, А.Н. Лапшин, *ХИМИЯ*, **2012**, 3, 87-91.

[12] ANS, *Measurement of the Leachability of Solidified Low-Level Radioactive Waste By a Short Term Test Procedure*, ANS-16.1-1986, American Nuclear Society, La Grange Park, IL, **1986**.

[13] D. L. Parkhurst, C. A. J. Appelo, C.A.J., *Description of input and examples for PHREEQC version 3-A computer program for speciation, batch-reaction, one-dimensional transport, and inverse geochemical calculations: U.S. Geological Survey Techniques and Methods*, book 6, chap. A43, 497, **2013**

APPENDIX

Table A1

(a). Output of *SVDdiagnostic* for problematic cases of Rietveld refinements of $Ca_{10}(SiO_4)_3(SO_4)_3Cl_2$.

PRECONDITIONED normal matrix
Condition number for matrix of normal equations = 0.123E+03
Error propagation is likely to spoil 2 trailing decimal digits out of probably 14.
Problem well conditioned for double-precision matrix inversion.
Eigenvectors for F00_Ca12.out ranked according to eigenvalues are printed as columns below

Eigenvector # :		1 ..	27	28	29	30	31	32	33	34
bkg1	1:	-0.343 ..	0.049	0.119	-0.103	-0.438	0.456	-0.012	-0.292	0.000
bkg2	2:	-0.076 ..	-0.163	-0.045	0.042	-0.154	0.006	0.011	-0.280	-0.023
bkg3	3:	0.282 ..	-0.142	0.206	-0.545	-0.205	-0.087	0.022	-0.005	0.010
bkg4	4:	0.006 ..	-0.261	-0.122	0.045	-0.130	0.232	0.005	0.049	-0.030
bkg5	5:	0.005 ..	0.027	0.225	-0.407	-0.178	-0.004	0.020	-0.047	0.016
bkg6	6:	0.016 ..	-0.146	-0.042	-0.039	-0.021	0.029	0.011	0.024	-0.024
bkg7	7:	-0.008 ..	0.102	0.180	-0.272	-0.092	0.047	0.011	0.058	0.026
zero_error	8:	0.002 ..	0.001	-0.062	-0.011	0.026	0.035	0.746	-0.018	-0.009
peaktypey	9:	0.064 ..	0.055	0.013	0.074	-0.370	-0.414	0.031	0.169	-0.015
Ascale	10:	-0.279 ..	0.010	0.001	0.075	-0.373	-0.513	0.078	0.248	-0.017
Aalat	11:	0.014 ..	-0.080	0.042	-0.025	0.140	0.091	0.009	-0.040	0.018
Ablat	12:	-0.004 ..	0.059	0.145	0.080	-0.088	-0.015	0.043	0.002	-0.018
Aclat	13:	-0.001 ..	-0.011	-0.141	-0.062	-0.018	-0.053	0.016	0.020	-0.001
F00sz	14:	-0.114 ..	0.011	-0.081	0.203	-0.289	0.166	-0.012	0.070	-0.010
F00scale	15:	-0.413 ..	-0.007	0.039	-0.170	0.322	-0.386	-0.025	-0.583	0.019
F00alat	16:	-0.011 ..	0.098	-0.032	-0.007	0.021	0.033	0.631	-0.060	-0.018
F00clat	17:	0.012 ..	-0.133	-0.035	-0.016	0.043	0.042	0.154	0.029	0.004
Ca1z	18:	0.001 ..	-0.124	0.057	-0.013	0.048	-0.045	0.018	0.015	-0.003
Ca1occ	19:	-0.315 ..	0.058	0.068	-0.107	-0.014	0.008	-0.019	0.029	-0.704
Ca2x	20:	0.035 ..	0.153	-0.046	-0.022	0.129	-0.147	-0.006	0.044	0.032
Ca2y	21:	0.014 ..	0.144	-0.056	-0.117	0.174	-0.098	-0.006	0.038	0.037
Ca2occ	22:	-0.313 ..	0.002	0.087	-0.051	-0.063	0.016	0.014	0.043	0.703
Bx	23:	0.029 ..	0.140	0.443	0.278	-0.036	-0.087	0.016	-0.041	-0.004
By	24:	-0.001 ..	0.117	0.364	0.279	-0.027	0.007	0.025	-0.033	-0.023
O1x	25:	-0.065 ..	0.440	-0.214	-0.027	-0.022	0.104	-0.041	0.031	0.020
O1y	26:	0.056 ..	0.300	-0.257	-0.047	-0.015	0.088	-0.034	-0.011	0.012
Bbeq	27:	0.395 ..	-0.007	-0.224	0.237	-0.320	-0.166	-0.017	-0.601	0.005
O2x	28:	-0.037 ..	-0.202	0.255	0.186	0.063	0.054	0.013	-0.014	-0.010
O2y	29:	-0.012 ..	-0.182	0.210	0.110	0.046	0.029	0.014	-0.029	-0.022
O3x	30:	0.018 ..	-0.318	0.014	0.046	0.061	-0.030	0.042	0.035	-0.017
O3y	31:	0.015 ..	-0.349	0.031	0.076	0.077	-0.015	0.022	0.053	0.016
O3z	32:	0.005 ..	0.192	0.221	0.141	0.098	0.074	0.016	-0.046	0.013
Clz	33:	-0.108 ..	0.196	0.053	0.176	0.071	0.043	0.029	0.016	0.018
Cabeq	34:	0.392 ..	0.242	0.333	-0.080	0.044	0.031	0.023	-0.086	-0.013

Eigenvalues :	0.412E+01 ..	0.284E+00	0.257E+00	0.241E+00	0.181E+00	0.170E+00	0.143E+00	0.102E+00	0.335E-01

Table A1

(b). Output of *SVDdiagnostic* for problematic cases of Rietveld refinements of $Ca_{10}(SiO_4)_3(SO_4)_3Cl_{1.6}F_{0.4}$.

PRECONDITIONED normal matrix

Condition number for matrix of normal equations = 0.921E+02
Error propagation is likely to spoil 2 trailing decimal digits out of probably 14.

Problem well conditioned for double-precision matrix inversion.

Eigenvectors for F04_Ca12.out ranked according to eigenvalues are printed as columns below

Eigenvector # :	1 ..	25	26	27	28	29	30	31	32
bkg1 1:	-0.360 ..	-0.121	0.021	-0.004	0.370	0.599	-0.003	0.180	0.033
bkg2 2:	-0.108 ..	-0.102	-0.072	-0.068	-0.429	0.108	0.011	0.239	0.038
bkg3 3:	0.275 ..	0.045	0.500	0.138	0.280	-0.106	0.004	0.064	0.021
bkg4 4:	0.052 ..	0.002	0.095	-0.051	-0.537	0.252	-0.007	-0.130	-0.009
bkg5 5:	0.001 ..	0.030	0.294	0.094	0.219	0.002	0.007	0.133	0.029
bkg6 6:	0.021 ..	0.009	0.128	-0.004	-0.361	0.052	0.001	-0.059	0.008
zero_error 7:	0.000 ..	0.000	0.000	-0.043	0.005	0.011	0.749	-0.043	0.038
Ascale 8:	-0.181 ..	0.046	-0.006	0.025	0.007	-0.010	0.029	-0.055	0.012
Aalat 9:	0.000 ..	-0.014	-0.003	-0.011	0.001	0.001	0.046	0.000	0.001
Ablat 10:	0.002 ..	0.005	0.009	-0.006	0.001	-0.004	0.034	-0.005	0.002
Aclat 11:	0.001 ..	0.008	-0.006	0.005	-0.001	0.005	0.035	0.000	0.001
Crytalsz 12:	-0.154 ..	-0.054	-0.145	-0.049	0.050	0.369	-0.010	-0.096	-0.008
F04scale 13:	-0.417 ..	-0.081	0.007	0.025	-0.096	-0.454	0.029	0.630	0.121
F04alat 14:	-0.013 ..	-0.001	-0.006	0.050	0.007	0.011	0.599	-0.025	0.029
F04clat 15:	0.019 ..	-0.030	0.011	-0.018	-0.002	0.005	0.251	-0.020	0.008
Ca1z 16:	0.001 ..	0.071	0.074	-0.052	0.002	-0.040	-0.001	0.000	0.006
Ca1occ 17:	-0.312 ..	0.025	-0.084	0.054	0.127	-0.018	-0.049	-0.174	0.663
Ca2x 18:	0.020 ..	0.192	-0.274	-0.036	0.034	-0.161	0.015	0.014	-0.015
Ca2y 19:	0.040 ..	0.186	-0.253	0.030	0.017	-0.152	0.030	-0.005	-0.042
Ca2occ 20:	-0.325 ..	-0.014	0.000	-0.020	0.095	0.001	0.033	0.077	-0.718
Cabeq 21:	0.387 ..	-0.417	-0.485	-0.197	0.252	-0.062	0.001	0.081	-0.009
Clz 22:	-0.105 ..	0.063	-0.118	-0.107	-0.088	0.028	0.021	0.056	0.037
Bx 23:	0.062 ..	0.301	-0.069	-0.489	0.110	-0.038	-0.020	0.065	0.006
Bbeq 24:	0.409 ..	0.136	-0.012	0.093	-0.070	0.366	0.031	0.630	0.112
By 25:	-0.029 ..	0.261	-0.001	-0.413	0.035	0.059	0.019	0.061	0.044
O1x 26:	-0.068 ..	-0.098	-0.305	0.248	-0.027	0.052	-0.023	-0.011	-0.021
O1y 27:	0.037 ..	-0.123	-0.122	0.274	-0.046	0.037	-0.019	0.038	0.004
O2x 28:	-0.066 ..	-0.076	0.152	-0.424	-0.002	0.020	-0.028	-0.009	0.033
O2y 29:	-0.017 ..	-0.088	0.140	-0.285	-0.003	0.028	-0.013	0.006	0.044
O3x 30:	0.012 ..	-0.461	0.107	-0.126	-0.024	-0.068	0.033	-0.003	0.051
O3y 31:	0.019 ..	-0.525	0.178	-0.174	-0.050	-0.067	-0.011	-0.008	0.013
O3z 32:	0.011 ..	-0.017	-0.110	-0.188	-0.029	-0.004	-0.016	0.059	0.016

Eigenvalues :	0.403E+01 ..	0.361E+00	0.310E+00	0.286E+00	0.280E+00	0.165E+00	0.137E+00	0.899E-01	0.438E-01

Table A1

(c). Output of *SVDdiagnostic* for problematic cases of Rietveld refinements of $Ca_{10}(SiO_4)_3(SO_4)_3Cl_{1.2}F_{0.8}$.

PRECONDITIONED normal matrix

Condition number for matrix of normal equations = 0.880E+02
Error propagation is likely to spoil 2 trailing decimal digits out of probably 14.

Problem well conditioned for double-precision matrix inversion.

Eigenvectors for F08_Ca12.out ranked according to eigenvalues are printed as columns below

Eigenvector #:	1	..	32	33	34	35	36	37	38	39
bkg1	1:	-0.365	..	0.362	-0.302	0.440	-0.104	-0.271	0.106	0.201	0.096
bkg2	2:	-0.086	..	-0.304	-0.116	0.056	0.090	-0.236	-0.030	0.045	0.017
bkg3	3:	0.293	..	0.100	-0.054	-0.145	0.136	-0.025	-0.035	-0.067	-0.006
bkg4	4:	0.012	..	-0.491	-0.078	0.201	-0.138	0.053	0.067	0.057	-0.012
bkg5	5:	0.006	..	0.094	-0.075	-0.040	0.077	-0.068	-0.018	-0.022	0.006
bkg6	6:	0.037	..	-0.365	-0.016	0.019	-0.019	0.010	0.021	-0.002	-0.021
zero_error	7:	0.035	..	-0.040	0.287	0.408	0.546	0.134	0.055	0.062	-0.026
Asz	8:	-0.096	..	-0.035	0.058	-0.082	-0.032	0.123	-0.095	0.726	0.127
peaktypey1	9:	0.091	..	0.034	-0.272	-0.322	0.260	0.290	-0.026	0.502	0.035
Ascale	10:	-0.317	..	0.049	-0.433	-0.264	0.432	0.269	0.097	-0.321	-0.148
Aalat	11:	0.029	..	0.020	0.004	0.023	-0.033	-0.044	-0.016	-0.029	0.014
Ablat	12:	0.028	..	-0.057	0.001	0.010	0.011	-0.015	0.002	0.004	-0.003
Aclat	13:	0.022	..	0.004	0.015	0.040	0.060	0.027	-0.001	0.049	-0.001
peaktypey2	14:	-0.067	..	-0.008	0.068	-0.138	0.020	-0.102	0.743	0.062	0.095
peaktypey3	15:	0.062	..	-0.117	0.120	-0.189	0.023	-0.071	0.475	0.036	0.048
Qscale	16:	-0.179	..	-0.128	0.059	-0.090	0.033	0.046	-0.370	-0.036	-0.052
Qalat	17:	-0.007	..	0.011	-0.017	-0.018	0.008	-0.005	0.005	-0.004	-0.005
Qclat	18:	-0.007	..	-0.005	0.011	0.018	-0.003	0.012	-0.005	0.007	0.000
F08sz	19:	-0.099	..	0.092	-0.284	0.213	-0.011	0.085	0.053	0.020	-0.015
F08scale	20:	-0.405	..	-0.052	0.292	-0.350	0.248	-0.550	-0.164	0.041	0.099
F08alat	21:	-0.028	..	-0.038	0.250	0.321	0.388	0.101	0.046	0.029	-0.019
F08clat	22:	-0.036	..	0.001	0.107	0.132	0.213	0.035	-0.001	0.019	-0.008
Ca1z	23:	0.011	..	0.003	0.000	-0.003	0.022	0.008	-0.014	-0.008	-0.009
Ca1occ	24:	-0.252	..	0.169	0.059	-0.025	-0.044	-0.092	0.053	0.139	-0.673
Ca2x	25:	0.010	..	0.095	0.128	-0.068	0.046	-0.009	-0.013	-0.018	0.041
Ca2y	26:	-0.011	..	0.098	0.129	-0.043	0.053	-0.020	-0.016	-0.022	0.038
Ca2occ	27:	-0.249	..	0.096	-0.031	0.007	0.023	0.130	-0.047	-0.141	0.680
Cabeq	28:	0.370	..	0.491	0.154	-0.048	0.039	-0.073	-0.021	0.021	0.042
Clz	29:	0.055	..	-0.009	0.032	-0.036	0.021	-0.027	-0.027	-0.006	0.017
Bbeq	30:	0.397	..	-0.102	-0.418	0.072	0.310	-0.540	-0.068	0.065	0.043
Bx	31:	0.052	..	0.055	-0.045	0.002	0.007	-0.016	-0.008	0.009	0.015
By	32:	-0.056	..	-0.003	-0.057	0.091	-0.012	-0.049	-0.022	0.025	0.015
O1x	33:	-0.032	..	-0.045	0.006	-0.007	-0.037	0.025	0.007	0.002	0.029
O1y	34:	0.035	..	-0.105	0.007	-0.038	-0.045	-0.013	-0.001	0.023	0.029
O2x	35:	0.007	..	0.010	-0.032	0.089	-0.042	0.003	0.018	0.012	-0.017
O2y	36:	-0.028	..	-0.018	-0.042	0.067	-0.039	-0.025	0.030	0.028	-0.028
O3x	37:	0.028	..	0.060	0.110	0.009	-0.002	0.004	-0.010	-0.002	-0.010
O3y	38:	-0.006	..	0.056	0.101	-0.009	-0.031	0.032	-0.016	-0.025	0.006
O4z	39:	-0.014	..	0.000	0.047	0.022	-0.068	-0.051	-0.003	0.054	0.001

Eigenvalues	:	0.409E+01	..	0.279E+00	0.175E+00	0.172E+00	0.153E+00	0.911E-01	0.713E-01	0.626E-01	0.465E-0

Table A1

(d). Output of *SVDdiagnostic* for problematic cases of Rietveld refinements of $Ca_{10}(SiO_4)_3(SO_4)_3Cl_{0.8}F_{1.2}$.

PRECONDITIONED normal matrix

Condition number for matrix of normal equations = 0.904E+02
Error propagation is likely to spoil 2 trailing decimal digits out of probably 14.

Problem well conditioned for double-precision matrix inversion.

Eigenvectors for F12.out ranked according to eigenvalues are printed as columns below

Eigenvector #:		1 ..	26	27	28	29	30	31	32	33
bkg1	1:	-0.360 ..	-0.219	-0.137	0.146	0.398	-0.523	-0.072	0.231	0.043
bkg2	2:	-0.095 ..	0.428	-0.126	-0.123	0.039	-0.152	-0.086	0.274	0.018
bkg3	3:	0.279 ..	-0.301	-0.110	-0.046	-0.175	0.024	-0.059	0.074	0.017
bkg4	4:	0.012 ..	0.430	-0.052	-0.416	0.131	-0.147	0.000	-0.074	-0.026
bkg5	5:	0.017 ..	-0.238	-0.073	-0.035	-0.069	-0.046	-0.043	0.070	0.015
bkg6	6:	0.042 ..	0.305	-0.031	-0.286	-0.027	0.002	-0.010	-0.007	-0.018
zero_error	7:	0.022 ..	-0.054	0.120	-0.077	0.161	0.168	-0.706	-0.041	-0.023
peaktypey	8:	0.070 ..	0.122	-0.107	0.198	-0.443	-0.150	-0.171	-0.143	-0.036
Ascale	9:	-0.285 ..	0.092	-0.137	0.194	-0.542	-0.187	-0.245	-0.213	-0.072
Aalat	10:	0.000 ..	0.078	-0.020	0.067	-0.110	-0.056	-0.042	-0.010	0.019
Ablat	11:	0.021 ..	-0.048	0.103	-0.044	0.132	0.069	0.017	0.009	-0.005
Aclat	12:	0.005 ..	-0.046	-0.049	-0.017	0.002	-0.007	0.001	0.007	-0.011
Crytalsz	13:	-0.118 ..	0.070	-0.071	0.099	0.136	-0.346	-0.084	-0.093	-0.021
F04scale	14:	-0.431 ..	0.073	0.041	0.048	-0.232	0.436	0.020	0.635	0.098
F04alat	15:	-0.024 ..	-0.029	0.089	-0.041	0.123	0.128	-0.534	-0.025	-0.021
F04clat	16:	-0.013 ..	-0.025	0.031	-0.056	0.094	0.093	-0.252	-0.004	0.002
Ca1z	17:	-0.011 ..	-0.057	0.008	-0.025	-0.017	0.028	-0.006	-0.012	-0.007
Ca1occ	18:	-0.261 ..	-0.090	-0.095	0.093	0.050	0.021	0.023	0.068	-0.698
Ca2x	19:	-0.018 ..	0.054	-0.505	-0.063	0.047	0.096	-0.049	0.052	0.037
Ca2y	20:	0.012 ..	-0.053	-0.391	-0.109	0.056	0.106	-0.052	0.064	0.038
Ca2occ	21:	-0.260 ..	-0.066	-0.024	0.076	0.004	-0.027	-0.026	-0.131	0.695
Cabeq	22:	0.167 ..	0.015	-0.134	-0.045	-0.036	0.002	-0.012	0.034	0.010
beqca	23:	0.390 ..	0.148	-0.356	0.562	0.247	0.151	-0.036	0.117	0.039
Bx	24:	0.036 ..	0.234	0.035	0.226	0.011	-0.014	0.000	-0.006	0.014
By	25:	-0.058 ..	0.202	0.072	0.115	0.050	-0.076	-0.019	0.015	0.017
Bbeq	26:	0.407 ..	-0.014	0.192	-0.046	-0.213	-0.416	-0.153	0.573	0.044
O1x	27:	-0.048 ..	0.056	-0.173	-0.147	-0.015	-0.004	0.008	-0.024	0.018
O1y	28:	0.056 ..	0.015	-0.085	-0.220	-0.021	0.026	0.008	0.005	0.015
O2x	29:	0.021 ..	0.107	0.330	0.165	0.068	-0.007	0.028	-0.028	-0.010
O2y	30:	-0.027 ..	0.091	0.297	0.111	0.056	-0.028	0.037	0.008	-0.025
O3y	32:	-0.012 ..	0.261	0.106	0.199	0.051	0.113	-0.021	-0.039	0.009
O3z	33:	-0.005 ..	0.025	0.137	0.082	0.092	0.048	0.034	0.014	-0.016

Eigenvalues : 0.405E+01 .. 0.322E+00 0.281E+00 0.265E+00 0.198E+00 0.178E+00 0.156E+00 0.905E-01 0.448E-01.

Table A1

(e). Output of *SVDdiagnostic* for problematic cases of Rietveld refinements of $Ca_{10}(SiO_4)_3(SO_4)_3Cl_{0.4}F_{1.6}$.

PRECONDITIONED normal matrix

Condition number for matrix of normal equations = 0.895E+02
Error propagation is likely to spoil 2 trailing decimal digits out of probably 14.

Problem well conditioned for double-precision matrix inversion.

Eigenvectors for F16.out ranked according to eigenvalues are printed as columns below

Eigenvector #:	1	..	26	27	28	29	30	31	32	33
bkg1	1:	-0.367	..	0.190	0.027	0.172	-0.619	0.187	0.121	-0.253	-0.068
bkg2	2:	-0.093	..	-0.057	0.194	-0.038	-0.121	0.092	0.159	-0.270	-0.031
bkg3	3:	0.279	..	0.188	0.087	-0.103	0.133	0.045	0.114	-0.069	-0.016
bkg4	4:	0.006	..	-0.172	0.211	-0.295	-0.233	0.015	-0.046	0.033	0.018
bkg5	5:	0.012	..	0.131	0.059	-0.072	0.010	0.046	0.068	-0.065	-0.018
bkg6	6:	0.043	..	-0.122	0.159	-0.215	-0.003	-0.011	-0.005	-0.008	0.015
zero_error	7:	0.017	..	0.010	-0.071	-0.080	-0.123	-0.573	0.461	0.052	0.027
peaktypey	8:	0.060	..	0.052	0.038	0.084	0.240	0.222	0.352	0.153	0.064
Ascale	9:	-0.315	..	0.138	0.063	0.020	0.326	0.310	0.490	0.288	0.131
Aalat	10:	0.005	..	-0.585	0.117	0.120	-0.022	0.054	0.125	0.012	-0.012
Ablat	11:	0.010	..	0.541	-0.208	-0.058	0.020	-0.080	-0.130	-0.026	-0.010
Aclat	12:	0.015	..	0.009	0.015	-0.122	-0.016	-0.060	-0.001	0.011	0.004
Crytalsz	13:	-0.109	..	0.070	0.011	0.087	-0.293	0.162	0.157	0.099	0.031
F04scale	14:	-0.437	..	-0.076	-0.012	0.058	0.479	-0.188	-0.027	-0.619	-0.139
F04alat	15:	-0.019	..	-0.063	-0.049	-0.032	-0.112	-0.460	0.326	0.029	0.021
F04clat	16:	-0.010	..	0.125	-0.027	-0.053	-0.029	-0.221	0.178	0.021	0.002
Ca1z	17:	-0.011	..	0.071	0.000	-0.042	0.022	-0.018	0.000	0.009	0.007
Ca1occ	18:	-0.238	..	0.048	0.043	0.087	-0.035	-0.018	-0.057	-0.119	0.691
Cabeq	19:	0.386	..	0.156	0.238	0.687	-0.016	-0.103	0.030	-0.108	-0.040
Ca2x	20:	-0.015	..	0.087	0.498	0.048	0.020	-0.057	0.015	-0.052	-0.033
Ca2y	21:	0.008	..	0.137	0.407	-0.027	0.018	-0.106	-0.002	-0.065	-0.038
Ca2occ	22:	-0.240	..	0.053	0.003	0.045	-0.008	0.031	0.049	0.185	-0.682
Clz	23:	0.188	..	-0.050	0.120	-0.051	0.024	0.036	0.018	-0.037	-0.007
Bx	24:	0.022	..	-0.161	-0.051	0.205	0.005	0.048	0.049	0.013	-0.005
By	25:	-0.045	..	-0.238	-0.083	0.131	-0.068	0.054	0.057	-0.001	-0.006
O1x	26:	-0.047	..	-0.038	0.222	-0.121	-0.015	-0.020	-0.023	0.016	-0.011
O1y	27:	0.049	..	-0.033	0.172	-0.202	-0.023	-0.055	-0.061	-0.028	-0.016
Bbeq	28:	0.403	..	-0.011	-0.227	-0.201	-0.053	0.306	0.377	-0.525	-0.063
O2x	29:	0.025	..	-0.088	-0.301	0.111	-0.033	-0.036	-0.019	0.022	-0.003
O2y	30:	-0.028	..	-0.094	-0.261	0.054	-0.043	-0.017	-0.018	-0.017	0.012
O3x	31:	0.004	..	-0.054	0.040	0.238	0.038	-0.049	0.024	-0.004	0.005
O3y	32:	0.001	..	-0.091	-0.080	0.198	0.058	-0.072	-0.008	0.042	-0.004
O3z	33:	-0.014	..	-0.015	-0.131	0.060	-0.048	-0.069	-0.086	-0.039	0.001

Eigenvalues	: 0.408E+01	..	0.306E+00	0.282E+00	0.262E+00	0.181E+00	0.168E+00	0.156E+00	0.800E-01	0.456E-01

Table A1

(f). Output of *SVDdiagnostic* for problematic cases of Rietveld refinements of $Ca_{10}(SiO_4)_3(SO_4)_3F_2$.

PRECONDITIONED normal matrix

Condition number for matrix of normal equations = 0.194E+03
Error propagation is likely to spoil 2 trailing decimal digits out of probably 14.

Problem well conditioned for double-precision matrix inversion.

Eigenvectors for F20_Ca1.out ranked according to eigenvalues are printed as columns below

Eigenvector #:		1 ..	26	27	28	29	30	31	32	33
bkg1	1:	-0.360 ..	-0.127	-0.045	-0.022	-0.470	0.085	-0.038	0.470	0.239
bkg2	2:	-0.087 ..	0.213	0.138	-0.175	-0.198	0.257	-0.103	0.023	0.166
bkg3	3:	0.261 ..	0.107	0.308	-0.118	-0.019	0.214	-0.092	-0.220	-0.017
bkg4	4:	0.033 ..	0.317	0.342	-0.253	-0.164	-0.049	0.026	0.168	-0.051
bkg5	5:	0.018 ..	0.078	0.215	-0.078	-0.073	0.111	-0.053	-0.076	0.038
bkg6	6:	0.038 ..	0.271	0.266	-0.182	-0.003	0.031	-0.013	0.007	-0.029
zero_error	7:	0.027 ..	-0.021	0.004	-0.026	0.026	-0.268	-0.704	0.025	-0.023
peaktypey1	8:	0.097 ..	0.054	-0.103	-0.035	0.002	0.136	-0.033	-0.312	-0.048
Ascale	9:	-0.362 ..	-0.025	-0.062	0.019	-0.325	0.149	-0.100	-0.703	-0.126
alat	10:	0.011 ..	0.038	0.121	0.059	0.074	0.022	-0.014	0.052	0.016
blat	11:	-0.032 ..	0.115	-0.068	0.119	0.073	-0.030	-0.095	0.025	-0.006
clat	12:	-0.018 ..	-0.042	0.010	-0.107	0.002	0.071	0.021	0.020	0.026
Crystalsz	13:	-0.137 ..	-0.110	-0.172	0.059	-0.273	0.314	-0.113	0.201	-0.552
peaktypey2	14:	0.155 ..	0.028	0.042	0.029	0.219	0.338	-0.085	0.213	-0.597
F20scale	15:	-0.424 ..	0.034	-0.006	0.079	0.590	0.481	-0.161	0.042	0.291
alat	16:	-0.020 ..	0.025	-0.025	0.007	0.039	-0.209	-0.533	0.018	-0.016
clat	17:	-0.018 ..	-0.033	0.037	-0.052	-0.008	-0.093	-0.277	0.007	-0.012
Ca1z	18:	-0.010 ..	-0.074	0.075	0.002	0.027	-0.017	0.003	0.002	-0.002
beqCa1	19:	0.267 ..	-0.068	-0.052	0.042	0.060	0.040	-0.026	0.007	0.051
Ca2x	20:	0.007 ..	-0.313	0.175	-0.325	0.079	0.071	-0.009	-0.021	0.010
Ca2y	21:	-0.022 ..	-0.318	0.091	-0.342	0.136	0.062	-0.015	0.005	0.011
beqCa2	22:	0.347 ..	-0.121	-0.221	0.013	-0.063	0.030	0.008	-0.016	0.094
Bx	23:	0.014 ..	0.207	0.196	0.233	-0.038	0.015	0.002	-0.010	0.006
By	24:	-0.039 ..	0.258	0.119	0.176	-0.066	0.035	0.006	0.022	0.008
beqF	25:	0.224 ..	-0.031	-0.078	-0.009	0.023	0.042	-0.010	0.009	0.043
O1x	26:	-0.015 ..	0.168	-0.242	-0.429	-0.013	-0.006	0.004	0.022	-0.005
O1y	27:	0.026 ..	0.210	-0.176	-0.455	0.033	0.048	-0.016	0.037	0.005
beqS	28:	0.423 ..	-0.054	-0.132	0.136	-0.262	0.481	-0.223	0.038	0.359
O2x	29:	0.030 ..	0.136	0.156	0.235	0.024	-0.024	-0.001	0.035	-0.008
O2y	30:	-0.014 ..	0.232	0.064	0.150	-0.022	0.015	-0.035	0.042	-0.002
O3x	31:	-0.023 ..	0.305	-0.381	-0.080	0.057	0.004	0.002	0.001	0.012
O3y	32:	0.008 ..	0.360	-0.384	-0.017	0.064	-0.024	0.031	0.003	-0.005
O3z	33:	-0.022 ..	0.076	-0.018	0.060	0.025	-0.011	0.005	0.065	0.024

Eigenvalues	: 0.411E+01 ..	0.345E+00	0.333E+00	0.288E+00	0.188E+00	0.158E+00	0.146E+00	0.718E-01	0.212E-01